UNIVERSITÄT ZU LÜBECK

From the Department of Internal Medicine I
of the University of Lübeck
Director: Prof. Dr. med. Dr. h.c. Hendrik Lehnert

Resistance is futile - A collective of epigenetically reprogrammed genes leads to diet-induced hepatic insulin resistance.

Dissertation
for Fulfillment of Requirements
for the Doctoral Degree
of the University of Lübeck

– From the Department of Natural Sciences –

Submitted by
Cathleen Geißler
from Lübben

Lübeck 2019

First referee: Dr. rer. nat. Henriette Kirchner

Second referee: Prof. Dr. rer. nat. Kristina Kusche-Vihrog

Date of oral examination: 27.01.2020

Approved for printing. Lübeck, 29.01.2020

Declaration

Hereby I declare that I have written the present dissertation without any assistance of third parties and have not used outside sources without declaration in the text. This dissertation has not been submitted in the same or similar version, not even in part, to any other authority for grading.

Erklärung

Ich versichere, dass ich die Dissertation ohne fremde Hilfe angefertigt und keine anderen als die angegebenen Hilfsmittel verwendet habe. Weder vorher noch gleichzeitig habe ich andernorts einen Zulassungsantrag gestellt oder diese Dissertation vorgelegt. Ich habe mich bisher noch keinem Promotionsverfahren unterzogen.

Lübeck, September 2019 .....

(Cathleen Geißler)

"*There's still much to do, still so much to learn.*"

Captain Jean-Luc Picard

Contents

List of Figures

List of Tables

Abbreviations

ΔCt	ΔCt value, calculated by $\Delta\text{Ct} = Ct_{\text{Target}} - Ct_{\text{Housekeeper}}$
µg	Microgram
µl	Microliter
µM	Micromolar, micromol per liter
µm	Micrometer
/5Biosg/	Biotinylation
Acaca	Gene encoding acetyl-CoA carboxylase 1
Acacb	Gene encoding acetyl-CoA carboxylase 2
Acadl	Gene encoding acyl-CoA dehydrogenase, long chain
ACC	Acetyl-CoA carboxylase
ACLY	ATP citrate lyase
Acox1	Gene encoding peroxisomal acyl-coenzyme A oxidase 1
ADP	Adenosine diphosphate
Akt	Protein kinase B (PKB)
AMPK	AMP-activated protein kinase
ANOVA	Analysis of variance
ApoE	Apolipoprotein E
APS	Ammonium persulfate
ATP	Adenosin triphosphat
BCA	Bicinchoninic acid
bp	Base pairs
BSA	Bovine serum albumin
C57BL/6	Common laboratory inbred mouse strain
CD36	Cluster of differentiation 36/platelet glycoprotein 4/fatty acid translocase (FAT)
cDNA	Complementary DNA
cds	Coding sequences
CHARM	Comprehensive high-throughput arrays for relative methylation
ChoRE	Carbohydrate response element
ChREBP	Carbohydrate response element binding protein
CPT1	Carnitine palmitoyltransferase 1
cRNA	Complementary RNA, *in vitro* transcribed from cDNA
Ct	Threshold cycle in qRT-PCR
Cu^{1+}	Monovalent cupper ion
Cu^{2+}	Divalent cupper ion
CYP4a	CYP4 subfamily A
DABG	Detection above background
dATPαS	Deoxyadenosine α-thio triphosphate
DEG	Differentially expressed gene
DEPC	Diethyl-pyro-carbonate, used to remove RNAases from water
DMR	Differentially methylated region
DNA	Deoxyribonucleic acid
dNMP	Deoxynucleotide monophosphate
DNMT	DNA methyltransferase, enzyme adding methyl-groups to the 5'-position of cytosine
dNTP	Deoxynucleotide triphosphate
DTT	Dithiothreitol
DUSP6	Dual specificity phosphatase 6
EDTA	Ethylene-diamine-tetraacetic acid, a chelating molecule
ELISA	Enzyme-linked immunosorbent assay

ERK	Extracellular signal-regulated kinase, also called MAPK
FAS	Fatty acid synthase
Fasn	Gene encoding fatty acid synthase
FC	Fold change
FDR	False discovery rate
FGF	Fibroblast growth factor
FGFR	Fibroblast growth factor receptor
Fig.	Figure
FRS2α	Fibroblast growth factor receptor substrate 2α
frw	Forward primer
G6PC	Glucose-6-phosphatase
G6PT	Glucose-6-phosphate transporter
Galnt2	Gene encoding polypeptide N-acetylgalactosaminyltransferase 2
GDP	Guanosine diphosphate
GLUT4	Glucose transporter 4
GTP	Guanosine triphosphate
GWAS	Genome-wide association study
HFD	High fat diet
HFHS	High fat-high sucrose diet
HK	Housekeeper
Hprt	Gene encoding hypoxanthine phosphoribosyltransferase 1
Ile	Isoleucin
InsRec	Insulin receptor
kcal	Kilocalories
KEGG	Kyoto Encyclopedia of Genes and Genomes
Klb	Gene encoding β-Klotho
LDH	Lactate dehydrogenase
Leu	Leucin
logFC	Logarithmic fold change
M.SssI	CpG Methyltransferase from Spiroplasma sp. strain MQ1
m/s	Meter per second
MAPK	Mitogen-activated protein kinase, also called ERK
McrBC	Restriction enzyme specifically cleaving DNA containing methylated cytosine
MELUR	Ministerium für Energiewende, Landwirtschaft, Umwelt und ländliche Räume
mg	Milligram
mg/kg	Milligram per kilogram
$MgCl_2$	Magnesium chloride
min.	Minutes
miRNA	MicroRNA
mM	Millimolar, millimol per liter
mm	Millimeter
mRNA	Messenger RNA
mTORC	Mammalian target of rapamycin complex
NAD^+	Nicotinamide adenine dinucleotide, oxidized form of NADH
NADH	Nicotinamide adenine dinucleotide, reduced form of NAD^+
NAFLD	Non-alcoholic fatty liver disease
NEFA	Non-esterified fatty acids
ng	Nanogram
ng/μl	Nanogram per microliter
nm	Nanometer
NP-40	Nonidet P-40, Octoxinol 9
pAkt	Phosphorylated Akt
PCA	Principal component analysis
Pck1	Gene encoding phosphoenolpyruvate carboxykinase 1
PCR	Polymerase chain reaction
PEPCK	Phosphoenolpyruvate carboxykinase
Pi	Phosphate
PI3K	Phosphoinositid-3-kinase
PK	Pyruvate kinase
Pklr	Gene encoding liver-type pyruvate kinase
PLCγ	Phospholipase C γ

PMSF	Phenylmethylsulfonyl fluoride
PPAR	Peroxisome proliferator-activated receptors
Ppara	Gene encoding PPARα
Pparg	Gene encoding PPARγ
PPi	Diphosphate/pyrophosphate
Ppia	Gene encoding peptidylprolyl isomerase A (cyclophilin A)
PPRE	PPAR responsive element
PVDF	Polyvinylidene difluoride
qRT-PCR	Quantitative real-time polymerase chain reaction
ref-sample	Reference sample
rev	Reverse primer
RIPA	Radioimmunoprecipitation assay buffer
RNA	Ribonucleic acid
ROX	Carboxy-X-rhodamine, passive reference dye
Rpl37	Gene encoding ribosomal protein L37
rpm	Revolutions per minute
RXR	Retinoid receptor X
s	Seconds
SAH	S-adenosylhomocysteine
SAM	S-adenosylmethionine
SCD1	Stearoyl-CoA desaturase 1
SD	Standard deviation
SDS	Sodium dodecyl sulfate
SDS-PAGE	Sodium dodecyl sulfate polyacrylamide gel electrophoresis
SEM	Standard error of the mean
seq	Sequencing primer
Sgms2	Gene encoding sphingomyelin Synthase 2
SIK3	Salt-Inducible Kinase 3
SIRT1	Sirtuin 1
SMS2	Sphingomyelin Synthase 2
SNP	Single-nucleotide polymorphism
SPRY	Sprouty
SREBP	Sterol regulatory element-binding proteins
STAT	Signal transducers and activators of transcription
Suppl.	Supplement
Tab.	Table
TAE	Tris-Acetat-EDTA
TBS	Tris-buffered saline
TCA	Tricarboxylic acid or citric acid cycle
TE	Tris-EDTA
TEMED	N,N,N',N'-tetramethylethane-1,2-diamine
TET	Ten-eleven translocation, enzyme removing DNA methylation
Tris	Tris(hydroxymethyl)aminomethane
UTR	Untranslated region
V	Volt
Val	Valin
WGA	Whole genome amplification
WGBS	Whole-genome bisulfite sequencing
wk	Week

Abstract

The increasing prevalence of obesity and type 2 diabetes represents a major global challenge. One reason for this is the lack of long-acting, efficient anti-diabetic therapies which is also the result of our incomplete understanding of the disease causes. Type 2 diabetes is associated with epigenetic changes and it was shown that diabetic subjects and insulin resistant mice have altered DNA methylation. However, it is unclear if changes of DNA methylation are causal or consecutive for insulin resistance. Therefore, in the scope of this thesis a longitudinal study with diet-induced obese mice fed with high fat diet (HFD) was performed to investigate the development of insulin resistance and the associated DNA methylation changes in a time-resolved manner.

The phenotypical characterization of the diet-induced obese mice revealed impaired whole-body glucose tolerance as well as development of fatty liver after five weeks of feeding. Already one week of HFD feeding led to transcriptional changes as measured by gene expression microarrays and alterations of metabolic pathways. This is even more pronounced after 12 weeks of HFD feeding, the HFD week 12 group is clearly distinguishable from the other groups solely by the transcriptomic changes. Furthermore, feeding HFD for 12 weeks leads to alterations of the fatty acid metabolism and the peroxisome proliferator-activated receptor (PPAR) signaling pathway. Whole genome bisulfite sequencing revealed that this is associated with extensive changes of DNA methylation in the HFD group. Here, it was shown for the first time that the vast increase of hepatic *Fgf21* gene expression in insulin resistance is associated with significant hypomethylation at two CpG sites within exon 1. The alterations of DNA methylation precede the development of whole-body glucose intolerance and likely occur before manifestation of hepatic insulin resistance.

Taken together, the study presented here could show that insulin resistance is associated with extensive metabolic changes and this is presumably induced by alterations of DNA methylation. This provides new, valuable insights in the development of insulin resistance which could be used for the design of novel anti-diabetic drugs.

Zusammenfassung

Die zunehmende Prävalenz von Adipositas und Typ 2 Diabetes stellt eine große globale Herausforderung dar. Es fehlen noch immer langfristig wirksame Therapien gegen Typ 2 Diabetes, weil die Ursachen der Erkrankung bisher nur unvollständig aufgeklärt sind. Typ 2 Diabetes ist mit Veränderungen der DNA-Methylierung assoziiert, es ist allerdings unklar, ob DNA-Methylierung kausal oder konsekutiv für die Erkrankung ist. Um die Entstehung der Insulinresistenz und die damit assoziierten DNA-Methylierungsmuster zu untersuchen wurde im Rahmen dieser Doktorarbeit eine longitudinale Studie mit Diät-induzierten adipösen Mäusen durchgeführt.

Die phänotypische Charakterisierung des Mausmodells zeigte, dass nach fünf Wochen Hochfettdiät (HFD)-Fütterung die systemische Glucosetoleranz vermindert ist und die Tiere eine Fettleber entwickelt haben. Bereits eine Woche HFD-Fütterung führte zu größtenteils verminderter Transkription metabolischer Gene. Nach zwölf Wochen hochkalorischer Diät waren diese Veränderung noch stärker ausgeprägt und die Diät-induzierten adipösen Mäuse konnten allein anhand der Genexpression von den anderen experimentellen Gruppen unterschieden werden. Darüber hinaus waren Gene des Fettstoffwechsels und des Peroxisom-Proliferator-aktivierte Rezeptoren (PPAR)-Signalwegs verändert. Mittels 'whole-genome bisulfite sequencing' konnte gezeigt werden, dass die veränderte Genexpression von Veränderungen der DNA-Methylierung begleitet wird. So ist zum Beispiel der Anstieg der *Fgf21*-Transkription bei Insulinresistenz mit einer signifikanten Hypomethylierung an zwei CpG-Dinucleotiden innerhalb von Exon 1 assoziiert. Diese epigenetischen Modifikationen gehen der Entstehung der systemischen Glucoseintoleranz voraus und werden wahrscheinlich bereits vor Manifestation der hepatischen Insulinresistenz etabliert.

Zusammenfassend konnte gezeigt werden, dass HFD-induzierte Insulinresistenz mit Veränderungen des Fettstoffwechsels einhergeht und vermutlich durch DNA-Methylierung reguliert wird. Die hier präsentierte Studie ermöglicht neue Einblicke in die Entstehung von Insulinresistenz und eröffnet damit neue Mechanismen, die für die Entwicklung von anti-diabetischen Medikamenten genutzt werden könnten.

1

Introduction

1.1 Epigenetics

"*Change is the essential process of all existence.*"

Mr. Spock

Epigenetics describe inheritable, reversible modifications of DNA and histones to differentially modulate gene expression without changing the underlying DNA sequence [125, 144]. Epigenetics include histone modifications, DNA methylation at CpG dinucleotides, and also post-transcriptional regulation of gene expression by non-coding RNAs, such as microRNAs (Fig. 1.1) [138, 171].

Histone modifications regulate accessibility of DNA for the RNA polymerase II and transcription factors by modulating chromatin packaging [138, 144]. The four histones are organized as octameric core wrapped by 147 bp of DNA to form a nucleosome [144]. The histone tails are exposed and can be modified, among others, by phosphorylation, methylation, and acetylation [144]. The cumulative effect of many different modifications at a nucleosome determines if transcription is favored or inhibited [144]. This so-called histone code is very dynamic [144].

DNA methylation describes the addition of a methyl group to the 5'-position of a cytosine in the sequence context of CpG dinucleotides (a cytosine followed by a guanine) [101]. DNA methylation in mammals was also identified in other sequence contexts, but the functions of these modifications are not well understood yet [101]. DNA methylation is associated with silencing of genes and retrotransposons, genomic imprinting and X-chromosome inactivation as well as chromosomal stability by DNA methylation of repeat regions, such as centromeres [55, 101, 138].

During development, extensive epigenetic reprogramming occurs which is associated with two genome-wide demethylation events [55]. The first epigenetic reprogramming takes place in primordial germ cells, the second during early embryonic development [44, 55]. Furthermore, cell type-specific DNA methylation patterns are established during differentiation [44]. The time frame of remethylation is a crucial period, because environmental factors could potentially influence DNA methylation [44, 138]. DNA methylation depends on one-carbon metabolism which in turn depends

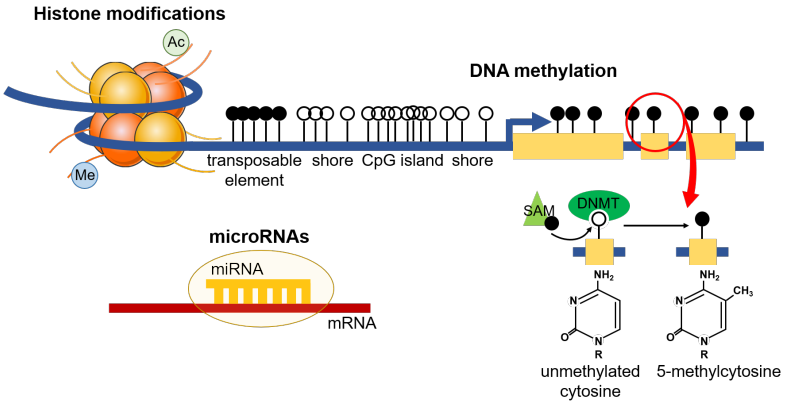

Figure 1.1: Overview of epigenetic mechanisms. Epigenetics comprise of histone modifications, microRNAs, and DNA methylation at cytosines in CpG dinucleotides. Modifications at histone tails regulate the accessibility of DNA for the transcriptional machinery, whereas microRNAs suppress translation or induce degradation of mRNAs. DNA methylation regulates gene transcription, silences transposable elements, and is associated with genomic imprinting. DNA methylation is established by DNA methyltransferases (DNMT) by transferring the methyl group of S-adenosylmethionine (SAM) to the 5'-position of cytosine. DNA methylation was extensively studied at CpG islands, regions of approximately 200 bp containing a high CpG density, which are commonly unmethylated. They are surrounded by an approximately 2 kb long CpG shore with decreasing CpG density. Within gene bodies, DNA methylation levels are higher compared to promoter regions.

on dietary micronutrients, especially folate [125, 157]. Folate is important for methionine production which is converted to S-adenosylmethionine (SAM), the universal methyl donor [125, 157]. The methyl group of SAM is covalently added to the 5'-position of cytosine by DNA methyltransferases, the enzymes establishing DNA methylation of CpG dinucleotides, resulting in the conversion of SAM to S-adenosylhomocysteine (SAH) [125]. SAH inhibits SAM-dependent methyltransferases and a continuous hydrolysis of SAH is important to maintain DNA methylation [44].

There are three isoforms of DNA methyltransferases (DNMTs): DNMT1, DNMT3A, and DNMT3B [44]. DNA methyltransferase 1 transfers the DNA methylation pattern to newly synthesized DNA strands during DNA replication, hence, it is called maintenance methyltransferase [55, 144]. It preferentially methylates hemimethylated DNA and possesses an auto-inhibitory mechanism preventing *de novo* methylation [55, 144]. DNMT1 plays a crucial role in embryonic development and knockout of DNMT1 in differentiated cells is lethal [102]. DNMT3A and DNMT3B are *de novo* methyltransferases methylating fully unmethylated or hemimethylated CpG sites [44, 102]. They are mainly active during development to establish methylation patterns in the course of epigenetic reprogramming and lack of these enzymes is lethal [44, 102].

DNA methylation can be removed passively by DNA replication or actively by ten-eleven translocation (TET) methylcytosine dioxygenases [101, 216]. Humans possess three TET enzymes with different tissue-specific gene expression: TET1-3 [216]. Active DNA demethylation is independent of DNA replication and includes the oxidation of 5-methylcytosine to 5-hydroxymethylcytosine, 5-formylcytosine, and/or 5-carboxylcytosine [216]. This is caused by different activities of the TET

isoforms, at least in humans TET1 and TET2 show higher activity for 5-methylcytosine [216]. Subsequently, the oxidized cytosines are removed by DNA base-excision repair [216].

It is suggested that over 80% of the CpG sites in the human genome are methylated, except for those in CpG islands and regulatory sequences [55, 142]. CpG islands are approximately 200 bp long regions found mainly within promoters with 10-fold higher CpG density compared to the rest of the genome (Fig. 1.1) [44, 55, 101]. CpG islands are surrounded by an approximately 2 kb long CpG shore which contains lower CpG density [44]. CpG islands in somatic cells often show less than 10% DNA methylation and this is associated with nucleosome-depleted regions [101, 142]. Methylated CpG islands in promoter regions are associated with silenced genes, however, it is not fully understood if DNA methylation initiates silencing or represents a mechanism to reinforce the silenced state [98, 101].

Recently, also DNA methylation outside of CpG islands, within the gene body, got more and more attention [98, 142]. Compared to promoter regions, gene bodies are in general CpG poor but extensively methylated [98, 101]. It was suggested that gene body DNA methylation functions in suppression of intragenic transcription start sites for more efficient transcriptional elongation [98]. However, this does not sufficiently explain the abundance of gene body DNA methylation [98]. Gene body DNA methylation is associated with open chromatin and transcription, therefore, DNA accessibility seems to determine gene body DNA methylation by influencing the binding of methyltransferases to DNA [98, 101]. Silenced genes are characterized by compact chromatin which allows no binding of methyltransferases to DNA leading to low DNA methylation levels [98]. Gene expression needs opening of the chromatin for transition of the RNA polymerase making DNA accessible for methyltransferases [98]. Highly expressed genes exhibit a high density of RNA polymerases which interferes with the binding of methyltransferases and thus, decreases DNA methylation [98]. In conclusion, low and high expressed genes show lowest DNA methylation, whereas moderately expressed genes show highest DNA methylation levels [98]. But DNA methylation also varies within gene bodies dependent on CpG site location, for example exons show higher DNA methylation than introns and first exon DNA methylation differs from the more downstream exons [21, 101, 251].

DNA methylation at enhancers could have regulatory functions, for example DNA methylation at transcription factor binding sites modifies binding of methylation-sensitive transcription factors [101]. Furthermore, methylated CpG sites at specific motifs can favor the binding of methyl-CpG-binding domain proteins which prevent the binding of transcription factors [86]. Thereby, DNA methylation influences gene expression [86].

1.1.1 Measurement of DNA methylation

The measurement of DNA methylation gets more and more attention in the clinics for biomarker identification to refine diagnostics of various diseases, such as cancer or type 2 diabetes [113, 174].

Several methods for DNA methylation quantification were developed, but they differ in the amount and quality of required input DNA, sensitivity, specificity, robustness, and costs [119]. Furthermore, bioinformatic data analysis and interpretation becomes increasingly important and can represent the bottleneck [174]. Whole-genome approaches are used for high-throughput analysis of a large number of loci and provide quantitative DNA methylation information [174]. However, measurement of genome-wide DNA methylation is not free of disadvantages: The methods are often cost-intensive, suffer from library bias, and special equipment is needed [174]. Therefore, DNA methylation measurement in specific genes or regions of interest are also popular. Many of these methods are based on bisulfite-converted DNA, because during PCR amplification DNA methylation information is lost [115]. Bisulfite treatment is the gold standard for measurement of DNA methylation, because it is qualitative, quantitative, efficient, and achieves single-base resolution [130]. To distinguish between methylated cytosines and unmethylated cytosines DNA is treated with bisulfite salt and a buffer leading to a low pH [130]. After thermal denaturation, unmethylated cytosines are sulfonated and deaminated converting them to uracil sulfonate (Fig. 1.2 (a)) [115]. The last step of the bisulfite conversion is a desulfonation reaction leading to uracil (Fig. 1.2 (b)) [115]. Methylated cytosines are not affected by this treatment (Fig. 1.2 (c)) [115]. By performing a bisulfite PCR previously unmethylated cytosines appear as thymine, whereas methylated cytosines stay cytosine [115]. This leads to a reduction of the number of bases in the DNA from four to three and the sense and antisense DNA strands are no longer complementary to each other [115]. The bisulfite-converted DNA is then analyzed. Disadvantages of bisulfite treatment are the harsh conditions leading to fragmentation of DNA and the risk of incomplete conversion [130]. This section gives a short overview of methods for genome-wide and gene-specific DNA methylation measurement methods.

Whole-genome bisulfite sequencing (WGBS). WGBS couples bisulfite conversion of DNA with next-generation sequencing and thereby, achieves single-base resolution [166, 245]. Next-generation sequencing is a sequence-by-synthesis method starting with the preparation of a library of adapter-ligated DNA fragments [90]. Bisulfite treatment can precede or succeed fragmentation, however, bisulfite conversion prior adapter ligation reduces bias [90, 176]. The adapter-ligated DNA fragments are loaded into a flow cell which contains oligonucleotides complementary to the adapters [90]. Subsequently, each immobilized fragment is amplified and sequenced [90]. For data analysis the reads are mapped to a reference genome and DNA methylation is determined by the ratio of cytosines and thymines at a specific CpG site [245].

BeadChip arrays. The probably best-known array-based method is the Infinium Human Methylation 450K BeadChip array which allows the measurement of over 450 000 CpG sites in 99% of all known genes [119]. However, the array contains mainly probes for promoter and other regulatory regions [119]. Initially, DNA is bisulfite-converted followed by whole-genome amplification for

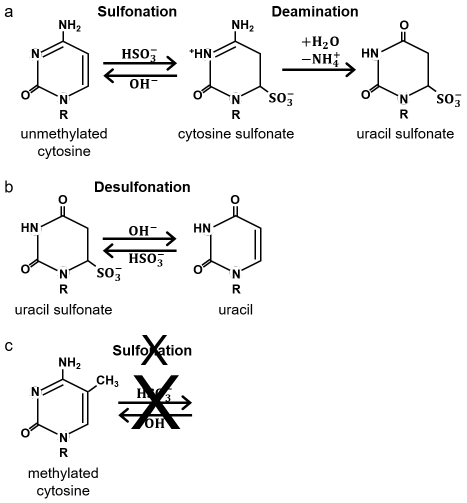

Figure 1.2: Schematic illustration of the bisulfite reaction. (a) Unmethylated cytosine is sulfonated by treatment with bisulfite salt, high temperatures, and a low pH leading to cytosine sulfonate. The subsequent deamination converts cytosine sulfonate to uracil sulfonate. (b) The final step of the bisulfite conversion is the desulfonation which produces uracil. (c) Methylated cytosine is not converted and remains cytosine in the final bisulfite-converted DNA. Schematic illustration modified from Kristensen and Hansen (2009) [115].

subsequent fragmentation and hybridization with oligonucleotides [174]. The oligonucleotides are designed as pairs, one complementary to unmethylated DNA (thymine) and the other to methylated DNA (cytosine) [119, 174]. This is followed by labeling of the hybridized DNA fragments to generate a detectable product [119]. To determine DNA methylation, the ratio of the signals for the probe pairs is calculated [119]. The array has single-base resolution, is less time-consuming compared to sequencing-approaches, and only small DNA amounts are necessary [174, 252]. Disadvantages are the limitation of probe design, because they can generate artifacts [47, 174]. Since bisulfite treatment results in DNA with only three bases instead of four, this can introduce cross-reactivity of the probes, it is estimated that 10-25% of all probes are unspecific [47]. Moreover, the Infinium Human Methylation 450K BeadChip is only available for humans but not for other species and only high DNA methylation changes can be detected [47, 119].

Comprehensive high-throughput arrays for relative methylation (CHARM).

CHARM is a genome-wide and array-based approach which, in contrary to many other array-based DNA methylation measurement methods, is not restricted to CpG islands and promoter regions but can also assess regions with low CpG density [122, 173]. CHARM uses McrBC, a restriction enzyme cleaving methylated DNA, to fractionate the DNA and enrich unmethylated sequences [173, 252]. Besides McrBC digestion, mock digestion is performed which represents the input fraction of DNA [122]. Both digested and undigested DNA is labeled differently and co-hybridized to a microarray [122]. Methylated sequences will be found in the undigested input fraction and are reduced in the digested fraction [122].

Bisulfite pyrosequencing. The gold standard for measuring DNA methylation is bisulfite pyrosequencing, a sequence-by-synthesis method using a coupled enzyme reaction to detect the incorporation of a nucleotide [5, 166, 174]. DNA is bisulfite-converted and after PCR amplification with a biotinylated primer the PCR product is pyrosequenced [174]. After hybridization of the sequencing primer to the PCR product an enzyme mixture as well as a substrate mixture is added followed by the first nucleotide [191]. The enzyme mixture contains DNA polymerase, ATP sulfurylase, apyrase, and luciferase [191]. The substrate reagent consists of adenosine-5'-phosphosulfate and luciferin [5]. Only one nucleotide at a time is dispensed [5]. If the nucleotide is complementary to the template sequence it is incorporated by the DNA polymerase which generates a diphosphate (also called pyrophosphate, PPi) [5]. Each individual incorporation generates one diphosphate. Therefore, the amount of PPi is equimolar to the number of complementary nucleotides [5]. The PPi is used by the ATP sulfurylase to produce ATP from adenosine-5'-phosphosulfate [5]. The ATP is utilized by the luciferase to convert luciferin to oxyluciferin which is accompanied by the release of light [5]. The light is proportional to the amount of ATP and therefore, to the number of incorporated nucleotides [5]. The light signal is detected and used for the calculation of DNA methylation level [191]. The apyrase degrades the unincorporated nucleotides [5]. To discriminate between ATP generated by the ATP sulfurylase and ATP which is normally used as nucleotide for incorporation in the new DNA strand, Qiagen provides deoxyadenosine α-thio triphosphate (dATPαS) for sequencing [191]. DNA methylation at a CpG site is determined by the ratio of incorporated thymine to cytosine [119]. Bisulfite pyrosequencing is an easy and fast method with high reproducibility [174]. Furthermore, with bisulfite pyrosequencing a single-base resolution is achieved, but only about 100 bp can be maximally sequenced at a time [119]. Therefore, only a region of interest can be studied and it is not suited for high-throughput approaches [174].

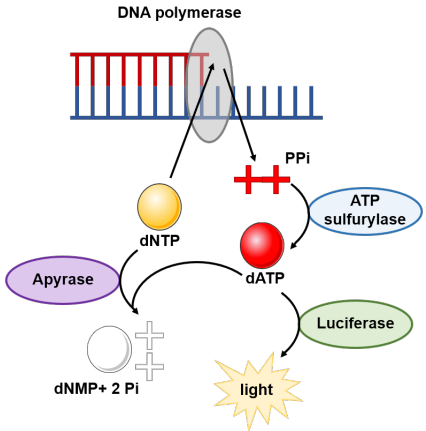

Figure 1.3: Overview of the coupled enzyme reaction of bisulfite pyrosequencing. The incorporation of a nucleotide (dNTP) by the DNA polymerase produces a diphosphate (PPi) which is used by the ATP sulfurylase for the generation of ATP. ATP is a substrate of the luciferase which produces light in equimolar amounts to the number of incorporated nucleotides. Nucleotides which were not incorporated and ATP are degraded by the apyrase. Modified according to the 'PyroMark Q48 Autoprep User Manual' [191].

1.1.2 DNA methylation and disease

The reversibility of epigenetic modifications provides genomic flexibility to respond to changing environments, however, epigenetic changes can also induce pathological alterations [157, 215]. Cancer might be the best-known example for a disease associated with changes of DNA methylation [101, 157]. Cancer is associated with a genome-wide DNA hypomethylation and *de novo* hypermethylation in promoter regions of tumor suppressor genes [75, 101]. This leads to silencing of these genes favoring the development of tumors [101].

However, environmental induced alterations of DNA methylation can also induce other noncommunicable diseases, such as asthma, obesity, neurodegenerative disorder, psychological disorder, nonalcoholic hepatosteatosis, and type 2 diabetes [75, 157, 215]. For instance, it was shown that obese non-diabetic and type 2 diabetic individuals show DNA hypomethylation in genes regulating glucose metabolism resulting in a potential shift of the hepatic metabolism to increased glycolysis and *de novo* lipogenesis [110]. Important milestones of epigenetic studies of the development of type 2 diabetes were transgenerational studies. It was observed that maternal undernutrition during early pregnancy leads to uterine growth retardation, low birth weight, and long-term alterations of the metabolism with higher risk for type 2 diabetes and obesity in the offspring [125]. However, hepatic epigenetic alterations associated with type 2 diabetes can also be acquired later in life without any metabolic deteriorations of the parents [163, 256].

1.2 Whole-body energy homeostasis

The whole-body energy metabolism is regulated by balancing energy intake with energy expenditure to maintain body weight [63]. During fasting conditions, the pancreas secretes glucagon which stimulates hepatic glycogen degradation and gluconeogenesis to prevent a drop of blood glucose levels [198]. Furthermore, adipose tissue lipolysis rate is increased and non-esterified fatty acids (NEFA) are supplied as substrate for fatty acid β-oxidation and energy production [58, 100]. Postprandially, the digestion of food provides a plethora of nutrients and circulating blood glucose levels increase [58, 100]. This induces insulin secretion by pancreatic β-cells stimulating insulin-dependent glucose uptake in adipose tissue and skeletal muscle by insulin-responsive glucose transporter type 4 (GLUT4) [198]. However, only 5-10% of circulating glucose is taken up by adipose tissue, most of the glucose is transported into skeletal muscles and insulin-independently into liver [3, 58, 218]. Moreover, insulin induces glycogen synthesis and *de novo* lipogenesis by simultaneously inhibiting fatty acid β-oxidation and glucose production [100, 117, 198]. In adipose tissue, insulin inhibits lipolysis and circulating free fatty acid levels are reduced [58]. The pancreatic insulin secretion is further promoted by gut-derived peptide hormones called incretins which are secreted upon a meal [198]. Also other metabolic tissues secrete signaling molecules which are important for inter-organ

communication and influence metabolism [93]. Several peripheral endocrine and metabolic signals can be integrated by the hypothalamus to regulate food intake and energy expenditure centrally [109]. This indicates an extensive crosstalk between different tissues to regulate metabolism.

1.3 The liver as metabolic tissue

The liver is a central organ for metabolic coordination due to its functions in synthesis, breakdown, storage, and redistribution of nutrients [178]. The liver is able to recognize the availability of nutrients to regulate and maintain systemic requirements, for example it plays a role in biotransformation of xenobiotics and bile acid synthesis [108, 178]. Furthermore, it is the major tissue for carbohydrate and lipid metabolism and regulates systemic glucose levels under different nutritional conditions [100]. Since all these processes take place in parallel, the liver parenchyma is functionally divided into different metabolic zones which also contain various cell types [108]. The smallest structural unit is called lobule, a hexagonal structure with a central vein [108]. Each corner of the lobule consists of a branch from the portal vein, hepatic artery, and bile duct and is called portal triad [108]. The hepatocytes within a lobule radiate out from the central vein to the portal triad and have contact to blood vessels at each side [108]. In the blood vessels, liver-residing macrophages, so-called Kupffer cells, are found and in the space between endothelial cells and hepatocytes hepatic stellate cells, which store fat and vitamin A, are located [108]. In terms of function, the acinus is the important hepatic unit which is obtained by connecting two portal triads with two adjacent central veins [108]. Within these units, the hepatocytes substantially differ in their subcellular, biochemical, and physiological function leading to a metabolic zonation [108]. Thereby, opposing pathways are separated and substrate competition is minimized [108]. For example gluconeogenesis and fatty acid β-oxidation take place in the periportal zone where hepatocyte receive blood rich in nutrients, oxygen, and hormones, whereas *de novo* lipogenesis and glycolysis take place in the perivenous zone near the central vein [81, 108, 117]. This also means that metabolic enzymes show a zonated location, although zonation is quiet dynamic and can switch depending on physiological and pathophysiological conditions [81].

1.3.1 Hepatic fatty acid metabolism

Fatty acids are the most frequent storage form of energy containing approximately twice as much energy than carbohydrates and proteins [152, 169]. Furthermore, they represent important components of membranes, act as signaling molecules, serve as post-translational modifications, and regulate the activity of transcription factors [8, 169]. Hepatic fatty acid content is determined by fatty acid uptake, synthesis, degradation, and export [184]. Intracellular fatty acid concentration

and localization is tightly regulated and in healthy subjects the liver stores only a small amount of fat [8]. Due to the lipotoxic potential of fatty acids they are stored as neutral triglycerides [8].

Fatty acids and triglycerides can be synthesized in hepatocytes *de novo* from acetyl-CoA in a process called *de novo* lipogenesis [9, 184, 206]. A diet rich in carbohydrates activates *de novo* lipogenesis, whereas fasting and a high fat supply inhibits *de novo* lipogenesis [169, 206]. Increased rates of *de novo* lipogenesis are associated with metabolic diseases [206]. The first step to synthesize fatty acids is the conversion of citrate to acetyl-CoA by ATP-citrate lyase (ACLY) [8]. Acetyl-CoA is converted to malonyl-CoA by acetyl-CoA carboxylase (ACC) [206]. There are two isoforms of ACC: ACC1 and ACC2 [206]. Malonyl-CoA derived from ACC1 is used by the multifunctional enzyme fatty acid synthase (FAS) to catalyze the whole reaction of palmitic acid/stearic acid synthesis [8, 169, 206]. Since FAS is the rate-limiting enzyme of *de novo* lipogenesis it is extensively regulated, for instance insulin and substrate availability activate FAS, whereas glucagon inhibits FAS [169]. The nutritional state also impacts FAS activity, a high amount of intracellular fatty acids decreases FAS activity [169]. Fatty acids synthesized by FAS can be converted to unsaturated fatty acids by SCD1 which inserts a double bond resulting in mono-unsaturated fatty acids, such as palmitoleate and oleate [151].

De novo lipogenesis is regulated on the transcriptional level by sterol regulatory element binding protein 1c (SREBP-1c) and carbohydrate response element binding protein (ChREBP) [206]. SREBP-1c is an important regulator of lipid and cholesterol metabolism and itself is regulated by insulin on the transcriptional level and by post-translational processing [73, 206, 207]. ChREBP is activated by glucose-6-phosphate and binds to the carbohydrate response element (ChoRE) of target genes, for example *Fasn*, *Acaca*, and *Pklr* [206, 207]. Both ChREBP and SREBP-1c ensure that *de novo* lipogenesis is only active when glucose and insulin are present [207].

The uptake of non-esterified fatty acids derived from adipose tissue lipolysis is mediated by for example fatty acid translocase (FAT)/CD36 [8, 169]. To metabolize fatty acids after entry into the cell they have to be activated by thioesterification resulting in fatty acyl-CoA which can be oxidized for energy generation [8, 169]. During mitochondrial β-oxidation, fatty acids are oxidized to acetyl-CoA which can be completely oxidized in the TCA cycle or incompletely by ketogenesis [8]. Fatty acids longer than 14 carbons enter the mitochondria with the aid of carnitine palmitoyltransferase 1 (CPT1) [169]. The mitochondrial β-oxidation is coupled with *de novo* lipogenesis by malonyl-CoA synthesized by ACC2 which inhibits CPT1 and therefore, prevents the simultaneous activity of β-oxidation and *de novo* lipogenesis [169, 206].

The mitochondrial β-oxidation oxidizes short-chain, medium-chain, and long-chain fatty acids, but very long-chain fatty acids are degraded by peroxisomal β-oxidation [169]. The processes differ in the first step, in peroxisomes the initial dehydrogenation is replaced by an oxidation reaction which produces H_2O_2 [169]. Peroxisomal β-oxidation results in shortened fatty acids which can be

fully oxidized by mitochondria [169]. Furthermore, peroxisomes do not possess an electron transport chain resulting in the production of less ATP compared to mitochondrial β-oxidation, but this pathway is helpful for the cell to handle a high availability of fatty acids [169]. Long-chain fatty acids can also be oxidized by CYP4A ω-oxidation to dicarboxylic acid [169]. All these oxidative pathways are co-operatively regulated and important for hepatic lipid homeostasis [169].

Feeding a diet very rich in fat will activate ketogenesis producing ketone bodies [169]. However, this results in less ATP compared to β-oxidation, but the conversion into water-soluble molecules is also a strategy for redistribution of energy [169].

Lipids represent not only an energy source, they are also important for membrane biogenesis [27]. Membranes consist of a variety of lipid species, for instance sphingolipids, of which sphingomyelin is the most abundant complex sphingolipid in mammals [27, 64]. The last step of sphingomyelin synthesis is catalyzed by sphingomyelin synthase 2 (SMS2), encoded by *Sgms2* [155]. SMS2 is also involved in the regulation of lipid drafts which are crucial for the correct compartmentalization of signaling pathways [136].

Also cholesterol is an essential component of membranes and the substrate for bile acid synthesis [27, 37]. It was suggested that SIK family kinase 3 (encoded by *Sik3*), a member of the AMPK-related kinase family, regulates cholesterol and bile acid metabolism but also functions in suppressing hepatic gluconeogenesis [94, 232].

1.3.2 Hepatic glucose metabolism

One important function of the liver is to maintain blood glucose levels in a physiological range despite changing energy demands of the body [178]. In the postprandial state, blood glucose levels rise and the liver shifts its metabolic pathways to glucose consumption and storage [178]. About 10-25% of the glucose is taken up by hepatocytes, mainly by GLUT2 [178]. In hepatocytes, glucose is phosphorylated to glucose-6-phosphate by glucokinase [178].

Increased glucose-6-phosphate levels stimulate glycogen synthesis by allosteric activation of glycogen synthase and simultaneously inhibit glycogenolysis by inhibiting glycogen phosphorylase [178]. Glycogen is the storage form of glucose and can be used for rapid release of glucose into the blood stream [73]. Glucose-6-phosphate can also enter glycolysis and the pentose phosphate pathway [178]. Glycolysis represents the critical pathway for glucose catabolism in most tissues to generate energy [73]. During glycolysis, glucose is metabolized to pyruvate which can be completely oxidized in mitochondria to generate ATP or used for *de novo* lipogenesis [201]. Glycolysis is predominantly active in the fed state when glucose levels are high [201]. The important, rate-limiting enzymes of glycolysis are glucokinase, phosphofructokinase-1, and liver-type pyruvate kinase (PK) [73]. These enzymes are regulated allosterically to couple their activity to the energy demands [73]. Glycolysis is also regulated on the transcriptional level during fed conditions by SREBP-1c and ChREBP [73].

In the post-absorptive phase, when glucose absorption in the intestine is completed, hepatic glucose production represents the major source of blood glucose [178]. This is especially important for tissues which solely rely on glucose as energy source, such as the brain [178]. Initially, hepatic glucose production is mainly determined by glycogenolysis, with prolonged fasting (more than 30 hours), gluconeogenesis becomes more and more predominant, because glycogen stores are depleted [73, 178]. During gluconeogenesis glucose is synthesized from fructose, lactate, alanine, or glycerol [3, 73]. Initially, the precursor molecules are converted to pyruvate which is carboxylated to oxaloacetate by pyruvate carboxylase [3]. This is followed by the synthesis of phosphoenolpyruvate by phosphoenolpyruvate carboxykinase (PEPCK) [3]. PEPCK catalyzes a rate-limiting step of gluconeogenesis [201]. In a series of reactions, which are the reversion of glycolysis, glyceraldehyde-3-phosphate is synthesized and reacts further to fructose-1,6-bisphosphate [3, 76]. Fructose-1,6-bisphosphate is converted to glucose-6-phosphate [3]. Glucose-6-phosphate from both gluconeogenesis and glycogenolysis is transported into the endoplasmic reticulum by the glucose-6-phosphate transporter (G6PT) and dephosphorylated by the glucose-6-phosphatase (G6PC) [178]. The resulting glucose is released into the bloodstream by GLUT2 [178].

1.4 Type 2 diabetes

Type 2 diabetes developed to a global health problem and the prevalence is steadily increasing [259]. The International Diabetes Federation estimated that 425 million adults aged 20-79 years suffered from diabetes in 2017 and this number will further increase to estimated 629 million cases in 2045 [38]. Due to diabetes-associated co-morbidities, type 2 diabetes often leads to premature death [175]. It is estimated that type 2 diabetes accounts for 9.9% of the global all-cause mortality among people aged 20-99 years in 2017 [38].

Diabetes mellitus encompasses a group of metabolic disorders with the key symptom chronic hyperglycemia which can be caused by reduced production of insulin by pancreatic β-cells or the inability of insulin to induce signaling in its target tissues, called insulin resistance [87].

Type 2 diabetes is caused by interactions of environmental, genetic, and behavioral factors making the disease multi-factorial [87, 175]. Often, type 2 diabetes is part of the metabolic syndrome, alongside with obesity, hyperlipidemia, and hypertension [175]. In the last decades, obesity developed to a primary risk factor for type 2 diabetes, it was estimated that obesity is involved in about 55% of all type 2 diabetes cases [87, 175].

1.4.1 Type 2 diabetes pathogenesis and therapy

Increased calorie intake and little physical activity leads to a positive energy balance resulting in obesity and associated development of insulin resistance [202]. Insulin resistance develops in adi-

pose tissue, skeletal muscle, liver, brain, and vasculature [58]. In adipose tissue and skeletal muscle, insulin resistance leads to impaired glucose uptake [205]. In liver, insulin resistance is characterized by the inability of insulin to inhibit hepatic glucose production [117]. The resulting hyperglycemia is compensated by increased pancreatic insulin secretion leading to hyperinsulinemia accompanied by elevated β-cell mass and β-cell function [16, 190]. However, in the long term this leads to β-cell dysfunction, β-cell failure, and apoptosis resulting in type 2 diabetes [190]. Additionally, without any therapeutic actions chronic hyperglycemia leads to long-term micro- and macrovascular damage as well as damage of several organs resulting in for example atherosclerosis, renal failure, and neuropathy [87].

Excess calorie intake also leads to accumulation of lipids not only in adipose tissues, but also for instance in skeletal muscle and liver [205]. Non-alcoholic fatty liver disease (NAFLD) is the most common chronic liver disease in western countries with a global prevalence in adults of 25% [96, 145]. NAFLD often precedes insulin resistance and hepatic lipid accumulation impairs insulin sensitivity, but insulin resistance also favors hepatic lipid accumulation [89, 145]. Intriguingly, hepatic insulin resistance is associated with increased gluconeogenesis and simultaneously increased *de novo* lipogenesis, termed selective insulin resistance [117]. For development of selective insulin resistance liver zonation could play a role [118]. It is suggested that hepatocytes in the periportal zone develop insulin resistance, whereas cells in the perivenous zone show enhanced insulin signaling [117]. The periportal zone is the main site of gluconeogenesis and the perivenous zone is the main location of *de novo* lipogenesis [118].

Different insulin-sensitive tissues vary in their insulin sensitivity and therefore, insulin resistance does not develop uniformly throughout the body [16]. For humans, it was reported that skeletal muscle shows early disturbances, but the liver seems to be more severely affected [45]. In high fat diet-fed rodents, insulin resistance develops rapidly in liver and adipose tissue, but in skeletal muscle much more slowly [16, 58].

There are several pharmacological therapies available to reduce hyperglycemia, but all anti-diabetic drugs show only a short effectiveness of some years [226]. When monotherapy is no longer sufficient to achieve an HbA1c lowering effect, different anti-diabetic drugs can be combined [226]. However, about 50% of the patients need insulin therapy within 10 years of disease progression which can be combined with oral anti-diabetic drugs [28, 226]. This demonstrates that more efficient diabetic drugs are needed for an effective disease control. Consequently, prevention strategies are of utmost importance [87, 226]. Lifestyle modifications towards healthier eating behavior and more exercise would be of primary interest, especially for patients with prediabetes, to delay progression and complications [226].

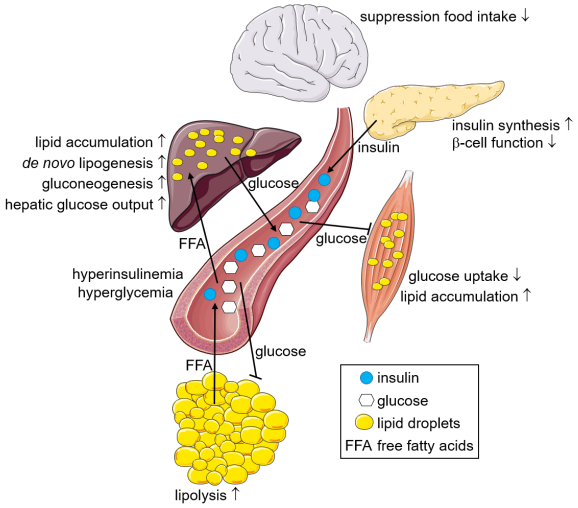

Figure 1.4: Insulin resistance involves multiple tissues. Insulin resistance is characterized by a reduced response of target tissues to insulin leading on the whole-body level to impaired glucose lowering effects and hyperglycemia [87]. Affected are tissues such as adipose tissue, skeletal muscle, liver, and brain [58]. In adipose tissue and skeletal muscles insulin resistance leads to impaired glucose uptake which is further exacerbated by elevated hepatic glucose production due to hepatic insulin resistance [117, 205]. The hyperglycemia is compensated by increased pancreatic insulin secretion leading to hyperinsulinemia and in the long term to β-cell dysfunction, β-cell failure, and apoptosis [16, 190]. Insulin resistance is commonly associated with excess calorie intake resulting in lipid accumulation in adipose and non-adipose tissues [205]. The lipid accumulation is further facilitated by the inability of insulin to suppress adipose tissue lipolysis leading to increased fatty acid release into the blood stream [205].

1.5 PPARα-FGF21 pathway

1.5.1 Peroxisome proliferator-activated receptors

Peroxisome proliferator-activated receptors (PPAR) are nuclear receptors which regulate nutrient-dependent gene expression upon activation by specific ligands [72, 123]. The receptors were first described as molecules inducing proliferation of peroxisomes in rodents which can induce liver cancer, however, this was not observed in humans [53, 72].

PPARs are fatty acid sensors controlling cellular proliferation, differentiation, and several metabolic pathways to maintain metabolic flexibility [53, 72, 123]. Furthermore, PPARα and PPARγ, two isoforms of the PPARs, were shown to possess anti-inflammatory effects [53].

The structure of PPARs is similar to other nuclear receptors, but they have an unusually large ligand binding pocket for different fatty acid species and derivatives [123]. The endogenous ligands are derived from diet, *de novo* lipogenesis, and lipolysis. Therefore, PPAR activation is coupled to the nutritional status [53]. For instance, it was shown that high fat diet feeding induces gene expression of target genes of PPARα and PPARβ/δ [53]. Tissue-dependent target gene specificity is achieved by epigenetic mechanisms, for example macrophage-specific binding regions of PPARγ are inaccessible in white adipocytes due to repressive histone modifications [53].

Upon ligand binding, PPARs get activated which induces a conformational change enabling the

heterodimerization with retinoid receptor X (RXR), followed by binding to the PPAR responsive element (PPRE) of target genes [72, 123]. To activate gene expression, the PPAR-RXR complex associates with co-activators [74]. In general, PPARs activate gene expression, however, gene expression of proinflammatory genes is inhibited by PPARs [20]. The consensus PPRE consists of two hexanucleotides separated by a variable base: AGGTCA-N-AGGTCA [74].

1.5.2 The three PPAR isoforms PPARα, PPARβ/δ, and PPARγ

Three isoforms of PPAR exist, PPARα, PPARβ/δ, and PPARγ, which bind to the same DNA binding motif but regulate different genes [53, 72]. The discrimination between different target genes is achieved by different tissue expression which is associated with different chromatin modifications and transcription factor sets [53]. Additionally, the PPAR isoforms have different ligand specificity [123, 127]. Also their functions differ, PPARα and PPARβ/δ activate catabolic processes, whereas PPARγ promotes energy storage [123]. PPARβ/δ and PPARγ have insulin sensitizing effects but PPARα not [123].

PPARα

PPARα is expressed in hepatocytes, enterocytes, endothelial cells, smooth muscle cells, and immune cells [123]. It is a key regulator of hepatic mitochondrial and peroxisomal fatty acid oxidation and binds long-chain unsaturated fatty acids, eicosanoids, and hypolipidemic drugs [74, 123]. PPARα is the main PPAR isoform in the liver regulating fatty acid metabolism during nutritional transition phases [53]. Under fasting conditions, PPARα induces fatty acid uptake, fatty acid β-oxidation, and ketogenesis [18, 123]. In the fed state, it activates *de novo* lipogenesis to provide energy during starvation [53, 123]. Besides fatty acid metabolism, it is thought that PPARα also regulates glucose metabolism, for example by increasing gluconeogenesis rate in mice [53, 69, 123, 189]. Therefore, PPARα plays a role in metabolic flexibility by coupling nutrient utilization to nutrient availability [53]. *Ppara* gene expression is decreased in NAFLD, a state of metabolic inflexibility, whereas feeding mice a high fat diet increases *Ppara* gene expression and PPARα signaling [53, 180].

PPARα activators, such as fibrates, are used in the clinics as therapy for dyslipidemia [53]. Fibrates have no effect on glucose homeostasis in type 2 diabetic subjects, but prediabetic patients benefit from fibrate therapy indicating that an activation of PPARα prevents the progression from prediabetes to type 2 diabetes [53].

PPARβ/δ

PPARβ/δ is found in skeletal muscle, adipocytes, macrophages, lung, brain, skin, and hepatocytes and also regulates fatty acid metabolism, enhances insulin sensitivity, increases energy expenditure, and acts anti-inflammatory [53, 123]. Thereby, PPARβ/δ activation combines the beneficial

metabolic effects of PPARα and PPARγ on lipid and glucose homeostasis and improves hepatic insulin sensitivity [53].

PPARγ

For PPARγ three splice variants were identified, PPARγ1, -2, and -3, which exhibit a tissue-specific gene expression [123]. PPARγ1 is found in many tissues, whereas PPARγ2 is exclusively expressed in adipose tissue [123]. PPARγ3 is found in macrophages, intestine, and white adipose tissue [123]. PPARγ is especially important for adipose tissue function, where it regulates fatty acid uptake and storage, adipogenesis, adipokine production, and has insulin sensitizing effects [123]. Increased PPARγ gene expression in the liver of rodents can be induced by high fat diet feeding and is associated with hepatic steatosis [6, 123]. Synthetic PPARγ ligands are used as anti-diabetic drugs, but due to side effects their usage is limited [53].

1.5.3 Fibroblast growth factors

Fibroblast growth factors (FGF) represent a large family with a variety of functions [60]. In mice and humans 22 FGF genes were identified which can be divided into eight subfamilies [222]. Normally, FGFs bind to heparin/heparan sulfate proteoglycans which impairs the diffusion of FGFs and acts as cofactor to regulate FGF receptor (FGFR) signaling [179]. However, the endocrine FGFs show low affinity to heparin/heparan sulfate and are secreted [179]. To induce signaling, these FGFs need to bind to a receptor and co-receptor in their target tissues [60, 179].

Fibroblast growth factor 21 (FGF21) belongs to the endocrine FGFs and represents an important metabolic regulator controlling hepatic and adipocyte metabolism, for example bile acid, carbohydrate, and lipid metabolism [60, 161, 179]. It is suggested that plasma FGF21 in mice is almost exclusively derived from the liver, although also other metabolic tissues express *Fgf21* [222]. However, FGF21 plasma level in mice and humans substantially differ, already between different subjects plasma FGF21 shows a great variance [222].

FGF21 has multiple beneficial effects on energy homeostasis and insulin sensitivity [65]. The main function is to induce metabolic adaptations in response to fasting, including ketogenesis, gluconeogenesis, and fatty acid oxidation [65, 222]. Administration of recombinant FGF21 to HFD-fed mice or genetic obesity and diabetes models results in metabolically beneficial effects, such as increased fat utilization and energy expenditure, decreased body weight, whole-body fat mass, and liver triglycerides [57, 222]. FGF21 improves glucose tolerance, insulin sensitivity, and hepatic steatosis as well as normalizes hyperinsulinemia and glycemia [219, 222]. In adipose tissues, the main site of FGF21 action, FGF21 stimulates glucose and fatty acid uptake, potentiates PPARγ activity, and increases mitochondrial activity [65, 222]. FGF21 has also central effects, it increases energy expenditure, reduces food intake as well as sugar consumption [222]. It is currently controversial if

FGF21 has direct effects on the liver, although it was observed that FGF21 seems to stimulate hepatic fatty acid oxidation, ketogenesis, and hepatic insulin sensitivity as well as suppresses hepatic *de novo* lipogenesis [222]. However, to induce these metabolically beneficial effects very high therapeutic doses need to be administered which exceed the physiological concentrations [65].

FGF21 is also elevated by overnutrition and in pathological states, such as NAFLD and type 2 diabetes, and correlates with hepatic fat content as well as steatosis [57, 65, 222].

Regulation of *Fgf21* gene expression

Gene expression of *Fgf21* is under control of several nutritional and endocrine signals and many transcription factors are involved in the transcriptional regulation [222].

Fgf21 gene expression is tissue-specific regulated by PPARα and PPARγ [222]. An activation of PPARγ induces higher *Fgf21* gene expression in white adipose tissue, mainly under fed conditions [53, 222]. In the liver, *Fgf21* gene expression is stimulated by PPARα, especially during fasting, leading to activation of fatty acid oxidation and ketogenesis [53, 57, 222].

At least in humans, overnutrition and refeeding induces *FGF21* gene expression, possibly due to increased dietary carbohydrates which upregulate *FGF21* mRNA level by activating ChREBP [57]. In mice, hepatic *Fgf21* gene expression can be induced by a high fat-low carbohydrate or ketogenic diet [57, 222].

Fgf21 gene expression is also regulated by different hormones, such as glucagon which increases *Fgf21* mRNA and FGF21 blood level, and insulin which also slightly increases FGF21 blood level [222]. However, regarding the regulation by insulin, differences between mice and humans seem to exist [222]. There are also studies hinting to an autoregulation of the *Fgf21* gene expression by plasma FGF21 [57]. The administration of FGF21 induced a decrease in *Fgf21* gene expression [57].

FGF21 signaling

FGF21 binds to and activates the FGF receptor tyrosine kinases FGFR1c and FGFR3c, but to induce signaling also the co-receptor β-Klotho is necessary [222]. It is thought that the differential expression of β-Klotho determines the FGF21 tissue specificity [222]. In mice, β-Klotho is found in liver, pancreas, and adipose tissue [222]. Upon binding, the FGF receptor dimerizes and gets transautophosphorylated [179]. FGFR substrate 2α (FRS2α), constitutively bound to its binding site in the juxtamembrane region of FGFR, gets phosphorylated which induces the activation of RAS-MAPK and PI3K-Akt pathways [179]. The activation of the PI3K-Akt pathway leads for example to inhibition of FoxO1 and activation of mTORC1 [179]. Besides RAS-MAPK and PI3K-Akt, the activation of FGFR also results in the phosphorylation of PLCγ and STAT [179].

The FGF signaling is regulated by receptor internalization and degradation but also by inhibition of the signaling itself [179]. For example, Sprouty (SPRY) inhibits RAS-MAPK and regulates the PI3K-Akt pathway [179]. Dual specificity phosphatase 6 (DUSP6), an ERK-specific MAPK phosphatase, is a negative feedback regulator of FGFR signaling by dephosphorylation of ERK1/2 [179].

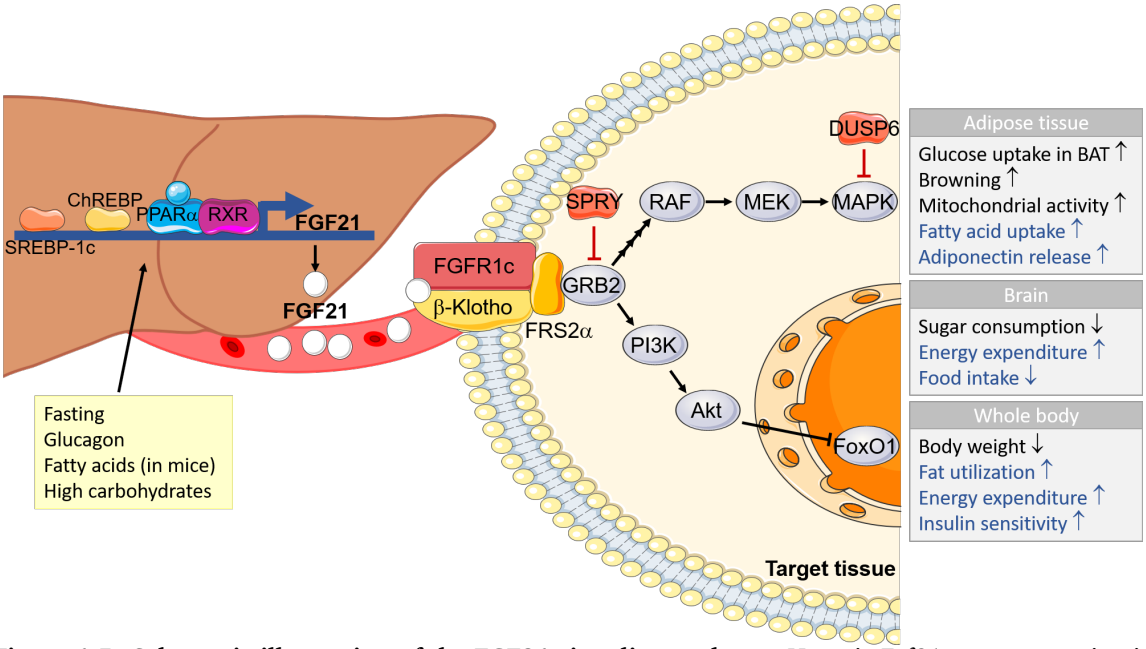

Figure 1.5: Schematic illustration of the FGF21 signaling pathway. Hepatic *Fgf21* gene expression is stimulated by for example fasting, glucagon, a high carbohydrate diet, and in mice by fatty acids. These stimuli act via various transcription factors, such as PPARα-RXR complex, ChREBP, and SREBP-1c. Hepatic FGF21 is secreted into the blood stream. At target tissues, FGF21 binds to the FGF receptor 1c (FGFR1c) as well as β-Klotho and induces phosphorylation of FGFR substrate 2α (FRS2α) which further activates for instance PI3K-Akt signaling and the RAS-MAPK pathway. In adipose tissue, FGF21 signaling stimulates browning, mitochondrial activity, fatty acid uptake as well as adiponectin release. In brown adipose tissue FGF21 induces glucose uptake. Central effects of FGF21 include reduced sugar consumption, reduced food intake, and increased energy expenditure. On the whole-body level, FGF21 activity is apparent as reduced body weight, increased fat utilization, energy expenditure, and insulin sensitivity. FGF21 signaling can be inhibited by Sprouty (SPRY) and Dual specificity phosphatase 6 (DUSP6). FGF21 effects which are similar in humans and mice are shown in black, FGF21 effects shown in mice but without human data are shown in blue. Modified according to Staiger et al. (2017) [222] and Ornitz and Itoh (2015) [179].

2

Objectives of this study

The prevalence of obesity is steadily increasing in our modern society and since it is a primary risk factor for type 2 diabetes also the number of patients suffering from insulin resistance and type 2 diabetes increases vastly [87, 259]. Type 2 diabetes has a strong genetic component, but the so far identified diabetes-associated genetic factors cannot explain sufficiently the development of the disease [7, 46]. Environmental factors play a crucial role in the disease pathogenesis, for instance eating behavior and physical activity [87], but the detailed causes of obesity and type 2 diabetes are not elucidated yet. This contributes to the lack of long-acting, efficient diabetes therapies.

Epigenetics represent the link between environment and genetics and it was reported multiple times that diabetic subjects show altered DNA methylation compared to healthy controls [13, 110, 163, 224]. Therefore, the aim of this thesis was to study if DNA methylation is causal or consecutive for the development of obesity and insulin resistance. The knowledge about the epigenetic component of the disease would contribute to a deeper understanding of the type 2 diabetes pathogenesis which in turn is crucial for the design of efficient new therapies and prevention strategies.

The specific objectives of this thesis were to

- Investigate the development of insulin resistance in a longitudinal study with diet-induced obese mice.
- Identify differentially expressed genes in liver which are regulated by DNA methylation and putting them into context with the phenotype.

In contrary to endpoint studies, this allows the time-resolved tracking of the development of insulin resistance and the study is unique regarding the epigenetic research question.

3

Materials

3.1 Manufacturers

A Acculab (Sartorius group, Göttingen, Germany); Affymetrix (Thermo Fisher Scientific, Santa Clara, CA, USA); Altromin (Lage, Germany); AppliChem Panreac (Illinois Tool Works Inc., Chicago, Il, USA); Applied Biosystems (Thermo Fisher Scientific, Waltham, MA, USA); **B** Bayer (Leverkusen, Germany); Becton Dickinson (Franklin Lakes, NJ, USA); Berlin-Chemie (Berlin, Germany); Biochrom (Merck, Darmstadt, Germany); Bio-Rad (Hercules, CA, USA); BioTEK (Winooski, VT, USA); BMG Labtech (Ortenberg, Germany); **C** Calbiochem (Merck, San Diego, CA, USA); Carl Roth (Karlsruhe, Germany); Cayman Chemicals (Ann Arbor, MI, USA); Cell Signaling Technology (Danvers, MA, USA); Charles River (Wilmington, MA, USA); cti (Idstein, Germany); **D** Dako Denmark A/S (Glostrup, Denmark); **E** Edmund Bühler (Bodelshausen, Germany); Eppendorf (Hamburg, Germany); **F** Feather (Osaka, Japan); Fisher Scientific (Thermo Fisher Scientific, Schwerte, Germany); Fluka Biochemika (Honeywell, Buchs, Switzerland); F.S.T. (Fine Science Tools, Vancouver, BC, Canada); **G** Gilson (Middleton, WI, USA); GraphPad Software (San Diego, CA, USA); Greiner Bio-One (Kremsmünster, Austria); **H** Hartmann (Heidenheim, Germany); Heidolph (Schwabach, Germany); Heraeus (Hanau, Germany); Hirschmann (Eberstadt, Germany); Honeywell (Morristown, NJ, USA); Hybaid (Thermo Fisher Scientific, Waltham, MA, USA); **I** IDT (Coralville, IA, USA); IKA (Staufen im Breisgau, Germany); Invitrogen (Thermo Fisher Scientific, Waltham, MA, USA); Isolab Laborgeräte (Wertheim, Germany); **K** Kern (Balingen-Frommern, Germany); Knittel Gläser (Braunschweig, Germany); Korff (Oberbipp, Switzerland); **L** Labinco (Breda, The Netherlands); Leica Biosystems (Nussloch, Germany); Liebherr (Biberach an der Riß, Germany); Life Technologies (Thermo Fisher Scientific, Carlsbad, CA, USA); **M** MathWorks (Natick, MA, USA); Medistar (Koblenz, Germany); Medite (Burgdorf, Germany); Meditrade (Kiefersfelden, Germany); Merck Millipore (Darmstadt, Germany); Microsoft (Redmond, WA, USA); Morphisto (Frankfurt am Main, Germany); **N** neoLab (Heidelberg, Germany); Nerbe Plus (Winsen/Luhe, Germany); New England Biolabs (Ipswich, MA, USA); Nikon (Tokio, Japan); Novex (Thermo Fisher Scientific, Waltham, Massachusetts, USA); **P** Peqlab (VWR,

Radnor, PA, USA); Phoenix Instrument (Garbsen, Germany); Promega (Fitchburg, WI, USA); **Q** Qiagen (Hilden, Germany); **R** Ratiopharm (Ulm, Germany); Research Diets (New Brunswick, NJ, USA); Roche (Basel, Switzerland); RStudio (Boston, MA, USA); **S** Sarstedt (Nümbrecht, Germany); Sartorius (Göttingen, Germany); Siemens (Munich, Germany); Sigma Aldrich (St. Louis, MO, USA); Simport Scientific (Beloeil, QC, Canada); Systec (Linden, Germany); **T** Thermo Fisher Scientific (Waltham, MA, USA); Th. Geyer (Renningen, Germany); **U** Unipro (Novosibirsk, Russia); **V** VWR (Radnor, PA, USA); **Z** Ziegra Eismaschinen (Isernhagen, Germany)

3.2 Devices

Device	Manufacturer
Autoclave CX-65	Systec
Centrifuge 5430 R	Eppendorf
Centrifuge MC 6 (mini), stripes	Sarstedt
Centrifuge MC 6 (mini), tubes	Sarstedt
ChemiDoc™ Touch	Bio-Rad
Comb, 12-well, 1.0 mm	Novex
Dual short period timer TR 118 OS	Carl Roth
Fisherbrand Bead Mill 24 Homogenizer	Fisher Scientific
Fixed-angled rotor F-35-6-30 (for 15 ml and 50 ml tubes)	Eppendorf
Flake ice maker	Ziegra Eismaschinen
Freezer Hera Freeze HFU T Series (-80°C)	Thermo Fisher Scientific
Freezer Comfort GP 3513 Index 20F/001 (-20°C)	Liebherr
GeneChip® Fluidics Station 450	Affymetrix
GeneChip® Scanner 3000	Affymetrix
Glucometer ACCU-CHECK®	Roche
Hybridization oven H-9360	Hybaid
Hybridization oven Shake'n'Stack	Hybaid
Ice pan, 4 l and 9 l	Fisher Scientific
Incubator Hood TH 30	Edmund Bühler
Instrument trays	Th. Geyer
Magnetic stirrer	VWR
Magnetic stirrer Combimag RCT	IKA
Microscope Eclipse Ci-L	Nikon
Microwave	Siemens
Mini Blot Module	Invitrogen
Mini centrifuge Galaxy MiniStar	VWR
Mini Gel Tank	Invitrogen
Multichannel pipette for 10 µl and 300 µl	Eppendorf
Multifuge 3 SA	Heraeus
Multistep pipette Multipette® E3	Eppendorf
Multistep pipette Pipetman P20M, 2-20 µl	Gilson
PerfectBlue™ gel system, Mini L (12 x 14 cm)	Peqlab
PerfectBlue™ gel system, Mini S (7 x 8 cm)	Peqlab

pH meter PB-11	Sartorius
Pipettes for 10 µl, 20 µl, 100 µl, 200 µl, 1000µl	Eppendorf
Pipetus^{R}	Hirschmann
Plate shaker Titramax 100	Heidoplh
Power supply PowerPac^{TM} Basic	Bio-Rad
Precision scale, Atilon	Acculab
Precision scale, 440-47N	Kern
Precision scale, PCB 1000-1	Kern
Precision scale, PT 1200	Sartorius
Precision scale, SE 203 LR	VWR
Preparation tray with PVC mat	Carl Roth
PyroMark Q48 Autoprep	Qiagen
Rack, 18 apertures, 17.2 mm	Sarstedt
Rack, falcons	Sarstedt
Rack IsoFreeze^{R} for PCR set-up	Sarstedt
Rack, microcentrifuge tube	VWR
Rack, PCR tubes, 96-well	TH. Geyer
Refrigerator Mediline LKexv 3910 Index 24E/001	Liebherr
Refrigerator Mediline LKUexv 1610 Index 23A/001	Liebherr
Rotor FA-45-48-11 for 1.5 ml and 2.0 ml tubes	Eppendorf
Semi-automated rotary microtome RM2245	Leica Biosystems
Spectrophotometer for microplate 'Epoch'	BioTEK
SPECTROstar Nano	BMG Labtech
Staining jar macro	Isolab Laborgeräte
SureCast^{TM} Gel Handcast Station	Invitrogen
SureCast^{TM} glass plates	Invitrogen
Surgical instruments	F.S.T.
Swing-bucket Rotor A-2-MTP	Eppendorf
Swivel roller mixer RS-TR 5	Phoenix Instrument
Thermo cycler Mastercycler^{R} nexus gradient	Eppendorf
Thermo cycler Mastercycler^{R} nexus X2e	Eppendorf
Thermometer	Th. Geyer
Thermomixer 5437	Eppendorf
Thermomixer C	Eppendorf
Tilt shaker Silent rocker	cti
QuantStudio 5	Thermo Fisher Scientific
Quantus^{TM} Fluorometer	Promega
Vortex mixer 7-2020	neoLab
Vortex mixer L46	Labinco
Vortex mixer, mini	Fisher Scientific
Wellwash^{TM} Versa Microplate Washer	Thermo Fisher Scientific

3.3 Consumables

Consumable	**Manufacturer**
ACCU-CHECK^{R} Aviva blood glucose test stripes	Roche
Adhesive PCR seal	Sarstedt

Aluminium foil (0.03 mm x 300 mm x 100 m)	Korff
Control diet #1310 (chow diet)	Altromin
Cellulose swab	Meditrade
Clariom^{TM} D Assay, mouse	Affymetrix
Collection tubes, 2 ml	Qiagen
Combitips advanced^{R} FOR 0.1, 0.2, 0.5, 2.5, 5.0, and 10 ml	Eppendorf
Eclipse^{TM} needle, 27Gx3/4	Becton Dickinson
Extension set for syringes	Becton Dickinson
Falcon, 15 ml and 50 ml	Sarstedt
High fat diet D12492	Research Diets
Histosette^{R} I Tissue Processing/Embedding cassettes	Simport Scientific
Marking tape, 19 mm x 55 m	Th. Geyer
MicroAmp^{R} clear adhesive film	Life Technologies
MicroAmp^{R} EnduaPlate^{TM} optical 96-well	Life Technologies
Microplate, 96-well, PS, F bottom, transparent	Greiner Bio-One
Microplate, 96-well, F, transparent	Sarstedt
Microscope slides Star Frost, 76x26 mm	Knittel Gläser
Microtome blades, type 819, low profile	Leica Biosystems
Microvette^{R} CB 300 K2E	Sarstedt
Membrane filter Millipore, 0.1 µm	Merck Millpore
MoliNea^{R} absorbing underlay	Hartmann
Parafree Disposable Base Mold	Leica Biosystems
PCR plates, 0.2 ml	Sarstedt
PCR stripes 'Multiply-µStrip', 0.2 ml	Sarstedt
PCR stripe lid chain	Sarstedt
PCR tubes, 0.5 ml	Promega
Pipette tips with filter for 10 µl, 100 µl, 200 µl, 1000 µl	Nerbe Plus
Pipette tips with filter for 10 µl and 20 µl	Sarstedt
Pipette tips without filter for 10 µl	Nerbe Plus
Precellys^{R} ceramic beads	VWR
PyroMark Q48 Absorber Strips	Qiagen
PyroMark Q48 Discs	Qiagen
Reaction tubes low binding, 1.5 ml	Sarstedt
Reaction tubes, 2 ml and 5 ml	Eppendorf
Rotilabo^{R}-Blotting papers, 1.5 mm thickness	Carl Roth
SafeSeal reaction tube, 1.5 ml	Sarstedt
Safety-Multifly^{R} 21G with tube, 200 mm	Sarstedt
Scalpel	Feather
Screw cap micro tubes	Sarstedt
Serological pipette for 5 ml, 10 ml, and 25 ml	Sarstedt
Syringes for 1 ml and 20 ml	Becton Dickinson
Syringes, insulin 0.5 ml	Becton Dickinson
Transfer membrane Immobilon-P	Merck Millipore

3.4 Chemicals

Chemical	Manufacturer
Acetic acid	Merck Millipore
Adenosine diphosphate (ADP)	Sigma Aldrich
Adenosine triphosphate (ATP)	Sigma Aldrich
Agarose broad range	Carl Roth
Ammonium persulfate (APS)	Carl Roth
Bovine serum albumin (BSA)	Sigma Aldrich
cOmplete^{TM}, EDTA-free Protease Inhibitor Cocktail tablet	Roche
Dipotassium hydrogen phosphate (K_2HPO_4)	Carl Roth
Disodium hydrogen phosphate (Na_2HPO_4)	Merck Millipore
Dithiothreitol (DTT)	Sigma Aldrich
DEPC-treated water	Life Technologies
DNA Away	Fisher Scientific
D(+) Glucose, 99.5%, water free	Carl Roth
Ethanol absolute	Th. Geyer
Ethanol, 70%, denatured	Th. Geyer
Ethylene glycol-bis(β-aminoethyl ether)-N,N,N',N'-tetraacetic acid (EGTA)	Sigma Aldrich
Glycine (for electrophoresis)	Sigma Aldrich
Histoplast Paraffin	Thermo Fisher Scientific
Hydrochloric acid (HCl)	Merck Millipore
Isopropanol for molecular biology	Fisher Scientific
Ketamine, 10%	Medistar
Magnesium chloride ($MgCl_2$)	Sigma Aldrich
Manganese (II) chloride ($MnCl_2$)	Sigma Aldrich
Methanol	Honeywell
Milk powder	Carl Roth
Nicotinamide adenine dinucleotide (NADH)	Sigma Aldrich
N,N,N',N'-tetramethylethane-1,2-diamine (TEMED)	Sigma Aldrich
Oxaloacetic acid	Sigma Aldrich
Phenylmethylsulfonyl fluoride (PMSF)	Sigma Aldrich
S-Adenosyl methionine (SAM)	New England Biolabs
Sodium chloride (NaCl), pure, solid	AppliChem Panreac
Sodium deoxycholate	Sigma Aldrich
Sodium dodecyl sulfate (SDS)	Carl Roth
Sodium fluoride	Sigma Aldrich
Sodium orthovanadate	Sigma Aldrich
Trizma^{R} Base	Sigma Aldrich
Octoxinol 9 (Nonidet P-40, NP-40)	Fluka Biochemika
Phosphoenol pyruvic acid	Sigma Aldrich
Potassium chloride (KCl)	Merck Millipore
Potassium dihydrogen phosphate (KH_2PO_4)	Merck Millipore
Protease inhibitor cocktail set V, EDTA-free	Calbiochem
RNase ZAP	Th. Geyer
Rompun, 2% (Xylazin)	Bayer

Trichloroacetic acid	Sigma Aldrich
Trichloromethane (Chloroform)	Carl Roth
Tris-HCl	Carl Roth
Tween^{R} 20 for molecular biology	AppliChem Panreac
Ultra-pure water	Biochrom
Xylol	

3.5 Enzymes and size markers

Enzymes/size marker	Manufacturer
GeneRuler 100 bp DNA Ladder	Life Technologies
L-Lactic dehydrogenase (LDH)	Sigma Aldrich
M. SssI (CpG) Methyltransferase	New England Biolabs
PageRuler^{TM} Prestained Protein Ladder 10-170 kDa	Thermo Fisher Scientific
Pyrophosphatase	Thermo Fisher Scientific
Pyruvate kinase (PK)	Sigma Aldrich
RNase A	Qiagen

3.6 Antibodies

Antibody	Source	Dilution	Manufacturer
Akt #9272	Rabbit	1:1000	Cell Signaling Technology
Phospho-Akt (Ser473) #4060	Rabbit	1:1000	Cell Signaling Technology
Anti-Rabbit Immunoglobulins/HRI	Goat	1:5000	Dako Denmark A/S

3.7 Commercial kits

Kit	Manufacturer
Clarity Max^{TM} Western ECL Substrate	Bio-Rad
EpiTect^{R} Fast DNA Bisulfite Kit	Qiagen
Fast Start Universal SYBR Green Master	Roche
GeneChip^{TM} WT PLUS Reagent Kit	Thermo Fisher Scientific
GeneChip^{TM} Hybridization, Wash and Stain Kit	Thermo Fisher Scientific
High-Capacity cDNA Reverse Transcription Kit	Applied Biosystems
miRNeasy Mini Kit	Qiagen
ONE dsDNA kit	Promega
Pierce^{TM} BCA Protein Assay Kit	Thermo Fisher Scientific
PyroMark PCR Kit	Qiagen
PyroMark Q48 Advanced CpG Reagents	Qiagen
QIAamp^{R} Fast DNA Tissue Kit	Qiagen
QuantiFluor^{R} ONE dsDNA System	Promega
QuantiNova^{TM} Probe PCR Kit	Qiagen
Rat/Mouse Insulin ELISA (EZRMI-13K)	Merck Millipore

REPLI-g^{R} Mini Kit	Qiagen
RNase-Free DNase Set	Qiagen
TGX Stain-Free^{TM} FastCast^{TM} Acrylamide Starter Kit, 10%	Bio-Rad
Triglyceride Colorimetric Assay Kit	Cayman

3.8 Commercial buffers and solutions

Buffer/solution	Manufacturer
Dulbecco's phosphate-buffered saline (DPBS)	Life Technologies
EDTA solution, pH 8.0	AppliChem Panreac
Eosin G solution, 0.5% for microscopy	Carl Roth
Hemalum solution acid acc. to Mayer	Carl Roth
Heparin-sodium 25 000, 5 ml	Ratiopharm
3x SDS Blue Loading Dye	New England Biolabs
Lugol solution	Sigma Aldrich
NEBuffer 2, 10x	New England Biolabs
Paraformaldehyde, 4% in PBS, pH 7.4	Morphisto
Pertex^{R} mounting medium	Medite
PyroMark Q48 Magnetic Beads	Qiagen
Restore^{R} PLUS Western Blot Stripping Buffer	Thermo Fisher Scientific
Krebs-Ringer bicarbonate buffer	Sigma Aldrich
SDS blue loading buffer, 3x	New England Biolabs
SYBR Safe DNA gel stain	Life Technologies
Sodium chloride (NaCl) solution, 0.9%, sterile	Berlin-Chemie
TE buffer, 1x and 20x	Promega

3.9 Self-made buffers and solutions

Enzyme activity homogenization buffer, pH 7.0

9 mM KH_2PO_4; 85 mM K_2HPO_4; 1 mM DTT

Glucose solution, 20%

2 g glucose in 10 ml saline

Glucose solution, 25%

2.5 g glucose in 10 ml saline

Krebs-Ringer bicarbonate buffer with 1U/ml heparin

Lugol reaction mix

30 ml KCl (25% w/v); 500 µl Lugol solution; 200 µl 5 M HCl

Milk-TBS

5% milk powder in TBS

PBS

137 mM NaCl; 2.7 mM KCl; 2 mM KH_2PO_4; 10 mM Na_2HPO_4

PEPCK sample buffer

65 mM Tris-HCl (pH 8.0); 6 mM $MgCl_2$; 15 µM $MnCl_2$; 0.875 mg/ml BSA; 4.65 mM ADP;
4.65 mM ATP; 0.575 mM NADH; 5.4 U/ml L-Lactic dehydrogenase (LDH);
5.4 U/ml Pyruvate kinase (PK)

PK sample buffer

65 mM Tris-HCl (pH 8.0); 11.5 mM $MgCl_2$; 0.875 mg/ml BSA; 4.65 mM ADP;
0.575 mM NADH; 5.4 U/ml L-Lactic dehydrogenase (LDH)

RIPA buffer

150 mM NaCl; 50 mM Tris (pH 7.4); 0.25% Sodium deoxycholate; 1% NP-40;
1mM EDTA (pH 8.0)

RIPA-based lysis buffer

To 10 ml RIPA buffer add 1 cOmplete^{TM} EDTA-free Protease Inhibitor Cocktail tablet;
10 mM sodium fluoride; 1 mM sodium orthovanadate;
add 1 mM PMSF immediately before use

Running buffer (10x)

0.25 M Tris; 1.92 M Glycine; 1% SDS

TAE buffer (50x)

2 M Tris; 0.05 M EDTA (pH 8.0); 5.71% glacial acetic acid

TBST buffer (10x), pH 7.4

100 mM Tris; 1.5 M NaCl

TBS buffer (1x), pH 7.4

10x TBS; 0.1% Tween^{R} 20

Transfer buffer (1x)

0.025 M Tris; 0.192 M Glycine; 20% Methanol

3.10 Oligonucleotides

All primers listed below (tab. 3.8, 3.9) were synthesized by IDT as 25 nmole DNA Oligo. The lyophilized and desalted primers were dissolved in TE buffer to obtain a concentration of 100 µM. An exception are the sequencing primers which were dissolved in 'Annealing Buffer' of the *PyroMark Q48 Adavanced CpG Reagent Kit* to a concentration of 4 µM.

Bisulfite PCR primer

To perform a PCR with bisulfite-converted DNA bisulfite-primer must be used. For subsequent pyrosequencing one primer has to be biotinylated (indicated as '/5BiosG/') for purification of the PCR product.

Gene	Sequence	Amplicon
Acacb (NM_133904) (intron 5)	frw AGTTTTTGTTGGTATTAAGGTATTAGTTAA rev /5BiosG/CCAAACACAAAATCATTTTTACC seq GGTATTAAGGTATTAGTTAAGTT	135 bp
Acacb (NM_133904) (exon 5-intron 5)	frw GGTGGGGGTTGGGAAGAT rev /5BiosG/CACCCCTTCCCCTCCCAAA seq TTAGAGTTGTTGTGTAAATA	244 bp
Cd36 (NM_001159558) (exon 1)	frw AGGATTGGAATGTTTAGGATGTTA rev /5BiosG/TCTAAAACAACTTACTTACCCAATCACA seq AATGTTTAGGATGTTAATG	204 bp
Fgf21 (NM_020013) (exon 1)	frw /5BiosG/GGGGATTTAATATAGGAGAAATAGTTAT rev AAAATCCCAACTCTAAATCTCATC seq CTCATCCATTCCATCA	191 bp
Fgf21 (NM_020013) (promoter)	frw TGAATTTTTAGTTGAGAAGATATTAAGGTTGTTT rev /5BiosG/AACCCCCCCATTACATCATC seq1 TAGAAATATTAGAATTTATATTTAGA seq2 AGATATTAAGGTTGTTTGGTG	183 bp
G6pc (NM_008061) (exon 1-intron 1)	frw TGGTTTTATTTTAAAGAGATTGTGGGTAT rev /5BiosG/AACCATTTCTCTACCCATCAC seq TAAAGAGATTGTGGGTAT	123 bp
Galnt2 (NM_139272) (intron 7)	frw TTTTTGGTTTTGTAGTGTGGAT rev /5BiosG/CCTATCACAAACCAAAACTATACAAT seq TTTGAGTTTGAGTTATG	145 bp
Pck1 (NM_011044) (exon 2)	frw AGTTTGTTTTAGGTAGTGAGGAAGT rev /5BiosG/ATAACACCCTCCTCCTACATA seq GTGGAAGGTAATGTTTAGT	134 bp
Pklr (NM_013631) (intron 1)	frw /5BiosG/TTGGGGGTTAGAGTTTAGGAATT rev ACCTTTAATCCAAACTCTACAAAC seq ACAAACAAACCAAAAAAAAT	93 bp
Ppara (NM_011144) (intron 2)	frw GTAGTAAAGAAAGGGTTTTGAGGG rev /5BiosG/CCCAAACTATTAAAAAACTTACAACAATCC seq1 AGGTTTATGTGTGGG seq2 AGTAAAGAAAGGGTTTTG	182 bp
Scd1 (NM_009127) (intron 3)	frw GTTAGTTAAGTGGTGGGTAATAGG rev /5Biosg/TCAAACTAACCTCTACCTTCACA seq GTTGGGATTAAAGGTATG	155 bp
Sgms2 (NM_028943) (intron 3)	frw /5BiosG/AGATATATGTGTTTGTTTTATAGAATTAG rev CCACAATCACTCCTAACAACC seq CACAATCACTCCTAACA	122 bp
Sik3 (NM_027498) (intron 1)	frw /5Biosg/GGATTATTTGTTAATAGTTAAGTATAGAG rev CACCAAACAACTTTATAACTATCTCAA seq ATAACTATCTCAAATAACCATAC	150 bp

Primer for SYBR green-based qRT-PCR

Gene	Sequence	Amplicon
Cd36 (NM_001159558)	frw ATGGGCTGTGATCGGAACTG rev GTCTTCCCAATAAGCATGTCTCC	110 bp
Fgf21 (NM_020013)	frw GCTCTCTATGGATCGCCTCA rev TTGTAACCGTCCTCCAGCAG	74 bp
Hprt (NM_013556)	frw GCAGTACAGCCCCAAAATGG rev AACAAAGTCTGGCCTGTATCCAA	85 bp
Ppid (NM_026352)	frw TCACAACAGTTCCGACTCCTC rev ACCTCTACATTTTCAAGCGTCC	100 bp
Ppara (NM_011144)	frw AGAGCCCCATCTGTCCTCTC rev ACTGGTAGTCTGCAAAACCAAA	153 bp
Pparg (NM_011146)	frw GAGAGGTCCACAGAGCTGATT rev TCGCTGATGCACTGCCTATG	103 bp
Pklr (NM_013631)	frw TCAAGGCAGGGATGAACATTG rev CACGGGTCTGTAGCTCAGTG	131 bp
Scd1 (NM_009127)	frw TTCTTGCGATACACTCTGGTGC rev CGGGATTGAATGTTCTTGTCGT	98 bp

TaqMan assays

TaqMan assays were ordered from Thermo Fisher Scientific.

Gene	Assay	Amplicon
Acacb (NM_133904)	Mm01204671_m1 (FAM)	98 bp
Fasn (NM_007988)	Mm00662319_m1 (FAM)	67 bp
G6pc (NM_008061)	Mm00839363_m1 (FAM)	116 bp
Hprt (NM_013556)	Mm03024075_m1 (VIC)	131 bp
Pck1 (NM_011044)	Mm00440637_g1 (FAM)	117 bp
Rpl37a (NM_026069)	Mm01253851_g1 (VIC)	77 bp

3.11 Software

Software	Version	Manufacturer
Affymetrix Launcher		Affymetrix
Gen5™	2.00.17	BioTek
GraphPad Prism® 7	version 7.01	GraphPad Software
Image J	version 1.51h	NIH
Image Lab™	version 5.2.1 build 11	Bio-Rad
MATLAB	version R2018b	MathWorks
Microsoft Office		Microsoft
NIS-Elements Analysis	4.30.00	Nikon
NIS-Elements D	4.30.00	Nikon
PyroMark® Assay Design	version 2.0.1.15	Qiagen
PyroMark® Q48 Autoprep Software	version 2.4.2 build 3	Qiagen
QuantStudio™ Design & Analysis Software	version 1.3.1	Applied Biosystems
R	version 3.5.3	The R Foundation
RStudio®	version 1.1.414	RStudio
SPECTROstar Nano	version 2.10	BMG Labtech
SPECTROstar Nano - Data Analysis	version 3.01 R2 build 41	BMG Labtech
Transcriptome Analysis Console	version 4.0.0.25	Thermo Fisher Scientific
Unipro UGENE	version v1.25.3	Unipro

4

Methods

4.1 Animal experiments

4.1.1 Longitudinal methylation study

Male wildtype C57BL/6N mice were obtained from Charles River at 3-4 weeks of age. Mice were housed in groups of four under constant temperature and 12h/12h light/dark cycle. Mice had *ad libitum* access to water and food. After one week of acclimation mice were randomized into two groups and fed *ad libitum* with either chow diet (Breeding diet #1314, obtained from Altromin) or high fat diet (HFD D12492 with 60 kcal% fat mainly from lard, obtained from Research Diets) for 1, 2, 4, 5, 6, 7, 8, or 12 weeks (eight mice per group and time point, for overview of study see fig. 4.1). The diet composition is provided in section 7 A. Body weight was measured twice a week. At the indicated time points mice underwent an intraperitoneal glucose tolerance test. The day after, mice were anaesthetized with a mixture of ketamin and xylazin (120mg/kg body weight ketamin and 16mg/kg body weight Rompun 2% (xylazin)) and sacrificed by cervical dislocation. Blood was collected by cardiac puncture and mice were perfused with Krebs-Ringer bicarbonate buffer with a final concentration of heparin of 1U/ml. The liver was removed, snap frozen, and stored at -80°C. All procedures were conform with local ethical guidelines, considered the three R's, and were approved under the reference number V242-59721/2016 4(111-9/16)_Kirchner by the MELUR Schleswig–Holstein, Germany.

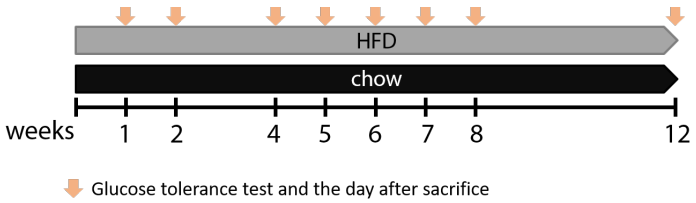

Figure 4.1: Study design of the longitudinal experiment. Mice were divided into two groups and fed for up to 12 weeks with either chow diet or high fat diet with 60 kcal% fat mainly from lard. After 1, 2, 4, 5, 6, 7, 8, and 12 weeks of feeding eight mice of each group underwent an intraperitoneal glucose tolerance test and the day after were sacrificed.

4.1.2 Plasma preparation

Whole blood was obtained by cardiac puncture during sacrifice and transferred into microvettes with EDTA. After a short mixing the blood was immediately stored on ice for maximal 30 to 60 minutes. The microvettes were centrifuged for 15 minutes at 2000xg and the plasma was transferred into a new tube and stored at -80°C.

4.1.3 Intraperitoneal glucose tolerance test

A glucose tolerance test is performed to examine how fast an individual can clear a glucose bolus which is determined by pancreatic insulin secretion and re-synthesis as well as insulin sensitivity of peripheral tissues. The intraperitoneal glucose administration was chosen to prevent the release of incretins which would stimulate insulin secretion.

Prior performing the intraperitoneal glucose tolerance test mice were weighted and transferred into a new cage without food but *ad libitum* access to water. The mice were fasted for six hours and fasting glucose levels were determined by obtaining blood from the tail vein and measuring with a glucometer. Afterwards, glucose was injected intraperitoneally (chow group: 2 g glucose/kg body weight of a 20% glucose solution, HFD group: 1.5 g glucose/kg body weight of a 25% glucose solution) and glucose levels were measured after 15, 30, 60, and 120 minutes. The glucose tolerance test was performed in the light phase. After the last measurement at 120 minutes the mice were provided with food again. For statistical analysis glucose concentration was plotted over the time and the area under the curve was calculated.

4.1.4 Liver samples of mice fed with high fat-high sucrose diet

Liver samples of mice fed with high fat-high sucrose diet (HFHS) (D12331 with 58 kcal% fat mainly from coconut oil, obtained from Research Diets) or chow diet (standard diet LM-485, obtained from Harlan Teklad) were generously provided by Dr. Paul Pfluger from the Institute for Diabetes and Obesity, Helmholtz Zentrum München. The diet composition is provided in section 7 A. The mice were fed for 20 weeks. After sacrifice, liver was collected and homogenized with liquid nitrogen.

4.2 Molecular biological methods

4.2.1 DNA isolation

Genomic DNA was isolated from liver with the *QIAamp^R Fast DNA Tissue Kit*. Maximal 25 mg snap-frozen liver tissue was homogenized in buffer and enzyme mix with ceramic beads in the *Fisherbrand Bead Mill 24 Homogenizer* using following settings: Speed: 5 m/s, time: 20 s, cycle: 2, delay: 15 s. For processing of several samples, a mastermix of the homogenization buffer was prepared. The DNA isolation was performed according manufacturer's instructions. The DNA was eluted in 100 µl 'ATE' buffer. After concentration measurement genomic DNA was stored for long-term at -20°C.

4.2.2 Quantification of DNA

DNA was quantified using the *Quantus^{TM} Fluorometer* with the *QuantiFluor^R ONE dsDNA System kit*. The quantification is based on a fluorescent dye intercalating in double-stranded DNA. Shortly, 200 µl 'QuantiFluor ONE dsDNA Dye' was dispensed into 0.5 ml PCR tubes and 1 µl of TE buffer (blank), 'QuantiFluor ONE Lambda DNA standard' (corresponds to 400 ng), or sample was added. The reaction mix was vortexed, spun down, and incubated for five minutes in the dark. The concentration was measured with the 'ONE DNA' protocol.

4.2.3 RNA isolation

Total hepatic RNA was isolated using the *miRNeasy Mini Kit*. Approximately 25 mg of snap-frozen liver was homogenized in 'QIAzol Lysis Reagent' with following settings: Speed: 5 m/s, time: 20 s, cycle: 2, delay: 15 s. The homogenate was incubated for five minutes at room temperature. Subsequently, it could be frozen at -80°C for storage or directly used for RNA isolation. If the homogenate was frozen it was thawed in the heating block at 37°C. The RNA was isolated according manufacturer's instructions. After the first wash step with 'RWT' buffer a DNase I digestion was performed. Afterwards, wash steps were carried out according protocol. Prior elution, the spin column was placed into a new collection tube and centrifuged an additional time. RNA was eluted in 50 µl pre-warmed (56°C) RNase-free water and stored for long-term at -80°C.

4.2.4 Quantification of RNA

RNA was quantified spectrophotometrically with the *Epoch*^{TM} *microplate spectrophotometer*. The measurement was performed with 2 µl RNA in duplicates. As blank, RNase-free water was used. The sample concentration and quality were analyzed with the *Gen5*^{TM} software and *Excel*. Samples with a concentration exceeding 1000 ng/µl were diluted with RNase-free water and measured again.

4.2.5 Bisulfite conversion of genomic DNA

Theoretical background

To differentiate between methylated and unmethylated CpG sites DNA is bisulfite converted by treatment with bisulfite salt. The bisulfite-converted DNA is amplified and subsequently sequenced by bisulfite pyrosequencing (Fig. 4.2).

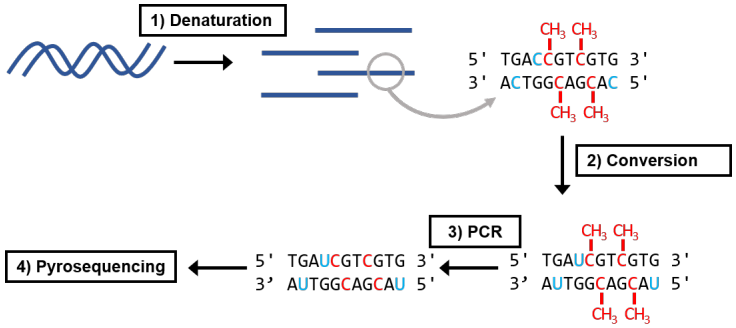

Figure 4.2: Schematic illustration of the bisulfite conversion and subsequent workflow. Genomic DNA is denatured and subsequently bisulfite converted. This leads to a conversion of unmethylated cytosine to uracil, whereas methylated cytosine is not affected and remains cytosine. The bisulfite conversion is followed by a bisulfite PCR to amplify the desired gene product for bisulfite pyrosequencing to determine the percentage of DNA methylation.

Bisulfite conversion

Genomic DNA was bisulfite converted with the *EpiTect*^{R} *Fast Bisulfite Conversion kit* according to manufacturer's instructions. Initially, DNA was diluted to 2 µg in 20 µl with DEPC-treated water. The protocol for high-concentration samples was used. After adding bisulfite solution and DNA protect buffer the reaction mix was mixed thoroughly until the buffer turned blue indicating the correct pH for conversion. The bisulfite reaction was carried out in a thermo cycler with following program:

Table 4.1: Program for bisulfite conversion

Step	Time	Temperature
Denaturation	5 min.	95°C
Incubation	30 min.	60°C
Denaturation	5 min.	95°C
Incubation	20 min.	60°C
Hold	forever	4°C

After the incubation the samples can be stored overnight at 4°C. The conversion and clean-up were continued according instructions of the kit manual. To avoid contamination of the spin column with flow-through last drops in the collection tubes were removed by tapping the tubes on tissue. To dry the spin columns after the last wash step an additional centrifugation with new collection tubes was performed to remove residual liquid. Afterwards, the spin columns were dried by incubation at 60°C for five minutes in a heating block. The bisulfite converted DNA was eluted from the spin column by adding 40 µl of elution buffer and incubation for one minute at room temperature. Bisulfite converted DNA was stored at -20°C.

4.2.6 Bisulfite polymerase chain reaction

A polymerase chain reaction (PCR) amplifies *in vitro* a desired DNA sequence located between two short oligonucleotides with known sequence (primer) by repeated denaturation, hybridization, and elongation [162]. The amplification of bisulfite-converted DNA is challenging, because the DNA contains only three bases instead of four and therefore, is less complex [115]. Thus, bisulfite PCRs were performed using the *PyroMark PCR Kit* which is optimized for bisulfite DNA. For subsequent bisulfite pyrosequencing analysis one primer needs to be biotinylated. The mastermix contains the HotStartTaq DNA polymerase and an optimized PCR buffer with 1.5 mM $MgCl_2$. The PCR mix was pipetted as followed:

Table 4.2: Reaction mix for bisulfite PCR

Component	Final concentration	Volume/reaction
PyroMark PCR MasterMix (2x)	1x	12.5 µl
CoralLoad Concentrate (10x)	1x	2.5 µl
Forward primer (10 µM)	0.2 µM	0.5 µl
Reverse primer (10 µM)	0,2 µM	0.5 µl
RNase-free water		8.0 µl
Bisulfite-DNA	10-20 ng	1.0 µl
Total volume		25 µl

The PCR reaction was performed with the program in table 4.3, the primer annealing temperatures as well as the cycle numbers are shown in table 4.4.

Table 4.3: Program for bisulfite PCR

Step	Temperature	Time	Cycles
Activation	95°C	15 min.	1
Denaturation Annealing Extension	94°C primer-dependent 72°C	30 s 30 s 30 s	35-45
Final extension	72°C	10 min.	1
Hold	4°C	forever	

Table 4.4: Annealing temperature, cycle number, amplicon size, and template strand of primer used in this study

Gene	Annealing Temp.	Cycles	Amplicon	Template strand
Acacb, NM_133904 (intron 5)	51.5°C	42	135 bp	upper strand, forward
Acacb, NM_133904 (exon 5-intron 5)	59.5°C	42	244 bp	upper strand, forward
Cd36, NM_001159558 (exon 1)	56°C	46	204 bp	lower strand, forward
Fgf21, NM_020013 (exon 1)	56°C	42	191 bp	lower strand, reverse
Fgf21, NM_020013 (promoter)	56°C	45	183 bp	upper strand, forward
G6pc, NM_008061 (exon 1-intron 1)	56°C	42	123 bp	upper strand, forward
Galnt2, NM_139272 (intron 7)	56°C	43	145 bp	upper strand, forward
Pck1, NM_011044 (exon 2)	56°C	42	134 bp	upper strand, forward
Pklr, NM_013631 (intron 1)	52°C 52°C	48 49	93 bp	lower strand, reverse (Nested PCR)
Ppara, NM_011144 (intron 2)	56°C	42	182 bp	upper strand, forward
Scd1, NM_009127 (intron 3)	56°C	47	155 bp	upper strand, forward
Sgms2, NM_028943 (intron 3)	56°C	42	122 bp	upper strand, reverse
Sik3, NM_027498 (intron 1)	56°C	42	150 bp	upper strand, reverse

4.2.7 Agarose gel electrophoresis

After PCR, the biotinylated product was verified on 1% agarose gel regarding quantity and correct size. The agarose was dissolved in 1x TAE buffer by boiling in a microwave. Afterwards, the agarose

was cooled down slightly and 'SYBR Safe DNA gel stain' was added (1 µl per 10 ml gel). 'SYBR Safe' stains DNA by intercalating but is less hazardous than ethidium bromide. Agarose gels with a size of 120 x 140 mm or 70 x 80 mm were cast and after polymerization 4 µl of the samples and 'GeneRuler 100 bp DNA Ladder' were loaded. The loading dye ('CoralLoad') was included in the PCR mastermix. The DNA was separated in a horizontal gel chamber with 1x TAE buffer for 20 minutes at 150 V. The gel was visualized with the *ChemiDoc^{TM} Touch Imaging System* and the gel pictures were analyzed with *Image J*.

4.2.8 Bisulfite pyrosequencing

The pyrosequencing was performed using the *PyroMark Q48 Autoprep*. Prior pyrosequencing, a bisulfite PCR for the region of interest was performed as described in section 4.2.6. The sequencing primer was designed together with the PCR primer (section 4.6.2). For programming of the sequencing assay the *PyroMark Q48 Autoprep* software was used with the 'CpG Assay' mode. To generate the dispensation order of the nucleotides, the sequence of the region of interest before bisulfite treatment was pasted into the assay. After setting up the sequencing assay a 'New Run' was programmed in the *PyroMark Q48 Autoprep* software. For several samples automatic sequencing primer dispensation was chosen.

After every third to fourth run a pyrophosphate clean was performed. A pyrophosphate contamination appears as high background and peaks in control dispensations. Only nucleotide cartridges are affected. The pyrophosphate clean was conducted according to the *PyroMark Q48 Autoprep* instruction manual.

The sequencing reagents were equilibrated to room temperature prior sequencing. The sequencing primer was used in a concentration of 4 µM, diluted in 'Annealing Buffer'. The *PyroMark Q48 Autoprep* was prepared according device instructions. The disc was loaded with 3 µl 'PyroMark Q48 Magnetic Beads' and 10 µl biotinylated PCR product. After inserting the disc into the pyrosequencer the run was started. If manual primer loading was chosen 2 µl of sequencing primer were added after PCR product clean up. The final concentration of the sequencing primer was 800 nM in 10 µl reaction mix. After finishing the run, the cartridges were cleaned with ultra-pure water according to the cleaning program. Afterwards, the cartridges were left unlocked to prevent condensation and the absorber strip was carefully removed.

The percentage of DNA methylation was determined by measuring the amount of thymine and cytosine at the position with possible DNA methylation and calculating the ratio of both signals. The data were analyzed with the *PyroMark Q48 Autoprep* software and *Excel*.

Bisulfite pyrosequencing controls

To measure DNA methylation by pyrosequencing a preceding amplification step is necessary, otherwise, the sensitivity of the pyrosequencer would be insufficient to detect the region of interest. However, amplification of bisulfite DNA is challenging, because unmethylated alleles are preferentially amplified (although preferential amplification of the methylated allele was rarely observed, too) [159]. To test if PCR primer display a PCR bias DNA methylation controls were generated. The controls consist of completely unmethylated genomic DNA and completely methylated genomic DNA which are bisulfite converted and mixed to obtain bisulfite DNA with 0%, 50%, and 100% methylation. The methylation controls were sequenced once for each assay. Furthermore, the primer and the PCR product were tested for unspecific binding.

Preparation of the unmethylated DNA. For generation of unmethylated DNA a whole-genome amplification (WGA) of genomic DNA was performed with the *REPLI-g*^{R} *Mini Kit* which is based on isothermal multiple displacement amplification. Multiple displacement amplification uses random, hexameric primer which anneal to denatured DNA [221]. The DNA polymerase amplifies the DNA by strand-displacement synthesis at a constant temperature generating DNA structures with multiple branches [221]. The whole-genome amplification was performed according manufacturer's instructions. Shortly, DNA was denatured by adding buffer D1 and incubation for three minutes at room temperature. Afterwards, the stop solution as well as the 'REPLI-g Mini DNA Polymerase' and the 'REPLI-g Mini Reaction Buffer' was added. The reaction mix was incubated for 16 h at 30°C. Afterwards, the 'REPLI-g Mini DNA Polymerase' was inactivated for three minutes at 65°C. The WGA was stored at -20°C.

Preparation of the 100% methylated DNA. To generate 100% methylated genomic DNA, it was *in vitro* methylated by the CpG methyltransferase M. SssI. This methyltransferase is expressed in E. coli from a gene originating from the Spiroplasma sp. strain MQ1 [150]. Firstly, the S-adenosyl methionine (SAM) stock with 32 mM was diluted to 1600 µM with nuclease-free water. The reaction mix was prepared as described below and mixed by pipetting.

Table 4.5: Reaction mix for *in vitro* DNA methylation

Component	Volume/reaction
10x NEBuffer 2	2 µl
SAM (1600 µM)	1 µl
DNA	up to 4 µg
M. SssI	1 µl
Nuclease-free water	variable
Total volume	20 µl

The reaction mix was incubated at 37°C for four hours. Afterwards, the methyltransferase was inactivated by heating the samples to 65°C for 20 minutes and the reaction mix was purified by drop dialysis using 0.1 µm membrane filter.

Primer controls. The primer quality is a crucial factor for reliable sequencing results. Unspecific primer binding or self-priming by looping of the PCR product would lead to unspecific signals. Therefore, each sequencing assay and the self-designed primer were validated by primer controls. To exclude the formation of primer dimer the sequencing primer, the biotinylated primer, and the sequencing and biotinylated primer together were sequenced without PCR product. Furthermore, also the PCR product alone, without sequencing primer, was sequenced to exclude self-priming by looping. Only if every single control was negative the assay was used for sequencing of the samples.

4.2.9 cDNA synthesis

RNA was diluted to 2 µg in 10 µl with DEPC-treated water in PCR stripes and reverse transcribed into cDNA using the *High-Capacity cDNA Reverse Transcription kit* according manufacturer's instructions. Shortly, a mastermix according table 4.6 was prepared and 10 µl mastermix were added to the RNA dilution. After mixing and short centrifugation, RNA was reverse transcribed in a thermo cycler with the program in table 4.7. For measuring of mRNA levels by qRT-PCR cDNA was diluted to 5 ng/µl with DEPC-treated water and stored at -20°C.

Table 4.6: Reaction mix for cDNA synthesis

Component	Volume/reaction
10x RT buffer	2.0 µl
25x dNTP Mix (100 mM)	0.8 µl
10x RT Random Primers	2.0 µl
MultiScribe™ Reverse Transcriptase	1.0 µl
RNase Inhibitor	1.0 µl
Nuclease-free H_2O	3.2 µl
RNA (2 µg)	10 µl
Total volume	20.0 µl

Table 4.7: Program for cDNA synthesis

Step	Temperature	Time
1	25°C	10 min.
2	37°C	120 min.
3	85°C	5 min.
4	4°C	forever

4.2.10 Quantitative real time PCR

A quantitative real time PCR (qRT-PCR) is based on the principle of a conventional PCR but allows the quantification of the input material after each amplification step. Therefore, qRT-PCR is used to determine expression of genes of interest. There are different chemistries available to detect the amount of DNA during PCR [11]. Here, intercalating fluorescent dyes and fluorescent probes were used. The common feature of both chemistries is the proportionally increasing fluorescence with increasing number of amplification product [11]. Thus, the fluorescent signal can be used for quantification of the number of amplicons after each cycle. In the course of this thesis, SYBR green and TaqMan probes were used. SYBR green is an intercalating fluorescent dye which binds double-stranded DNA non-sequence specifically [11]. In solution and bound to single-stranded DNA it emits almost no fluorescence [11, 116]. With amplification of DNA the amount of double-stranded DNA increases and therefore, also the SYBR green fluorescence. After each elongation cycle the fluorescence is measured. qRT-PCR with SYBR green is inexpensive, but SYBR green will also bind to unspecific amplification products. To check the specificity, a melt curve analysis is performed after each qRT-PCR [116, 197]. The melting temperature of DNA depends on the GC content, the length of the product and the sequence, thus, unspecific PCR products and primer dimer can be distinguished from the desired PCR product [116]. For generation of a melt curve the temperature is increased gradually to 95°C which leads to denaturation of the double-stranded PCR products and release of the dye [116]. The decreasing fluorescence is continuously recorded. If the primers are specific and only one product is amplified the melting curve shows only one peak. Additionally, a standard curve is measured to determine the efficiency of the primer.

TaqMan assays consist of unlabeled primer and a TaqMan probe. The probe is labeled with a fluorescent dye at the 5'-end and a quencher at the 3'-end and binds specifically to the target downstream of the forward primer [116]. The probe itself cannot be extended [11]. The intact probe does not emit any fluorescence due to quenching of the dye. After annealing of primer and probe to the DNA the *Taq* DNA polymerase synthesizes the new DNA strand. When encountering the

probe the 5'-3' exonuclease activity of the DNA polymerase degrades the probe and thereby releases the fluorescent dye from the quencher resulting in emission of fluorescence proportionally to the amount of PCR product [11]. The TaqMan chemistry is very sensitive and allows multiplexing of several assays when fluorescent dyes with different emission wavelength are used. However, TaqMan assays are also more cost-intensive, but each commercial assay is validated.

To control for possible variances of the optical system of the thermo cycler a passive reference dye is included in each qRT-PCR (for both SYBR green and TaqMan). This dye emits a fluorescence which is independent of the PCR reaction and it does not influence the amplification. Here, ROX (carboxy-X-rhodamine) was used as reference dye.

SYBR green-based qRT-PCR

For SYBR green-based qRT-PCR the *Fast Start Universal SYBR Green Master*, which already contains ROX, was used. The primer were designed as described in section 4.6.2. For validation and obtaining the amplification efficiency a standard curve was performed. The standard was generated by mixing undiluted cDNA of all samples and diluting this mixture 1:10. This first dilution represents the first standard sample with the highest concentration. Starting from this sample a 1:4 serial dilution was performed to generate a standard curve with six decreasing concentrations. The efficiency is calculated with the slope of the standard curve, obtained by plotting the logarithmic concentrations against the Ct values.

The primer stocks were diluted to a 5 µM working solution. The mastermix for the desired sample number in duplicates was prepared as indicated in table 4.8 without cDNA and mixed. 4 µl cDNA and 6 µl mastermix were pipetted in each well of a MicroAmp^{R} EnduaPlate^{TM} optical 96-well plate and the plate was sealed. To remove bubbles and collect the reaction mix at the bottom of the wells the plate was centrifuged for two minutes at 450xg. If the plate was prepared for a later run it was stored in the dark. The qRT-PCR was performed with the *QuantStudio 5* and the program described in table 4.9 was used. The qRT-PCR results were analyzed with the cloud version of the *QuantStudio^{TM} Design & Analysis Software* and *Excel*. Potential housekeeping genes were analyzed with the NormFinder algorithm [10]. *Ppia* was identified as best suited and thus, was used for normalization. Relative gene expression was calculated with the comparative quantification method, considering the efficiency of the PCR reaction which was determined by measuring a standard curve. As reference sample a chow mouse with a Ct value similar to the mean value of the chow group of each time point was chosen. For each week a separate reference sample was used of the corresponding chow group. The reference sample for the target gene and the housekeeping gene (HK) was the same. Following formulas were used for the calculation of the fold change with Ct - Ct value, ref-sample - reference sample, HK - housekeeping gene:

$$\text{Efficiency} = 10^{\left(\frac{-1}{\text{slope}}\right)}$$

$$\text{Fold change} = \frac{\text{Efficiency}_{\text{target}}{}^{(\text{Ct(ref-sample Target)-Ct(sample target)})}}{\text{Efficiency}_{\text{HK}}{}^{(\text{Ct(ref-sample HK)-Ct(sample HK)})}}$$

The statistics was performed on the ΔCt values calculated by $\Delta\text{Ct} = Ct_{\text{Target}} - Ct_{\text{HK}}$.

Table 4.8: Reaction mix for SYBR green-based qRT-PCR

Component	Final Concentration	Volume/reaction
FastStart Universal SYBR Green Master (2x)	1x	5.0 µl
Forward Primer (5 µM)	250 nM	0.5 µl
Reverse Primer (5 µM)	250 nM	0.5 µl
cDNA	20 ng	4.0 µl
Total volume		10.0 µl

Table 4.9: Program for SYBR green-based qRT-PCR

Step	Temperature	Time	Cycle
Activation	95°C	10 min.	
Denaturation	95°C	15 s	40
Annealing/Extension	60°C	1 min.	
Melt curve analysis			
Denaturation	95°C	15 s	
Extension	60°C	1 min.	
Melting analysis	95°C	0.15°C/s, 1 s	

TaqMan-based qRT-PCR

To measure gene expression by TaqMan assays the *QuantiNova™ Probe PCR Kit* was used. The components of the kit, the TaqMan assay, and cDNA was thawed and subsequently mixed. The mastermix was prepared as indicated in table 4.10 for the desired sample number in duplicates without cDNA and mixed. 6 µl of mastermix and 4 µl of cDNA were dispensed into a MicroAmp® EnduaPlate™ optical 96-well plate. The plate was centrifuged for two minutes at 450xg and the PCR was carried out in the *QuantStudio 5* with the program described in table 4.11. The PCR results were analyzed with the cloud version of the *QuantStudio™ Design & Analysis Software* and *Excel*. The housekeeping genes were identified with the NormFinder algorithm [10]. The best results were achieved with the geometric mean of *Rpl37* and *Hprt*. Relative gene expression was calculated with following formula with Ct - Ct value, ref-sample - reference sample, HK - housekeeping gene:

$$\text{Fold change} = \frac{2^{(\text{Ct(ref-sample Target)-Ct(sample target)})}}{2^{(\text{Ct(ref-sample HK)-Ct(sample HK)})}}$$

The amplification efficiency of TaqMan assays is presumed to be 100% which means in each cycle the amount of DNA doubles. Therefore, the base of the exponent was 2. This formula corresponds

to the ΔΔCt method. As reference sample for each time point a chow mouse of the corresponding chow group was used with a Ct value which corresponds approximately to the mean value of this chow group. The statistics was performed on the ΔCt values calculated by $\Delta Ct = Ct_{\text{Target}} - Ct_{\text{HK}}$.

Table 4.10: Reaction mix for Taqman-based qRT-PCR

Component	Final Concentration	Volume/reaction
QuantiNova Probe PCR Master Mix (2x)	1x	5.0 µl
QN ROX Reference Dye	1x	0.05 µl
TaqMan assay	0.4 µM primer, 0.2 µM probe	0.5 µl
DEPC-treated H_2O		4.5 µl
cDNA	20 ng	4.0 µl
Total volume		10µl

Table 4.11: Program for Taqman-based qRT-PCR

Step	Temperature	Time	Cycle
Activation	95°C	2 min.	
Denaturation	95°C	5 s	40
Annealing/Extension	60°C	30 s.	

4.2.11 Transcriptome profiling with gene expression microarrays

For genome-wide gene expression measurement RNA was applied to Clariom^{TM} D microarrays for mouse. The Clariom^{TM} D measures coding and non-coding genes, exons, and alternative splice variants. The Affymetrix microarrays are based on perfect match-mismatch probe pairs [92]. For each target sequence a probe perfectly complementary to the sequence and a probe with one mismatch in the middle is present on the array [92]. This allows to control for unspecific binding [92].

For the transcriptome profiling seven metabolic normal chow mice of week 1 and week 12 as well as eight HFD mice of week 1 and week 12 with the severest phenotype were chosen. RNA was isolated from liver tissue as described in section 4.2.3. The preparation of the samples was performed with the *GeneChip^{TM} WT PLUS Reagent Kit* according to manufacturer's instructions. As input 250 ng RNA of each sample was used as well as 250 ng of the Poly-A RNA controls. After hybridization, the microarrays were washed and stained with the *GeneChip^{R} Fluidics Station 450* and measured with the *GeneChip^{R} Scanner 3000*.

The microarrays were analyzed with the *Transcriptome Analysis Console* software with the analysis type 'Expression (Gene + Exon)'. As summarization method 'Gene + Exon - SST-RMA' and as ANOVA method 'ebayes' was used. A probe set was considered expressed if at least 50% of the detection above background (DABG) values were below the DABG threshold. A gene was considered differentially expressed with a linear fold change ≥1.5 or ≤-1.5 and a FDR p value <0.05.

4.2.12 Whole-genome bisulfite sequencing

The whole-genome bisulfite sequencing (WGBS) was performed by the sequencing core facility of the Max Planck Institute for Molecular Genetics in collaboration with Professor Alexander Meissner.

The sequencing was performed with two metabolic normal chow mice of week 12 and the two HFD mice with the severest phenotype of week 12. The whole-genome bisulfite sequencing was performed as described in Kretzmer et al. [114]. Briefly, strand-specific methylC-seq libraries of genomic DNA were prepared using the *TruSeq DNA Methylation Kit* by Illumina (San Diego, CA, USA). The adapter-ligated fragments with 200 bp insert length were bisulfite converted with the *EZ DNA Methylation Kit* by Zymo Research (Irvine, CA, USA). The adapters contained methylated cytosines, which remained unchanged by bisulfite treatment, to achieve a balanced base distribution within the fragments. This is important to pass the sequencing quality checks. After bisulfite conversion a PCR with eight cycles was performed and the libraries were paired-end sequenced with the *NovaSeq 6000* sequencing system (Illumina).

After sequencing, the sequences were trimmed by 13.5% and the reads were mapped to the mouse reference genome mm9 using 'segemehl' in its bisulfite methylC-seq mode. At least 185 million reads could be aligned, corresponding to approximately 93%. The methylation calling was performed with 'BSMAP'. The minimal coverage was set to 10x of each CpG site. The differentially methylated regions (DMRs) were identified using 'metilene'. A DMR was defined as a genomic region with maximal 2000 bp containing at least 10 CpG sites with an average difference of DNA methylation between the groups of 10%.

The annotation was performed with the 'annotatr'-package in *R* [29]. As input, a BED-file containing the genomic location (assembly: mm9) of the DMR was used. DMRs with higher DNA methylation in HFD mice and DMRs with lower DNA methylation in HFD mice were imported separately. The bar graph was generated by specifying the results as 'annotated_regions' and 'annotated_random', respectively. It is possible that one DMR is annotated with multiple annotations, for example when a long differentially methylated region spans an exon-intron boundary it is annotated with exons, introns, and exon-intron boundary. Then, this DMR counts for all these annotations in the bar graph.

4.3 Measurement of hepatic macromolecules

4.3.1 Triglyceride assay

Triglycerides are lipids consisting of three fatty acids bound to a glycerol backbone. The *Triglyceride Colorimetric Assay Kit* used here is based on the enzymatic hydrolysis of triglycerides into fatty acids and glycerol by lipoprotein lipase. The glycerol is phosphorylated by glycerol kinase to glycerol-3-phosphate which is subsequently oxidized by glycerol phosphate oxidase resulting in dihydroxyacetone phosphate and hydrogen peroxide. The peroxidase converts hydrogen peroxide

with 4-aminoantipyrine and N-Ethyl-N-(3-sulfopropyl)-*m*-anisidine to the purple Quinoneimine dye which is measured spectroscopically at 530-550 nm.

Hepatic triglycerides were determined according to the instruction manual with minor changes of the preparation of the homogenate. Initially, 50-60 mg snap-frozen liver was homogenized in 250 µl diluted 'NP40 Substitute Assay Reagent' containing protease inhibitor cocktail (1:100 diluted EDTA-Free Protease Inhibitor Cocktail Set V) at following settings: Speed: 5 m/s, time: 20 s, cycle: 1. The homogenate was heated two times to 90°C for three minutes. Between the heating steps the samples were cooled down to room temperature. Afterwards, the samples were centrifuged at 4°C and 10 000xg for 10 minutes. The further sample preparation was performed as described in the kit manual. When transferring the supernatant, the fat layer on top was thoroughly included. The supernatant was diluted as follows with NP40 buffer provided by the kit:

	week 1	week 2	week 4	week 5	week 8	week 12
chow	1:5	1:5	1:5	1:5	1:5	1:5
HFD	1:5	1:5	1:5	1:6	1:10	1:15

The assay was conducted according manufacturer's instructions in duplicates including the standard. The assay was measured with the *SPECTROstar Nano* and the data were analyzed with the *SPECTROstar Nano - Data Analysis* software and *Excel*. The absorbance was blank-corrected and by taking into account the standard curve the triglyceride content was calculated:

$$\text{Triglycerides } [mg/dl] = \frac{(\text{corrected absorbance})–(\text{y-intercept})}{\text{slope}}$$

The calculated triglyceride concentration was corrected by the dilution factor and normalized to the amount of input tissue.

4.3.2 Glycogen assay

Glycogen is a polysaccharide consisting of glucose monomers and can be detected by iodine which forms a colored complex with glycogen [233]. For determination of hepatic glycogen, 20-30 mg snap-frozen liver tissue was homogenized in 1 ml 5% trichloroacetic acid and incubated for 30 minutes at room temperature. Afterwards, the samples were centrifuged at room temperature for 10 minutes at >16 000xg to remove tissue debris and 150 µl of the supernatant were mixed with 300 µl >95% ethanol. Each sample was measured as triplicate, therefore, from each homogenate three times 150 µl supernatant was dispensed into a new tube and incubated for 20-24 hours at 4°C to precipitate the glycogen. After incubation the samples were centrifuged for 30 minutes at >16 000xg and the supernatant was discarded. The pellet was air-dried to remove remaining ethanol and solved in 75 µl Lugol reaction mix by vortexing. The Lugol reaction mix contains Lugol solution, a 1:2 iodine:potassium iodide solution. The samples should turn orange-red. To assure a stable color samples were incubated for 10 minutes at room temperature. The samples were pipetted into a 96-well

microplate and the absorbance was measured with the *SPECTROstar Nano* at 600 nm. As blank Lugol solution was used. The data were analyzed with the *SPECTROstar Nano - Data Analysis* software and *Excel*. The absorbance was background-corrected and normalized to input tissue weight.

4.4 Histology

Hematoxylin eosin staining is used for microscopic evaluation of tissues [33]. Hematoxylin stains DNA, therefore, the nucleus appears blue, whereas eosin stains cytoplasm and extracellular matrix reddish-pink [33]. Fat deposits are not directly visible, because lipophilic substances are washed out during the deparaffining process and appear as round whitish spaces [33].

4.4.1 Paraffin embedding of paraformaldehyde-fixed liver

Directly after sacrifice livers were fixed in 4% paraformaldehyde solution for 24 hours at 4°C. The livers were transferred into Tissue Processing/Embedding cassettes for subsequent dehydration. Since paraffin is a lipophilic substance water needs to be removed from the tissue:

1. 2x 2 min. with 1x PBS
2. 3x 20 min. with 50% ethanol
3. 3x 20 min. with 70% ethanol

After the last wash step the livers were stored in 70% ethanol for up to 14 days at 4°C. For further dehydration the 70% ethanol was removed and the tissue was washed at room temperature on a magnetic stirrer:

1. 3x 20 min. with 95% ethanol
2. 3x 20 min. with 100% ethanol
3. 3x 10 min. with xylol

After the last xylol step the cassettes were transferred into a paraffin bath at 60°C for one hour. The paraffin bath was changed twice and the livers remained in the third paraffin bath overnight. Subsequently, the tissue was embedded with paraffin.

4.4.2 Preparation of paraffin slices

To prepare paraffin slices the paraffin blocks were frozen at -20°C overnight. The liver was cut in 5 µm slices and placed on a microscopic slide. To smooth the tissue slice, the slide was carefully dipped in water maintained at 45-50°C. Afterwards, the slides were dried for one hour at 65°C in an incubator and stored at room temperature.

4.4.3 Hematoxylin eosin staining

The hematoxylin eosin staining was performed for four HFD-fed mice and four chow-fed mice of week 1, 8, and 12. Hematoxylin and eosin are aqueous solutions, therefore, the liver slices need to be deparaffinated and rehydrated prior staining. Initially, eosin and hematoxylin were filtered and eosin was acidified with 100-120 µl acidic acid. The slices were deparaffinated by subsequent wash steps with decreasing ethanol concentration:

1. 2x 20 min. xylol
2. 2x 5 min. 100% ethanol
3. 1x 5 min. 96% ethanol
4. 1x 5 min. 80% ethanol
5. 1x 10 min. 70% ethanol
6. Short dipping in dH_2O

After deparaffination the slices were incubated for 10 minutes in hematoxylin, shortly dipped in dH_2O, and rinsed with tap water for 15 minutes. After washing for one to two minutes in fresh dH_2O the slices were stained for three minutes with eosin. Afterwards, the slices were dehydrated by subsequent wash steps with increasing ethanol concentration:

1. Short dipping in dH_2O
2. 30 s in fresh 70% ethanol
3. 30 s in fresh 80% ethanol
4. 30 s in fresh 96% ethanol
5. 30 s in fresh 100% ethanol
6. 2x 10-15 min. xylol

Two drops of Pertex^R mounting medium were applied to the slides and they were covered with the coverslips. The slides were dried overnight. The analysis of the tissue slices was performed with the *Nikon Eclipse Ci-L microscope* with 10x magnification.

4.5 Protein biochemical methods

4.5.1 Western blot analysis

Western blots for Akt and Akt with phosphorylated Ser473 (pAkt) were performed for unstimulated mice fed for 1, 2, 4, 8, and 12 weeks with chow or HFD.

4.5.1.1 Isolation of hepatic proteins

Hepatic proteins were isolated from 20-30 mg snap-frozen liver with RIPA-based lysis buffer. The tissue was homogenized with 250 µl buffer in the *Fisherbrand Bead Mill 24 Homogenizer* with following settings: Speed: 5 m/s, time: 20 s, cycle: 1.

The homogenate was centrifuged at maximum speed and 4°C for 20 minutes. Afterwards, the supernatant was transferred into a new tube and centrifuged a second time at maximum speed and 4°C for 20 minutes. The supernatant was transferred in a new tube and stored on ice for subsequent protein quantification.

4.5.1.2 Quantification of proteins

Protein concentrations were measured with the *Pierce™ BCA Protein Assay Kit* which is based on the reduction of Cu^{2+}/Cu^{1+} by proteins in alkaline solution. The chelation of Cu^{1+} by bicinchoninic acid (BCA) results in a colored complex which can be detected spectroscopically. Before starting the measurement of the samples, the protein standard was thawed on ice, the protein lysate was diluted 1:20, and the working reagent was prepared according manufacturer's manual. The measurement was performed in duplicates in a 96-well plate suited for absorbance detection. 10 µl of samples and standards were pipetted into the plate and 200 µl of the working reagent was added. The plate was sealed with an adhesive PCR seal, mixed for 30 seconds on a plate shaker, and incubated for 30 minutes at 37°C. Afterwards, the reaction mix had to cool down for 20 minutes to room temperature before measuring the protein concentration spectroscopically with the *SPECTROstar Nano* at 562 nm. The protein concentration was analyzed using the *SPECTROstar Nano - Data Analysis* software and *Excel*.

4.5.1.3 SDS polyacrylamide gel electrophoresis

The gels for the SDS polyacrylamide gel electrophoresis (SDS-PAGE) were prepared with the *TGX Stain-Free™ FastCast™ Acrylamide Starter Kit* which represents a modified Laemmli system. This kit provides premixed 'Tris-Glycine eXtended (TGX) acrylamide/bis-acrylamide' solutions containing trihalo compounds which react with proteins upon UV light activation and produce fluorescent light. This stain-free technology allows the visualization of the total protein amount on a western blot membrane without additional staining and replaces the use of a housekeeper protein. For normalization of the western blot bands the total protein per lane was used [42].

The gels were cast with the *SureCast™ Gel Handcast Station* with 1.0 mm thickness. For the 10% SDS polyacrylamide resolver gel 'Resolver A', 'Resolver B', 10% APS, and TEMED were mixed. After polymerization, the stacking gel was cast by mixing 'Stacker A', 'Stacker B', 10% APS, and TEMED and the comb was inserted.

For SDS-PAGE the protein lysates were diluted to 30 µg/8 µl with RIPA buffer. To apply the samples to the gel 4 µl 'SDS Blue Loading Dye' were added and the samples were denatured for 10 minutes at 98°C in a heating block. In addition to the samples, also 8 µl of the 'PageRuler™ Prestained Protein Ladder 10-170 kDa' were subjected to the SDS polyacrylamide gel. The gel electrophoresis was conducted in the vertical *Mini Gel Tank* with 'running buffer' for 1 to 1.5 h at 100 V.

After electrophoresis the stain-free dye in the gel was immediately activated by radiating with UV light for one minute.

4.5.1.4 Electro-transfer of proteins

Subsequently, the proteins were transferred to a polyvinylidene difluoride membrane (PVDF) by a semi-wet transfer. Prior transfer, the membrane was activated by shortly washing in methanol, followed by washing in deionized water and equilibration in transfer buffer. The electro-transfer was performed with the *Mini Blot Module* for one hour at 20 V.

4.5.1.5 Immunological detection of Akt and phosphorylated Akt

The detection of Akt and phosphorylated Akt was performed with antigen-specific primary antibodies and a horseradish peroxidase-coupled secondary antibody. The primary antibodies were diluted 1:1000 in 5% milk powder dissolved in TBS and the secondary antibody was diluted 1:5000 in 5% TBS-milk.

Following electro-transfer, the membrane was incubated for one hour in 5% TBS-milk to block unspecific binding sites. Afterwards, the membrane was transferred into the primary antibody dilution and incubated overnight at 4°C on a tube roller. After washing the membrane three to four times in TBST for about five minutes, the membrane was incubated with the secondary antibody dilution for 1 h at room temperature. Subsequently, the membrane was washed again three to four times with TBST for about five minutes. The detection of the antibody was performed by enhanced chemiluminescence with the *Clarity Max^{TM} Western ECL Substrate*. The method is based on the oxidation of luminol in the presence of peroxide by the horseradish peroxidase, which is coupled to the secondary antibody, generating light. Directly prior detection, 0.5 ml 'Clarity Max^{TM} Western Peroxide Reagent' and 0.5 ml 'Clarity Max^{TM} Western Luminol/Enhancer Reagent' was mixed and applied to the membrane. After detection with the *ChemiDoc^{TM} Touch Imaging System*, the membrane was stripped by incubation in 10 ml 'Restore^{R} PLUS Western Blot Stripping Buffer' for 20 minutes. The membrane was shortly washed in TBST and blocked for 1 h in 5% TBS-milk. Afterwards, the membrane was incubated overnight at 4°C with the primary anti-phosphorylated Akt antibody. The detection took place as described for Akt.

The western blots were quantified with the *Image Lab* software. The band intensity of total protein, Akt, and phosphorylated Akt was determined densitometrically. Both Akt and phosphorylated Akt were normalized to total protein and the pAkt/Akt ratio was calculated. One animal of each group and time point was present on each western blot. To reduce interblot variance the ratios of each blot were normalized to chow week 1 present on the same blot.

4.5.2 Enzyme activity assay

For determination of the activity of different enzymes a coupled enzyme reaction was used which oxidizes nicotinamide adenine dinucleotide from NADH to NAD^+. NAD^+ has an absorption maximum at 260 nm and NADH has an additional maximum at 340 nm, therefore, the oxidation is spectroscopically traceable by measuring the absorption at 340 nm.

For phosphoenolpyruvate carboxykinase (PEPCK) and pyruvate kinase (PK) activity assays 30-50 mg snap-frozen liver were homogenized in 500 µl 'Enzyme activity homogenizing buffer'. Following settings were used for homogenization: Speed: 5 m/s, time: 20 s, cycle: 1. The homogenate was centrifuged at full speed and 4°C for 20 minutes. The fat on top was discarded and the infranatant was transferred into a new tube and subsequently centrifuged for one hour at full speed and 4°C. The infranatant was transferred into a new tube for subsequent measurement. Due to temperature differences the PEPCK assay was measured first and the PK assay afterwards.

4.5.2.1 Phosphoenolpyruvate carboxykinase activity assay

To measure phosphoenolpyruvate carboxykinase (PEPCK) activity, liver homogenate was incubated with oxaloacetate, the substrate of PEPCK, leading to the production of phosphoenolpyruvate. This was converted to pyruvate by pyruvate kinase (PK), forming ATP from ADP. The final reaction was the synthesis of lactate from pyruvate by lactate dehydrogenase (LDH) which was accompanied by the oxidation of NADH to NAD^+. The reaction is illustrated in figure 4.3. The oxidation of NADH is measured spectroscopically. The samples were measured in duplicates.

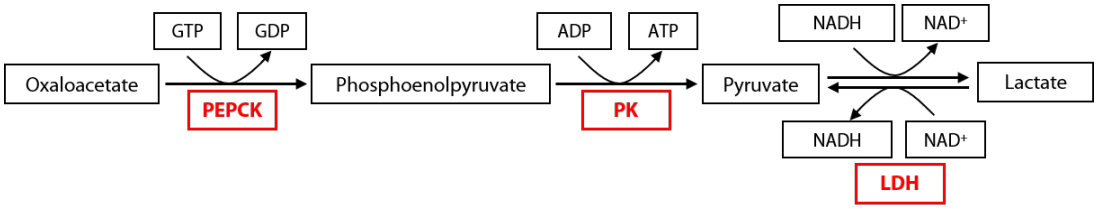

Figure 4.3: Reaction of the phosphoenolpyruvate carboxykinase activity assay.

Before starting with the assay the temperature of the *SPECTROstar Nano* plate reader was set to 25°C. A 5 mM oxaloacetate solution (final concentration: 0.5 mM) and the 'PEPCK sample buffer' were freshly prepared and the buffer was incubated for 15 minutes at room temperature. The infranatant was diluted 1:500 in 'Enzyme activity homogenizing buffer'. For baseline measurement 150 µl sample buffer were pipetted into a 96-well plate and measured spectroscopically at 340 nm until the slope was constant. Subsequently, 25 µl oxaloacetate was added and shortly mixed on an orbital shaker. After measuring about five cycles, 75 µl homogenate was added. As control for the non-enzymatic decay of oxaloacetate 75 µl 'Enzyme activity homogenizing buffer' instead of homogenate was used. The absorbance was measured at 340 nm every 30 seconds for about 15 minutes until the slope was constant.

4.5.2.2 Pyruvate kinase activity assay

To measure the activity of pyruvate kinase (PK) liver homogenate was incubated with phosphoenolpyruvate which was converted to pyruvate by the PK. Pyruvate in turn was converted to lactate by lactate dehydrogenase using NADH as cosubstrate. The reaction is illustrated in figure 4.4. The oxidation of NADH to NAD^+ is measured spectroscopically at 340 nm. The samples were measured in duplicates.

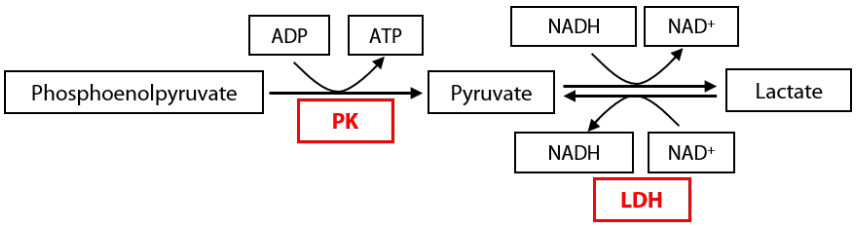

Figure 4.4: Reaction of the pyruvate kinase activity assay.

To measure PK activity the temperature of the *SPECTROstar Nano* plate reader was set to 30°C. A 5 mM phosphoenolpyruvate solution (final concentration: 0.5 mM) as well as the 'PK Sample Buffer' were freshly prepared. The buffer was incubated for 15 minutes at room temperature. The infranatant was diluted 1:30 with 'Enzyme activity homogenizing buffer'. For baseline measurement 150 µl 'PK sample buffer' were measured spectroscopically at 340 nm in a 96-well plate until the slope was constant. Afterwards, 25 µl phosphoenolpyruvate was added and shortly mixed on an orbital shaker. After about five cycles of measuring 75 µl homogenate or 'Enzyme activity homogenizing buffer' as blank was added. The reaction was tracked spectroscopically every 30 seconds at 340 nm for about 15 minutes until the slope was constant.

4.5.2.3 Analysis of enzyme activity data

After measuring the enzyme activity, the protein concentration of the liver homogenate was determined as described in section 4.5.1.2 for normalization of the data.

The data analysis was carried out with the *SPECTROstar Nano - Data Analysis* software and *Excel*. The enzyme activity assay generated a signal curve with linear decrease of the absorption at 340 nm. Within the linear range, eight measurement points were used to determine the slope. The specific enzyme activity was calculated with

$$\text{Activity} = \frac{|\text{slope/min}| \cdot \text{pathlength correction factor for 96-well plate} \cdot \text{end volume}}{\text{extinction coefficient of NADH} \cdot \text{sample volume}}$$

Pathlength correction factor for 96-well plate:	3.045 cm^{-1}
End volume:	250 µl
Extinction coefficient of NADH:	6178 l/(mol · cm)
Sample volume:	75 µl

The specific enzyme activity in M/min was converted to nmol/(ml · min) by multiplication with $1 \cdot 10^6$. The values were normalized to protein concentration and the dilution factor was considered. Finally, the specific enzyme activity was expressed as nmol/(mg · min).

4.5.3 Insulin enzyme-linked immunosorbent assay

For insulin measurement the enzyme-linked immunosorbent assay (ELISA) *Rat/Mouse Insulin ELISA* was used. The assay is a Sandwich ELISA consisting of a monoclonal mouse anti-rat insulin antibody coated to the microtiter plate and a biotinylated polyclonal antibody against the antibody-bound insulin. The ELISA was performed according manufacturer's instructions. Shortly, 10 µl of rat insulin standard, quality controls, and plasma samples were dispensed into the provided microplate in duplicates to immobilize the insulin to the antibody. The biotinylated anti-insulin detection antibody was added and the plasma-antibody mixture was incubated for two hours at room temperature with moderate shaking. After washing the plate with the *Wellwash^{TM} Versa Microplate Washer* to remove unbound material, the enzyme solution was added and incubated for 30 minutes at room temperature and moderate shaking. After removing free enzyme conjugates the substrate solution was added and the color was developed for 20 minutes. After adding the stop solution, the absorbance was measured at 450 nm and 590 nm with the spectrophotometric microplate reader *Epoch* within five minutes after adding the stop solution. The absorbance at 450 nm was corrected by subtracting the absorbance at 590 nm. The data were analyzed with *GraphPad Prism 7*. The unknown sample concentrations were computed by 4-parameter logistic fitting of the standard.

4.6 Bioinformatics and *in silico* methods

4.6.1 Identification of potential candidate genes

First candidate genes were identified by analyzing preliminary human DNA methylation data of seven non-obese, seven obese non-diabetic, and eight obese type 2 diabetic subjects [110]. Furthermore, literature (tab. 4.12) and different databases were used, such as the 'DisGeNET' database containing numerous genes associated with diseases identified by for example GWAS, animal models, and publications [15]. To check if the identified genes are differentially expressed in obese mice the 'Attie Lab Diabetes Database' was used [105]. CpG sites identified in human data were searched in the 'UCSC

Genome Browser' (http://genome.ucsc.edu/, [106]) and converted into the mouse genome assembly mm9. The gene structure was investigated and regulatory sequences were studied using the ORegAnno Track in the 'UCSC Genome Browser' as well as the *Unipro UGENE* software [131, 172].

Table 4.12: Publications used for identification of candidate genes

Publication	Data	Method	Subjects
Kirchner et al. 2016 [110]	DNA methylation	Illumina 450 K array	7 non-obese, 7 obese non-diabetic, and 8 obese type 2 diabetic humans
Keller et al. 2008 [105]	gene expression	custom ink-jet microarrays by Agilent Technologies	lean and obese C57BL/6 and BTBR mice
Kwon et al. 2012 [121]	gene expression	Illumina MouseWG-6 v2.0 expression beadchip	C57BL/6 fed with HFD or normal diet for up to 24 weeks
Multhaup et al. [163]	DNA methylation	CHARM	C57BL/6 mice fed with high fat or low fat diet for 12 weeks
Zhang et al. 2017 [256]	RNA-seq and bisulfite DNA sequencing	Illumina HiSeq 2000	C57Bl/6J fed high fat-high sucrose or low fat-low sucrose diet

4.6.2 Primer design

Design of bisulfite primer

The bisulfite primer were designed with the *PyroMark Assay Design 2.0* software. The sequence of interest was exported from the 'UCSC Genome Browser' (http://genome.ucsc.edu/, [106]). Additional 1000 bp downstream and upstream were added to the sequence of interest. The sequence was copied in the 'Original Sequence Editor' of the *PyroMark Assay Design 2.0* software which automatically performs a bisulfite conversion. After choosing the target sequence for which primers should be designed, the assay design was started with standard settings. The resulting primer sets were evaluated regarding mispriming sites, annealing temperatures, position of the sequencing primer regarding the first CpG site, possible primer dimers, and the computed score for primer set quality. Goal of the primer design was to maximize the score. The primer could be designed as a forward assay with the biotinylation at the reverse primer, or as a reverse assay with the biotinylation at the forward primer. Moreover, the upper or the lower strand could be used.

Design of SYBR green primer

Primer for SYBR green-based qRT-PCR were designed with the NCBI tool 'Primer-BLAST' [250]. 'Primer-BLAST' uses Primer3 for the primer design and BLAST to align the primer to the mouse genome for detection of unspecific binding. For the primer design the reference sequence of the gene of interest was used. The desired product should be larger than 70 bp, the primer should have

an annealing temperature of 60°C ± 3°C, and span an exon-intron junction. Only primer without any unspecific binding sites as well as primer dimer were chosen.

4.6.3 Analysis of differentially expressed genes

Venn diagram

The venn diagram of differentially expressed, coding genes for the comparisons 'chow: week 12 vs. week 1', 'HFD: week 12 vs. week 1', 'week 1: HFD vs. chow', and 'week 12: HFD vs. chow' was created with the 'VennDiagram' package implemented in *R* [36].

Pathway analysis

For differentially expressed genes identified by gene expression microarrays as well as genes which possess one or more differentially methylated regions measured by WGBS a pathway analysis with 'DAVID Functional Annotation Tool' (version 6.8) was performed [84, 85]. A pathway analysis is used to study if altered genes are associated with specific biological processes or are related in their function. For the pathway analysis a list with gene symbols was used, but with 'DAVID Functional Annotation Tool' only gene symbol lists with maximal 3000 entries can be processed. Therefore, multiple entries for the same gene as well as predicted genes were removed.

For differentially expressed genes only KEGG pathways with Bonferroni p value <0.05 were considered for subsequent plotting of the fold enrichment. The top 10 significantly enriched pathways were illustrated as circle plot with the 'GOplot' package in *R* [238]. The results of the pathway analysis for the WGBS data were plotted as bar graph using *GraphPad Prism*^{R} *7*.

Principal component analysis

To get an overview of the transcriptome data a principal component analysis (PCA) was performed. This statistical technique reduces the dimensionality of large data sets and simultaneously retains most of the variation of the data [195, 196]. The PCA performs geometric projections of the data onto lower dimensions, so-called principal components, which are linear combinations of the original variables [132, 195]. In the context of PCA, variables are experimental conditions and observations correspond to the measured gene expression [195]. The principal components represent new variables which describe as much of the variance as possible from the original data [195]. The maximal number of principal components corresponds to the number of samples or observations, depending on which is smaller [132].

The principal component analysis was performed in *MATLAB* with the function 'pca'. As input, all genes including predicted genes and those which have no gene symbol yet were used as long as they were expressed in at least one condition (a gene could be turned on or off in obesity and insulin

resistance). This yields 64 524 genes. For calling the 'pca' function, the data needed to be a matrix with rows representing the animals and columns representing the genes. The PCA was calculated with the command

```
[score,latent,explained] = pca(Data);
```

The principal component scores, saved in 'score', represented the data set in the principal component space, 'latent' contained the variance of each principal component ('eigenvalues'), and 'explained' described the percentage of total variance of each component. The data saved in 'score' were used to draw the three-dimensional scatter plot in *MATLAB* with the function 'scatter3'.

Clustering

Large and complex data sets, such as gene expression microarray data, are elusive for humans. Clustering algorithms sort objects based on their similarity in groups, so called clusters, and therefore, can be used to identify structures in these data [209]. Clustering is an unsupervised method, the algorithm does not know the group membership of the data points [199]. There are different kinds of cluster algorithms, here, clustering algorithms based on hierarchy and partition were considered [247]. Hierarchical clustering groups objects which have a small distance to each other together [209]. Usually, it is visualized as a tree, called dendrogram, with the root representing one big cluster containing all objects and the leaves representing the individual objects [209]. A strength of hierarchical clustering is its suitability for data with arbitrary shape, but it has a high time complexity [247]. Partitioning algorithms have no hierarchical structure and need a specification of the cluster number by the user beforehand [211]. According to the desired number of clusters the algorithm assigns cluster centers randomly in the data space [209]. The distance of each object to the cluster center is calculated and the objects are grouped in the cluster to which the distance is smallest [209]. The centers of the newly formed clusters are recalculated and the process is iterated for a given number. To cluster the gene expression microarray data the probably most famous partitioning cluster algorithm 'kmeans' was used. 'Kmeans' has a high computing efficiency but does only cluster effectively spherical data sets [247]. Furthermore, it is sensitive to outliers, the results depend on the predefined cluster number, and the algorithm can get stuck in a local optimum [247].

Gene expression microarrays generate a large amount of data and although cluster algorithms are well suited to handle big data a reduction of the complexity by PCA can improve the run time, clustering efficiency, and accuracy of the clustering algorithm [225]. The principal component analysis was performed as described in section 4.6.3. It is assumed that principal components whose contribution to the total variance is small contain irrelevant information and noise, thus, only a subset of principal components was used for cluster analysis [23, 129]. When choosing the number of principal components, the total variance explained by these should be at least 70% [23]. A scree

plot, showing the variance each individual principal component is accounting for as well as the cumulative variance, can be helpful to choose the right number of principal components [23]. The scree plot was created in *MATLAB* with the function shown in section C. As input, 'latent', containing the principal component variances, was used as computed in section 4.6.3.

Hierarchical clustering by Ward was performed on the first 15 principal components. The method by Ward is an agglomerative or bottom-up approach, it starts with each object as an individual cluster and subsequently merges similar clusters together into successively larger cluster [209]. As distance measure the euclidean distance was used. The distances were calculated using the function 'dist' of the package 'stats' in *R* with 'score' as input (generated as described in section 4.6.3). The distance matrix was used to create the dendrogram in *R* with 'hclust' and the 'ward.D2'-method. The resulting 'hclust'-object was plotted.

To perform 'kmeans' clustering the optimal cluster number was determined by the silhouette width, the gap statistic, and the within-sum-of-squares approach. For each method the desired clustering algorithm must be specified, in this case 'kmeans'. The silhouette width is a measure for the quality of clustering for different cluster numbers [23, 200]. For visualization the average silhouette width was plotted against the cluster number. The method is implemented in the *R*-package 'factoextra' with the 'fviz_nbclust' function for 'silhouette'. The gap statistic compares the total intra-cluster variation for different numbers of cluster with their expected values from a reference distribution without any clustering [229]. The gap statistic was performed using the 'fviz_nbclust' function for 'gap_stat' in *R*. A third method to estimate the optimal cluster number is the within-sum-of-squares approach which was calculated using the 'fviz_nbclust' function for 'wss' in *R*. After identification of the optimal cluster number 'kmeans' clustering was performed using the 'kmeans' function of the 'stats' package in *R* with 15 principal components and following parameters:

```
kmeans(15PC, 3, iter.max = 1000, algorithm = "Hartigan-Wong",
trace=TRUE, nstart=100)
```

4.7 Statistics

Phenotyping data of the longitudinal methylation study were analyzed by 2-way ANOVA with comparison of the mean of the groups for every time point without matching followed by Holm-Sidak correction for multiple testing using *GraphPad Prism*^{R} *7*. A p value smaller 0.05 was treated as statistically significant: *p<0.05, **p<0.01, ***p<0.001, ****p<0.0001.

For statistical analysis of DNA methylation data CpG sites were considered independent of each other. For longitudinal data on DNA methylation CpG sites were analyzed separately by 2-way ANOVA as described before. Data of the HFHS-fed mice were analyzed by multiple t-tests assuming same standard deviations and using statistical significance with Holm-Sidak correction for multiple testing.

Line graphs represent the mean ± standard deviation (SD). Box plots illustrate the 25th to the 75th percentile and the whiskers are ranging from the minimal to maximal value. The line within the box represents the median and the '+' the mean.

Quantitative RT-PCR data are shown as mean log fold change ± standard error of the mean (SEM). The fold change of the HFD group at a particular time point was normalized to the corresponding chow group. Two-way ANOVA was performed on ΔCt values using *GraphPad Prism*^{R} *7* as described before.

Western blot analysis was performed for eight mice per group and time point. The blot pictures were analyzed with the *Image Lab*^{TM} software, the normalization was carried out in *Excel*, and the statistical analysis by 2-way ANOVA as described before was performed in *GraphPad Prism*^{R} *7*.

Gene expression microarrays were analyzed with the *Transcriptome Analysis Console*. Genes were considered as differentially expressed with a linear fold change $\geq$1.5 or $\leq$-1.5 and a false discovery rate (FDR) p value $<$0.05.

5

Results

5.1 Metabolic phenotype of mice of the longitudinal methylation study

5.1.1 Glucose tolerance and insulin sensitivity

In order to investigate the epigenetic changes during the development of insulin resistance mice fed with either high fat diet (HFD) or chow diet were metabolically characterized. After 1, 2, 4, 5, 6, 7, 8, and 12 weeks of feeding eight mice of each group underwent an intraperitoneal glucose tolerance test to assess insulin secretion from the pancreas as well as insulin sensitivity of peripheral tissues.

Already after one week of feeding HFD mice had significantly higher body weight compared to chow-fed controls (Fig. 5.1 (a), $p_{\text{week 1}}=0.0042$, $p_{\text{week 2-12}}<0.0001$) and developed obesity with further HFD feeding. The glucose tolerance of HFD mice was significantly impaired after one week (Fig. 5.1 (b), $p_{\text{week 1}}=0.0463$). At week 5, HFD mice developed significant glucose intolerance which deteriorated with further HFD feeding (Fig. 5.1 (b), $p_{\text{week 5}}=0.0003$). Plasma insulin levels were determined after 1, 2, 4, 8, and 12 weeks of feeding. At week 1, both groups showed a high variance, therefore, conclusions had to be drawn carefully. At week 2 and 4, HFD-fed mice showed slightly, non-significantly increased insulin levels. After eight and 12 weeks of HFD feeding, insulin levels were significantly increased compared to chow-fed controls of the same week (Fig. 5.1 (c), $p_{\text{week 8-12}}<0.001$). Despite increased insulin levels HFD mice were not able to effectively clear the glucose bolus in the glucose tolerance test suggesting that mice became insulin resistant at the latest of eight weeks of feeding.

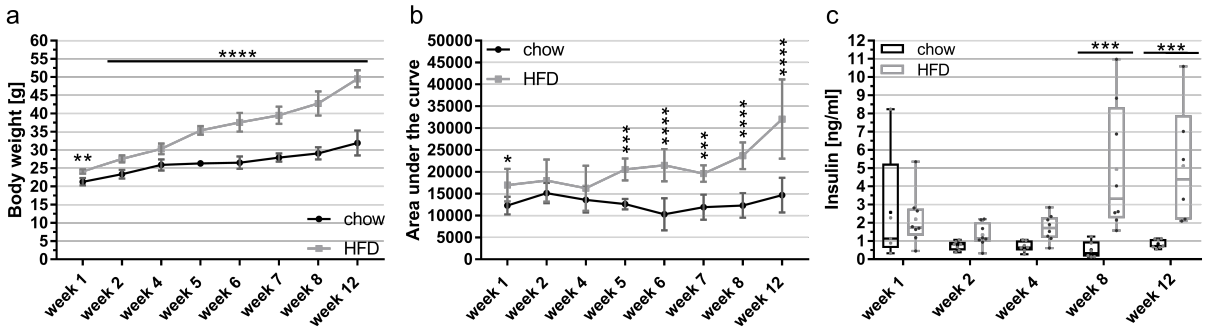

Figure 5.1: High fat diet-fed mice became obese and developed insulin resistance after five weeks of feeding. (a) Body weight of mice was determined at the day of the glucose tolerance test. HFD mice were compared to chow mice of the same week. Already after one week of feeding HFD mice weighted significantly more than chow mice. Two-way ANOVA followed by Holm-Sidak correction; $p_{week}<0.0001$; $p_{diet}<0.0001$; $p_{interaction}<0.0001$; n=7-16/group. (b) The intraperitoneal glucose tolerance test revealed that HFD-fed mice showed significantly impaired glucose tolerance at week 1 and as of week 5. Two-way ANOVA followed by Holm-Sidak correction; $p_{week}<0.0001$; $p_{diet}<0.0001$; $p_{interaction}<0.0001$; n=7-16/group. (c) Insulin levels were determined in plasma of non-fasted animals. HFD mice showed significantly increased insulin levels as of week 8. Two-way ANOVA followed by Holm-Sidak correction; $p_{week}=0.0181$; $p_{diet}<0.0001$; $p_{interaction}=0.0022$; n=5-8/group.

The plasma non-esterified fatty acids were slightly increased in the HFD group after four weeks of HFD feeding (Suppl. fig. 7.1, $p_{week\ 8}=0.0214$).

With an intraperitoneal glucose tolerance test the whole-body glucose tolerance and insulin sensitivity is assessed. However, a discrimination between different peripheral tissues is not possible, but liver, adipose tissue, and skeletal muscles develop insulin resistance at different time points [111, 230, 242]. To study hepatic insulin resistance, phosphorylation status of Akt at Ser473 was determined by immunoblotting (Fig. 5.2). In an insulin sensitive state, binding of insulin to its receptor induces phosphorylation of Akt by for example mTORC2, whereas insulin resistance leads to decreased Akt phosphorylation [184, 207].

There were no significant differences between chow and HFD mice (Fig. 5.2 (b)), although there was a trend towards higher Akt phosphorylation at Ser463 at week 1 in the HFD group. After week 2, HFD mice showed slightly lower Akt phosphorylation compared to chow-fed controls. This could indicate the development of hepatic insulin resistance in HFD mice after week 2, preceding whole-body insulin resistance.

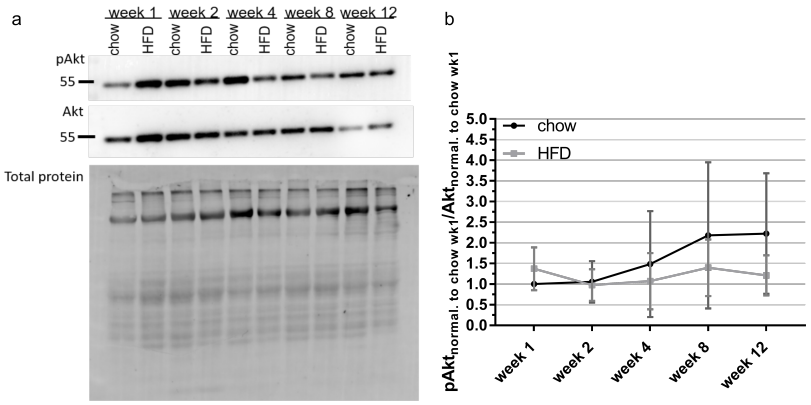

Figure 5.2: Hepatic Akt phosphorylation was slightly decreased in HFD-fed mice after two weeks of feeding. Hepatic Akt phosphorylation was analyzed by immunoblotting. (a) Representative western blot of pAkt, Akt, and total protein. (b) Phosphorylated Akt/total Akt ratio, normalized to chow week 1 on each western blot. HFD-fed mice possessed slightly lower pAkt levels as of week 4. Two-way ANOVA followed by Holm-Sidak correction; n=7/group.

5.1.2 Hepatic triglyceride and glycogen content

High fat diet feeding leads to severe alterations of the liver phenotype (reviewed in [80] and [104]) with extensive changes of macromolecules and cellular processes [50, 192, 230].

Already at week 1, HFD-fed mice showed significantly increased triglyceride levels (Fig. 5.3 (a), $p_{week\ 1}$=0.0365). Between week 4 and week 5, the triglyceride content strongly increased and reached a plateau after five weeks of HFD feeding (Fig. 5.3 (a), $p_{week\ 4\text{-}12}$<0.0001). Thus, manifestation of insulin resistance was accompanied by development of a fatty liver.

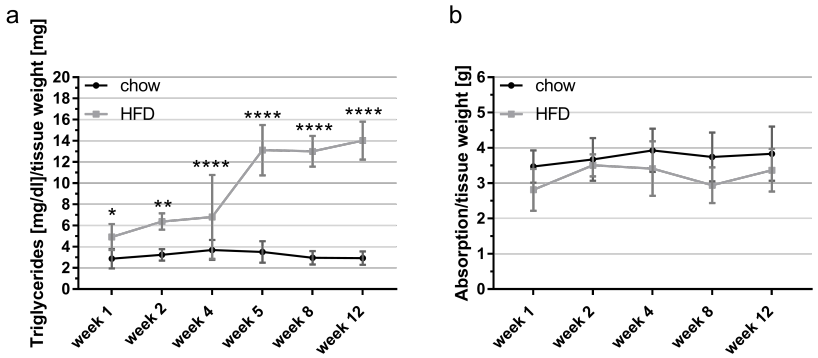

Figure 5.3: Hepatic triglycerides were elevated in diet-induced obese mice, whereas glycogen content was not altered. (a) Hepatic triglyceride levels are significantly increased in HFD mice at all time points. p_{week}<0.0001; p_{diet}<0.0001; $p_{interaction}$<0.0001; n=7-16/group. (b) Hepatic glycogen content showed no significant differences between the groups. p_{diet}=0.0003; n=8/group. Two-way ANOVA followed by Holm-Sidak correction.

The glycogen amount was not significantly altered in HFD-fed mice (Fig. 5.3 (b)), although glycogen levels appeared slightly lower in the HFD group. This indicates that glycogen metabolism

was not affected by impaired insulin signaling.

To evaluate the liver phenotype microscopically a hematoxylin eosin staining was performed (Fig. 5.4). There were no microscopical differences between the chow animals. In the HFD group, increasing fat accumulation with progressing development of obesity was observed (Fig. 5.4). At week 1, no differences between chow and HFD mice were visible. After eight weeks of feeding, HFD mice began to accumulate lipid droplets. The number of fat vacuoles were drastically increased in the HFD group at week 12. This fits with the results from the triglyceride assay which revealed a significant elevation of hepatic triglycerides at week 8 and 12 (Fig. 5.3). Taken together, mice fed a diet rich in fat for at least eight weeks developed a fatty liver.

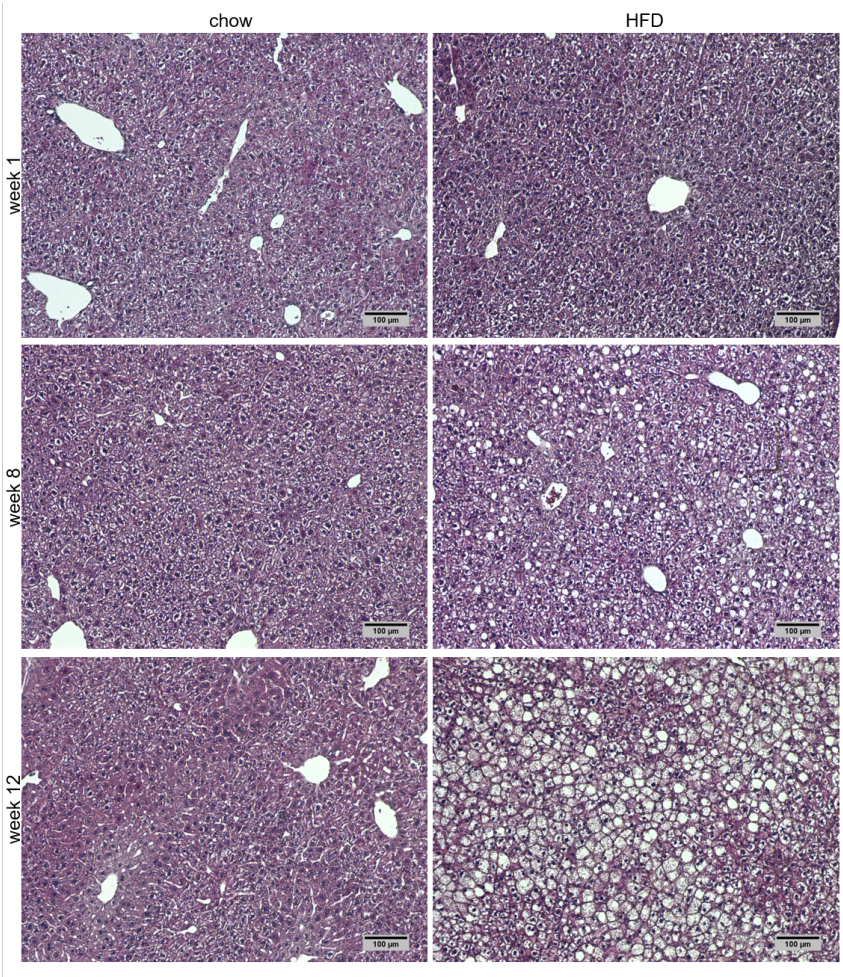

Figure 5.4: HFD-fed mice showed fat accumulation in hepatocytes. Evaluation of the liver morphology of chow and HFD mice by hematoxylin and eosin staining. After 12 weeks of feeding, the number and size of lipid droplets increased drastically in the HFD group. Representative pictures for week 1, 8, and 12 of four animals per group and time point in total. Pictures were taken with a 10x magnification, the scale bar represents 100 µm.

5.2 Gene expression microarrays

The underlying hypothesis of this thesis is that DNA methylation is involved in diabetes pathogenesis by altering hepatic gene expression. For mice no sensitive high-throughput techniques for identification of differentially methylated genes exist, therefore, gene expression microarrays were measured to identify differentially expressed genes at first. Subsequently, the transcriptome data set was used to search for genes which could be potentially regulated by DNA methylation. The transcriptome profiling was performed for mice fed for one and 12 weeks with either chow diet or HFD. When focusing at one time point, HFD mice were compared to chow mice of the same week. When comparing mice within one diet group, week 12 was compared to week 1.

5.2.1 Descriptive analysis of transcriptome data

Number of altered genes

The total number of differentially expressed genes is given in table 5.1. The comparison 'chow: week 12 vs. week 1' included genes affected by an age effect (Tab. 5.1, fig. 5.5). Ageing leads to epigenetic changes which can result in changes of gene expression [141]. Moreover, ageing is a risk factor for type 2 diabetes [154]. Therefore, the chow group served as a control for the confounding factor age.

When comparing HFD-fed mice of week 12 with HFD mice fed for one week, effects due to the different nutrient composition of the diets were excluded. In total, 1597 genes were altered (Tab. 5.1) of which 865 were unique for this comparison and 122 genes were affected by the different age of the animals (Fig. 5.5). 227 genes were already altered after one week of HFD feeding and were not affected by age (Fig. 5.5). 434 genes were also altered after 12 weeks of feeding and age-independent (Fig. 5.5).

Comparing the HFD group of one time point to the corresponding chow group eliminated the age effect. The comparison 'week 1: HFD vs. chow' included genes which were acutely altered by HFD feeding (Tab. 5.1). Of these 443 genes in total, 124 were unique for this comparison and 22 genes were also found in the comparison of both chow-groups (Fig. 5.5). 70 genes were also altered after 12 weeks of feeding but were not included in the comparison of both HFD groups. These genes changed after one week of HFD feeding and maintained their expression level for the whole period of the study. The 227 age-independent genes, which were also present in the 'HFD: week 12 vs. week 1' comparison, changed their gene expression due to the prolonged HFD feeding (Fig. 5.5).

At week 12, 793 genes were altered between HFD- and chow-fed mice (Tab. 5.1). Of these, 231 genes were unique for this comparison, 58 genes showed an age-effect, and 383 genes were also present in the comparison of both HFD groups (Fig. 5.5). HFD feeding led to extensive transcriptomic alterations which changed with continuing HFD feeding to adapt to the increased caloric intake.

Table 5.1: Total number of differentially expressed genes (DEGs). HFD mice at week 1 and week 12 were compared to chow mice at week 1 and week 12, respectively. Moreover, for each diet group week 12 was compared to week 1. Furthermore, the number of up- and downregulated genes is shown.

Comparison	Total DEGs	Upregulated	Downregulated
week 1: HFD vs. chow	443	114	329
week 12: HFD vs. chow	793	436	357
HFD: week 12 vs. week 1	1597	1082	515
chow: week 12 vs. week 1	263	180	83

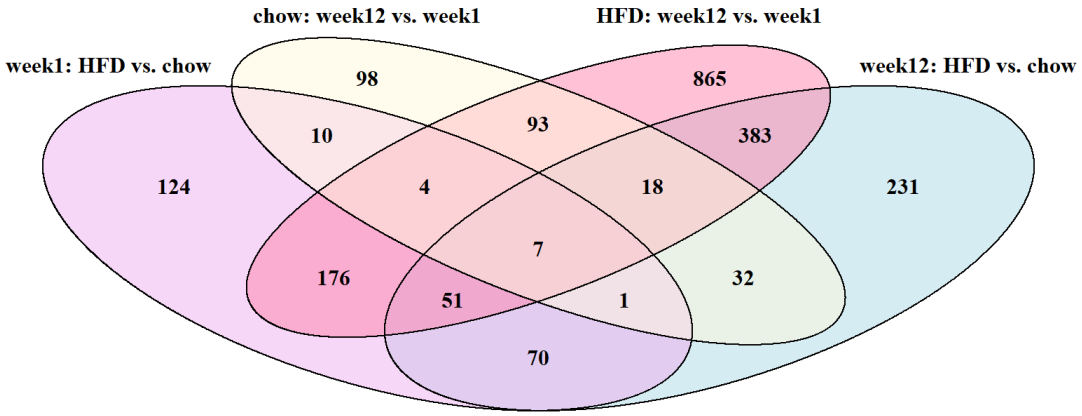

Figure 5.5: Venn diagram of differentially expressed genes. The total number of DEGs for each comparison ('week1: HFD vs. chow', 'week12: HFD vs. chow', 'chow: week12 vs. week1', 'HFD: week12 vs. week1') is shown in the colored bubbles. The overlap of the bubbles indicates genes which were differentially expressed in several comparisons. 'week 1: HFD vs. chow' and 'week12: HFD vs. chow' describes the comparison of the HFD group to the chow group at week 1 and week 12, respectively. 'chow: week12 vs. week1' and 'HFD: week12 vs. week1' depicts the comparison of mice fed for 12 weeks to mice fed for one week with the indicated diet.

Principal component analysis

Genome-wide approaches become more and more popular in research, because a large number of data can be acquired at once. To make the large amount of data graspable for humans statistical and visualization tools need to be applied. Usually, the first step of the analysis is performing a principal component analysis (PCA). This statistical technique is used to reduce the dimensions of complex data sets with simultaneously maintaining most of the variation and thereby facilitating further analysis [195, 196]. The principal components represent new variables which describe as much of the variance of the original data as possible [195]. The function yielded 29 principal components, because the variance of the thirtieth principal component was zero. To illustrate how much variance is explained by each principal component as well as the cumulative variance explained by combining several principal components a scree plot was created (Fig. 5.6). In a scree plot, the percentage of explained variance is plotted against the number of principal components. The scree plot visualized

that the first two principal components explain the greatest proportion of variance, about 26.00%. By adding the third principal component 32.78% can be explained.

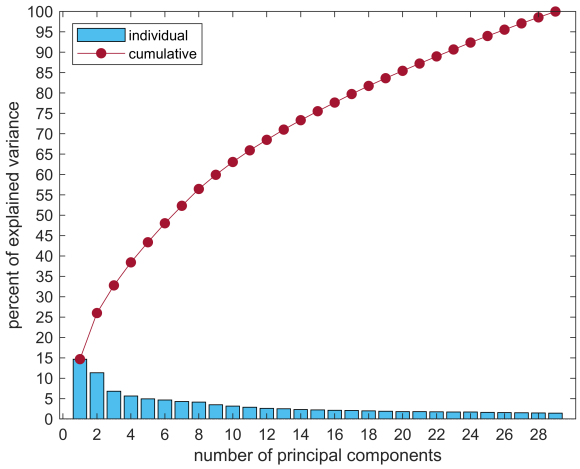

Figure 5.6: Scree plot of the principal components. The x-axis represents the individual principal components and the y-axis shows the percentage of explained variance. The variance explained by each individual principal component is shown as blue bars and the global variance, which is explained by combining the principal components, as red line.

For visualization, the first three principle components were plotted (Fig. 5.7). Principal component 1 explained 14.68% of the variance and therefore, indicates the direction in which the data showed the largest variation. Along this axis both HFD groups were distinguishable from each other (Fig. 5.7). Both chow groups were overlapping and could not be clearly discriminated (Fig. 5.7). The HFD week 12 group could also be differentiated from both chow groups indicating wide-ranging transcriptomic alterations (Fig. 5.7). Both chow groups and the HFD week 1 group were flanking each other with a minor overlap, suggesting that already one week of HFD feeding led to distinct changes of the transcriptome (Fig. 5.7).

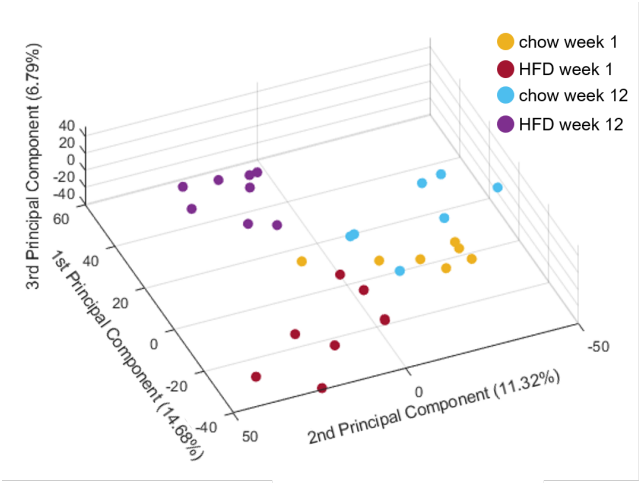

Figure 5.7: Principal component analysis of the transcriptome data. The first three principal components, which explained in total 32.78% of the variance, were plotted. The individual animals are shown as colored dots, the color states the group membership.

Cluster analysis

The aim of this thesis was to investigate if DNA methylation changes are causal or consecutive for the development of obesity and insulin resistance. Since DNA methylation changes lead to altered gene expression it was initially examined if the groups show transcriptomic differences. This would be the prerequisite for the search of differentially methylated genes. To analyze the transcriptomic differences between the groups cluster algorithms were applied. There are two main types of clustering algorithms, hierarchical and partitioning clustering, which have different advantages and disadvantages (see section 4.6.3) [211, 247]. To achieve reliable results hierarchical clustering as well as the partitioning cluster algorithm 'kmeans' was performed.

The clustering was performed on the first 15 principal components which explained in total 75% of the variance (Fig. 5.6, suppl. data in section 7 C).

The hierarchical clustering revealed that HFD week 12 was clearly distinguishable from the other groups, because it separated directly after the root of the clustering tree (Fig. 5.8 (a)). The other groups, HFD week 1 and both chow groups, could not be discriminated from each other as clearly (Fig. 5.8 (a)). The mice of the HFD week 1 group showed similar gene expression, because they were in the same region of the dendrogram (Fig. 5.8 (a)). The chow groups could not be distinguished from each other, they were mixed up in the dendrogram (Fig. 5.8 (a)). One chow week 1 mouse even clustered with the HFD week 1 group, other chow mice formed their own small cluster on the right side of the dendrogram, and the remaining mice formed a mixed chow week 1 and chow week 12 cluster (Fig. 5.8 (a)). The hierarchical clustering could not reliable determine the total number of clusters. Since all animals of the HFD week 1 group seemed to cluster together, but the chow groups were mixed up three clusters could be hidden in the data.

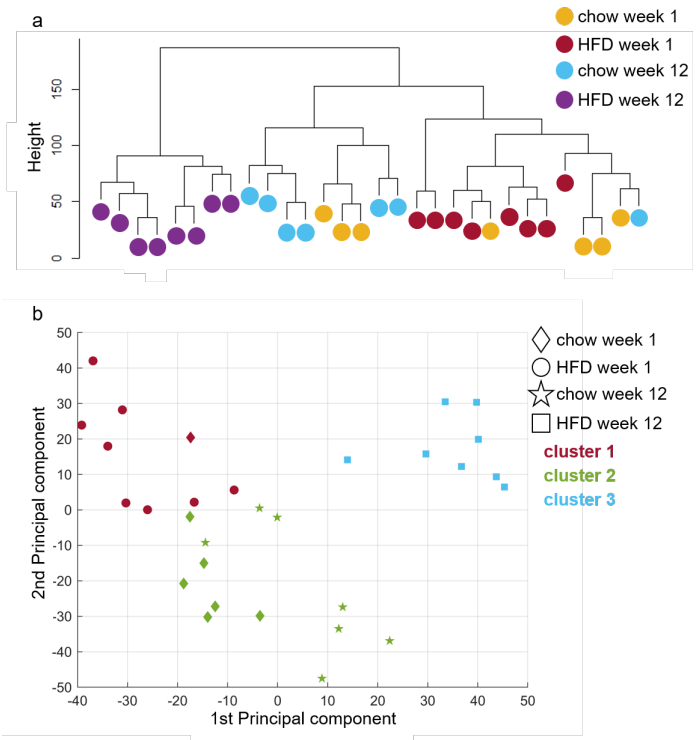

Figure 5.8: Hierarchical clustering and 'kmeans' clustering of the first 15 principal components of the transcriptome data. (a) Hierarchical clustering. Individual animals are indicated as dots, group membership is indicated by color. The height indicates the distance between individual animals. (b) The results of the clustering analysis by 'kmeans' are shown by plotting the first and second principal component. Cluster are indicated with different colors and group membership of the animals is represented by different symbols.

To confirm this clustering also the partitioning cluster algorithm 'kmeans' was applied. For 'kmeans', the cluster number needs to be specified beforehand. Therefore, the optimal cluster number was determined by computing the silhouette width, the gap statistic, and the within-sum-of-squares. However, these methods are approximative approaches. The silhouette width shows the quality of clustering for different cluster numbers, the higher the silhouette width, the better the cluster discrimination [23]. The silhouette plot indicated three cluster as the best cluster number (Suppl. fig. 7.2).

The gap statistic compares the total intra-cluster variation for different cluster numbers to a reference distribution [229]. The optimal number of clusters will maximize the gap statistic and this was true for three cluster (Suppl. fig. 7.3) [229].

The within-sum-of-squares method determines the compactness of cluster. When the total within sum of squares was plotted against the number of clusters, the optimal cluster number could not be clearly determined, however, the slope seems to flatten at five clusters (Suppl. fig. 7.4).

'Kmeans' was performed with three clusters and revealed that the HFD group at week 12 formed its own cluster (Fig. 5.8 (b) cluster 3), as already shown by the hierarchical clustering (Fig. 5.8 (a)). HFD mice fed for one week formed another individual cluster, but also one chow mouse fed

for one week was grouped into this cluster (Fig. 5.8 (b) cluster 1) which was also predicted by the hierarchical clustering (Fig. 5.8 (a)). The remaining chow week 1 mice clustered together with chow mice fed for 12 weeks (Fig. 5.8 (b) cluster 2). Diet-induced obese and insulin resistant mice showed distinct transcriptomic alterations discriminating them from mice fed high fat diet for only a short period and mice fed a standard diet. But also short-term HFD feeding led to gene expression changes which distinguished these mice from control animals.

Identification of altered pathways

After descriptive analysis of differentially expressed genes the pathways, in which these genes are involved, were examined. After one week of feeding, 'Metabolic pathways' and 'Fatty acid metabolism' pathways were already altered in HFD mice (Fig. 5.9 (a)). After 12 weeks of feeding, 'Metabolic pathways' attained higher relevance, pathways of the 'Fatty acid metabolism' (for instance 'Fatty acid degradation') were still significantly enriched, and the 'Peroxisome proliferator-activated receptor (PPAR) signaling pathway' was altered (Fig. 5.9 (b)). After one week of feeding the top 10 significantly enriched pathways were all in all downregulated, whereas after 12 weeks of feeding some pathways, such as 'Fatty acid degradation' or 'Peroxisomes', were upregulated. When focusing only on HFD mice fed for 12 weeks compared to HFD mice fed for one week, it emerged that genes of the 'Metabolic pathways', pathways of the fatty acid metabolism, and the 'PPAR signaling' got upregulated due to the prolonged HFD feeding (Fig. 5.9 (c)). Peroxisome proliferator-activated receptors are transcription factors regulating the fatty acid metabolism. This suggests a deregulation of the hepatic fatty acid metabolism.

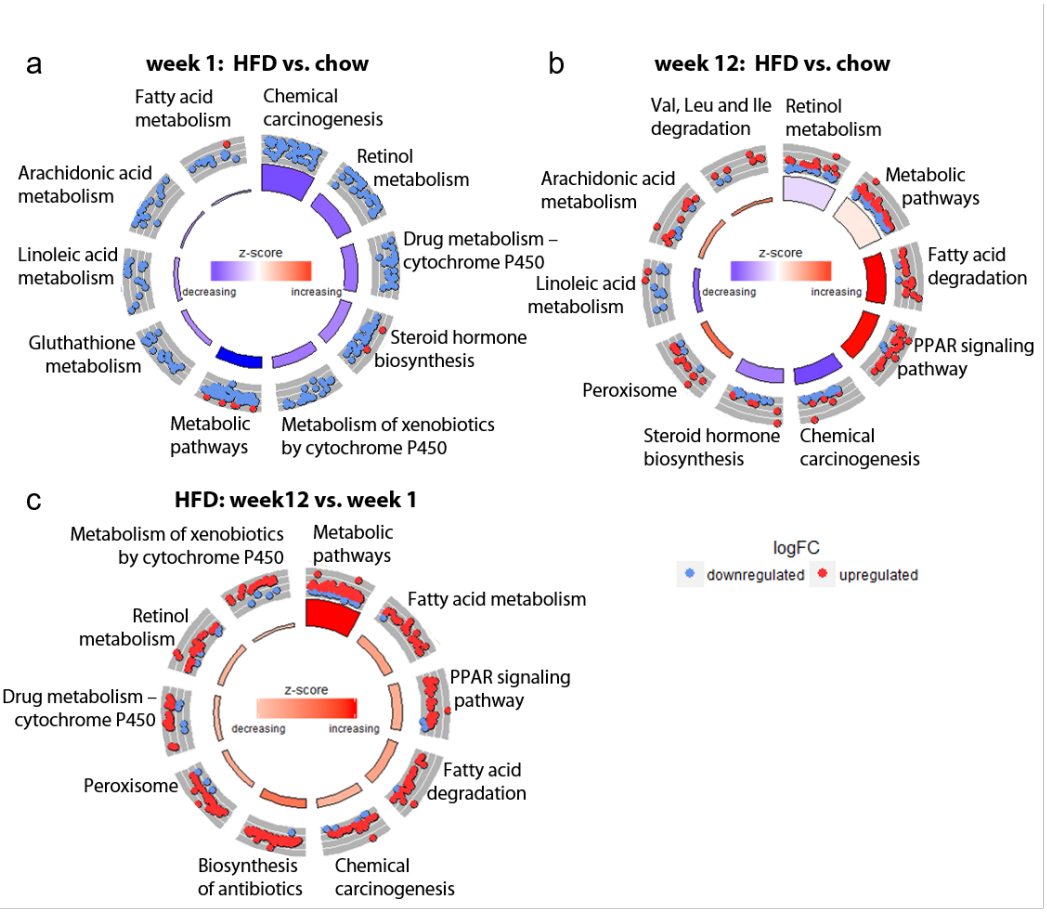

Figure 5.9: 'PPAR signaling' and pathways of the fatty acid metabolism were enriched after 12 weeks of HFD feeding. The top 10 significantly enriched pathways are shown. The dots represent the number of differentially expressed genes belonging to the pathway. Blue dots indicate downregulated genes in the HFD group and the HFD week 12 group, respectively. Red dots indicate upregulated genes in the HFD group and HFD week 12 group, respectively. The size of the rectangles under the dots visualizes the number of genes in one pathway, the color estimates if the whole pathway is more upregulated (red) or downregulated (blue). (a) Pathway analysis for differentially expressed genes in HFD animals compared to chow-fed controls after one week. (b) Pathway analysis for differentially expressed genes in HFD animals compared to chow-fed controls after 12 weeks. (c) Pathway analysis for differentially expressed genes in HFD animals fed for 12 weeks compared to HFD mice fed for one week. Bonferroni-corrected p values are shown in section 7 E. z-score: Number of upregulated genes minus number of downregulated genes divided by the square root of the count.

5.2.2 Validation of differentially expressed genes

The pathway analysis revealed a deregulation of the peroxisome proliferator-activated receptor (PPAR) signaling pathway after 12 weeks of feeding. Because PPARs regulate the fatty acid metabolism, the validation of gene expression data was focused on PPARs and some of their target genes. There are three isoforms of the PPARs: PPARα, PPARβ/δ, and PPARγ with specific, but also overlapping functions [18]. The gene expression microarrays revealed that after 12 weeks of HFD feeding *Ppara* and *Pparg* were significantly differentially expressed (Fig. 5.10), but not PPARβ/δ (data for

PPARβ/δ not shown), thus, the focus was on PPARα and PPARγ. The linear fold change measured by gene expression microarrays of *Ppara* and *Pparg* and their target genes are shown in figure 5.10. *Ppara* gene expression was slightly increased at week 1 in HFD mice and the mRNA level further increased with prolonged HFD feeding until week 12. At week 12, HFD mice had significantly elevated *Ppara* mRNA level (Fig. 5.10, FDR $p_{week\ 12}$=0.0063). *Pparg* was initially significantly decreased in the HFD group, but after 12 weeks of feeding HFD mice showed a significant increase of *Pparg* mRNA levels (Fig. 5.10, FDR $p_{week\ 1}$=0.0272, FDR $p_{week\ 12}$=0.0004). Both *Ppar* isoforms were deregulated on the gene expression microarray, indicating that also their target genes could be altered.

The fatty acid translocase *Cd36* is a transmembrane protein transporting fatty acids into the cell [8]. Its gene expression was not altered after one week of feeding but increased vastly after 12 weeks of HFD (Fig. 5.10, FDR $p_{week\ 12}$=1.10E-14). Stearoyl-CoA desaturase (SCD1) inserts the first cis-double bond in saturated fatty acids resulting in mono-unsaturated fatty acids [151, 203]. At the beginning of the study *Scd1* was significantly downregulated in HFD mice, but mRNA level increased with further HFD feeding to approximately chow levels (Fig. 5.10, FDR $p_{week\ 1}$=2.08E-06). The fatty acid synthase (FAS, *Fasn*) is the rate-limiting enzyme of *de novo* lipogenesis synthesizing mainly palmitate from malonyl-CoA [8, 9]. The gene expression of *Fasn* was similar to *Scd1*, at the beginning mRNA level were significantly downregulated in HFD mice, but with further feeding gene expression increased (Fig. 5.10, FDR $p_{week\ 1}$=0.0012). *Acacb* encodes the acetyl-CoA carboxylase 2 (ACC2) which catalyzes the conversion of acetyl-CoA to malonyl-CoA [206]. Malonyl-CoA synthesized by ACC2 negatively regulates fatty acid β-oxidation [8]. *Acacb* was significantly downregulated for the whole period of feeding (Fig. 5.10, FDR $p_{week\ 1}$=0.0004, FDR $p_{week\ 12}$=0.0165). FGF21 is a prominent PPARα target gene and functions as metabolic regulator [65]. *Fgf21* was not altered after one week of HFD feeding, but gene expression increased with further feeding and reached significance after 12 weeks (Fig. 5.10, FDR $p_{week\ 12}$=1.60E-06).

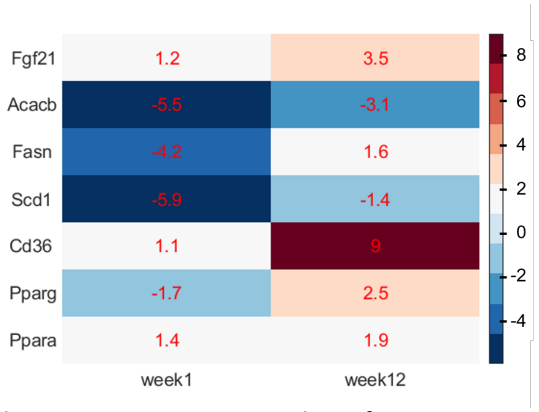

Gene	p value Week 1	Week 12
Fgf21	0.827	1.60E-06
Acacb	0.0004	0.0165
Fasn	0.0012	0.4982
Scd1	2.08E-06	0.1465
Cd36	0.7735	1.10E-14
Pparg	0.0272	0.0004
Ppara	0.1808	0.0063

Figure 5.10: Gene expression of PPARα target genes was altered. The linear fold change at week 1 and week 12 of PPARα, PPARγ, and selected target genes is shown as heatmap. A positive fold change is indicated by a red color and corresponds to higher gene expression in HFD mice compared to chow mice. The FDR p values are shown in the table on the right side.

As already indicated by the pathway analysis, PPARs and genes of the fatty acid metabolism were deregulated after 12 weeks of HFD feeding. However, gene expression microarrays need to be validated, because the quality of the data depends strongly on the platform and procedure [158]. For the mere validation only mice of week 1, 2, 4, 8, and 12 were used. To get a better time resolution of alterations of selective targets also week 5, 6, and 7 was added. *Ppara* was significantly higher expressed in HFD mice after one week of feeding (Fig. 5.11 (a), $p_{week\ 1}$=0.0224). At week 2, gene expression of both groups did not differ, but after week 2 mRNA level were significantly increased again in HFD-fed mice and remained elevated for the whole feeding period (Fig. 5.11 (a), $p_{week\ 4}$=0.0003, $p_{week\ 5\text{-}12}$<0.0001). *Pparg* gene expression was significantly decreased in HFD mice at week 2 and 4 (Fig. 5.11 (b), $p_{week\ 2}$=0.0129, $p_{week\ 4}$=0.0015). Afterwards, gene expression rose above chow levels and reached significance at week 12 (Fig. 5.11 (b), $p_{week\ 12}$=0.0004). The gene expression microarray data for *Ppara* and *Pparg* were confirmed by qRT-PCR indicating the induction of the PPAR signaling due to HFD feeding.

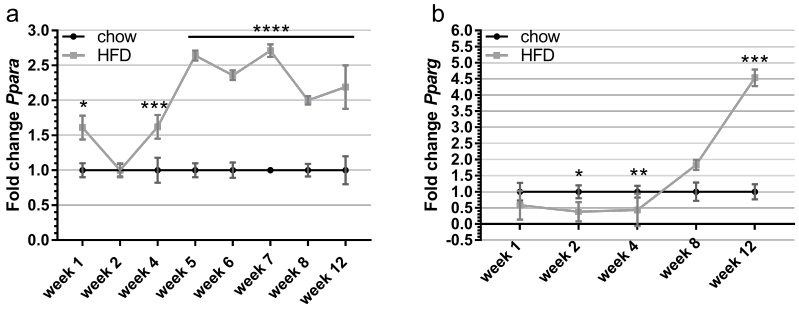

Figure 5.11: *Ppara* and *Pparg* were upregulated in hepatic insulin resistance. (a) Gene expression of *Ppara*. n=7-16/group; p_{week}<0.0001; p_{diet}<0.0001; $p_{interaction}$=0.0004. (b) Gene expression of *Pparg*. n=7-8/group; p_{week}<0.0001; $p_{interaction}$<0.0001. Two-way ANOVA followed by Holm-Sidak correction.

Cd36 gene expression was significantly upregulated as from week 8 (Fig. 5.12 (a), $p_{week\ 8\text{-}12}$<0.0001). *Fasn* was significantly downregulated at week 1 and week 2 ($p_{week\ 1}$<0.0001, $p_{week\ 2}$=0.0282), but afterwards, gene expression increased and at week 8 and 12 mRNA level were comparable to the chow group (Fig. 5.12 (b)). *Scd1* was significantly downregulated for the whole feeding period, although mRNA level increased slightly between week 4 and 8 (Fig. 5.12 (c), $p_{week\ 1\text{-}4}$<0.0001, $p_{week\ 8}$=0.0002, $p_{week\ 12}$=0.0006). Also *Acacb* was significantly downregulated for the whole study period (Fig. 5.12 (d), $p_{week\ 1\text{-}12}$<0.0001).

Fgf21 was significantly upregulated in HFD mice after one week of feeding, but mRNA level decreased to chow levels at week 2 (Fig. 5.12 (e), $p_{week\ 1}$=0.0131). After week 2, gene expression of *Fgf21* was elevating constantly until week 7. At week 8, mRNA level were decreased slightly, but between week 8 and 12 gene expression increased vastly (Fig. 5.12 (e), $p_{week\ 4\text{-}12}$<0.0001).

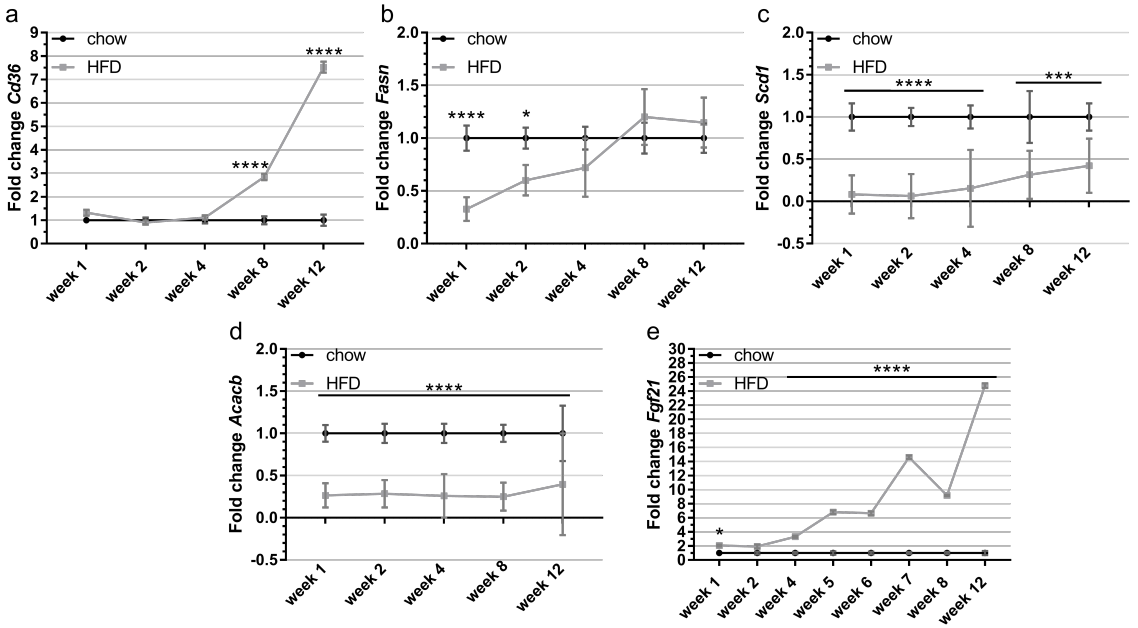

Figure 5.12: Validation of gene expression microarray results. (a) Gene expression of *Cd36* (p_{week}<0.0001; p_{diet}<0.0001; $p_{interaction}$<0.0001). (b) Gene expression of *Fasn* (p_{week}<0.0001; p_{diet}<0.0001; $p_{interaction}$=0.0002). (c) Gene expression of *Scd1* (p_{week}<0.0001; p_{diet}<0.0001; $p_{interaction}$<0.0001). (d) Gene expression of *Acacb* (p_{diet}<0.0001). (e) Gene expression of *Fgf21* (p_{week}<0.0001; p_{diet}<0.0001; $p_{interaction}$<0.0001). Two-way ANOVA followed by Holm-Sidak correction (a)-(d) n=7-8/group; (e) n=7-16/group.

5.3 DNA methylation of validated, differentially expressed genes

After identification of differentially expressed genes, *Cd36*, *Scd1*, and *Fgf21* were selected for measuring DNA methylation. *Cd36* showed a vast increase in mRNA levels between week 4 and week 12 (Fig. 5.12 (a)), leading to the hypothesis that this increase was due to changes of DNA methylation. Since *Cd36* can be expressed from three different promoters several protein coding transcripts exist (see ensembl entry for ENSMUSG00000002944 ([254]), [210]) and the SYBR green primer set measured all of them. The most upstream and the most downstream promoter can be activated by PPARs [210]. The most upstream promoter is also the one predominantly used in liver [210]. Therefore, the measured CpG sites were located within the most upstream first exon, but no differences between chow and HFD mice at any time point were identified (Fig. 5.13).

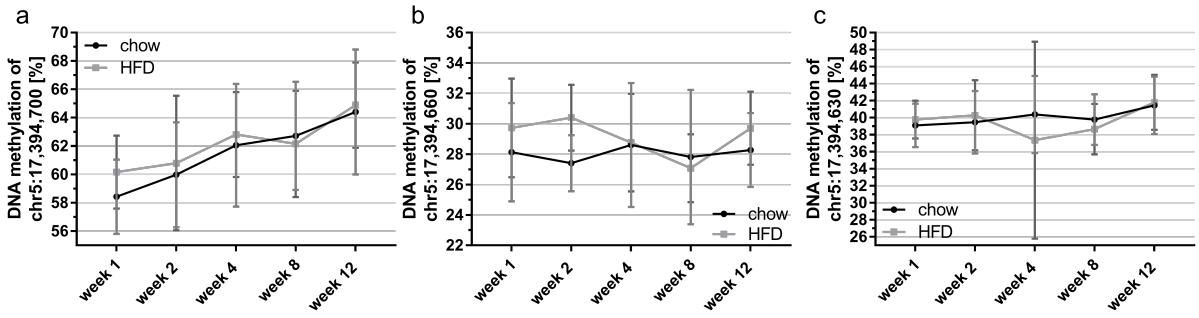

Figure 5.13: DNA methylation of *Cd36* at three CpG sites within exon 1 was not altered. DNA methylation in liver of mice of the longitudinal methylation study at (a) chr5:17,394,700 (p_{week}=0.0012); (b) chr5:17,394,660; and (c) chr5:17,394,630 (*Cd36* transcript: 203). Two-way ANOVA followed by Holm-Sidak correction; n=7-8/group; assembly: mm9.

DNA methylation of *Scd1* was measured at four CpG sites within intron 3. Gene expression of *Scd1* was already altered after one week of HFD feeding and between week 4 and week 8 mRNA levels were slightly increased (Fig. 5.12 (c)). Therefore, changes of DNA methylation were expected at week 1 or between week 4 and 8. At CpG 1 (Fig. 5.14 (a), $p_{week\ 2}$=0.0241), CpG 2 (Fig. 5.14 (b), $p_{week\ 4}$=0.0079, $p_{week\ 8}$=0.0003), and CpG 4 (Fig. 5.14 (c), $p_{week\ 4}$=0.0024, $p_{week\ 8}$=0.0284) small differences in DNA methylation were identified at some time points, but these marginal differences had most likely no physiological relevance. The pyrosequencer has an inaccuracy of 1%, leaving less than 1% difference, and after establishment the alterations did not persist with further feeding. At CpG 3, DNA methylation between HFD and chow mice significantly differed by 4% at week 4 and 5% at week 12. (Fig. 5.14 (c), $p_{week\ 4}$=0.0008, $p_{week\ 12}$<0.0001). Since the difference in DNA methylation was abolished at week 8 the regulatory function is unclear.

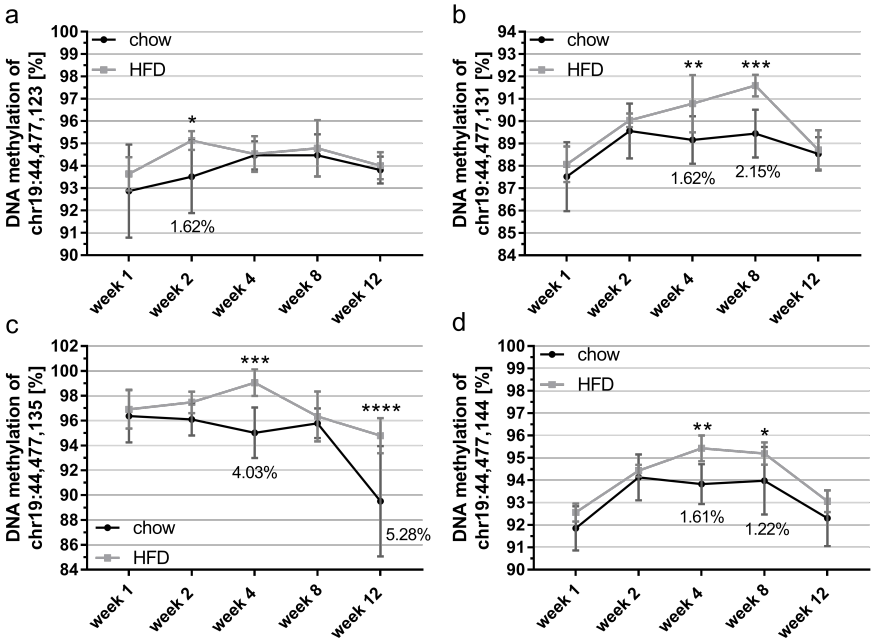

Figure 5.14: DNA methylation of *Scd1* at four CpG sites within intron 3 showed no physiological relevant alterations. Hepatic DNA methylation of mice of the longitudinal methylation study at (a) chr19:44,477,123 (p_{week}=0.0061; p_{diet}=0.0231); (b) chr19:44,477,131 (p_{week}<0.0001; p_{diet}<0.0001; $p_{interaction}$=0.0328); (c) chr19:44,477,135 (p_{week}<0.0001; p_{diet}<0.0001; $p_{interaction}$0=0.0030), and (d) chr19:44,477,144 (p_{week}<0.0001; p_{diet}<0.0001). Two-way ANOVA followed by Holm-Sidak correction; n=6-8/group; assembly: mm9.

For *Fgf21*, two CpG sites within exon 1 were measured (Fig. 5.15 (c)). DNA methylation at CpG 1 was significantly reduced as from week 5 with a difference of about 10% between HFD and chow mice (Fig. 5.15 (a), $p_{week\ 5}$=0.0019, $p_{week\ 6}$=0.0019, $p_{week\ 7}$=0.0038, $p_{week\ 8}$<0.0001, $p_{week\ 12}$=0.0014). At CpG 2, DNA methylation between HFD-fed mice and chow-fed mice was significantly reduced at week 8 (Fig. 5.15 (b), $p_{week\ 8}$=0.0004), but as from week 4, HFD mice showed decreased DNA methylation of at least 5% (Fig. 5.15 (b)). DNA methylation at each CpG site correlated with *Fgf21* gene expression (Suppl. fig. 7.5 (a) CpG site 1: r=0.5457, p<0.0001, suppl. fig. 7.5 (b) CpG site 2: r=0.4231, p<0.0001). Therefore, *Fgf21* is likely regulated by DNA methylation.

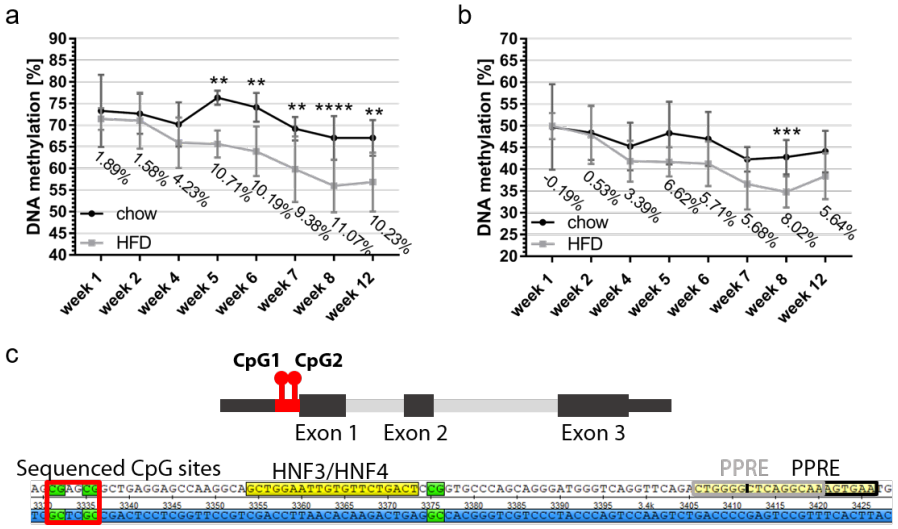

Figure 5.15: DNA methylation of *Fgf21* at two CpG sites within exon 1 shows significant alterations. Hepatic DNA methylation of mice of the longitudinal methylation study at (a) chr7:52,870,685 (p_{week}<0.0001; p_{diet}<0.0001; $p_{interaction}$=0.01) and (b) chr7:52,870,690 (p_{week}<0.0001; p_{diet}<0.0001). (a) The CpG sites were located in exon 1, in close proximity to predicted HNF3/HNF4 binding motifs as well as two PPAR responsive elements. Two-way ANOVA followed by Holm-Sidak correction; n=6-8/group; assembly: mm9.

5.4 Whole-genome bisulfite sequencing

Of the three measured genes, *Fgf21* was the only one which was likely regulated by DNA methylation at the here investigated loci (Fig. 5.15). The gene expression microarrays allowed the identification of differentially expressed genes, but the search for differentially methylated CpG sites or regions was nonetheless challenging. Measuring every single CpG site in a gene by bisulfite pyrosequencing is not possible, because depending on the sequence context assay design can be difficult and it is too cost and time intensive. Consequently, whole-genome bisulfite sequencing (WGBS) was performed for easier identification of differentially methylated genes. This method is based on next-generation sequencing and can measure in principle every single CpG site within the genome [166]. Initially, a pilot study with two HFD and two chow mice fed for 12 weeks was performed. The two HFD mice with the most extreme phenotype and two chow mice with a metabolic normal phenotype were chosen for whole-genome bisulfite sequencing.

5.4.1 Descriptive analysis of the whole-genome bisulfite sequencing data

As a first step the data were analyzed regarding differentially methylated regions (DMRs). These regions contain several CpG sites which are differentially methylated between the groups in the same direction [194]. Differentially methylated regions were defined as a region with maximal 2000 bp containing at least 10 CpG sites with a mean difference in DNA methylation between the groups of

10%. In total, 6016 DMRs were identified of which 1778 (29.6%) were hypomethylated and 4238 (70.4%) were hypermethylated in HFD mice (Fig. 5.16, Tab. 5.2). Thus, HFD feeding led mainly to an increase of DNA methylation.

Annotation of differentially methylated regions

The identified DMRs were annotated with genomic features such as exons or introns, because the effect of altered DNA methylation depends on the genomic position [21, 101]. With only few exceptions the proportion of hyper- and hypomethylated differentially methylated regions in individual annotations mirrored the distribution of total DMRs, with 70% to 75% hypermethylated DMRs and 25% to 30% hypomethylated DMRs (Tab. 5.2). The majority of DMRs was located in introns, followed by intergenic regions, exons, and exon-intron/intron-exon boundaries (Fig. 5.16, tab. 5.2). This could indicate that most of the exonic DMRs were located around these boundaries (Fig. 5.16, tab. 5.2). Only a small number of DMRs was found in promoter regions. However, this was not astonishing, because a fine regulation of gene expression by DNA methylation was expected and not an on or off switching. The smallest number of DMRs was found in 5'- and 3'-untranslated regions (5'-/3'-UTR) (Fig. 5.16, tab. 5.2). In UTRs, slightly more DMRs were hypomethylated compared to the overall distribution of hyper- and hypomethylated DMRs (Tab. 5.2). When focusing on CpG islands, only few DMRs were located directly within an island, most of the hypermethylated DMRs were located in shores (Fig. 5.16, tab. 5.2). This was expected, because CpG islands are in general not methylated [142]. In enhancer regions about half of the DMRs were hyper- and hypomethylated, unlike the DMRs in other genomic regions (Fig. 5.16, tab. 5.2). This could suggest a functional importance of DNA methylation in enhancers.

Table 5.2: Annotation and numbers of differentially methylated regions. Annotations with total number of differentially methylated regions (DMRs) as well as the number and percentage of DMRs which are hyper- and hypomethylated in HFD mice.

Annotation	Number	Hypermethylated DMRs	Hypomethylated DMRs
Total DMRs	**6016**	**4238 (70.4%)**	**1778 (29.6%)**
Introns	3047	2158 (70.8%)	889 (29.2%)
Intergenic	1948	1346 (69.1%)	602 (30.9%)
Exons	1250	889 (71.1%)	361 (28.9%)
Coding sequences (cds)	976	709 (72.6%)	267 (27.4%)
Exon-intron boundaries	922	670 (72.7%)	252 (27.3%)
Intron-exon boundaries	903	645 (71.4%)	258 (28.6%)
CpG shores	589	451 (76.6%)	138 (23.4%)
1 to 5 kb	549	420 (76.5%)	129 (23.5%)
Enhancers	422	247 (58.5%)	175 (41.5%)
First exons	348	247 (71.0%)	101 (29.0%)
CpG shelves	331	239 (72.2%)	92 (27.8%)
Promoters	317	230 (72.6%)	87 (27.4%)
CpG islands	297	216 (72.7%)	81(27.3%)
5'-UTR	214	146 (68.2%)	68 (31.8%)
3'-UTR	207	138 (66.7%)	69 (33.3%)

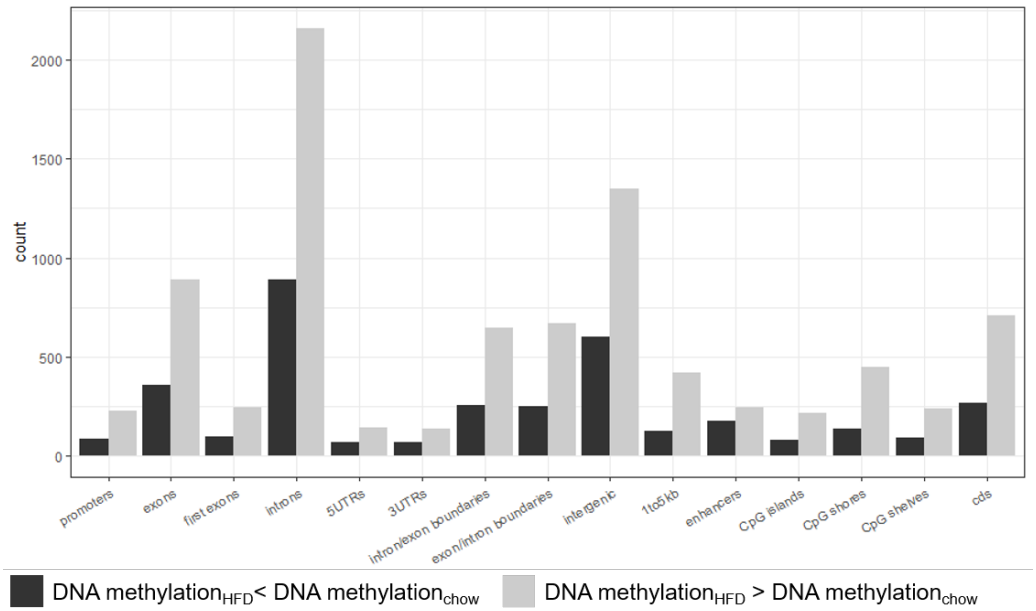

Figure 5.16: Annotation of the differentially methylated regions. If multiple annotations were assigned to one DMR, the DMR counts for all these annotations in the graph. The y-axis depicts the number of DMRs for the different annotation, the x-axis represents the annotation name. Black bars show DMRs which are hypomethylated in HFD, gray bars show hypermethylated DMRs.

Pathway analysis of genes with differentially methylated regions

To get an overview of the functions of genes possessing at least one differentially methylated region, a pathway analysis was performed yielding 111 enriched KEGG pathways of which 13 were significant (Fig. 5.17, Bonferroni-corrected p value <0.05). Interestingly, 'Insulin resistance' and 'Metabolic pathways' were among these pathways, but also pathways without any relevance for the liver were significantly enriched, such as 'Insulin secretion' and 'Axon guidance' (Fig. 5.17).

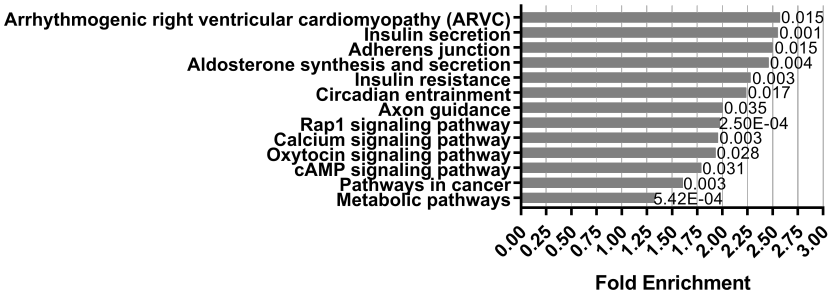

Figure 5.17: Pathway analysis of genes with at least one differentially methylated region. Only significantly enriched pathways are shown (Bonferroni-corrected p value < 0.05). Interestingly, genes of 'Metabolic pathways' and 'Insulin resistance' contain differentially methylated regions. The x-axis shows the fold enrichment, the y-axis depicts the significantly enriched KEGG pathway.

However, only changes of DNA methylation which have an impact on gene expression are of interest, because only these alterations will possibly lead to changes of the phenotype. To refine the pathway analysis only genes which were differentially expressed at week 12 on the gene expression microarrays and which show at least one differentially methylated region were analyzed. The join between both data sets yielded 159 genes and the pathway analysis revealed 18 enriched KEGG pathways of which only 'Metabolic pathways' were significant (Fig. 5.17, Bonferroni-corrected p value = 0.00028). Similar to the pathway analysis of the gene expression microarrays, also the 'PPAR signaling pathway' as well as pathways of the fatty acid metabolism ('Fatty acid degradation', 'Fatty acid metabolism') were enriched (Fig. 5.17). This demonstrates that HFD feeding not only led to alterations of PPARs and fatty acid metabolism on transcriptome level, but also on DNA methylation level.

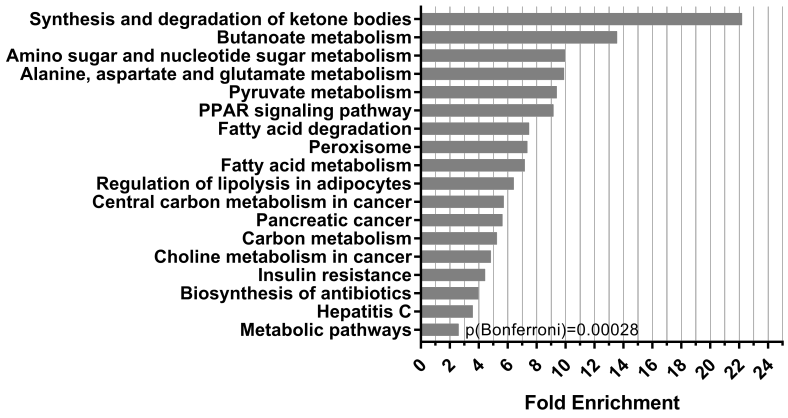

Figure 5.18: Pathway analysis of differentially expressed genes with at least one differentially methylated region. Pathway analysis was performed for genes which were differentially expressed at week 12 on the gene expression microarrays and possessed at least one differentially methylated region. Shown are all hits of the pathway analysis, only 'Metabolic pathways' were significantly enriched (Bonferroni-corrected p value=0.00028). As already shown for the gene expression microarrays, the 'PPAR signaling pathways' as well as the 'Fatty acid metabolism' was altered. The x-axis shows the fold enrichment, the y-axis depicts the significantly enriched KEGG pathway.

5.4.2 Analysis of differentially methylated regions in the entire cohort

With the WGBS data, differentially methylated regions and CpG sites can be identified easily. However, DNA methylation should always be analyzed in connection with gene expression data. Therefore, DMRs of genes, whose gene expression was already measured, were examined in more detail (Fig. 5.25, 5.29 (b), 5.11, 5.12). *Acacb*, *G6pc*, *Ppara*, *Pklr*, and *Scd1* possessed at least one differentially methylated region (Tab. 5.3) with a difference in DNA methylation between HFD and chow mice ranging from 10.00% to 21.40%.

Table 5.3: Differentially methylated regions of differentially expressed genes. The differentially methylated regions of *Acacb*, *G6pc*, *Galnt2*, *Ppara*, *Pklr*, *Scd1*, and *Sik3* are listed in the table. Next to genomic position, mean DNA methylation for each group as well as the difference and p value is shown. Assembly: mm9; Diff. - difference between HFD and chow.

Gene	Chr	Start	End	Mean chow	Mean HFD	Diff.	p value
Acacb	5	114,649,174	114,649,948	65.57%	53.81%	11.76%	0.0097
Acacb	5	114,629,255	114,629,625	17.33%	38.73%	-21.40%	0.00021
G6pc	11	101,233,598	101,234,042	78.54%	68.45%	10.09%	0.025
G6pc	11	101,231,528	101,232,409	26.89%	37.54%	-10.65%	0.034
Galnt2	8	126,838,337	126,838,796	34.73%	53.31%	-18.58%	0.0029
Galnt2	8	126,788,563	126,788,896	38.89%	51.87%	-12.98%	0.015
Ppara	15	85,573,813	85,574,068	60.66%	46.75%	13.91%	0.033
Ppara	15	85,599,196	85,599,653	26.28%	36.35%	-10.06%	0.03
Ppara	15	85,572,582	85,573,103	20.12%	31.93%	-11.81%	0.00014
Ppara	15	85,601,768	85,602,233	20.31%	39.18%	-18.87%	0.000013
Pklr	3	88,946,204	88,946,921	83.14%	73.14%	10.00%	0.015
Scd1	19	44,480,231	44,481,433	32.48%	46.96%	-14.48%	0.0078
Scd1	19	44,472,946	44,473,854	60.45%	79.89%	-19.44%	0.003
Sik3	9	46,022,187	46,023,229	21.13%	35.78%	-14.64%	0.0012
Sik3	9	45,992,386	45,993,199	81.08%	66.17%	14.91%	0.00028
Sik3	9	46,007,435	46,008,046	17.59%	31.13%	-13.55%	0.0011

Especially interesting was the discovery of differentially methylated regions in *Ppara* (Tab. 5.3, fig. 5.19). PPARα is strongly regulated by posttranslational modifications and cofactors [20] and a regulation by DNA methylation was unexpected. For this reason, the DMRs of *Ppara* were analyzed in more detail. *Ppara* had four DMRs located within intron 2 of which three were higher methylated in HFD mice and one was lower methylated in HFD mice (Fig. 5.19). DMR 2 seemed particularly interesting, because it behaved differently from the other three DMRs (Fig. 5.19 (b)). This could indicate that the DMRs were located in different regulatory regions.

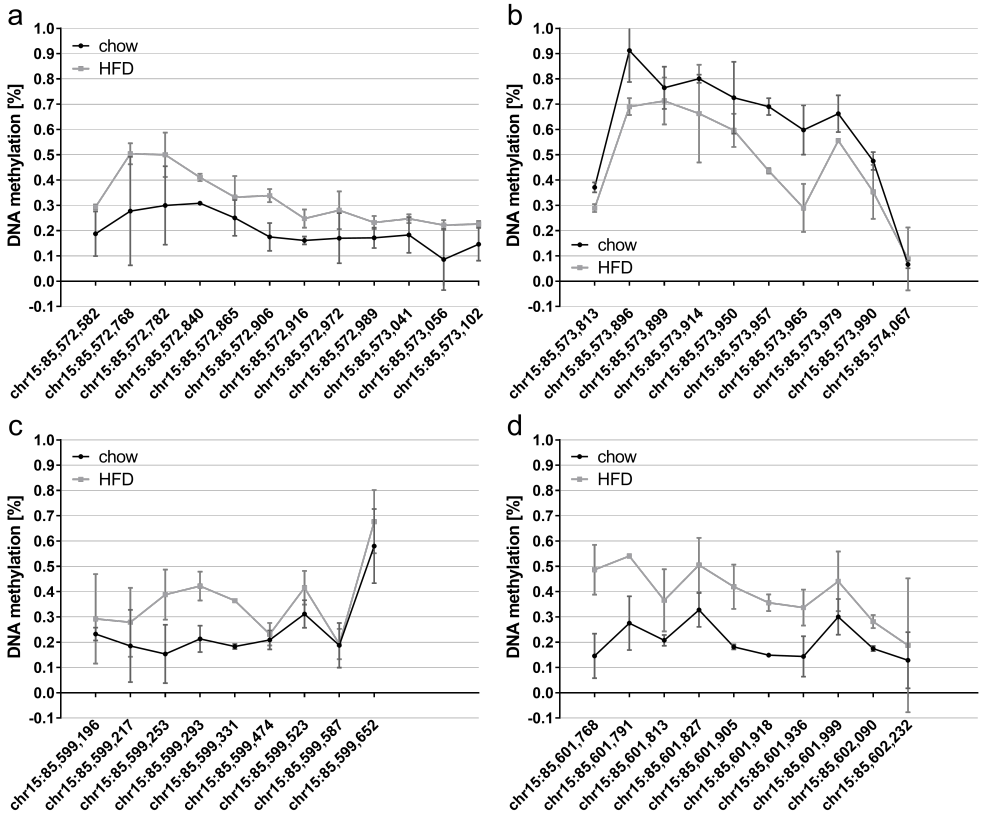

Figure 5.19: *Ppara* possessed four differentially methylated regions. The whole-genome bisulfite sequencing identified four differentially methylated regions within intron 2 of *Ppara ((a)-(d))*. No statistical test was performed, because only two animals per group were measured. Assembly: mm9.

The whole-genome bisulfite sequencing was performed for only two HFD and two chow mice of week 12. To test if the difference in DNA methylation was statistically significant this region was measured in the entire week 12 group by bisulfite pyrosequencing. The bisulfite pyrosequencing showed only a significant difference in DNA methylation for one CpG site (Fig. 5.20, $p_{chr15:85,573,914}$=0.0109). In contrast to the results of the WGBS, the bisulfite pyrosequencing revealed slightly lower DNA methylation for HFD-fed mice compared to chow mice. When looking at individual DNA methylation percentage values of the four animals subjected to WGBS, five of the eight data points could be reproduced well in the HFD group (Tab. 5.4). At position chr15:85,573,957; chr15:85,573,965; and chr15:85,573,990 DNA methylation measured by bisulfite pyrosequencing was higher than the values determined by WGBS (Tab. 5.4). In the chow group, only two data points matched the WGBS data (Tab. 5.4), the others showed lower DNA methylation compared to WGBS (Tab. 5.4). Consequently, DMR 2 in *Ppara* was not confirmed by bisulfite pyrosequencing in the entire week 12 group. Even the direct comparison of the individual values of mice measured by WGBS and bisulfite pyrosequencing showed considerable differences, especially in the chow group.

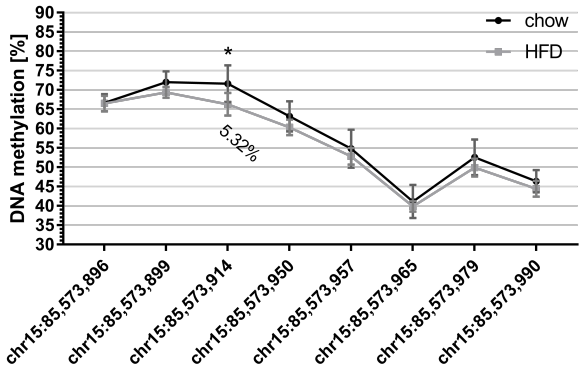

Figure 5.20: The second differentially methylated region of *Ppara* could not be confirmed by bisulfite pyrosequencing. DNA methylation at the second DMR of *Ppara* in the entire week 12 group. The x-axis depicts the genomic location of the CpG sites, the y-axis shows DNA methylation in percentage. Multiple t-tests assuming consistent standard deviation followed by Holm-Sidak correction; $p_{chr15:85,573,914}$=0.0109 n=7-8/group; assembly: mm9.

Table 5.4: Comparison of DNA methylation measured by bisulfite pyrosequencing and whole-genome bisulfite sequencing at individual CpG sites of DMR 2 of *Ppara*. Genomic position and DNA methylation percentage of each individual CpG site. Mean±SD, n=2/group.

	chow		HFD	
CpG site	WGBS	Pyrosequencing	WGBS	Pyrosequencing
chr15:85,573,896	91.20%±12.44%	67.15%±2.50%	69.05%±3.32%	64.84%±1.86%
chr15:85,573,899	76.50%±8.34%	73.04%±1.50%	71.25%±9.26%	70.57%±0.86%
chr15:85,573,914	80.05%±1.63%	69.30%±4.38%	66.30%±19.37%	67.71%±0.83%
chr15:85,573,950	72.55%±14.21%	64.18%±1.25%	59.65%±6.58%	59.83%±0.81%
chr15:85,573,957	69.05%±3.32%	57.27%±1.37%	43.65%±1.06%	52.86%±1.22%
chr15:85,573,965	59.80%±9.76%	42.11%±3.85%	28.95%±9.55%	40.52%±0.07%
chr15:85,573,979	66.25%±7.28%	54.89%±3.92%	55.60%±0.85%	50.02%±3.75%
chr15:85,573,990	47.50%±3.54%	47.69%±0.87%	35.35%±10.68%	44.49%±1.32%

In contrast to *Ppara*, *Fgf21* showed a significant difference in DNA methylation at two CpG sites already before performing WGBS (Fig. 5.15). These two CpG sites of *Fgf21* were surrounded by other CpG sites which could not be measured with the bisulfite pyrosequencing assay (Fig. 5.21, previously sequenced CpG sites are labeled with *). Thus, DNA methylation of *Fgf21* measured by WGBS was analyzed (Fig. 5.21). For *Fgf21*, no differentially methylated region was found, therefore, all CpG sites within *Fgf21* were examined.

In total, 15 CpG sites within the gene body and 1000 bp upstream of the transcriptional start site could be analyzed by WGBS after quality control. *Fgf21* contains about 35 CpG sites, thus, about one half was measurable in all four animals. The WGBS revealed that DNA methylation in *Fgf21* was decreased in HFD mice in the gene body, whereas CpG sites 1000 bp upstream of the transcriptional start site were hypermethylated in HFD-fed mice. The two CpG sites previously measured could not

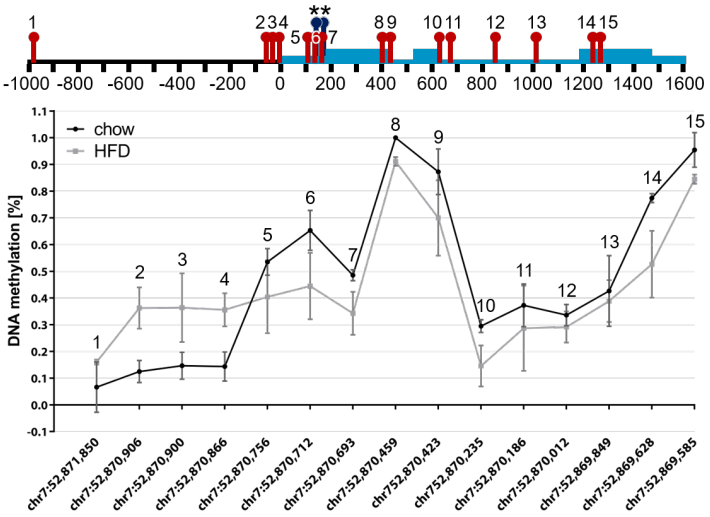

Figure 5.21: The whole-genome bisulfite sequencing identified 15 CpG sites within *Fgf21*. The CpG sites were located within the gene body and 1000 bp upstream of the transcriptional start site. The schematic illustration of the genomic region shows CpG sites in red with numbers corresponding to the graph below which also depicts the genomic location. The blue region represents the *Fgf21* gene with introns as blue lines, exons as blue rectangle, and untranslated regions as thick blue lines. Previously measured CpG sites are shown in the schematic illustration in blue and labelled with an asterisk (*). No statistical test was performed, because only two animals per group were measured. Assembly: mm9.

be analyzed by WGBS, because they were filtered due to the stringent quality control. However, the adjacent CpG sites 5, 6, and 7 showed similar differences in DNA methylation between HFD and chow mice and also absolute DNA methylation percentages were similar (Fig. 5.15 and 5.21).

The WGBS data indicated that DNA methylation in the promoter region was increased in HFD mice (Fig. 5.21). DNA hypermethylation in promoter regions is in general associated with repression of gene expression [101], but HFD-fed mice showed a large upregulation of *Fgf21* mRNA level at week 12. Therefore, the CpG sites 2, 3, and 4 were measured by bisulfite pyrosequencing for validation. Furthermore, whole-genome bisulfite sequencing was performed for only two HFD and two chow mice of week 12. To investigate the longitudinal development of DNA methylation differences also the animals of week 4, 5, 6, 7, 8, and 12 were measured. Week 1 and 2 was omitted, because the significant difference in DNA methylation at previously measured CpG sites developed between week 4 and 5. Besides the CpG sites measured by WGBS, four additional CpG sites located in proximity were sequenced. But for none of these CpG sites DNA methylation determined by WGBS could be reproduced by bisulfite pyrosequencing (Fig. 5.22).

The direct comparison of DNA methylation percentages of the mice measured by both methods revealed that DNA methylation of chow mice was approximately twice as high when measured by bisulfite pyrosequencing compared to WGBS (Tab. 5.5). The two HFD mice showed a 5% to 10% lower DNA methylation when measured by bisulfite pyrosequencing (Tab. 5.5). Thus, also for *Fgf21* the WGBS data could not be confirmed by bisulfite pyrosequencing.

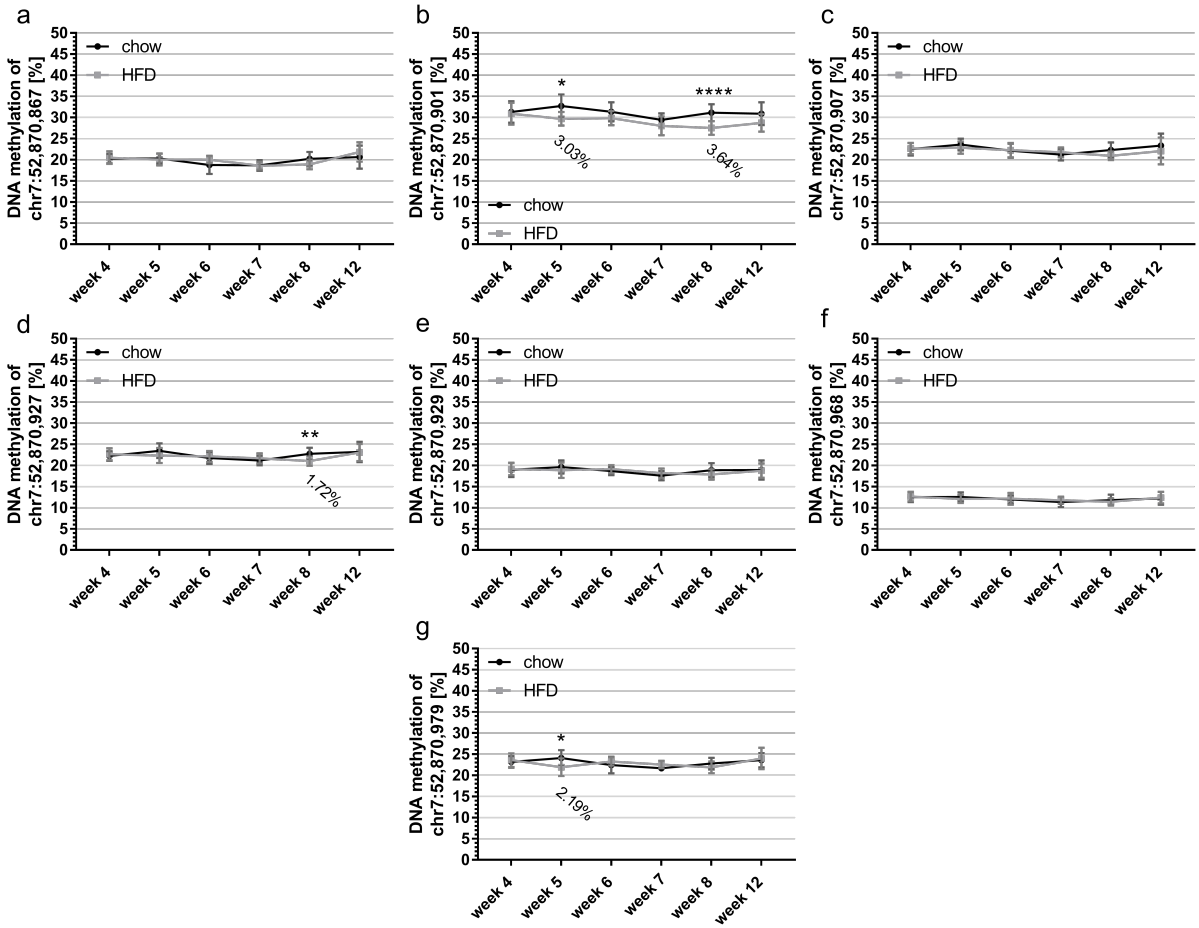

Figure 5.22: Hepatic DNA methylation of *Fgf21* at seven CpG sites in the promoter region was not altered. Hepatic DNA methylation of mice of the longitudinal methylation study. (a) chr7:52,870,867 (p_{week}<0.0001), (b) chr7:52,870,901 (p_{week}=0.0013; p_{diet}<0.0001), (c) chr7:52,870,907 (p_{week}=0.0149), (d) chr7:52,870,927 (p_{week}=0.0073; $p_{interaction}$=0.0389), (e) chr7:52,870,929, (f) chr7:52,870,968 (p_{week}=0.0111), (g) chr7:52,870,979 (p_{week}=0.0122; $p_{interaction}$=0.0345). Two-way ANOVA followed by Holm-Sidak correction; n=7-16/group; assembly: mm9.

Table 5.5: Comparison of the DNA methylation measured by bisulfite pyrosequencing and whole-genome bisulfite sequencing. Genomic position and DNA methylation percentage of the CpG sites sequenced by both methods. Mean±SD; n=2/group.

	chow		HFD	
CpG site	WGBS	Pyrosequencing	WGBS	Pyrosequencing
chr7:52,870,867	14.35%±5.44%	21.65%±5.12%	35.60 %±6.22%	24.79%±1.67%
chr7:52,870,901	14.65%±5.02%	31.61%±3.95%	36.40%±12.87%	31.60%±0.99%
chr7:52,870,907	12.46%±4.16%	23.85%±4.59%	36.25%±7.71%	25.54%±0.06%

5.5 Identification of potential candidate genes

5.5.1 Pilot experiments in mice fed with high fat-high sucrose diet

Additionally to the fishing approach for identification of potential candidate genes, also a targeted approach using previously published data and databases were used as described in section 4.6.1. At the beginning, DNA methylation of potential candidate genes was measured in mice fed high fat-high sucrose (HFHS) diet or chow diet for 20 weeks. Though, no RNA was available from these animals.

Acacb was studied due to differences of DNA methylation between low fat diet-fed and high fat diet-fed mice identified by CHARM microarrays in Multhaup et al. [163]. Furthermore, the 'Attie Lab Diabetes Database' showed gene expression differences between lean and ob/ob mice [105]. DNA methylation of *Acacb* was determined in two different regions in HFHS-fed and chow-fed mice. Within intron 5, two CpG sites with a significant difference between HFHS and chow mice were found (Fig. 5.23 (a), $p_{chr5:114,640,673}$=0.03, $p_{chr5:114,640,688}$=0.037). However, the measured difference in DNA methylation did not exceed the limits of measurement accuracy of the *PyroMark Q48 Autoprep* and therefore, was possibly not physiologically relevant. Within the exon 5-intron 5 boundary one CpG site was significantly altered in HFD mice, but also here the difference of DNA methylation was small (Fig. 5.23 (b), $p_{chr5:114,640,404}$=0.006).

Also *Sgms2*, *Galnt2*, and *Sik3* were identified as potential candidate genes due to differences in DNA methylation measured by CHARM microarrays [163]. Moreover, all three genes are associated with either diabetes, obesity and fatty acid/lipid metabolism, or glucose homeostasis as indicated by DisGeNET database [15]. For *Sgms2*, the enzyme catalyzing the last step of sphingomyelin synthesis [155], three of the five CpG sites showed a significant but small difference in DNA methylation of 2.7% (Fig. 5.23 (c), $p_{chr3:131,037,738}$=0.022, $p_{chr3:131,037,715}$=0.022, $p_{chr3:131,037,756}$=0.022). Considering the inaccuracy of the *PyroMark Q48 Autoprep* the measured difference was most probably due to biological variance. Polypeptide N-acetylgalactosaminyltransferase 2 (*Galnt2*) belongs to a large family of glycosyltransferases transferring N-acetylgalactosamine to serine or threonine residues [227]. Three CpG sites were measured within intron 7, but no differences between the groups were detected (Fig. 5.23 (d)). Also for *Sik3*, a member of the AMPK-related kinase family [94], no differences between the groups at three CpG sites within intron 1 were identified (Fig. 5.23 (e)).

The approach to identify potential candidate genes by *in silico* research yielded only small differences in DNA methylation. Thus, the strategy to identify candidate genes was changed by focusing on targets which are suggested to be altered in type 2 diabetes: Phosphoenolpyruvate carboxykinase (*Pepck*/*Pck1*) and glucose-6-phosphatase (*G6pc*). Both enzymes are key enzymes of gluconeogenesis and an increase in hepatic gluconeogenesis is reported for type 2 diabetes due to insulin resistance, contributing to hyperglycemia [14, 143, 201]. Therefore, it was assumed that both enzymes are

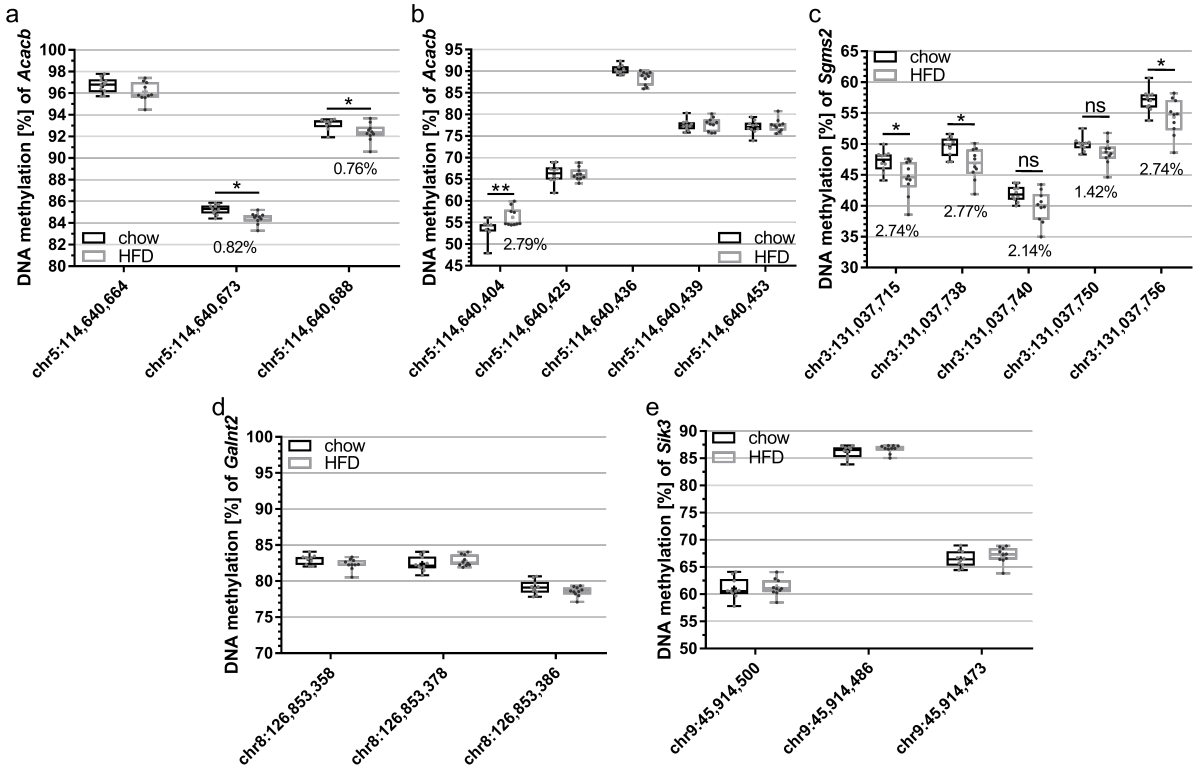

Figure 5.23: DNA methylation of potential candidate genes identified by a targeted approach. (a) DNA methylation at two CpG sites within intron 5 of *Acacb* showed only minor differences between the groups ($p_{chr5:114,640,673;\ chr5:114,640,688}<0.05$). (b) DNA methylation at one CpG sites within the exon 5-intron 5-boundary of *Acacb* was significantly altered ($p_{chr5:114,640,404}=0.006$). (c) DNA methylation of three CpG sites within intron 3 of *Sgms2* was altered ($p_{chr3:131,037,715\ -\ 131,037,756}<0.05$). (d) No alterations of DNA methylation at three CpG sites within intron 7 of *Galnt2* were detected. (e) DNA methylation at three CpG sites within intron 1 of *Sik3* showed no differences. The CpG site are considered independent of each other. Multiple t-tests assuming consistent variance followed by Holm-Sidak correction were performed for each data set.

altered in type 2 diabetes. For *G6pc* three CpG sites within the exon 1-intron 1 boundary were measured and a significant hypermethylation in the HFHS group was found for all CpG sites (Fig. 5.24 (a), $p_{chr11:101,229,311}=0.000255$, $p_{chr11:101,229,329}=0.000687$, $p_{chr11:101,229,354}=0.000687$). For *Pck1*, DNA methylation at four CpG sites within exon 2 was analyzed (Fig. 5.24 (b), $p_{chr2:172,979,008}=0.002$, $p_{chr2:172,979,027}=0.003$, $p_{chr2:172,979,036}=0.000723$, $p_{chr2:172,979,048}=0.008$). At all CpG sites, HFHS mice showed a higher DNA methylation compared to chow mice. For both genes a similar DNA methylation difference was measured for all investigated CpG sites, indicating a differentially methylated region.

5.5.2 Longitudinal investigation of *Pck1* and *G6pc*

Both *Pck1* and *G6pc* seemed to possess a small differentially methylated region which made them promising candidate genes. Therefore, the results were replicated in the longitudinal methylation

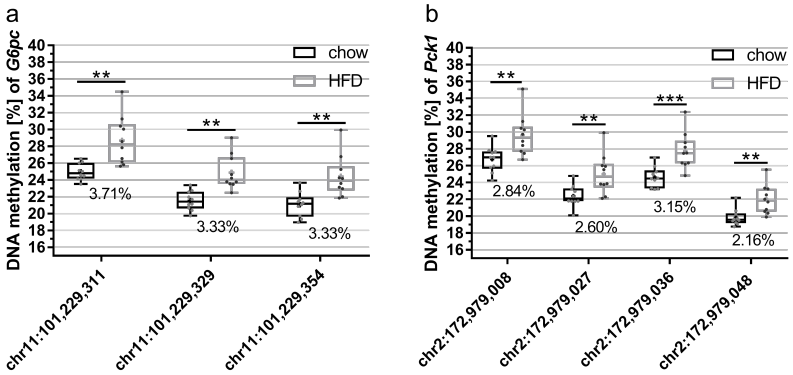

Figure 5.24: DNA methylation of *Pck1* and *G6pc* indicated a differentially methylated region. (a) DNA methylation of *G6pc* was measured at three CpG sites at the exon 1-intron 1-boundary. All CpG sites showed a significant higher DNA methylation in HFHS-fed mice ($p_{chr11:101,229,311 - 101,229,354}<0.001$). (b) DNA methylation at four CpG sites within exon 2 of *Pck1* was measured. At all CpG sites HFHS mice showed a significant hypermethylation ($p_{chr2:172,979,008;\ chr2:172,979,027;\ 172,979,048}<0.01$; $p_{chr2:172,979,036}<0.001$). Multiple t-tests assuming consistent variance followed by Holm-Sidak correction were performed for each data set.

study. It was shown that feeding a lard-based HFD induces robustly insulin resistance but feeding a high fat-high sucrose diet leads to a more moderate phenotype [177]. The hypothesis was that a more pronounced insulin resistance could lead to larger differences of DNA methylation. Furthermore, the longitudinal study allowed to investigate if differences in DNA methylation were causal or consecutive for insulin resistance.

Since no RNA was available for the HFHS study, gene expression of *Pck1* and *G6pc* was measured in mice of the longitudinal methylation study. *Pck1* showed no significant alterations in mRNA level at any time point between chow and HFD mice (Fig. 5.25 (a)). *G6pc* was significantly downregulated after one week of HFD feeding, but with further feeding mRNA level were comparable to chow mice (Fig. 5.25 (b), $p_{week\ 1}=0.0005$). These data suggest that *Pck1* expression was not altered at all in the diet-induced obese mouse model, whereas *G6pc* was only altered as acute response to HFD feeding.

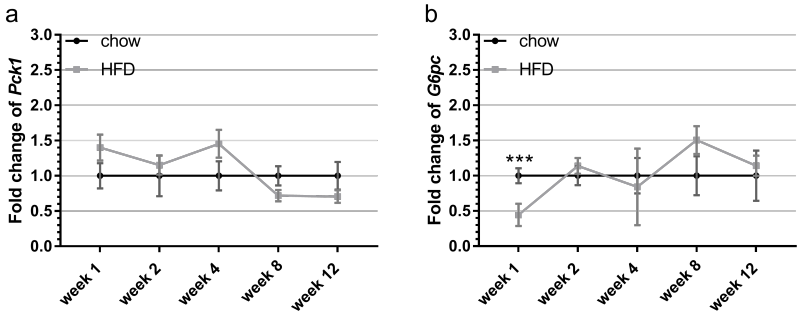

Figure 5.25: Gene expression of *Pck1* and *G6pc* was not altered in diet-induced obese mice. Hepatic gene expression of (a) *Pck1* (p_{week}=0.0079; $p_{interaction}$=0.0254) and (b) *G6pc* (p_{week}=0.0021; $p_{interaction}$=0.0003). *Pck1* showed no differences in mRNA level between the groups at any time point. *G6pc* mRNA level were decreased at week 1 in HFD mice, but afterwards gene expression fluctuated around chow levels. Two-way ANOVA of the ΔCt values followed by Holm-Sidak correction; n=8/group.

The increase in *Pck1* and *G6pc* gene expression described in the literature was not observed here and also the differences in DNA methylation measured for HFHS-fed mice was not reproducible (Fig. 5.26 and 5.27). The three measured CpG sites in *G6pc* were not differentially methylated between the groups at any time point (Fig. 5.26).

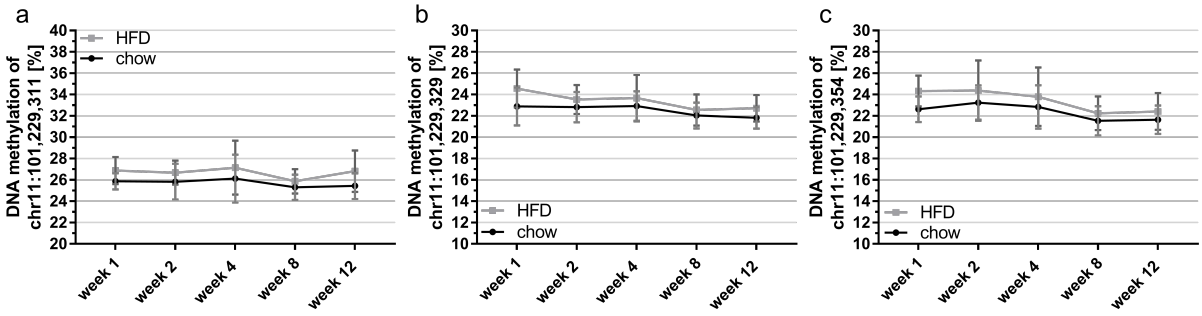

Figure 5.26: DNA methylation of *G6pc* at three CpG sites at the exon 1-intron 1-boundary showed no alterations. Hepatic DNA methylation of mice of the longitudinal methylation study at (a) chr11:101,229,311 (p_{diet}=0.0094), (b) chr11:101,229,329 (p_{week}=0.0285; p_{diet}=0.0094), and (c) chr11:101,229,354 (p_{week}=0.0102; p_{diet}=0.0136). *G6pc* showed no differences in DNA methylation at any CpG site. Two-way ANOVA followed by Holm-Sidak correction; n=7-8/group; assembly: mm9.

In *Pck1*, three CpG sites showed significantly but only slightly increased DNA methylation in HFD mice at week 1 (Fig. 5.27, $p_{chr2:172,979,027}$=0.0492, $p_{chr2:172,979,036}$=0.0099, $p_{chr2:172,979,048}$=0.0151), but the changes did not persist throughout the whole feeding period. Only CpG 4 showed a marginal difference in DNA methylation at week 12 (Fig. 5.27, $p_{chr2:172,979,048}$=0.0204). At least the direction of DNA methylation matched the previous results. However, *Pck1* seemed not to be epigenetically regulated.

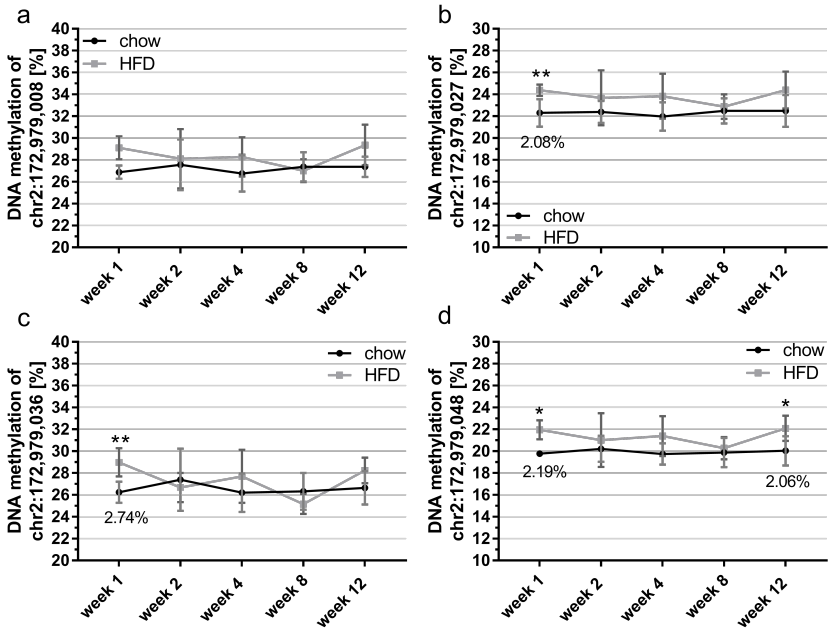

Figure 5.27: DNA methylation of *Pck1* at four CpG sites within exon 2 showed no alterations. DNA methylation was measured in liver of mice of the longitudinal methylation study at (a) chr2:172,979,008 (p_{diet}=0.0023), (b) chr2:172,979,027 (p_{diet}<0.0001), (c) chr2:172,979,036 (p_{week}=0.0257; p_{diet}=0.0432; $p_{interaction}$=0.0082), and (d) chr2:172,979,048 (p_{diet}<0.0001). Only marginal differences between the groups were identified. Two-way ANOVA followed by Holm-Sidak correction for each CpG site; n=7-8/group; assembly: mm9.

5.5.3 Phosphoenolpyruvate carboxykinase and pyruvate kinase activity in diet-induced obese mice

Often quantification of mRNA is an unsuitable measure for enzyme activity due to posttranslational modifications of proteins. Therefore, an activity assay for PEPCK was performed. PEPCK showed no significant differences at any time point between the groups, although it seemed slightly lower active in HFD mice (Fig. 5.28). In contrary to the previous assumption [76, 164, 213], PEPCK was not hyperactive in insulin resistant mice indicating that gluconeogenesis was not altered.

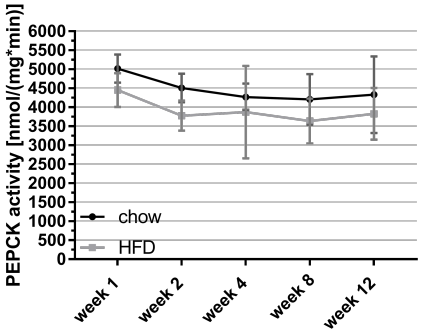

Figure 5.28: Enzyme activity of PEPCK was unaltered. Enzyme activity of PEPCK was slightly, but not significantly decreased in HFD mice. Two-way ANOVA followed by Holm-Sidak correction; p_{week}=0.0110; p_{diet}=0.0005; n=8/group.

Since glucose anabolism seemed not be altered, glucose catabolism by glycolysis was studied. Firstly, activity of pyruvate kinase (PK), the enzyme catalyzing the rate-limiting step in glycolysis [73], was measured.

PK activity was significantly decreased after two and four weeks of HFD feeding (Fig. 5.29 (a), $p_{week\ 2}$=0.0086, $p_{week\ 4}$=0.0315). After week 4, the activity increased and was slightly higher in HFD mice at week 12 (Fig. 5.29 (a)). To check if this was due to altered gene expression, mRNA level were measured (Fig. 5.29 (b)). *Pklr* gene expression increased between week 4 and week 8 and reached significance at week 12 (Fig. 5.29 (b), $p_{week\ 12}$=0.0008). To investigate if the increase was caused by altered DNA methylation, three CpG sites within intron 1 were measured in mice fed HFD or chow diet for 12 weeks, but no differences were detected (Fig. 5.29 (c)). However, by WGBS a differentially methylated region spanning exon 6, intron 6, exon 7, and intron 7 was identified (Tab. 5.3). The data suggested a lower glycolysis rate until four weeks of HFD feeding. With manifestation of whole-body glucose intolerance glycolysis rate increased.

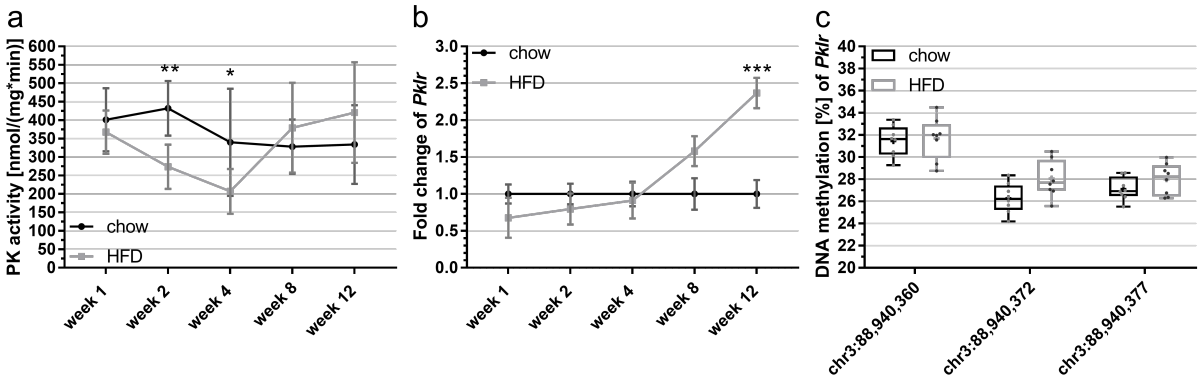

Figure 5.29: Enzyme activity of pyruvate kinase was significantly decreased after two and four weeks of HFD feeding, with developing glucose intolerance mRNA level and enzyme activity were increased. (a) Activity of PK. Two-way ANOVA followed by Holm-Sidak correction; p_{week}=0.0159; $p_{interaction}$=0.0014. (b) mRNA level of *Pklr* were significantly elevated at week 12 in the HFD group. Two-way ANOVA of the ΔCt values followed by Holm-Sidak correction; p_{week}=0.0009; $p_{interaction}$=0.0001. (c) Hepatic DNA methylation of *Pklr* was measured at three CpG sites within intron 1. No differences between the groups at any CpG site were detected. Multiple t-tests assuming consistent variance followed by Holm-Sidak correction were applied. All experiments performed with n=8/group.

6

Discussion

6.1 Longitudinal analysis of the development of insulin resistance

In the scope of this thesis a longitudinal study in mice was performed to investigate if changes of DNA methylation are causal or consecutive for the development of insulin resistance. The mice were fed a high fat diet (HFD) with 60 kcal% fat from lard and 6.7 kcal% from sucrose (HFD D12492) or chow diet for up to 12 weeks (Suppl. tab. 7 A). The longitudinal study allows a time-resolved tracking of changes of hepatic gene expression and DNA methylation as well as the development of insulin resistance.

6.1.1 Week 1: Adaptational mechanisms

First alterations of the phenotype were already evident after one week of HFD feeding. The rapid impairment of glucose tolerance was also reported by others, even after three days [230, 242]. It was suggested that this could be partly due to HFD overconsumption [137]. HFD is very palatable for mice and it was observed that they tend to overeat HFD when it is available *ad libitum*, probably due to hedonic hunger [137].

Although the whole-body glucose tolerance was significantly impaired after one week of HFD feeding, the hepatic insulin signaling, measured by insulin-stimulated Akt phosphorylation, seemed to be preserved. This was also reported by others which observed insulin resistance without changes of the insulin-stimulated Akt phosphorylation [58, 83, 230].

At week 1, plasma insulin levels in both groups showed a high variation which may be due to different reasons. For example the mice were not fasted at the time of sacrifice. The last meal of mice sacrificed early in the morning was not as long ago as for mice sacrificed four hours later. Furthermore, at the first day of sacrifice the handling and time management was not as experienced as for later time points.

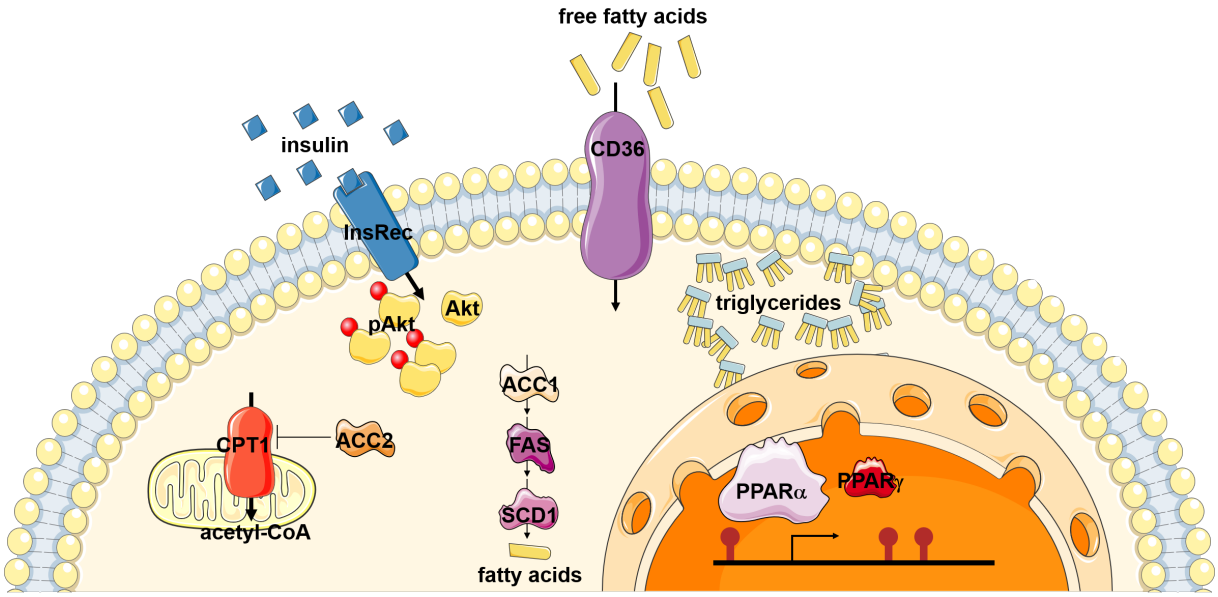

Figure 6.1: Acute high fat diet feeding induces adaptational mechanisms in the liver. Mice fed high fat diet for one week show impaired whole-body glucose tolerance despite slightly increased hepatic Akt phosphorylation. The metabolic alterations are accompanied by transcriptional changes. The downregulation of genes of *de novo* lipogenesis suggests a decreased *de novo* lipogenesis rate. Nevertheless, HFD-fed mice show increased hepatic triglyceride content. *Ppara* gene expression is upregulated after one week of HFD feeding, whereas *Pparg* is unaltered. DNA methylation was not altered in selected target genes.

The phenotypic alterations were accompanied by transcriptional changes, almost 450 genes were differentially expressed and the HFD mice are already distinguishable from the other groups solely by cluster analysis of the transcriptome. One week of HFD feeding induced changes of 'Metabolic pathways' as well as the 'Fatty acid metabolism', all in all, the pathways were mostly downregulated. However, no physiological significant alterations of DNA methylation were identified after one week in selected genes. This suggests that acute alterations are mainly induced by mechanisms which allow a fast response to changing environmental stimuli, such as mRNA degradation, post-translational modifications of transcription factors leading to inactivity, or favored formation of transcription factor-co-repressor-complexes. And from the energy supply point of view it is not necessary to upregulate pathways which produce energy providing molecules since they are abundant in the diet. Therefore, it is not surprising that *Acaca*, *Fasn*, and *Scd1* mRNA level were downregulated at week 1. It was shown for example that poly-unsaturated fatty acids negatively influence gene expression of *Scd1* by several different mechanisms independent of PPARs [151]. Since poly-unsaturated fatty acids are abundant in the HFD used here, this could be the reason for reduced *Scd1* transcription, however, the exact mechanism remains elusive.

Taken together, the results suggest that short-term HFD feeding for one week leads to reduced *de novo* lipogenesis rate. It was reported that a lard-based HFD can suppress *de novo* lipogenesis by simultaneously increasing triglyceride synthesis [9, 52, 95, 103]. One possible mechanism for this

observation could be the heterodimerization of PPARα with SIRT1 which makes PPARα a negative regulator of transcription [20]. The formation of the SIRT1-PPARα complex is favored by HFD feeding [20]. However, if a SIRT1-PPARα complex is formed, it seems to not persist throughout the study, because at week 8 and week 12 *Cyp4a10* and *Cyp4a14* as well as other genes strongly regulated by PPARα are upregulated (Suppl. fig. 7.8) [99, 156, 180]. It is also conceivable that other negative feedback mechanism induced by the high intake of fatty acids leads to downregulation of lipogenic genes.

Since *de novo* lipogenesis and fatty acid oxidation cannot be active simultaneously, a decrease of *de novo* lipogenesis rate could implicate a higher fatty acid oxidation rate [169, 206]. Fatty acid synthesis and degradation is coupled by ACC2-derived malonyl-CoA which inhibits CPT1 [169, 206]. CPT1 imports fatty acids into mitochondria for subsequent fatty acid β-oxidation [39]. *Acacb*, the gene encoding ACC2, was downregulated and *Cpt1a* was upregulated in HFD mice since week 1 (Suppl. fig. 7.9) [39]. However, the gene expression microarray data for genes involved in fatty acid oxidation, such as *Acadl*, *Hadha*, and *Acaa2*, showed no significant differences (Suppl. fig. 7.9) [193, 239]. Gene expression data alone are not enough to estimate the activity of a pathway due to for example post-translational modifications or allosteric inhibition/activation [51]. Furthermore, *Acacb* knockout mice show an increased fatty oxidation rate, leading to reduced fatty acid accumulation with positive effects on insulin sensitivity [1, 2]. The downregulation of *Acacb* could represent a mechanism to handle the elevated fatty acid load.

In conclusion, the metabolic alterations at week 1 are most likely compensatory mechanisms leading to short-term improvements of the glucose tolerance and the metabolism by inducing adaptational processes to cope with the high nutritional intake. Acute HFD feeding does not induce changes of DNA methylation, the alterations of gene expression could be caused by altered activity of transcription factors which in turn are controlled by the nutritional supply and needs of the organism.

6.1.2 Week 2 to week 5: Metabolic switch

After the initial impairments, whole-body glucose tolerance returned almost to control levels between week 1 and week 4. Insulin level at week 2 and 4 were slightly, but not significantly increased in the HFD groups. This could indicate a compensatory elevation of insulin secretion, possibly by increased β-cell mass, contributing to the improvement of whole-body glucose tolerance [177]. Mice have a great capacity to enlarge their β-cell mass and volume when fed a HFD without developing a progressive β-cell failure as observed in humans [177]. This is also the reason why mice do not develop a full type 2 diabetic phenotype.

Pyruvate kinase, the enzyme catalyzing the final and rate-limiting step of glycolysis [214], showed significantly decreased activity at week 2 and week 4, indicating reduced glycolysis rate. Glycolysis

breaks down glucose to pyruvate and thereby, generates ATP and intermediates for other pathways, such as glycogenesis and *de novo* lipogenesis [134, 243]. The decrease in pyruvate kinase activity is not accompanied by diminished mRNA levels, thus, post-transcriptional or post-translational mechanisms have to be responsible for the altered activity. The pyruvate kinase is for example allosterically inhibited by ATP, acetyl-CoA, and long-chain fatty acids which represent signals for sufficient energy supply and are most probably abundant in hepatocytes of HFD-fed mice [73]. Therefore, the decrease in PK activity could be a result of the nutritional overload due to HFD feeding. This could also be the reason for the downregulation of *Pparg* at week 2 and 4, because PPARγ stimulates fatty acid uptake and storage [123].

All these processes could represent compensatory mechanisms to manage the increased caloric intake, however, they are insufficient to rescue the phenotype. It appears that the liver already starts to develop hepatic insulin resistance after week 2, indicated by a decrease in hepatic pAkt/Akt ratio. Consequently, the mice developed whole-body glucose intolerance after five weeks of feeding. The starting increase in *Cd36* and *Fasn* gene expression suggests an elevation of fatty acid uptake and increased *de novo* lipogenesis which could contribute to the accumulation of hepatic triglycerides. Also gene expression of *Scd1* is slightly increased after week 4, but it is unlikely that this was induced by altered DNA methylation, because the differences were only minimal and did not persist over the whole feeding period. Two studies already indicated that HFD feeding induces increased DNA methylation of *Scd1* in the promoter region, though, the differences were also small and could be due to biological variance [34, 212]. Additionally, there is a discrepancy between humans and mice. Apart from the different number of functional *SCD* genes between the species (*Scd1-4* in mouse, *SCD* and *SCD5* in humans), mouse *Scd1* and human *SCD* share a high degree of homology and have the same function [255]. However, a study with subjects which lost weight identified increased DNA methylation in the *SCD* promoter region, but also here the changes of DNA methylation are only small [149]. This leads to the assumption that DNA methylation plays no central role in the regulation of *Scd1* gene expression.

These results could indicate a metabolic switch between week 2 and week 4 leading to the development of whole-body glucose intolerance at week 5. Also for ApoE*3-Leiden mice (mice expressing the ApoE*3Leiden and apoC1 gene cluster leading to a humanized lipoprotein profile [192]) fed with HFD with 45 kcal% fat it was observed that hepatic insulin resistance develops after 6 weeks [111]. This study reported hepatic triglyceride accumulation after development of insulin resistance, however, here hepatic triglycerides showed a vast increase at week 5, suggesting that hepatic insulin resistance and fatty liver develop simultaneously [111]. Similar to the pathway analysis results for week 12 reported here, Radonjic et al. observed in HFD-fed ApoE*3-Leiden mice that PPAR signaling as well as nearly all lipid metabolic pathways are altered [192]. Therefore, it was suggested that

PPARs could play a role in the metabolic switch from adaptational metabolic processes to insulin resistance [192]. Here, *Ppara* and *Pparg* gene expression started to increase after week 4 which could hint at a role of the PPARs in the metabolic switch in C57BL/6 mice as well.

6.1.3 Week 6 to week 12: Late phase

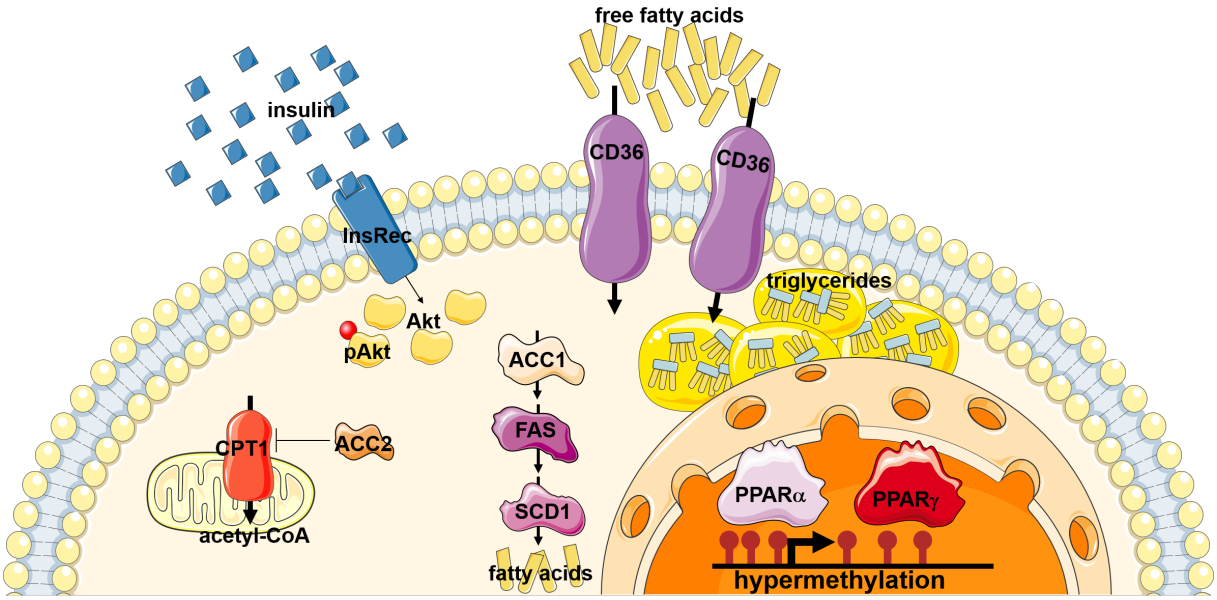

Figure 6.2: Chronic high fat diet feeding leads to development of insulin resistance. High fat diet feeding for 12 weeks induces whole-body as well as hepatic insulin resistance. This is accompanied by extensive alterations of the transcriptome and genome-wide DNA hypermethylation at differentially methylated regions. Gene expression of *Acaca*, *Fasn*, and *Scd1* could indicate that *de novo* lipogenesis rate is no longer suppressed HFD-fed mice. *Pparg* and *Cd36* are significantly increased after 12 weeks of HFD feeding, which likely contributes to extensive hepatic triglyceride storage.

After eight and 12 weeks of HFD feeding insulin level were significantly increased and whole-body glucose intolerance as well as hepatic insulin resistance was further deteriorated. At week 12, almost 800 genes were differentially regulated and about half of the differentially expressed genes were downregulated. Thus, the number of differentially expressed genes as well as the ratio of up- and downregulated genes changed from week 1 to week 12. The HFD mice fed for 12 weeks were clearly distinguishable from the other groups solely by the transcriptional changes, indicated by cluster analysis.

After 12 weeks of HFD feeding, both *Ppara* and *Pparg* show significantly increased gene expression in HFD mice which is accompanied by upregulation of their target genes, such as *Cd36*, *Fasn*, and *Fgf21*. It was shown that PPARγ induces lipid accumulation and storage, therefore, the upregulation of *Pparg* could favor development of hepatic steatosis [53, 123]. The increase in lipid accumulation could be mediated by the vast increase of *Cd36* gene expression [67]. Higher *Cd36* mRNA level are

associated with elevated protein level and translocation to the plasma membrane which results in higher fatty acid uptake into hepatocytes [78, 112, 182]. Increased hepatic triglyceride content is a marker for disordered fatty acid metabolism and associated with insulin resistance as well as the beginning of hepatic steatosis and NAFLD [78, 201, 230]. Taken together, this further worsens the liver phenotype towards steatosis.

At week 8, when the mice started to develop whole-body glucose intolerance and hyperinsulinemia, *Fasn* mRNA returned to chow level. High rates of *de novo* lipogenesis are associated with insulin resistance and chronically elevated insulin level and it was shown that ob/ob mice have increased *Fasn* mRNA level and FAS activity [9, 95, 206]. The upregulation of *Fasn* to chow levels could indicate an elevated accumulation of palmitate, which could have further deleterious effects on the liver phenotype [135, 167]. It was shown that products of *de novo* lipogenesis, especially of FAS, can activate PPARα [31, 32, 95, 193].

Besides the alterations of genes of the fatty acid metabolism, also *Pklr* was significantly upregulated at week 12 in the HFD group, however, not due to differences of DNA methylation. Pyruvate kinase activity is similar to chow level. Glycolysis metabolizes glucose to pyruvate which can be used for fatty acid synthesis during *de novo* lipogenesis [201]. Thus, glycolysis could fuel hepatic lipid accumulation.

The whole-genome bisulfite sequencing revealed that HFD feeding led to an extensive hypermethylation of differentially methylated regions. The pathway analysis identified 'PPAR signaling' and fatty acid metabolic pathways as altered indicating that DNA methylation changes contribute to the transcriptional alterations at week 12. Consequently, the development of insulin resistance is accompanied by extensive changes of DNA methylation. The majority of DMRs was located in introns, whereas promoter regions show much less DMRs. Epigenetic research focused for a long time primarily on DNA methylation at CpG islands in promoter regions, disregarding CpG methylation within gene bodies [101]. But in fact, CpG islands in promoter regions are usually unmethylated, whereas gene bodies, mostly being CpG-poor, are extensively methylated [101]. In gene bodies, DNA methylation is associated with transcribed genes, although the relationship between DNA methylation and gene expression is complex and dependent on genomic and cellular context [98, 101]. It was suggested, that DNA methylation in first exons is decisive for gene expression, because it was observed that lowly expressed genes have higher methylation within the first exon, whereas transcription of a gene requires hypomethylation of the first exon [21]. The two CpG sites with altered DNA methylation in *Fgf21* were located within exon 1 indicating that DNA methylation in exon 1 has indeed a regulatory role. However, also the CpG sites measured in *Cd36* were located within exon 1, but no differences were identified between the groups, although *Cd36* showed enormous upregulation of its gene expression. When looking at the whole-genome DNA methylation data, only 348 DMRs were located in the first exon and the majority of DMRs were found in introns and other exons. Taken

together, these results demonstrate that DNA methylation is strongly location-dependent. This could also explain why *Fgf21* was the only gene found to be regulated by DNA methylation by bisulfite pyrosequencing, because DMRs and CpG sites measured by bisulfite pyrosequencing were located in different exons or introns. Moreover, the whole-genome DNA methylation data show that also regions downstream of the first exon could be important for the regulation of gene expression.

6.1.4 Summary

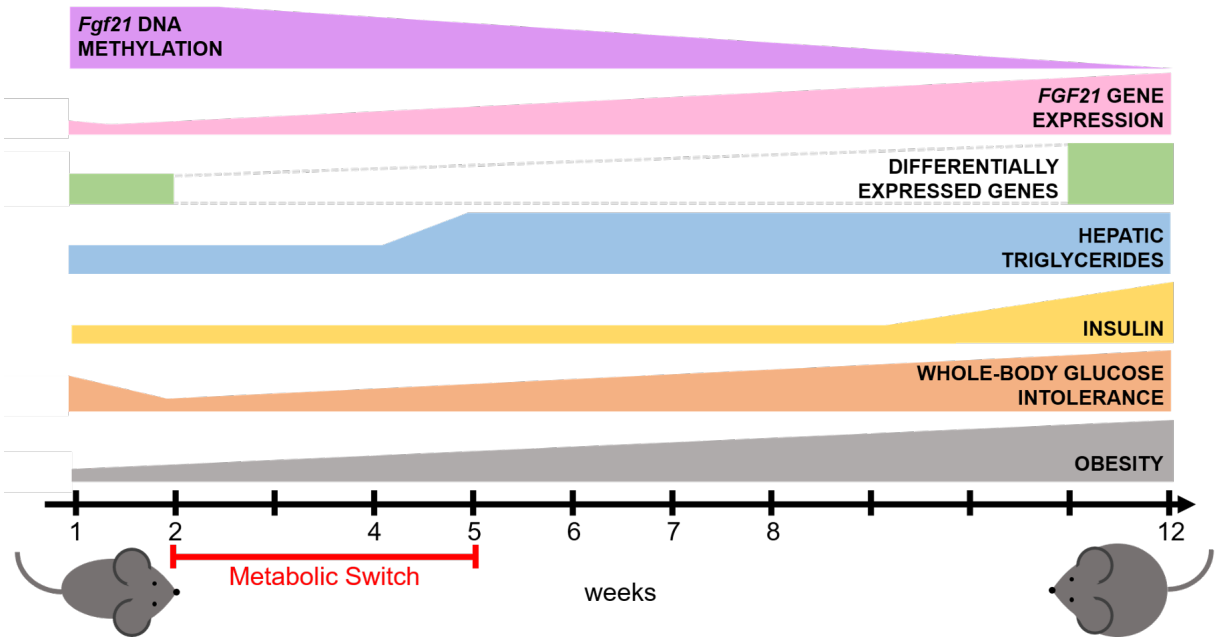

Figure 6.3: Summary of the significant alterations induced by HFD feeding. HFD feeding induces continuous body weight gain leading to obesity. Already one week of feeding a HFD induces significantly impaired whole-body glucose tolerance which improves during week 2 and 4. However, after five weeks of HFD feeding whole-body glucose tolerance cannot be maintained any longer. This is accompanied by significant increased insulin level after eight weeks. Hepatic triglyceride levels are already elevated after one week of HFD feeding, however, between week 4 and week 5 triglycerides show a further increase and reach a plateau afterwards. Also transcriptomic changes are evident after one week of HFD feeding and the number of differentially expressed genes further rises after 12 weeks. The differentially expressed genes include *Fgf21*, which is 24-fold upregulated at week 12. This increase in gene expression is accompanied by DNA hypomethylation at two CpG sites within exon 1.

Insulin resistance did not develop gradually but in distinct phases starting with an adaptational period characterized by impaired whole-body glucose tolerance without adversely affecting the insulin-stimulated Akt phosphorylation. Although no histological alterations of the liver were apparent yet, hepatic triglyceride content was already significantly increased which was accompanied by transcriptional changes of metabolic, especially lipogenic genes. The glucose tolerance was maintained in the following weeks probably due to compensatory mechanisms of other organs, such as small elevation of insulin level. However, these mechanisms failed during chronic HFD feeding and after

five weeks the mice developed whole-body glucose intolerance. This could represent a metabolic switch from compensatory processes to pathological alterations.

The development of insulin resistance in ApoE*3-Leiden mice fed with HFD with 45 kcal% fat for 30 weeks was also characterized by three phases, an early phase between one day and one week, a mid phase between two weeks and four weeks and a late phase between eight and 16 weeks [192]. This study showed that the most prominent transcriptomic alterations occur in the early and late phase and many genes change direction of expression during the time course of the study [192]. This was also observed for many genes in the study presented here. For example *Pparg* and *Fasn* were initially significantly downregulated, but gene expression increased with the development of glucose intolerance. This switch in gene expression is likely responsible for the deregulation of metabolic pathways contributing to the manifestation of insulin resistance. The hypothesis of this study was that altered gene expression is induced by changes of DNA methylation. This is supported by the observation that mice fed for 12 weeks with HFD are characterized by extensive DNA methylation alterations. Furthermore, DNA hypomethylation at two CpG sites within *Fgf21* developed during the time frame of the metabolic switch. Consequently, DNA methylation plays most probably a central role in the development of insulin resistance.

It was shown for C57BL/6 mice fed a HFD with 42 kcal% fat for 16 weeks that glucose intolerance develops after three days without any further deteriorations during the following feeding period [230]. Once insulin resistance was established, it did not worsen any further with longer HFD feeding [230]. This is in contrast to the results shown here, where glucose intolerance is initially significantly impaired but improved short-termly until final establishment. The discrepancies could be caused by feeding different fat amounts and different feeding periods [80].

Hepatic insulin resistance is strongly associated with hepatic triglyceride accumulation and many obese and type 2 diabetic patients have also non-alcoholic fatty liver disease (NAFLD) [124, 165, 184]. Here, HFD mice showed extensive triglyceride accumulation in the liver indicating development of hepatic steatosis which is strongly associated with insulin resistance [89].

Insulin stimulates hepatic glycogen synthesis [201]. Therefore, one would suggest higher glycogen level in HFD mice at week 1, when the liver shows high insulin sensitivity, and a decrease in glycogen level at later time points. The glycogen assay revealed that HFD mice showed a slight, but not significant decrease in hepatic glycogen amount during the whole feeding period. In the literature varying results for hepatic glycogen content in HFD-fed animals compared to controls are reported, ranging from reduced [120, 148] to increased glycogen levels [50, 170]. This could be for instance due to different fasting states of the animals, different animal models, diets, or handling of the liver after sacrifice.

6.2 Tools for targeted and fishing identification of possible candidate genes

For humans the Infinium Human Methylation 450K BeadChip array is available, a microarray format to measure genome-wide DNA methylation [174], but for mice no sensitive high-throughput techniques with single-base resolution exist. The available methods for mice, such as methylated DNA immunoprecipitation (MeDIP)-sequencing, have poor resolution and are still not considered reliable [41, 174]. Therefore, we exploited two different approaches for candidate gene identification: A targeted search by data mining and candidate fishing by transcriptomics and methylomics.

6.2.1 Omics-approaches for candidate fishing

DNA methylation contributes to the development of insulin resistance by altering gene expression. To identify differentially expressed genes, gene expression microarrays were performed. Subsequently, DNA methylation of differentially expressed genes was measured. Since it was shown that transcription factor binding sites play an important role in determining epigenetic conservation between species, the search for regions with altered DNA methylation was refined by analyzing predicted transcription factor binding sites using *Unipro UGENE* [22, 257]. Bisulfite pyrosequencing only assesses about 100 bp at once, consequently, regions with altered DNA methylation can easily be missed. Therefore, whole-genome bisulfite sequencing (WGBS) of two HFD and two chow mice of the longitudinal study was performed. However, the WGBS results could not always be reproduced by bisulfite pyrosequencing.

WGBS gets more and more attention, because it theoretically allows the measurement of every single CpG site within the genome, but it has still some difficulties to overcome [4]. As a result, bisulfite pyrosequencing still represents the gold standard to measure DNA methylation [228]. Both methods are based on bisulfite conversion of DNA and are sequence-by-synthesis approaches [90, 174]. WGBS needs the preparation of a library as well as extensive bioinformatic data analysis [166]. Bisulfite pyrosequencing has a much shorter analysis time but is limited by the requirement of primer design which can be challenging for very CpG-rich or CpG-poor regions [4, 43].

The most crucial step in both methods is the bisulfite conversion of DNA. A complete conversion of all unmethylated cytosines is essential for correct measurement of DNA methylation [115]. Furthermore, bisulfite treatment leads to fragmentation of DNA which could result in a distorted representation of genomic sequences by depletion of cytosine-rich and unmethylated DNA from the sequence pool leading to an overestimation of DNA methylation [176].

One reason for discrepancies between WGBS and pyrosequencing data for *Fgf21* and *Ppara* could be that the bisulfite DNA used for sequencing stems from different bisulfite treatments. The bisulfite-treated DNA for bisulfite pyrosequencing is also older than the bisulfite DNA which was freshly

prepared for WGBS. Repeated freeze-thaw cycles can lead to further degradation of the already very sensitive DNA resulting in the above-mentioned skewed representation of genomic sequences. When comparing WGBS and bisulfite pyrosequencing results, it is notable that for the promoter region in *Fgf21* bisulfite pyrosequencing overestimated DNA methylation for the chow group relative to WGBS, but underestimated DNA methylation for the HFD group. If the bisulfite DNA was degraded due to freeze-thaw cycles, one would expect a uniform difference between both methods. Moreover, it was reported that bisulfite pyrosequencing tends to underestimate DNA methylation which was not observed here [228].

An important determinant for the accuracy of the sequencing is the cycle number of the preceding PCR amplification. The bisulfite conversion is the main source for bias, but the PCR builds up on this and further amplifies these errors which may result in an enlargement of the bias [176]. Since the analysis is performed on the PCR product the accuracy of the PCR amplification is crucial for the sequencing result [159]. Bisulfite-converted DNA contains about 80% AT and 20% G which can lead to long regions consisting only of thymine [176]. This represents a challenge for polymerases and often leads to uneven amplification of methylated and unmethylated sequences, with unmethylated DNA preferentially amplified [115, 159, 176]. Since the bias is to some extent sequence-specific, some regions are more susceptible for a bias than others [176]. Also the slightly different denaturation temperatures of unmethylated and methylated sequences can contribute to the bias, for example sequences rich in GC could stay annealed during amplification [115, 217]. This results in most cases in an enrichment of unmethylated sequences in the PCR amplification [159]. A PCR amplification with as little cycles as possible is desired. For WGBS much less PCR cycles are used as for bisulfite pyrosequencing, thus, reducing the PCR bias [43]. However, to control for the PCR bias in bisulfite pyrosequencing quality controls were included in our study.

When analyzing whole-genome bisulfite data an important information is the coverage which describes the number of sequenced fragments (so-called reads) containing a given CpG site [241]. The NIH Roadmap Epigenomics Projects recommends a total coverage of 30x [258]. However, it was suggested that a coverage of 5x to 15x is enough for identification of differentially methylated regions, whereby the coverage for closely related samples needs to be higher as for more diverse samples [258]. For the three CpG sites measured by both methods in *Fgf21* the average coverage is between 13x and 14.75x, for the DMR in *Ppara* even between 13.75x and 18.75x. Therefore, the coverage fits the recommendation of 5x to 15x, but HFD feeding could represents a too weak intervention to induce large changes of DNA methylation and a higher coverage would be necessary. It needs to be considered that a coverage of 15x means that 15 reads, which is synonymous for 15 cells, were sequenced for one CpG site, but due to the heterogeneity of liver tissue the reads could origin from Kupffer cells or endothelial cells and not represent hepatocyte DNA methylation. Even if the reads stem from hepatocytes, DNA methylation could differ depending on the liver zonation.

In contrast to WGBS, DNA methylation of millions of cells is measured by bisulfite pyrosequencing, thus, the results represent an average of hepatic DNA methylation in a specific region. For future WGBS experiments a higher coverage would be necessary to compensate for this.

In conclusion, bisulfite pyrosequencing still represents the gold standard for measurement of DNA methylation and to ensure reliable results primer and methylation controls, additional to the ones provided by the analysis software, were included for the study presented here.

6.2.2 Targeted candidate gene identification by data mining

To identify potential candidate genes literature research, different databases, and preliminary human and mouse genome-wide DNA methylation data were utilized.

Although the mouse genome is about 14% smaller than the human genome, about 90% of the human and mouse genomes can be partitioned into conserved synteny regions [22, 160]. For 80% of human and 72% of mouse protein-coding genes a one-to-one orthologous gene exists [22, 160]. When focusing on functional regions in genes, it is notably that promoter regions show greater differences between mice and humans compared to gene body sequences [22]. For transcription factor binding motifs it was shown that primary consensus motifs for orthologous transcription factors are the same between the species, but secondary motifs can differ [22]. Therefore, the pool of target genes of a specific transcription factor seems to be conserved between mouse and humans [22]. A large proportion of DNA methylation is conserved in a tissue-specific manner between humans, mice, and rats [257]. This is associated with conservation of other epigenetic marks, such as histone modifications [163, 257]. The epigenetic conservation is determined by the conservation of the underlying DNA sequence and conserved regions often represent transcription factor binding motifs [257].

With this in mind, the data generated by Kirchner et al. [110] were initially used for identification of possible candidate genes. This data set consisted only of seven non-obese, seven obese non-diabetic, and eight obese type 2 diabetic subjects and therefore, is under-powered and shows a large intra-group variance [110]. The obstacle with the human data was the transfer of differentially methylated CpG sites into the mouse genome. If the CpG sites were present at all, they were mostly located in a different genomic context, for example in a different exon, and the changes of DNA methylation could not be reproduced in mice. The 450K array measures 485 000 CpG sites, but the majority is located in promoter regions and CpG islands [119, 186]. Since promoter regions vary widely between mice and humans compared to gene body sequences, the 450 K chip design could be responsible for the observed discrepancies [22]. Binding motifs of transcription factors and enhancers show higher conservation between mice and humans, therefore, subsequent approaches focused on these binding motifs and adjacent regions [22].

Despite the difficulties to reproduce the human data it was demonstrated in the past that mice are very well suited to increase the understanding of human diseases [12]. Human studies suffer from many confounding factors which could influence DNA methylation, it is difficult to control for environmental factors and results from different ethnic groups are not comparable [79]. The tissue availability is limited and human studies are most often based on easily accessible tissue, such as blood, which is well suited to study genetics, but epigenetic patterns are tissue specific [82, 168]. The limited tissue availability also impedes with mechanistic experiments. On the contrary, C57BL/6 are inbred mice which are genetically identical and do not possess any genetic variations influencing the phenotype within one strain [231]. Therefore, DNA methylation differences are solely the result of environmental factors and the environment in animal facilities is tightly controlled [163]. Moreover, mice of the same experimental group do not differ regarding their food composition. In conclusion, epigenetic studies in mice are much better controlled and therefore, very well suited for epigenetic basic research to understand disease mechanisms. This was the reason why previous studies in mice were used for identification of possible candidate genes, especially data from the CHARM microarray performed by Multhaup et al. [163]. The data set consisted of DNA methylation data from livers of C57BL/6 mice fed a high fat or low fat diet for 12 weeks [163]. *Sik3*, *Sgms2*, and *Galnt2* were chosen from this data for analysis in mice fed high fat-high sucrose diet or high fat diet. Although *Sik3* and *Galnt2* possess differentially methylated regions after 12 weeks of HFD feeding no differences in gene expression were identified, indicating that DNA methylation in these regions does not affect transcription. This demonstrates the importance of analyzing DNA methylation and gene expression simultaneously. Moreover, the DNA methylation data of Multhaup et al. could not be reproduced in the study presented here. The discrepancies could be due to different high fat and control diets, which induce a slightly different phenotype [80]. Multhaup et al. used as control diet a purified low fat diet with 10 kcal% from fat and 70 kcal% from carbohydrates, whereas here a chow diet was used [163]. Although the purified low fat diet is considered a very good control diet for high fat diet studies, the high carbohydrate content itself could have adversely effects on the metabolism. Furthermore, different feeding length were used (here, mice were fed with HFHS diet for 20 weeks), therefore, the mice are in different disease states. Multhaup et al. used isolated hepatocytes for DNA methylation analysis [163], whereas the results presented here were obtained from whole-liver homogenate, which contains also other cell types, such as Kupffer cells or endothelial cells. The isolation of hepatocytes involves the risk that RNA is degraded or the RNA composition is altered. Since DNA methylation needs to have an impact on gene expression to contribute to the pathogenesis of insulin resistance, it is important to analyze simultaneously hepatic mRNA. Liver tissue needs to be snap-frozen as rapid as possible to ensure the preservation of RNA levels in a state as native as possible. In contrast to the Multhaup study, the study presented here allows a more detailed picture

of the cellular alterations in insulin resistance and makes the first move to a more mechanistically oriented approach.

An additional confounding factor could be the pronounced zonation of the liver in periportal, intermediate, and pericentral zone [81, 108]. For example triglyceride accumulation occurs in a zonation-dependent manner [81]. Taking this into consideration, variations between different studies could occur because of using not the same liver lobe. Therefore, it would be best to homogenize the complete liver with liquid nitrogen. However, the homogenization is very time-consuming and was not possible in the longitudinal study due to the high sample size. The time between sacrifice of the first and last mouse was kept as minimal as possible to avoid different fasting states of the mice, because they were sacrificed during their resting phase.

6.3 PPAR-FGF21-Pathway

6.3.1 DNA methylation of Fibroblast Growth Factor 21

Fibroblast growth factor 21 (FGF21) has several positive metabolic effects and therefore, represents a promising target for the development of new drugs for type 2 diabetes, obesity, and nonalcoholic steatohepatitis (NASH). For example pegbelfermin, a FGF21 analogue, is currently in a phase 2a trial [35, 60, 208]. Because it was shown that plasma FGF21 is almost exclusively determined by hepatic *Fgf21* gene expression, studying regulation of hepatic *Fgf21* transcription would be valuable for novel intervention strategies [219, 222]. Nevertheless, the regulation of *Fgf21* gene expression is only scarcely studied [57]. Here, it is shown for the first time that *Fgf21* is likely epigenetically regulated in adult mice within exon 1, but not in the promoter region. DNA methylation in gene bodies is more prevalent than in promoters and especially at enhancers or transcription factor binding sites DNA methylation could be important for a fine-regulation of transcription [98, 101]. Since the transcription of *Fgf21* is not turned on or off in HFD mice but increased gradually, it seems reasonable that the difference in DNA methylation is found within the gene body. This is supported by the location of the altered CpG sites in *Fgf21*, they are in close proximity to a predicted HNF3/HNF4 binding motif and two PPAR response elements (PPRE). Intriguingly, there is a study on *Fgf21* DNA methylation in mice during the postnatal period showing that an activation of PPARα induced a demethylation of *Fgf21* [253]. These alterations, once established, remained stable throughout the later life [253]. In contrast to these findings, the diet-induced obese mice described here develop DNA hypomethylation of *Fgf21* in adulthood due to the development of insulin resistance, demonstrating that the epigenetic regulation of *Fgf21* is dynamic. The above-mentioned study also suggests a role of PPARα in inducing these epigenetic changes by recruitment of TET2 [253]. Additionally, it was demonstrated that also other PPARα target genes encoding enzymes of the β-oxidation show a ligand-activated PPARα-dependent DNA demethylation [56]. This is not observed in PPARα-knockout mice [56].

Similar results were described for long-term administration of the PPARα agonist WY-14643 which induces loss of DNA methylation in mouse liver [188]. Also PPARγ was reported to induce local DNA demethylation by recruiting TET enzymes [61, 253]. The two CpG sites of *Fgf21* studied here are located adjacent to two predicted PPREs, indicating that the observed DNA hypomethylation in HFD mice could be caused by a PPAR-dependent mechanism, leading to the tremendous upregulation of *Fgf21* gene expression. All three PPAR isoforms bind to PPAR responsive elements and the 5'-flanking region seems to play a role in the determination of the isoform-specific binding [235]. However, only very few genes are regulated by only one PPAR isoform [235]. In contrast to *Pparg*, *Ppara* was upregulated in HFD mice after week 2, suggesting that the *Fgf21* demethylation could be PPARα-dependent. Therefore, PPARα does not only activate *Fgf21* transcription, but likely also regulates *Fgf21* epigenetically.

It was reported that FGF21 administration leads to a decrease of its own gene expression indicating a negative feedback mechanism [70, 240]. This would implicate that high endogenous FGF21 levels could negatively feedback to regulate *Fgf21* gene expression. A negative feedback mechanism could contribute to the fluctuating *Fgf21* mRNA level in the HFD group, especially at week 7, 8, and 12. However, the effects of FGF21 on the liver itself are only scarcely studied. The ability of FGF21 to induce signaling in a tissue is determined by the presence of its co-receptor β-Klotho as well as FGF21's preferential receptor FGFR1, both are expressed in hepatocytes [60]. In the liver, FGF21 competes with FGF19 for β-Klotho, but in principle FGF21 should be able to induce signaling [60]. The negative feedback mechanism could be due to direct signaling, but also indirect effects are conceivable, for example secretion of factors by other tissues upon FGF21 signaling. In the end, gene expression of *Fgf21* was further increased in our study. The negative feedback mechanism could be overwritten by alterations of DNA methylation, allowing further elevation of gene expression. The upregulation could be an adaptational response to cope with nutritional overload. Although FGF21 has clear protective effects against insulin resistance, the elevated endogenous FGF21 level cannot rescue the phenotype which was also observed by others [17, 26, 60]. Processes supporting the development of insulin resistance seem to outweigh the positive effects of FGF21, so that the elevated *Fgf21* gene expression is insufficient. It is also possible that HFD-fed mice develop a resistance against FGF21, similar to insulin or leptin resistance [57, 222]. The existence of FGF21 resistance is controversially discussed. Resistances are most commonly mediated by a defect at the receptor level and for FGF21 it was shown that FGFR1, FGFR2, FGFR3 as well as its co-receptor β-Klotho are decreased in white adipose tissue in obesity, but FGF21 signaling, assessed by ERK phosphorylation, was not altered [49, 59, 62, 70]. On the other hand, others could show an impairment of the FGF21 signaling by reduced ERK phosphorylation [147]. These discrepancies could be due to the use of different animal models [70]. It was suggested that FGF21 resistance could be mediated by mechanisms downstream of the receptors, for example by an increased activation of dual-specific

phosphatase 6 (DUSP6) which dephosphorylates and turns off ERK1/2 [147]. DUSP6 was described to be increased in diet-induced obese mice [185, 244]. In the study presented here, HFD mice fed for 12 weeks showed a significant downregulation of hepatic *Fgfr1* and *Fgfr2* with a fold change of -1.41 and -1.46, respectively (Suppl. fig. 7.7, differentially expressed genes are defined by significant fold change of <-1.5/>1.5). The gene expression of β-Klotho was unaltered, but *Dusp6* showed a significant upregulation (fold change of 2.81, suppl. fig. 7.7). These results indicate that insulin resistance is associated with changes of the FGF21 signaling pathway, but for a definite conclusion protein level of the receptors and DUSP6 as well as ERK1/2 phosphorylation needs to be studied in FGF21 target tissues. However, ERK1/2 might not be the best readout for an activation of FGF21 signaling, because ERK1/2 is downstream of multiple signaling cascades [66]. Although the development of FGF21 resistance in obesity and type 2 diabetes is still under debate, the gene expression data could suggest a downregulation of hepatic FGF21 signaling.

6.3.2 Peroxisome proliferator-activated receptor α and γ

Peroxisome proliferator-activated receptors (PPARs) are nuclear receptors activated by fatty acids, eicosanoids, and oxidized fatty acids originating from diet, *de novo* lipogenesis, and lipolysis [18, 53, 123]. The PPARs are implicated in the pathophysiology of metabolic diseases and for PPARγ and PPARα agonistic drugs are already in clinical use for treatment of insulin resistance and dyslipidemia, respectively [48, 68, 74].

PPARα is predominantly expressed in liver and regulates for instance fatty acid oxidation under fasting conditions but can also coordinate *de novo* lipogenesis under fed conditions [53]. *Ppara* gene expression is extensively regulated by many different factors, such as leptin and glucocorticoids, therefore, the upregulation in the HFD group since week 4 can have multiple reasons [20]. It was reported that *Ppara* gene expression is activated by HFD feeding in liver of mice and rats [20, 128, 180]. Furthermore, *Ppara* is regulated by insulin [20]. Treatment of primary hepatocytes with insulin for three days reduced *Ppara* levels, whereas treatment of the cells with fatty acids, especially saturated fatty acids, positively regulated *Ppara* transcription [223]. A strong induction of *Ppara* gene expression is achieved by feeding a diet low in sucrose and with a high amount of poly-unsaturated fatty acids [107]. The HFD D12942 contains about one third poly-unsaturated fatty acids, suggesting that the diet composition used here favored the induction of *Ppara* gene expression and activation [177, 180]. For instance, PPARα is activated by palmitic acid, oleic acid, linoleic acid, and stearic acid which are all contained in the HFD [74, 107, 177]. Therefore, the increase in *Ppara* gene expression at week 1 could be due to the high dietary fatty acid amount and could represent a compensatory mechanism to manage the increased fatty acid load. The compensatory upregulation at week 1 could lead to a short-term improvement of the metabolism, indicated by normalization of *Ppara*

mRNA level at week 2. However, long-term HFD feeding inevitable leads to insulin resistance and chronic upregulation of *Ppara*, likely due to increased fatty acid uptake into the liver.

In addition to the regulation by hormones and metabolites, it was shown in cell culture experiments that human *PPARA* is able to positively regulate its own gene expression [187]. The human and mouse *Ppara* gene shares 91% homology, therefore, the autoregulation might also exist in mice explaining the fluctuating mRNA level during the feeding period [20, 181].

The PPARα activity can be assessed by measuring expression of genes which are strongly regulated by PPARα, prominent targets are *Cyp4a10* and *Cyp4a14* [99, 156, 180]. Both genes were upregulated at week 12 in HFD mice, as shown by the gene expression microarrays (Suppl. fig. 7.8), indicating that PPARα is indeed more active in HFD mice.

Moreover, it was reported that in humans *PPARA* mRNA level show high variability among individuals, which could indicate a strong regulation on the genetic and epigenetic level [20]. The whole-genome bisulfite sequencing revealed four differentially methylated regions within intron 2. This suggests that PPARα could be epigenetically regulated. Therefore, DMR 2 was measured in the whole group of week 12 by bisulfite pyrosequencing, but only one CpG site showed a significant difference in DNA methylation of 5%. These discrepancies between WGBS and bisulfite pyrosequencing are not only due to higher group size, but already obvious by comparing mean DNA methylation values of the two mice per group sequenced by WGBS as well as bisulfite pyrosequencing. Bisulfite pyrosequencing is the gold standard for measuring DNA methylation, therefore, regulation of *Ppara* by DNA methylation could not be confirmed [228]. An epigenetic regulation of *Ppara* was already suggested before, however, these studies focused on transgenerational experiments and DNA methylation was measured in the promoter region. For example it was shown that feeding pregnant rats a protein-restricted diet resulted in decreased DNA methylation in the promoter region of *Ppara* in the offspring [139]. In another study the offspring of male rats treated with streptozotocin and healthy females showed altered DNA methylation in the *Ppara* promoter [133]. In both studies the changes persisted into adulthood and the altered CpG sites were located within transcription factor binding motifs, thus, it was suggested that this has an impact on *Ppara* gene expression [133, 139]. However, absolute DNA methylation of the studied regions was very low, with maximal 10% of promoter methylation and also the differences between the groups were maximal 5%. Taken together, all these results are questioning the regulation of *Ppara* by DNA methylation.

PPARα is thought to be protective against hepatic steatosis and insulin resistance by activating fatty acid oxidation and therefore, reducing the lipid load within the liver [30, 53]. However, *Ppara* knockout mice are protected from developing insulin resistance under HFD feeding [69]. This suggests that PPARα plays a supportive role for development of insulin resistance under HFD-conditions.

PPARγ has important functions in adipogenesis, induces fatty acid uptake, and upregulates *de novo* lipogenesis and thereby promotes fatty acid storage in adipose tissue and liver [18, 53]. It was

already reported that HFD feeding activates *Pparg* gene expression and ob/ob as well as db/db mice show increased hepatic *Pparg* gene expression [54, 91, 127, 146, 153, 180].

Initially, *Pparg* was significantly downregulated in HFD mice, but gene expression increased continuously between week 4 and week 12. There are three isoforms of PPARγ and the SYBR green qRT-PCR primer measured all of them [123, 126]. PPARγ1 is expressed in several tissues, such as liver, whereas expression of PPARγ2 is mostly restricted to adipose tissue [123, 126]. It was reported that *Pparg2* is induced in primary mouse hepatocytes by oleic acid and insulin as well as in liver of diet-induced obese mice and its gene expression positively correlates with hepatic fat accumulation [54, 127, 236]. In contrast to *Pparg2*, *Pparg1* is not altered due to obesity and insulin resistance [127]. This could indicate that the increase in *Pparg* gene expression is due to higher transcription of *Pparg2*. However, this cannot explain the significant downregulation in the first four weeks of the study. Though, the downregulation of *Pparg* in the early stages of HFD feeding was also observed by others in ApoE*3 Leiden mice fed a HFD with 45 kcal% fat [192].

It was shown that a knockout of *Ppara* induces higher gene expression of *Pparg* as a compensatory mechanism [180]. It might be possible that this functions also the other way around: The elevated expression of *Ppara* could represent an inhibitory signal for the *Pparg* gene expression. After week 4, serious metabolic alterations could be the reason for the increase in *Pparg* gene expression.

6.4 High fat diet-induced alterations of genes of the glucose metabolism

Gluconeogenesis serves as energy supply in times of prolonged fasting when glycogen stores are depleted [201]. A key enzyme of the gluconeogenesis is phosphoenolpyruvate carboxykinase (PEPCK) which catalyzes the conversion of oxaloacetate to phosphoenolpyruvate [201]. The common last step of gluconeogenesis and glycogenolysis, the conversion of glucose-6-phosphate to glucose, is catalyzed by glucose-6-phosphatase (G6PC) [201]. The rate of gluconeogenesis is determined by the activity of the rate-limiting enzymes, but also the substrate availability plays a role [201]. Insulin negatively regulates gluconeogenesis by inhibiting gene expression of *Pck1* and *G6pc* [201]. In insulin resistance, insulin fails to inhibit gluconeogenesis resulting in increased hepatic glucose output [24].

PEPCK and G6PC level are strongly regulated on the level of transcription, for PEPCK no allosteric modifications were known for a long time [71, 248]. Conversely, the transcriptional regulation of *G6pc* is more complex compared to *Pck1*, although the promoter of both enzymes has some elements in common [204]. This led to the hypothesis that *Pck1* and *G6pc* could be epigenetically regulated. Initially, DNA methylation of *Pck1* and *G6pc* was measured in mice fed a high fat-high sucrose diet for 20 weeks and a differentially methylated regions was identified for each gene. Though, this was not replicated in mice fed a high fat diet for 12 weeks.

The high fat-high sucrose diet D12331 has a nearly identical fat content as the high fat diet D12492, but the fatty acid composition differs due to different fat sources (Suppl. tab. 7.1 and 7.2). The D12331 diet consists of over 90% saturated fatty acids (percentage of the total dry weight) making it more obesogenic than the HFD D12492 which contains only 32% saturated fatty acids (Suppl. tab. 7.1 and 7.2). On the other hand, the D12492 diet contains almost exclusively long-chain fatty acids, unlike the D12331 diet, which induces more effectively obesity than short- and medium chain fatty acids [80]. The diets also differ regarding their sucrose content, the D12331 diet contains about twice as much sucrose as the high fat diet D12492 (Suppl. tab. 7.1 and 7.2). The different diet compositions cause slightly different phenotypes, for example it was shown for a feeding period of eight weeks that HFD based on lard induces robustly insulin resistance, whereas the high fat-high sucrose diet leads to a moderate phenotype [177]. However, the mice presented here were fed for 20 weeks which probably elicited pronounced insulin resistance, but unfortunately no glucose tolerance data were available. In contrast, the mice of the longitudinal study were only fed for 12 weeks. This difference in feeding period can have marked impact on the phenotype and likely leads to different epigenetics. All these factors could have contributed to the different results of DNA methylation in *Pck1* and *G6pc*. This also demonstrates that diet-induced obesity caused by different high fat diets and feeding periods could lead to varying phenotypes and comparisons between different studies should be made carefully. Otherwise, also human diseases may vary between individuals and the analysis of different diet-induced obesity mouse models might reflect a good cross section of metabolic diseases.

It is thought that hyperglycemia in type 2 diabetes is induced by increased hepatic gluconeogenesis, because gene expression of *Pck1* and *G6pc* is no longer inhibited due to insulin resistance [76, 143, 213, 237]. Here, gene expression of *Pck1* and *G6pc* was not altered in glucose intolerant HFD-fed mice. Similar results were described in the literature. HFD-fed Sprague Dawley rats with or without nicotinamide and streptozotocin treatment and type 2 diabetic humans showed no differences in gene expression of *Pck1* and *G6pc* [183, 204]. Regarding *G6pc*, the studies are more inconsistent, because it was also reported that *G6pc* gene expression is increased in type 2 diabetes and corresponding animal models [88, 234]. In contrary to the prevailing opinion the results presented here, but also the literature, indicate that *Pck1* and *G6pc* gene expression is not altered in insulin resistance and might be of no significance for regulating the gluconeogenesis rate. And indeed, it was shown that gene expression of *Pck1* and *G6pc* is no adequate measure to estimate gluconeogenesis, *Pck1* transcription does not correlate with gluconeogenic flux [40]. Post-translational modifications of PEPCK and G6PC could be responsible for this observation, for instance PEPCK is a substrate for acetylation resulting in its degradation by the proteasome [97, 220, 246].

Hence, an enzyme activity assay for PEPCK was performed, but insulin resistance did not lead to alterations of PEPCK activity in our model. If gluconeogenesis is upregulated in insulin resistance, this is most probably not due to PEPCK. It was even suggested that PEPCK is not the essential enzyme

of gluconeogenesis as previously assumed [204]. In humans, it was shown that elevated gluconeogenesis rate is probably a symptom of advanced type 2 diabetes, because patients with moderate hyperglycemia displayed no alterations [19]. Mice do not develop a full type 2 diabetes phenotype which could explain the results [177]. Moreover, it is very unlikely that such an important pathway as gluconeogenesis is only regulated on the transcriptional level or by a few enzymes, for instance it was observed that allosteric regulation of pyruvate carboxylase as well as substrate availability plays a role [25, 204]. Additionally, many rodent models for type 2 diabetes also display increased plasma glucocorticoid levels which are known to upregulate gluconeogenesis and could represent a confounding factor [204]. Further insides into the metabolic role of PEPCK was gained by characterizing mice with impaired *Pck1* gene expression in liver. These mice showed no alterations of glycemia and it was suggested that PEPCK is not solely involved in gluconeogenesis but plays a more complex role in metabolism [25].

In conclusion, at least in the mouse model described here gluconeogenesis is only weakly regulated by *Pck1* and *G6pc* transcription or PEPCK activity. HFD feeding for 12 weeks might be too short to evoke differences in PEPCK and feeding a diet with high fat content seems to primarily alter fatty acid metabolism instead of glucose metabolism.

6.5 Conclusion

In the scope of this thesis it was investigated in diet-induced obese mice if changes of DNA methylation are cause or consequence of insulin resistance. It was shown that insulin resistance developed in distinct phases, with an early adaptational phase after one week of HFD feeding, followed by a metabolic switch resulting in the development of whole-body insulin resistance and fatty liver after five weeks. This is accompanied by extensive transcriptomic changes of metabolic pathways, especially the fatty acid metabolism. After 12 weeks of feeding, insulin resistance is associated with extensive epigenetic remodeling. Impairment of hepatic insulin sensitivity is accompanied by alterations of DNA methylation at two CpG sites within *Fgf21* which could be caused by PPARα-dependent DNA hypomethylation. Thus, alterations of hepatic DNA methylation likely precede the development of whole-body glucose intolerance and could be causal for the development of insulin resistance. Furthermore, the results presented here demonstrate that DNA methylation is strongly location-dependent and DNA methylation within gene bodies is important for the regulation of gene expression.

The altered DNA methylation patterns are acquired during adulthood, demonstrating that DNA methylation is dynamic in differentiated cells and not only during fetal development. Therefore, the here observed changes of DNA methylation are independent of epigenetic inheritance. This suggests that individuals can influence their own DNA methylation. For the human type 2 diabetes pathogenesis our data implicate that detrimental DNA methylation changes could be prevented by a healthy diet, emphasizing that lifestyle modifications are of special importance to slow down the type 2 diabetes pandemic.

In the future, mechanistic experiments will be necessary to examine the functional implications of altered DNA methylation. Whole-genome bisulfite sequencing and gene expression microarrays represent a great resource for future projects. For instance genes in particular overlaps of the venn diagram could be interesting targets to investigate and identify novel diabetes candidate genes. These genes can be further analyzed for example in knockout mice. This would help to narrow down disease-causing genes for the development of new drugs for diabetes therapy. Demethylating agents, such as the DNMT inhibitors 5-azacytidine and 5-aza-2'-deoxycytidine, are already used in the clinics for treatment of hematological tumors [77]. With the advances in CRISPR technology, for example the fusion of TET1 or DNMT3 to an inactive Cas9, a targeted DNA methylation editing is within reach and could be used not only for cancer but also metabolic diseases [140].

"*You will adapt.*"
The Borg

7

Supplement

A Diet composition

The mice of the longitudinal study were fed with the high fat diet D12492 (Research Diets) or the control diet #1310 (Altromin). The targeted approach was performed in mice fed for 20 weeks with the high fat-high sucrose diet D12331 (Research Diets) or the chow control diet LM-485 (Harlan Teklad).

Table 7.1: Nutrient composition of the diets. Diet composition according to manufacturer's information as well as Omar et al. [177] and Yang et al. [249].

Component	chow #1310	HFD D12492	chow LM-485	HFHS D12331
Total carbohydrates	59.0 kcal%	20 kcal%	58 kcal%	25 kcal%
- Sucrose		6.7 kcal%		12.6 kcal%
Total fat	14.0 kcal%	60 kcal%	17 kcal%	58 kcal%
- Saturated		19.2 kcal%	0.8 gram%	54.1 kcal%
- Monounsaturated		21.5 kcal%	1.3 gram%	1.4 kcal%
- Polyunsaturated		19.2 kcal%	2.9 gram%	2.5 kcal%
- Short-chain		0.0 kcal%		0.0 kcal%
- Medium-chain		0.1 kcal%		57.5 kcal%
- Long-chain		100.0 kcal%		42 kcal%
Protein	27.0 kcal%	20 kcal%	25 kcal%	17 kcal%

Table 7.2: Carbohydrate and fatty acid composition of the experimental diets. Carbohydrate and fatty acid composition according to manufacturer's information as well as Omar et al. [177] and Yang et al. [249].

Component	chow #1310	HFD D12492	chow LM-485	HFHS D12331
Sucrose	Disaccarides:	28 gram%		51 gram%
Corn Starch	5.4 gram%	0.0 gram%		0.0 gram%
Maltodextrin 10	Polysaccharides:	51 gram%	16.2 gram%	49 gram%
Cellulose	35.0 gram%	21 gram%		0.0 gram%
Caproic acid (C6)				0.6 gram%
Cyprylic acid (C8)				7.2 gram%
Capric acid (C10)				5.5 gram%
Lauric acid (C12)		0.1 gram%		44.3 gram%
Myristic acid (C14)		1.1 gram%		16.8 gram%
C15		0.1 gram%		0.0 gram%
Palmitic acid (C16)	0.5 gram%	19.6 gram%	0.6 gram%	8.8 gram%
Palmitoleic acid (C16:1)		1.3 gram%		0.0 gram%
C17		0.4 gram%		0.0 gram%
Stearic acid (C18)	0.2 gram%	10.6 gram%	0.2 gram%	10.1 gram%
Oleic acid (C18:1)	0.9 gram%	34.1 gram%	1.3 gram%	2.4 gram%
Linoleic ω-6 acid (C18:2)	2.2 gram%	28.8 gram%	2.6 gram%	3.8 gram%
Linolenic ω-3 acid (C18:3)	0.3 gram%	2.0 gram%	0.3 gram%	0.6 gram%
Arachidic acid (C20)	14.8 gram%	0.2 gram%		0.0 gram%
C20:1, C20:2, C20:3	18.5 gram%	1.5 gram%		0.0 gram%
Arachidonic acid (C20:4)		0.3 gram%		0.0 gram%

B Plasma non-esterified fatty acids

Plasma non-esterified fatty acids (NEFA) were determined with the *NEFA-HR(2)* assay and the NEFA Standard Solution by Fujifilm Wako Diagnostics (Mountain View, CA, USA). 'Reagent A' and 'Reagent B' were reconstituted according manufacturer's instructions. The standard was prepared by 1:2 serial dilution of the 1 mM standard solution with ultra-pure water to obtain a standard series with 1 mM, 0.5 mM, 0.25 mM, 0.125 mM, and 0.0625 mM. The assay was performed in a 96 well plate in duplicates and 4 µl of each sample, the standard, and ultra-pure water was used. The assay was started by adding 170 µl 'Reagent A' and incubating the reaction mix for 3 minutes at 37°C. 'Reagent A' contained acyl-CoA synthetase, CoA, ATP, 4-aminoantipyrine, and ascorbate oxidase. The acyl-CoA synthetase converts the non-esterified fatty acids by using ATP and CoA to acyl-COA, generating AMP and PPi as side products. After incubation, the plate was measured at 546 nm, with 660 nm as sub-wavelength. This measurement served as blank for the analysis. Subsequently, 85 µl 'Reagent B' were added and the plate was incubated for 5 minutes at 37°C. 'Reagent B' contained acyl-CoA oxidase, peroxidase, and 3-Methyl-N-Ethyl-N-(β-Hydroxyethyl)-Anilin (MEHA). The acyl-CoA oxidase

oxidizes the acyl-CoA to 2,3-trans-enoyl-CoA and H_2O_2. The hydrogen peroxide enables the oxidative condensation of MEHA with 4-aminoantipyrine by the peroxidase to a purple-colored product which is measured at 546 nm. To perform the background correction of the absorbance, the first measurement was corrected for the volume difference by multiplication with factor F: F=(Sample volume + 'Reagent A')/(sample volume + 'Reagent A' + 'Reagent B'). This corrected background-absorbance was subtracted from the absorbance of the second measurement. To calculate the NEFA concentration a linear regression of the standard was performed.

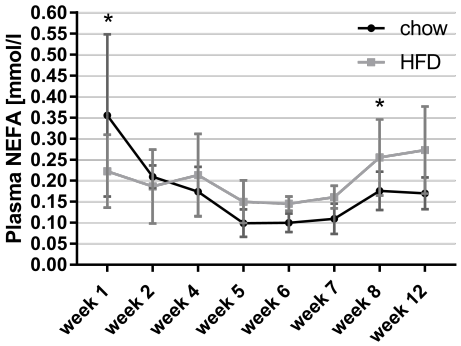

Figure 7.1: Plasma non-esterified fatty acids were slightly increased in diet-induced obese mice after week 4. The NEFA concentration in the HFD groups tend to be slightly higher compared to the controls after week 4. $p_{week}<0.0001$; $p_{diet}=0.0428$; $p_{interaction}=0.0055$; $p_{week\ 1}=0.0424$; $p_{week\ 8}=0.0214$Two-way ANOVA followed by Holm-Sidak correction; n=4-15/group.

C Principle component analysis

Principal component	**Individual variance** [%]	**Total variance** [%]
1	14.6766	14.6766
2	11.3188	25.9954
3	6.7859	32.7813
4	5.6514	38.4327
5	4.9359	43.3686
6	4.6616	48.0302
7	4.2873	52.3175
8	4.1304	56.4479
9	3.4753	59.9232
10	3.1463	63.0695
11	2.8608	65.9303
12	2.5773	68.5076
13	2.5084	71.016
14	2.3132	73.3292
15	2.2017	75.5309
16	2.1214	77.6523
17	2.0965	79.7488
18	1.9926	81.7414
19	1.8957	83.6371
20	1.8043	85.4414
21	1.7882	87.2296
22	1.753	88.9826
23	1.7013	90.6839
24	1.6954	92.3793
25	1.6142	93.9935
26	1.5518	95.5453
27	1.5389	97.0842
28	1.4752	98.5594
29	1.4405	99.9999

Code to generate the scree plot

Id: scree.m,v 1.7 2006/12/26 22:53:29 Mike Exp)

```
function [] = Screeplot(latent,alpha)
newplot
p = 100*latent/sum(latent);
pe = cumsum(p);
if ( nargin < 2 )
alpha = 0.05;
end
i = find(pe > 100*(1 - alpha),1);
```

```
if ( isempty(i) ), i = length(latent); end
if nargout > 0
y = [pe(1:i) p(1:i)];
end
bar(1:i, p(1:i), 'FaceColor', [0.3010 0.7450 0.9330]);
hold on
line(1:i, pe(1:i),'marker', 'o', 'color', [0.6350 0.0780 0.1840], 'markerfacecolor'
hold on
h = refline( 0, 100*alpha);
hold on
set(h, 'linestyle', '-.', 'color', 'k');
ax.YGrid = 'on';
xticks(0:2:29)
yticks(0:5:100)
xlabel('number of principal components' );
ylabel('percent of explained variance' );
legend( {'cumulative', 'individual'}, 'location', 'northwest' );
end
```

D Determination of optimal cluster number

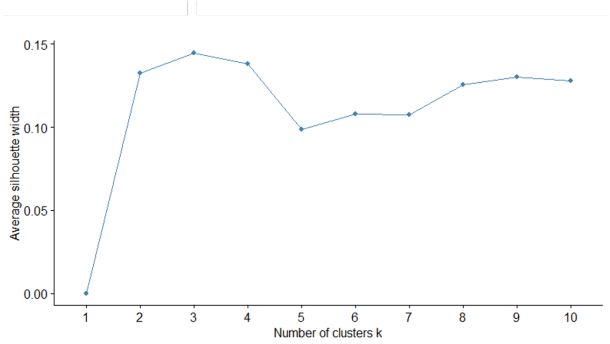

Figure 7.2: Silhouette plot to determine optimal cluster number.

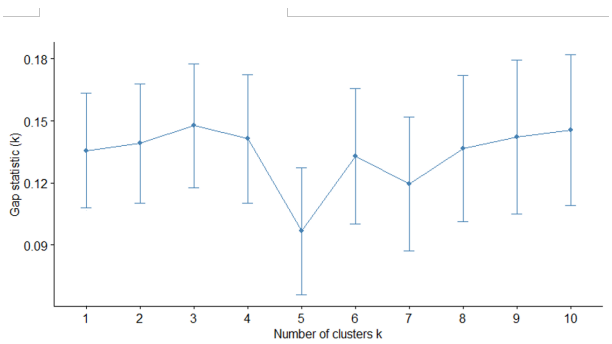

Figure 7.3: Plot of the gap statistic to determine optimal cluster number.

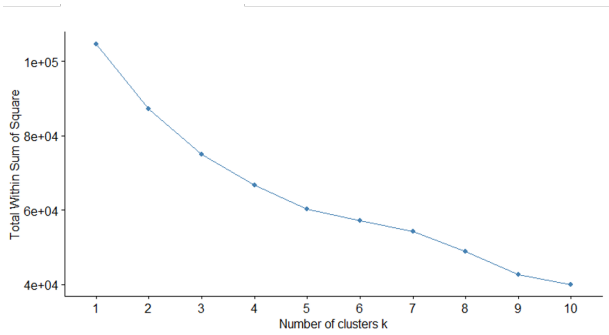

Figure 7.4: Plot of within sum of squares to determine optimal cluster number.

E p values of top ten significantly enriched pathways

Week 1: HFD vs. chow

Pathway	Fold enrichment	Bonferroni p value
Chemical carcinogenesis	18.32	1.65E-41
Retinol metabolism	14.53	4.75E-27
Drug metabolism - cytochrome P450	16.03	6.67E-23
Steroid hormone biosynthesis	12.61	1.33E-20
Metabolism of xenobiotics by cytochrome P450	15.31	2.01E-20
Metabolic pathways	2.79	2.33E-20
Glutathione metabolism	12.83	1.80E-12
Linoleic acid metabolism	12.54	1.15E-10
Arachidonic acid metabolism	7.49	9.08E-08
Fatty acid metabolism	9.99	5.54E-07

Week 12: HFD vs. chow

Pathway	Fold enrichment	Bonferroni p value
Retinol metabolism	9.52	2.26E-16
Metabolic pathways	2.41	2.86E-16
Fatty acid degradation	12.17	6.52E-13
PPAR signaling pathway	8.63	6.50E-12
Chemical carcinogenesis	7.85	1.28E-11
Steroid hormone biosynthesis	7.57	4.17E-10
Peroxisome	6.05	9.06E-06
Linoleic acid metabolism	7.53	7.72E-05
Arachidonic acid metabolism	5.29	1.56E-04
Valine, leucine, and isoleucine degradation	6.28	0.0016846

HFD: week12 vs. week 1

Pathway	Fold enrichment	Bonferroni p value
Metabolic pathways	2.30	3.18E-27
Fatty acid metabolism	8.43	2.78E-14
PPAR signaling pathway	6.45	5.55E-14
Fatty acid degradation	8.42	8.33E-14
Chemical carcinogenesis	5.79	4.16E-13
Biosynthesis of antibiotics	3.78	7.22E-13
Peroxisome	5.80	1.19E-11
Drug metabolism - cytochrome P450	6.51	1.87E-11
Retinol metabolism	5.22	6.00E-10
Metabolism of xenobiotics by cytochrome P450	5.91	6.89E-09

F Correlation of *Fgf21* gene expression with DNA methylation

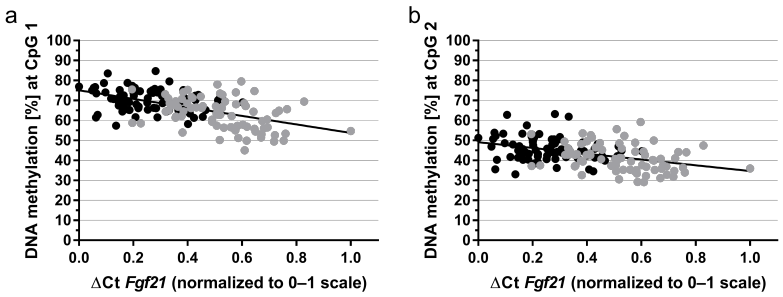

Figure 7.5: *Fgf21* gene expression correlates strongly with DNA methylation. ΔCt values of *Fgf21* were correlated with the DNA methylation at (a) CpG site 1 (r=0.5457, p<0.0001) and (b) CpG site 2 (r=0.4231, p<0.0001) by Pearson correlation. For visualization the ΔCt values were normalized to a 0-1 scale by applying the formula $1-((x_i - min(x))/(max(x) - min(x)))$, therefore, ΔCt values near 0 correspond to low gene expression and ΔCt values near 1 correspond to high gene expression. Chow mice are shown as black dots, HFD mice as gray dots.

G Gene expression microarray results for *Sik3*, *Sgms2*, and *Galnt2*

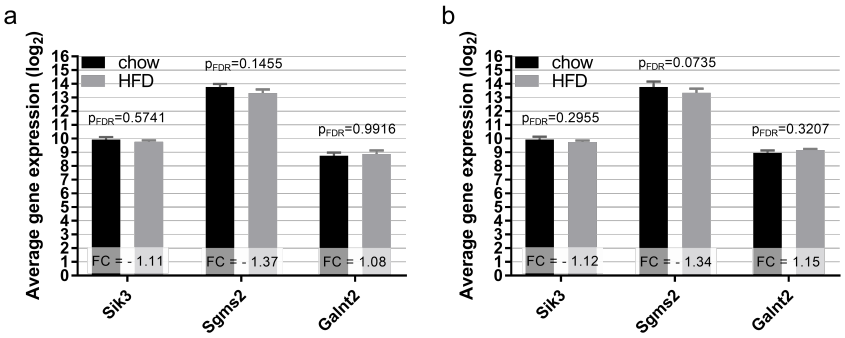

Figure 7.6: Gene expression microarray results for *Sik3*, *Sgms2*, and *Galnt2* at (a) week 1 and (b) week 12. The results are depicted as average $\log_2$ value±SD. The FDR p value (p_{FDR}) as well as the fold change (FC) is shown for each gene. n_{chow}=7, n_{HFD}=8.

H Gene expression microarray results for FGF receptors and *Dusp6*

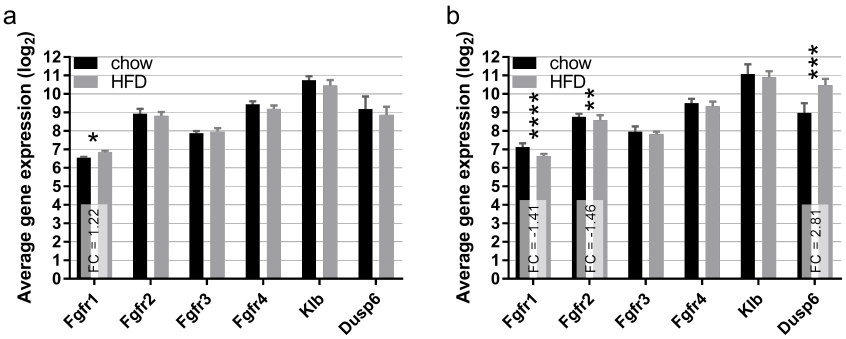

Figure 7.7: Gene expression microarray results for the FGF receptors and *Dusp6* at (a) week 1 and (b) week 12. The results are depicted as average $\log_2$ value±SD. The fold change (FC) and the significance (according to FDR p value) is shown for genes, which have an FDR p value smaller than 0.05. (However, differentially expressed genes are defined as having a fold change greater 1.5 or smaller -1.5 and a significant FDR p value.) n_{chow}=7, n_{HFD}=8.

I Gene expression microarray results for *Ppara*, *Cyp4a10*, and *Cyp4a14*

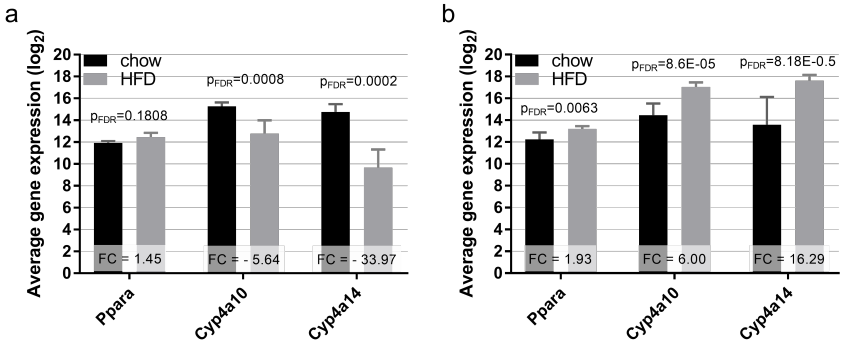

Figure 7.8: Gene expression microarray results for *Ppara*, *Cyp4a10*, and *Cyp4a14* at (a) week 1 and (b) week 12. The results are depicted as average $\log_2$ value±SD. The FDR p value (p_{FDR}) as well as the fold change (FC) is shown for each gene. n_{chow}=7, n_{HFD}=8.

J Gene expression microarray results for genes of β-oxidation and *de novo* lipogenesis

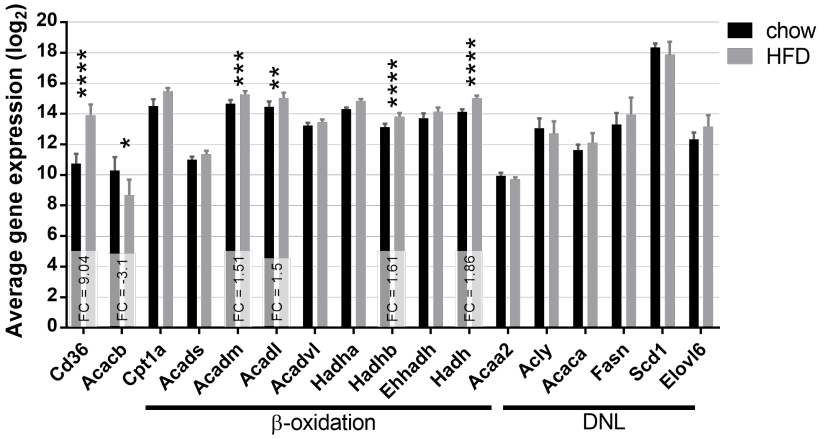

Figure 7.9: Gene expression microarray results for genes of β-oxidation and *de novo* lipogenesis. The gene expression is shown as average $\log_2$ value±SD. Differentially expressed genes are labeled with asterisks according to their FDR p value and the corresponding fold change (FC). n_{chow}=7, n_{HFD}=8.

K Top 50 differentially expressed, coding genes

To rank the top 50 differentially expressed genes the results of the *Transcriptome Analysis Console* were used and the genes were sorted according FDR p-value (FDR p-val).

HFD: week 12 vs. week 1

Top 50 differentially expressed genes according FDR p value

wk12 $\log_2$	wk1 $\log_2$	FC	FDR p-val	Gene symbol	Public gene ID
9.19	5.90	9.79	5.23E-17	Ar	NM_013476
11.57	7.43	17.69	4.38E-13	Acss3	NM_001142804; NM_198636
5.00	6.39	-2.63	4.43E-13	Igf2bp3	NM_023670
13.66	10.89	6.82	6.73E-13	Pctp	NM_008796
9.89	7.20	6.47	1.39E-11	Fitm1	NM_026808
15.71	12.61	8.55	1.39E-11	Aldh3a2	NM_007437
15.35	5.54	898.56	2.88E-11	Cyp2b9	NM_010000
8.08	6.58	2.81	3.11E-11	Gpc1	NM_016696
7.58	5.17	5.31	3.11E-11	Themis	NM_178666
10.67	7.86	7.02	3.85E-11	Pparg	NM_001127330; NM_011146
8.30	6.53	3.40	4.44E-11	Stap1	NM_019992
13.92	10.57	10.18	4.44E-11	Cd36	NM_001159555; NM_001159556; NM_001159557; NM_001159558; NM_007643
6.38	5.01	2.57	4.72E-11	Cdh18	NM_001081299
7.78	5.23	5.88	5.41E-11	C730002L08Rik	NR_045778
5.67	10.43	-27.18	7.32E-11	Adgrf1	NM_133776
12.32	11.08	2.37	8.50E-11	4931406C07Rik	NM_001199484; NM_001199485; NM_133732
13.39	11.73	3.16	8.50E-11	Entpd5	NM_001026214; NM_001286049; NM_001286058; NM_007647
15.03	8.21	113.31	8.50E-11	Mfsd2a	NM_029662
7.12	5.97	2.21	1.49E-10	Agpat9	NM_172715
10.53	7.64	7.44	1.66E-10	Lgals1	NM_008495

chow: week 12 vs. week 1

Top 50 differentially expressed genes according FDR p value

wk12 log_2	wk1 log_2	FC	FDR p-val	Gene symbol	Public gene ID
8.43	6.11	5.01	6.11E-12	Ar	NM_013476
4.97	6.25	-2.43	1.61E-11	Igf2bp3	NM_023670
5.85	4.81	2.06	1.57E-07	Grm8; Mir592	NM_008174
7.91	6.53	2.60	2.96E-07	Unc13b	NM_001081413; NM_021468
7.49	8.56	-2.10	1.78E-06	Lpl	NM_008509
7.04	9.38	-5.08	4.43E-06	Ndrg1	NM_008681
8.43	7.08	2.56	1.13E-05	Gm15433	XM_003084455.1
6.84	5.96	1.84	1.13E-05	Jph1	NM_020604
5.12	5.85	-1.67	2.66E-05	4930452B06Rik	NM_028934
6.74	5.98	1.70	2.69E-05	Snhg11	NM_175692
11.09	12.12	-2.04	4.94E-05	Sparc	NM_009242
8.11	7.28	1.79	4.94E-05	Acpp	NM_019807; NM_207668
8.21	6.48	3.31	5.16E-05	Ncam2	NM_001113208; NM_010954
7.88	7.15	1.65	5.35E-05	Gm7592; Csprs	ENSMUST00000159601
7.56	6.28	2.42	5.35E-05	Gm21760	ENSMUST00000179811
7.20	6.31	1.85	5.35E-05	Tiam2	NM_001122998; NM_001286757; NM_001286758; NM_011878
16.36	17.19	-1.78	5.35E-05	Cyp2c68	NM_001039555
7.79	6.61	2.27	5.83E-05	Gm29073	ENSMUST00000177713
14.97	15.86	-1.86	6.03E-05	Cyp2c69	NM_001104525
8.16	7.43	1.67	6.05E-05	Gm7609	NM_001081746

Week 1: chow vs. HFD

Top 50 differentially expressed genes according FDR p value

HFD log_2	chow log_2	FC	FDR p-val	Gene symbol	Public gene ID
7.92	10.12	-4.59	3.18E-10	Cyp3a16	NM_007820
10.75	13.47	-6.60	3.04E-09	Cyp3a41b; Cyp3a41a	NM_001105159; NM_017396_2
10.88	13.56	-6.43	3.37E-09	Cyp3a41a; Cyp3a41b	NM_017396
10.02	12.76	-6.69	4.88E-09	Cyp3a44	NM_177380
15.08	18.15	-8.40	4.88E-09	Cyp3a11	NM_007818
6.98	10.20	-9.34	8.26E-09	Cyp2c55	NM_028089
13.17	15.23	-4.17	1.04E-08	Ces2a	NM_001190330; NM_133960

7.43	10.20	-6.84	1.15E-08	Acss3	NM_001142804; NM_198636
11.55	14.38	-7.11	5.05E-08	Me1	NM_001198933; NM_008615
15.40	17.04	-3.12	7.63E-08	Gstm1	NM_010358
10.41	12.21	-3.47	9.99E-08	Gstm4	NM_001160411; NM_026764
8.66	10.27	-3.06	1.01E-07	Gstm6	NM_008184
7.39	9.23	-3.58	1.03E-07	Pik3c2g	NM_011084; NM_207683
6.44	8.75	-4.96	1.03E-07	Gstt3	NM_133994
10.64	12.25	-3.05	2.07E-07	Ethe1	NM_023154
6.97	10.22	-9.48	3.69E-07	9130409I23Rik	NM_001033819
10.97	13.06	-4.25	4.37E-07	Abcc3	NM_029600
5.13	6.40	-2.40	6.66E-07	Gm12499	ENSMUST00000121961
13.98	16.34	-5.11	9.56E-07	Cyp3a59	NM_001105160
10.72	12.95	-4.69	9.77E-07	Gstm2	NM_008183

Week 12: chow vs. HFD

Top 50 differentially expressed genes according FDR p value

HFD $\log_2$	chow $\log_2$	FC	FDR p-val	Gene symbol	Public gene ID
8.30	5.82	5.59	6.85E-14	Stap1	NM_019992
12.65	15.19	-5.81	8.47E-11	Ces2a	NM_001190330; NM_133960
15.35	5.34	1033.7	8.47E-11	Cyp2b9	NM_010000
14.87	12.8	4.17	8.47E-11	Fabp2	NM_007980
8.08	6.59	2.81	9.78E-11	Gpc1	NM_016696
7.12	5.97	2.21	1.03E-10	Agpat9	NM_172715
13.92	10.74	9.04	1.03E-10	Cd36	NM_001159555; NM_001159556; NM_001159557; NM_001159558; NM_007643
5.35	6.95	-3.03	1.92E-10	Slc13a2	NM_022411
13.45	8.92	23.04	5.49E-10	Vnn1	NM_011704
7.58	5.35	4.68	6.64E-10	Themis	NM_178666
5.67	10.24	-23.77	6.79E-10	Adgrf1	NM_133776
15.70	17.60	-3.71	6.79E-10	Gstp1	NM_013541
14.30	16.20	-3.75	6.79E-10	Gstp2	NM_181796
7.12	8.54	-2.69	8.51E-10	Itih5	NM_172471
10.28	11.99	-3.26	2.60E-09	Ccl9	NM_011338
11.74	10.52	2.34	3.80E-09	Lect2	NM_010702
8.40	9.95	-2.92	5.00E-09	Cyp3a16	NM_007820
5.91	5.02	1.85	5.00E-09	Mogat1	NM_026713
11.29	10.50	1.73	7.86E-09	Ech1	NM_016772
9.64	11.41	-3.41	1.04E-08	Slco2a1	NM_033314

References

[1] Lutfi Abu-Elheiga, Martin M. Matzuk, Khaled A. H. Abo-Hashema, and Salih J. Wakil. **Continuous Fatty Acid Oxidation and Reduced Fat Storage in Mice Lacking Acetyl-CoA Carboxylase 2**. *Science*, **291**(5513):2613–2616, March 2001.

[2] Lutfi Abu-Elheiga, Wonkeun Oh, Parichhher Kordari, and Salih J. Wakil. **Acetyl-CoA Carboxylase 2 Mutant Mice Are Protected against Obesity and Diabetes Induced by High-Fat/High-Carbohydrate Diets**. *Proceedings of the National Academy of Sciences of the United States of America*, **100**(18):10207–10212, September 2003.

[3] María M. Adeva-Andany, Noemi Pérez-Felpete, Carlos Fernández-Fernández, Cristóbal Donapetry-García, and Cristina Pazos-García. **Liver Glucose Metabolism in Humans**. *Bioscience Reports*, **36**(6):e00416, November 2016.

[4] Swarnaseetha Adusumalli, Mohd Feroz Mohd Omar, Richie Soong, and Touati Benoukraf. **Methodological Aspects of Whole-Genome Bisulfite Sequencing Analysis**. *Briefings in Bioinformatics*, **16**(3):369–379, May 2015.

[5] Ali Agah, Mariam Aghajan, Foad Mashayekhi, Sasan Amini, Ronald W. Davis, James D. Plummer, Mostafa Ronaghi, and Peter B. Griffin. **A Multi-Enzyme Model for Pyrosequencing**. *Nucleic Acids Research*, **32**(21):e166, December 2004.

[6] Maryam Ahmadian, Jae Myoung Suh, Nasun Hah, Christopher Liddle, Annette R. Atkins, Michael Downes, and Ronald M. Evans. **PPARγ Signaling and Metabolism: The Good, the Bad and the Future**. *Nature Medicine*, **19**(5):557–566, May 2013.

[7] Peter Almgren, Maarit Lehtovirta, Boris Isomaa, Leena Sarelin, Marja R. Taskinen, Valeria Lyssenko, Tiinamaija Tuomi, Leif Groop, and Botnia Study Group. **Heritability and Familiality of Type 2 Diabetes and Related Quantitative Traits in the Botnia Study**. *Diabetologia*, **54**(11):2811–9, November 2011.

[8] Michele Alves-Bezerra and David E. Cohen. **Triglyceride Metabolism in the Liver**. *Comprehensive Physiology*, **8**(1):1–8, December 2017.

[9] Fatima Ameer, Lisa Scandiuzzi, Shahida Hasnain, Hubert Kalbacher, and Nousheen Zaidi. **De Novo Lipogenesis in Health and Disease**. *Metabolism*, **63**(7):895–902, July 2014.

[10] Claus Lindbjerg Andersen, Jens Ledet Jensen, and Torben Falck Ørntoft. **Normalization of Real-Time Quantitative Reverse Transcription-PCR Data: A Model-Based Variance Estimation Approach to Identify Genes Suited for Normalization, Applied to Bladder and Colon Cancer Data Sets**. *Cancer Research*, **64**(15):5245–5250, August 2004.

[11] Manit Arya, Iqbal S. Shergill, Magali Williamson, Lyndon Gommersall, Neehar Arya, and Hitendra R. H. Patel. **Basic Principles of Real-Time Quantitative PCR**. *Expert Review of Molecular Diagnostics*, **5**(2):209–219, March 2005.

[12] Alan D. Attie, Gary A. Churchill, and Joseph H. Nadeau. **How Mice Are Indispensable for Understanding Obesity and Diabetes Genetics**. *Current opinion in endocrinology, diabetes, and obesity*, **24**(2):83–91, April 2017.

[13] Francisco Barajas-Olmos, Federico Centeno-Cruz, Carlos Zerrweck, Iván Imaz-Rosshandler, Angélica Martínez-Hernández, Emilio J. Cordova, Claudia Rangel-Escareño, Faustino Gálvez, Armando Castillo, Hernán Maydón, Francisco Campos, Diana Gabriela Maldonado-Pintado, and Lorena Orozco. **Altered DNA Methylation in Liver and Adipose Tissues Derived from Individuals with Obesity and Type 2 Diabetes**. *BMC Medical Genetics*, **19**(1):28, February 2018.

[14] Rita Basu, Visvanathan Chandramouli, Betty Dicke, Bernard Landau, and Robert Rizza. **Obesity and Type 2 Diabetes Impair Insulin-Induced Suppression of Glycogenolysis as Well as Gluconeogenesis**. *Diabetes*, **54**(7):1942–1948, July 2005.

[15] Anna Bauer-Mehren, Michael Rautschka, Ferran Sanz, and Laura I. Furlong. **DisGeNET: A Cytoscape Plugin to Visualize, Integrate, Search and Analyze Gene–Disease Networks**. *Bioinformatics*, **26**(22):2924–2926, November 2010.

[16] Roberto B. Bazotte, Lorena G. Silva, and Fabiana P. M. Schiavon. **Insulin Resistance in the Liver: Deficiency or Excess of Insulin?** *Cell Cycle*, **13**(16):2494–2500, October 2014.

[17] Eric D. Berglund, Candice Y. Li, Holly A. Bina, Sara E. Lynes, M. Dodson Michael, Armen B. Shanafelt, Alexei Kharitonenkov, and David H. Wasserman. **Fibroblast Growth Factor 21 Controls Glycemia via Regulation of Hepatic Glucose Flux and Insulin Sensitivity**. *Endocrinology*, **150**(9):4084–93, September 2009.

[18] Florian Blaschke, Yasunori Takata, Evren Caglayan, Ronald E. Law, and Willa A. Hsueh. **Obesity, Peroxisome Proliferator-Activated Receptor, and Atherosclerosis in Type 2 Diabetes**. *Arteriosclerosis, Thrombosis, and Vascular Biology*, **26**(1):28–40, January 2006.

[19] Guenther Boden, Xinhua Chen, and T. Peter Stein. **Gluconeogenesis in Moderately and Severely Hyperglycemic Patients with Type 2 Diabetes Mellitus**. *American Journal of Physiology-Endocrinology and Metabolism*, **280**(1):E23–E30, January 2001.

[20] Nadia Bougarne, Basiel Weyers, Sofie J. Desmet, Julie Deckers, David W. Ray, Bart Staels, and Karolien De Bosscher. **Molecular Actions of PPARα in Lipid Metabolism and Inflammation**. *Endocrine Reviews*, **39**(5):760–802, October 2018.

[21] Fabienne Brenet, Michelle Moh, Patricia Funk, Erika Feierstein, Agnes J. Viale, Nicholas D. Socci, and Joseph M. Scandura. **DNA Methylation of the First Exon Is Tightly Linked to Transcriptional Silencing**. *PLoS ONE*, **6**(1):e14524, January 2011.

[22] Alessandra Breschi, Thomas R. Gingeras, and Roderic Guigó. **Comparative Transcriptomics in Human and Mouse**. *Nature reviews. Genetics*, **18**(7):425–440, July 2017.

[23] Sandrine Brognaux, Thomas Drugman, and Marco Saerens. **Synthesizing Sports Commentaries: One or Several Emphatic Stresses?** *Proceedings of the International Conference on Speech Prosody*, pages 270–274, January 2014.

[24] Michael S. Brown and Joseph L. Goldstein. **Selective versus Total Insulin Resistance: A Pathogenic Paradox**. *Cell Metabolism*, **7**(2):95–96, February 2008.

[25] Shawn C. Burgess, Tian Teng He, Zheng Yan, Jill Lindner, A. Dean Sherry, Craig R. Malloy, Jeffrey D. Browning, and Mark A. Magnuson. **Cytosolic Phosphoenolpyruvate Carboxykinase Does Not Solely Control the Rate of Hepatic Gluconeogenesis in the Intact Mouse Liver**. *Cell metabolism*, **5**(4):313–320, April 2007.

[26] João Paulo G. Camporez, Mohamed Asrih, Dongyan Zhang, Mario Kahn, Varman T. Samuel, Michael J. Jurczak, and François R. Jornayvaz. **Hepatic Insulin Resistance and Increased Hepatic Glucose Production in Mice Lacking Fgf21**. *Journal of Endocrinology*, **226**(3):207–217, September 2015.

[27] Doralicia Casares, Pablo V. Escribá, and Catalina Ana Rosselló. **Membrane Lipid Composition: Effect on Membrane and Organelle Structure, Function and Compartmentalization and Therapeutic Avenues**. *International Journal of Molecular Sciences*, **20**(9):2167, May 2019.

[28] Adriana Florinela Cătoi, Alina Pârvu, Adriana Mureşan, and Luca Busetto. **Metabolic Mechanisms in Obesity and Type 2 Diabetes: Insights from Bariatric/Metabolic Surgery**. *Obesity Facts*, **8**(6):350–363, December 2015.

[29] Raymond G. Cavalcante and Maureen A. Sartor. **Annotatr: Genomic Regions in Context**. *Bioinformatics*, **33**(15):2381–2383, August 2017.

[30] Matthew C. Cave, Heather B. Clair, Josiah E. Hardesty, K. Cameron Falkner, Wenke Feng, Barbara J. Clark, Jennifer Sidey, Hongxue Shi, Bashar A. Aqel, Craig J. McClain, and Russell A. Prough. **Nuclear Receptors and Nonalcoholic Fatty Liver Disease**. *Biochimica et biophysica acta*, **1859**(9):1083–1099, September 2016.

[31] Manu V. Chakravarthy, Irfan J. Lodhi, Li Yin, Raghu R. V. Malapaka, H. Eric Xu, John Turk, and Clay F. Semenkovich. **Identification of a Physiologically Relevant Endogenous Ligand for PPARα in Liver**. *Cell*, **138**(3):476–488, August 2009.

[32] Manu V. Chakravarthy, Zhijun Pan, Yimin Zhu, Karen Tordjman, Jochen G. Schneider, Trey Coleman, John Turk, and Clay F. Semenkovich. **"New" Hepatic Fat Activates PPARα to Maintain Glucose, Lipid, and Cholesterol Homeostasis**. *Cell Metabolism*, **1**(5):309–322, May 2005.

[33] JOHN K. C. CHAN. **The Wonderful Colors of the Hematoxylin–Eosin Stain in Diagnostic Surgical Pathology**. *International Journal of Surgical Pathology*, **22**(1):12–32, February 2014.

[34] ALICE CHAPLIN, ANDREU PALOU, AND FRANCISCA SERRA. **Methylation Analysis in Fatty-Acid-Related Genes Reveals Their Plasticity Associated with Conjugated Linoleic Acid and Calcium Supplementation in Adult Mice**. *European Journal of Nutrition*, **56**(2):879–891, March 2017.

[35] EDGAR D. CHARLES, BRENT A. NEUSCHWANDER-TETRI, JUAN PABLO FRIAS, SUDEEP KUNDU, YI LUO, GIRIDHAR S. TIRUCHERAI, AND ROSE CHRISTIAN. **Pegbelfermin (BMS-986036), PEGylated FGF21, in Patients with Obesity and Type 2 Diabetes: Results from a Randomized Phase 2 Study**. *Obesity*, **27**(1):41–49, January 2019.

[36] HANBO CHEN AND PAUL C. BOUTROS. **VennDiagram: A Package for the Generation of Highly-Customizable Venn and Euler Diagrams in R**. *BMC Bioinformatics*, **12**(1):35, January 2011.

[37] JOHN Y. L. CHIANG AND JESSICA M. FERRELL. **Bile Acid Metabolism in Liver Pathobiology**. *Gene Expression*, **18**(2):71–87, May 2018.

[38] N. H. CHO, J. E. SHAW, S. KARURANGA, Y. HUANG, J. D. DA ROCHA FERNANDES, A. W. OHLROGGE, AND B. MALANDA. **IDF Diabetes Atlas: Global Estimates of Diabetes Prevalence for 2017 and Projections for 2045**. *Diabetes Research and Clinical Practice*, **138**:271–281, April 2018.

[39] YONG SOON CHO, JAE IL LEE, DONGKYU SHIN, HYUN TAE KIM, HA YUN JUNG, TAE GYU LEE, LIN-WOO KANG, YEH-JIN AHN, HYUN-SOO CHO, AND YONG-SEOK HEO. **Molecular Mechanism for the Regulation of Human ACC2 through Phosphorylation by AMPK**. *Biochemical and Biophysical Research Communications*, **391**(1):187–192, January 2010.

[40] STEPHANIE T. CHUNG, SHAJI K. CHACKO, AGNETA L. SUNEHAG, AND MOREY W. HAYMOND. **Measurements of Gluconeogenesis and Glycogenolysis: A Methodological Review**. *Diabetes*, **64**(12):3996–4010, December 2015.

[41] CHRISTINE CLARK, PRIIT PALTA, CHRISTOPHER J. JOYCE, CAROL SCOTT, ELIN GRUNDBERG, PANOS DELOUKAS, AARNO PALOTIE, AND ALISON J. COFFEY. **A Comparison of the Whole Genome Approach of MeDIP-Seq to the Targeted Approach of the Infinium HumanMethylation450 BeadChip for Methylome Profiling**. *PLoS ONE,* **7**(11):e50233, November 2012.

[42] ALEX D. COLELLA, NUSHA CHEGENII, MELINDA N. TEA, IAN L. GIBBINS, KERYN A. WILLIAMS, AND TIM K. CHATAWAY. **Comparison of Stain-Free Gels with Traditional Immunoblot Loading Control Methodology**. *Analytical Biochemistry*, **430**(2):108–110, November 2012.

[43] FLORENCE K. CRARY-DOOLEY, MITCHELL E. TAM, KEITH W. DUNAWAY, IRVA HERTZ-PICCIOTTO, REBECCA J. SCHMIDT, AND JANINE M. LASALLE. **A Comparison of Existing Global DNA Methylation Assays to Low-Coverage Whole-Genome Bisulfite Sequencing for Epidemiological Studies**. *Epigenetics*, **12**(3):206–214, January 2017.

[44] KRISTA S. CRIDER, THOMAS P. YANG, ROBERT J BERRY, AND LYNN B. BAILEY. **Folate and DNA Methylation: A Review of Molecular Mechanisms and the Evidence for Folate's Role**. *Advances in Nutrition*, **3**(1):21–38, January 2012.

[45] MICHAEL P. CZECH. **Insulin Action and Resistance in Obesity and Type 2 Diabetes**. *Nature medicine*, **23**(7):804–814, July 2017.

[46] CAJSA DAVEGÅRDH, SONIA GARCÍA-CALZÓN, KARL BACOS, AND CHARLOTTE LING. **DNA Methylation in the Pathogenesis of Type 2 Diabetes in Humans**. *Molecular Metabolism*, **14**:12–25, February 2018.

[47] SARAH DEDEURWAERDER, MATTHIEU DEFRANCE, MARTIN BIZET, EMILIE CALONNE, GIANLUCA BONTEMPI, AND FRANÇOIS FUKS. **A Comprehensive Overview of Infinium HumanMethylation 450 Data Processing**. *Briefings in Bioinformatics*, **15**(6):929–941, November 2014.

[48] GIUSEPPE DEROSA, AMIRHOSSEIN SAHEBKAR, AND PAMELA MAFFIOLI. **The Role of Various Peroxisome Proliferator-activated Receptors and Their Ligands in Clinical Practice**. *Journal of Cellular Physiology*, **233**(1):153–161, January 2018.

[49] JULIETA DÍAZ-DELFÍN, ELAYNE HONDARES, ROSER IGLESIAS, MARTA GIRALT, CARME CAELLES, AND FRANCESC VILLARROYA. **TNF-α Represses β-Klotho Expression and Impairs FGF21 Action in Adipose Cells: Involvement of JNK1 in the FGF21 Pathway**. *Endocrinology*, **153**(9):4238–4245, September 2012.

[50] Gyeong-Min Do, Hea Young Oh, Eun-young Kwon, Yun-young Cho, Su-kyung Shin, Hae-Jin Park, Seon-Min Jeon, Eunjung Kim, Cheol-Goo Hur, Tae-Sun Park, Mi-Kyung Sung, Robin A. McGregor, and Myung-Sook Choi. **Long-Term Adaptation of Global Transcription and Metabolism in the Liver of High-Fat Diet-Fed C57BL/6J Mice**. *Molecular Nutrition & Food Research*, **55**(S2):S173–185, September 2011.

[51] Sorin Draghici, Purvesh Khatri, Adi Laurentiu Tarca, Kashyap Amin, Arina Done, Calin Voichita, Constantin Georgescu, and Roberto Romero. **A Systems Biology Approach for Pathway Level Analysis**. *Genome Research*, **17**(10):1537–1545, September 2007.

[52] Joao A. G. Duarte, Filipa Carvalho, Mackenzie Pearson, Jay D. Horton, Jeffrey D. Browning, John G. Jones, and Shawn C. Burgess. **A High-Fat Diet Suppresses de Novo Lipogenesis and Desaturation but Not Elongation and Triglyceride Synthesis in Mice**. *Journal of Lipid Research*, **55**(12):2541–2553, December 2014.

[53] Vanessa Dubois, Jérôme Eeckhoute, Philippe Lefebvre, and Bart Staels. **Distinct but Complementary Contributions of PPAR Isotypes to Energy Homeostasis**. *The Journal of Clinical Investigation*, **127**(4):1202–1214, April 2017.

[54] Ulrika Edvardsson, Anna Ljungberg, and Jan Oscarsson. **Insulin and Oleic Acid Increase PPARγ2 Expression in Cultured Mouse Hepatocytes**. *Biochemical and Biophysical Research Communications*, **340**(1):111–117, February 2006.

[55] John R. Edwards, Olya Yarychkivska, Mathieu Boulard, and Timothy H. Bestor. **DNA Methylation and DNA Methyltransferases**. *Epigenetics & Chromatin*, **10**:23, May 2017.

[56] Tatsuya Ehara, Yasutomi Kamei, Xunmei Yuan, Mayumi Takahashi, Sayaka Kanai, Erina Tamura, Kazutaka Tsujimoto, Takashi Tamiya, Yoshimi Nakagawa, Hitoshi Shimano, Takako Takai-Igarashi, Izuho Hatada, Takayoshi Suganami, Koshi Hashimoto, and Yoshihiro Ogawa. **Ligand-Activated PPARα-Dependent DNA Demethylation Regulates the Fatty Acid β-Oxidation Genes in the Postnatal Liver**. *Diabetes*, **64**(3):775–784, March 2015.

[57] Anjeza Erickson and Régis Moreau. **The Regulation of FGF21 Gene Expression by Metabolic Factors and Nutrients**. *Hormone Molecular Biology and Clinical Investigation*, **30**(1), June 2016.

[58] Daniel J. Fazakerley, James R. Krycer, Alison L. Kearney, Samantha L. Hocking, and David E. James. **Muscle and Adipose Tissue Insulin Resistance: Malady without Mechanism?** *Journal of Lipid Research*, page jlr.R087510, July 2018.

[59] ffolliott M. Fisher, Patricia C. Chui, Patrick J. Antonellis, Holly A. Bina, Alexei Kharitonenkov, Jeffrey S. Flier, and Eleftheria Maratos-Flier. **Obesity Is a Fibroblast Growth Factor 21 (FGF21)-Resistant State**. *Diabetes*, **59**(11):2781–9, November 2010.

[60] Ffolliott M. Fisher and Eleftheria Maratos-Flier. **Understanding the Physiology of FGF21**. *Annual Review of Physiology*, **78**(1):223–241, 2016.

[61] Katsunori Fujiki, Akihiro Shinoda, Fumi Kano, Ryuichiro Sato, Katsuhiko Shirahige, and Masayuki Murata. **PPARγ-Induced PARylation Promotes Local DNA Demethylation by Production of 5-Hydroxymethylcytosine**. *Nature Communications*, **4**:2262, August 2013.

[62] José Miguel Gallego-Escuredo, Javier Gómez-Ambrosi, Victoria Catalan, Pere Domingo, Marta Cayetano i Giralt, Gema Frühbeck, and Francesc Villarroya. **Opposite Alterations in FGF21 and FGF19 Levels and Disturbed Expression of the Receptor Machinery for Endocrine FGFs in Obese Patients**. *International Journal of Obesity*, **39**(1):121–9, January 2015.

[63] Sofiya Gancheva, Tomas Jelenik, Elisa Álvarez-Hernández, and Michael Roden. **Interorgan Metabolic Crosstalk in Human Insulin Resistance**. *Physiological Reviews*, **98**(3):1371–1415, May 2018.

[64] Christopher R. Gault, Lina M. Obeid, and Yusuf A. Hannun. **An Overview of Sphingolipid Metabolism: From Synthesis to Breakdown**. *Advances in experimental medicine and biology*, **688**:1–23, January 2010.

[65] Xuan Ge, Yu Wang, Karen SL Lam, and Aimin Xu. **Metabolic Actions of FGF21: Molecular Mechanisms and Therapeutic Implications**. *Acta Pharmaceutica Sinica B*, **2**(4):350–357, August 2012.

[66] Helmuth Gehart, Susann Kumpf, Arne Ittner, and Romeo Ricci. **MAPK Signalling in Cellular Metabolism: Stress or Wellness?** *EMBO Reports*, **11**(11):834–840, November 2010.

[67] Jan F. C. Glatz and Joost J. F. P. Luiken. **Dynamic Role of the Transmembrane Glycoprotein CD36 (SR-B2) in Cellular Fatty Acid Uptake and Utilization**. *Journal of Lipid Research*, **59**(7):1084–1093, July 2018.

[68] Michèle Guerre-Millo, Philippe Gervois, Eric Raspe, Lise Madsen, Philippe Poulain, Bruno Derudas, Jean-Marc Herbert, Deborah A. Winegar, Timothy M. Willson, Jean-Charles Fruchart, Rolf K. Berge, and Bart Staels. **PPARα Activators Improve Insulin Sensitivity and Reduce Adiposity**. *Journal of Biological Chemistry*, **275**(22):16638–42, June 2000.

[69] Michèle Guerre-Millo, Christine Rouault, Philippe Poulain, Jocelyne André, Vincent Poitout, Jeffrey M. Peters, Frank J. Gonzalez, Jean-Charles Fruchart, Gérard Reach, and Bart Staels. **PPAR-α–Null Mice Are Protected from High-Fat Diet–Induced Insulin Resistance**. *Diabetes*, **50**(12):2809–2814, December 2001.

[70] Clarence Hale, Michelle M. Chen, Shanaka Stanislaus, Narumol Chinookoswong, Todd Hager, Minghan Wang, Murielle M. Véniant, and Jing Xu. **Lack of Overt FGF21 Resistance in Two Mouse Models of Obesity and Insulin Resistance**. *Endocrinology*, **153**(1):69–80, January 2012.

[71] Robert K. Hall, Xiaohui L. Wang, Leena George, Stephen R. Koch, and Daryl K. Granner. **Insulin Represses Phosphoenolpyruvate Carboxykinase Gene Transcription by Causing the Rapid Disruption of an Active Transcription Complex: A Potential Epigenetic Effect**. *Molecular Endocrinology*, **21**(2):550–563, February 2007.

[72] Martin Haluzík and M. Haluzík. **PPAR-Alpha and Insulin Sensitivity**. *Physiological Research*, **55**(2):115–122, January 2006.

[73] Hye-Sook Han, Geon Kang, Jun Seok Kim, Byeong Hoon Choi, and Seung-Hoi Koo. **Regulation of Glucose Metabolism from a Liver-Centric Perspective**. *Experimental & Molecular Medicine*, **48**(3):e218, March 2016.

[74] Lu Han, Wen-Jun Shen, Stefanie Bittner, Fredric B. Kraemer, and Salman Azhar. **PPARs: Regulators of Metabolism and as Therapeutic Targets in Cardiovascular Disease. Part I: PPAR-α**. *Future Cardiology*, **13**(3):259–278, May 2017.

[75] Timothy Hardy and Derek A. Mann. **Epigenetics in Liver Disease: From Biology to Therapeutics**. *Gut*, **65**(11):1895–1905, November 2016.

[76] Maximilian Hatting, Clint D. J. Tavares, Kfir Sharabi, Amy K. Rines, and Pere Puigserver. **Insulin Regulation of Gluconeogenesis**. *Annals of the New York Academy of Sciences*, **1411**(1):21–35, January 2018.

[77] Naoko Hattori, Magoichi Sako, Kana Kimura, Naoko Iida, Hideyuki Takeshima, Yoshitaka Nakata, Yutaka Kono, and Toshikazu Ushijima. **Novel Prodrugs of Decitabine with Greater Metabolic Stability and Less Toxicity**. *Clinical Epigenetics*, **11**(1), August 2019.

[78] Jinhan He, Jung Hoon Lee, Maria Febbraio, and Wen Xie. **The Emerging Roles of Fatty Acid Translocase/CD36 and the Aryl Hydrocarbon Receptor in Fatty Liver Disease**. *Experimental Biology and Medicine*, **236**(10):1116–1121, October 2011.

[79] Edith Heard and Robert A. Martienssen. **Transgenerational Epigenetic Inheritance: Myths and Mechanisms**. *Cell*, **157**(1):95–109, March 2014.

[80] Ahlke Heydemann. **An Overview of Murine High Fat Diet as a Model for Type 2 Diabetes Mellitus**. *Journal of Diabetes Research*, **2016**:2902351, July 2016.

[81] Brenda S. Hijmans, Aldo Grefhorst, Maaike H. Oosterveer, and Albert K. Groen. **Zonation of Glucose and Fatty Acid Metabolism in the Liver: Mechanism and Metabolic Consequences**. *Biochimie*, **96**(1):121–129, January 2014.

[82] Bernhard Horsthemke. **A Critical View on Transgenerational Epigenetic Inheritance in Humans**. *Nature Communications*, **9**(1):2973, July 2018.

[83] Andrew J. Hoy, Amanda E. Brandon, Nigel Turner, Matthew J. Watt, Clinton R. Bruce, Gregory J. Cooney, and Edward W. Kraegen. **Lipid and Insulin Infusion-Induced Skeletal Muscle Insulin Resistance Is Likely Due to Metabolic Feedback and Not Changes in IRS-1, Akt, or AS160 Phosphorylation**. *American Journal of Physiology - Endocrinology and Metabolism*, **297**(1):E67–E75, July 2009.

[84] Da Wei Huang, Brad T. Sherman, and Richard A. Lempicki. **Bioinformatics Enrichment Tools: Paths toward the Comprehensive Functional Analysis of Large Gene Lists**. *Nucleic Acids Research*, **37**(1):1–13, January 2009.

[85] Da Wei Huang, Brad T. Sherman, and Richard A. Lempicki. **Systematic and Integrative Analysis of Large Gene Lists Using DAVID Bioinformatics Resources**. *Nature Protocols*, **4**(1):44–57, January 2009.

[86] Qi Huang, Chaoyang Ma, Li Chen, Dan Luo, Rui Chen, and Fengxia Liang. **Mechanistic Insights into the Interaction between Transcription Factors and Epigenetic Modifications and the Contribution to the Development of Obesity**. *Frontiers in Endocrinology*, **9**:370, July 2018.

[87] Akhtar Hussain, Bjørgulf Claussen, Ambady Ramachandran, and Rhys Williams. **Prevention of Type 2 Diabetes: A Review**. *Diabetes Research and Clinical Practice*, **76**(3):317–326, June 2007.

[88] John C. Hutton and Richard M. O'Brien. **Glucose-6-Phosphatase Catalytic Subunit Gene Family**. *The Journal of Biological Chemistry*, **284**(43):29241–29245, October 2009.

[89] Samar H. Ibrahim, Petra Hirsova, Harmeet Malhi, and Gregory J. Gores. **Animal Models of Nonalcoholic Steatohepatitis: Eat, Delete, and Inflame**. *Digestive diseases and sciences*, **61**(5):1325–1336, May 2016.

[90] Illumina. **An Introduction to Next-Generation Sequencing Technology**.

[91] Mitsutaka Inoue, Takaaki Ohtake, Wataru Motomura, Nobuhiko Takahashi, Yayoi Hosoki, Shigeki Miyoshi, Yasuaki Suzuki, Hiroyuki Saito, Yutaka Kohgo, and Toshikatsu Okumura. **Increased Expression of PPARγ in High Fat Diet-Induced Liver Steatosis in Mice**. *Biochemical and Biophysical Research Communications*, **336**(1):215–222, October 2005.

[92] R. A. Irizarry. **Summaries of Affymetrix GeneChip Probe Level Data**. *Nucleic Acids Research*, **31**(4):e15, February 2003.

[93] Alison Iroz, Jean-Pierre Couty, and Catherine Postic. **Hepatokines: Unlocking the Multi-Organ Network in Metabolic Diseases**. *Diabetologia*, **58**(8):1699–1703, August 2015.

[94] Yumi Itoh, Masato Sanosaka, Hiroyuki Fuchino, Yasuhito Yahara, Ayako Kumagai, Daisaku Takemoto, Mai Kagawa, Junko Doi, Miho Ohta, Noriyuki Tsumaki, Nobuo Kawahara, and Hiroshi Takemori. **Salt-Inducible Kinase 3 Signaling Is Important for the Gluconeogenic Programs in Mouse Hepatocytes**. *The Journal of Biological Chemistry*, **290**(29):17879–17893, July 2015.

[95] Anne P. L. Jensen-Urstad and Clay F. Semenkovich. **Fatty Acid Synthase and Liver Triglyceride Metabolism: Housekeeper or Messenger?** *Biochimica et Biophysica Acta*, **1821**(5):747–753, May 2012.

[96] Anna Jeznach-Steinhagen, Joanna Ostrowska, Aneta Czerwonogrodzka-Senczyna, Iwona Boniecka, Urszula Shahnazaryan, and Alina Kuryłowicz. **Dietary and Pharmacological Treatment of Nonalcoholic Fatty Liver Disease**. *Medicina*, **55**(5):166, May 2019.

[97] Wenqing Jiang, Shiwen Wang, Mengtao Xiao, Yan Lin, Lisha Zhou, Qunying Lei, Yue Xiong, Kun-Liang Guan, and Shimin Zhao. **Acetylation Regulates Gluconeogenesis by Promoting PEPCK1 Degradation via Recruiting the UBR5 Ubiquitin Ligase**. *Molecular cell*, **43**(1):33–44, July 2011.

[98] Daudi Jjingo, Andrew B. Conley, Soojin V. Yi, Victoria V. Lunyak, and I. King Jordan. **On the Presence and Role of Human Gene-Body DNA Methylation**. *Oncotarget*, **3**(4):462–474, May 2012.

[99] Eric F. Johnson, Mei-Hui Hsu, Uzen Savas, and Keith J. Griffin. **Regulation of P450 4A Expression by Peroxisome Proliferator Activated Receptors**. *Toxicology*, **181-182**(1-3):203–206, December 2002.

[100] John G. Jones. **Hepatic Glucose and Lipid Metabolism**. *Diabetologia*, **59**(6):1098–1103, June 2016.

[101] Peter A. Jones. **Functions of DNA Methylation: Islands, Start Sites, Gene Bodies and Beyond**. *Nature Reviews Genetics*, **13**(7):484–492, July 2012.

[102] Peter A. Jones and Gangning Liang. **Rethinking How DNA Methylation Patterns Are Maintained**. *Nature reviews. Genetics*, **10**(11):805–811, November 2009.

[103] Donald B. Jump, Steven D. Clarke, Annette Thelen, and Marya Liimatta. **Coordinate Regulation of Glycolytic and Lipogenic Gene Expression by Polyunsaturated Fatty Acids.** *Journal of Lipid Research*, **35**(6):1076–1084, June 1994.

[104] Pâmela A. Kakimoto and Alicia J. Kowaltowski. **Effects of High Fat Diets on Rodent Liver Bioenergetics and Oxidative Imbalance**. *Redox Biology*, **8**:216–225, August 2016.

[105] Mark P. Keller, YounJeong Choi, Ping Wang, Dawn Belt Davis, Mary E. Rabaglia, Angie T. Oler, Donald S. Stapleton, Carmen Argmann, Kathy L. Schueler, Steve Edwards, H. Adam Steinberg, Elias Chaibub Neto, Robert Kleinhanz, Scott Turner, Marc K. Hellerstein, Eric E. Schadt, Brian S. Yandell, Christina Kendziorski, and Alan D. Attie. **A Gene Expression Network Model of Type 2 Diabetes Links Cell Cycle Regulation in Islets with Diabetes Susceptibility**. *Genome Research*, **18**(5):706–716, May 2008.

[106] W. James Kent, Charles W. Sugnet, Terrence S. Furey, Krishna M. Roskin, Tom H. Pringle, Alan M. Zahler, and and David Haussler. **The Human Genome Browser at UCSC**. *Genome Research*, **12**(6):996–1006, January 2002.

[107] Sander Kersten. **Integrated Physiology and Systems Biology of PPARα**. *Molecular Metabolism*, **3**(4):354–371, March 2014.

[108] Thomas Kietzmann. **Metabolic Zonation of the Liver: The Oxygen Gradient Revisited**. *Redox Biology*, **11**:622–630, January 2017.

[109] Jae Bum Kim. **Dynamic Cross Talk between Metabolic Organs in Obesity and Metabolic Diseases**. *Experimental & Molecular Medicine*, **48**(3):e214, March 2016.

[110] Henriette Kirchner, Indranil Sinha, Hui Gao, Maxwell A. Ruby, Milena Schönke, Jessica M. Lindvall, Romain Barrès, Anna Krook, Erik Näslund, Karin Dahlman-Wright, and Juleen R. Zierath. **Altered DNA Methylation of Glycolytic and Lipogenic Genes in Liver from Obese and Type 2 Diabetic Patients**. *Molecular Metabolism*, **5**(3):171–183, March 2016.

[111] Robert Kleemann, Marjan van Erk, Lars Verschuren, Anita M. van den Hoek, Maud Koek, Peter Y. Wielinga, Annie Jie, Linette Pellis, Ivana Bobeldijk-Pastorova, Thomas Kelder, Karin Toet, Suzan Wopereis, Nicole Cnubben, Chris Evelo, Ben van Ommen, and Teake Kooistra. **Time-Resolved and Tissue-Specific Systems Analysis of the Pathogenesis of Insulin Resistance**. *PloS One*, **5**(1):e8817, January 2010.

[112] Debby P. Y. Koonen, René L. Jacobs, Maria Febbraio, Martin E. Young, Carrie-Lynn M. Soltys, Huy Ong, Dennis E. Vance, and Jason R. B. Dyck. **Increased Hepatic CD36 Expression Contributes to Dyslipidemia Associated with Diet-Induced Obesity**. *Diabetes*, **56**(12):2863–2871, December 2007.

[113] Christin Krause, Helen Sievert, Cathleen Geissler, Martina Grohs, Alexander T El Gammal, Stefan Wolter, Olena Ohlei, Fabian Kilpert, Ulrike M Krämer, Meike Kasten, Christine Klein, Georg E Brabant, Oliver Mann, Hendrik Lehnert, and Henriette Kirchner. **Critical Evaluation of the DNA-Methylation Markers ABCG1 and SREBF1 for Type 2 Diabetes Stratification**. *Epigenomics*, **11**(8):885–897, June 2019.

[114] Helene Kretzmer, Stephan H. Bernhart, Wei Wang, Andrea Haake, Marc A. Weniger, Anke K. Bergmann, Matthew J. Betts, Enrique Carrillo-de-Santa-Pau, Gero Doose, Jana Gutwein, Julia Richter, Volker Hovestadt, Bingding Huang, Daniel Rico, Frank Jühling, Julia Kolarova, Qianhao Lu, Christian Otto, Rabea Wagener, Judith Arnolds, Birgit Burkhardt, Alexander Claviez, Hans G. Drexler, Sonja Eberth, Roland Eils, Paul Flicek, Siegfried Haas, Michael Humme, Dennis Karsch, Hinrik H. D. Kerstens, Wolfram Klapper, Markus Kreuz, Chris Lawerenz, Dido Lenzek, Markus Loeffler, Cristina López, Roderick A. F. MacLeod, Joost H. A. Martens, Marta Kulis, José Ignacio Martín-Subero, Peter Möller, Inga Nage, Simone Picelli, Inga Vater, Marius Rohde, Philip Rosenstiel, Maciej Rosolowski, Robert B. Russell, Markus Schilhabel, Matthias Schlesner, Peter F. Stadler, Monika Szczepanowski, Lorenz Trümper, Hendrik G. Stunnenberg, Ralf Küppers, Ole Ammerpohl, Peter Lichter, Reiner Siebert, Steve Hoffmann, and Bernhard Radlwimmer. **DNA-Methylome Analysis in Burkitt and Follicular Lymphomas Identifies Differentially Methylated Regions Linked to Somatic Mutation and Transcriptional Control**. *Nature genetics*, **47**(11):1316–1325, November 2015.

[115] Lasse Sommer Kristensen and Lise Lotte Hansen. **PCR-Based Methods for Detecting Single-Locus DNA Methylation Biomarkers in Cancer Diagnostics, Prognostics, and Response to Treatment**. *Clinical Chemistry*, **55**(8):1471–1483, August 2009.

[116] Jujiao Kuang, Xu Yan, Amanda J. Genders, Cesare Granata, and David J. Bishop. **An Overview of Technical Considerations When Using Quantitative Real-Time PCR Analysis of Gene Expression in Human Exercise Research**. *PLoS ONE*, **13**(5):e0196438, May 2018.

[117] Naoto Kubota, Tetsuya Kubota, Eiji Kajiwara, Tomokatsu Iwamura, Hiroki Kumagai, Taku Watanabe, Mariko Inoue, Iseki Takamoto, Takayoshi Sasako, Katsuyoshi Kumagai, Motoyuki Kohjima, Makoto Nakamuta, Masao Moroi, Kaoru Sugi, Tetsuo Noda, Yasuo Terauchi, Kohjiro Ueki, and Takashi Kadowaki. **Differential Hepatic Distribution of Insulin Receptor Substrates Causes Selective Insulin Resistance in Diabetes and Obesity**. *Nature Communications*, **7**:12977, October 2016.

[118] Tetsuya Kubota, Naoto Kubota, and Takashi Kadowaki. **Imbalanced Insulin Actions in Obesity and Type 2 Diabetes: Key Mouse Models of Insulin Signaling Pathway**. *Cell Metabolism*, **25**(4):797–810, April 2017.

[119] Sergey Kurdyukov and Martyn Bullock. **DNA Methylation Analysis: Choosing the Right Method**. *Biology*, **5**(1):3, January 2016.

[120] Masataka Kusunoki, Kazuhiko Tsutsumi, Tsutomu Hara, Hitoshi Ogawa, Takao Nakamura, Tetsuro Miyata, Fumihiko Sakakibara, Yoshitaka Fukuzawa, Takashi Suga, Shinichi Kakumu, and Yutaka Nakaya. **Correlation between Lipid and Glycogen Contents in Liver and Insulin Resistance in High-Fat Fed Rats Treated with the Lipoprotein Lipase Activator NO-1886**. *Metabolism*, **51**(6):792–795, June 2002.

[121] Eun-Young Kwon, Su-Kyung Shin, Yun-Young Cho, Un Ju Jung, Eunjung Kim, Taesun Park, Jung Han Yoon Park, Jong Won Yun, Robin A McGregor, Yong Bok Park, and Myung-Sook Choi. **Time-Course Microarrays Reveal Early Activation of the Immune Transcriptome and Adipokine Dysregulation Leads to Fibrosis in Visceral Adipose Depots during Diet-Induced Obesity**. *BMC Genomics*, **13**(1):450, September 2012.

[122] Christine Ladd-Acosta, Martin J. Aryee, Jared M. Ordway, and Andrew P. Feinberg. **Comprehensive High-Throughput Arrays for Relative Methylation (CHARM)**. *Current protocols in human genetics*, **Chapter 20**:Unit 20.1.1–19, April 2010.

[123] Shreekrishna Lamichane, Babita Dahal Lamichane, and Sang-Mo Kwon. **Pivotal Roles of Peroxisome Proliferator-Activated Receptors (PPARs) and Their Signal Cascade for Cellular and Whole-Body Energy Homeostasis**. *International Journal of Molecular Sciences*, **19**(4):949, March 2018.

[124] Cristina Lara-Castro and W. Timothy Garvey. **Intracellular Lipid Accumulation in Liver and Muscle and the Insulin Resistance Syndrome**. *Endocrinology and metabolism clinics of North America*, **37**(4):841–856, December 2008.

[125] Ho-Sun Lee. **Impact of Maternal Diet on the Epigenome during In Utero Life and the Developmental Programming of Diseases in Childhood and Adulthood**. *Nutrients*, **7**(11):9492–9507, November 2015.

[126] Ji-Eun Lee and Kai Ge. **Transcriptional and Epigenetic Regulation of PPARγ Expression during Adipogenesis**. *Cell & Bioscience*, **4**(1):29, May 2014.

[127] Yoon Kwang Lee, Jung Eun Park, Mikang Lee, and James P. Hardwick. **Hepatic Lipid Homeostasis by Peroxisome Proliferator-Activated Receptor Gamma 2**. *Liver Research*, **2**(4):209–215, December 2018.

[128] Young Lee, May-Yun Wang, Tetsuya Kakuma, Zhuo-Wei Wang, Evelyn Babcock, Kay McCorkle, Moritake Higa, Yan-Ting Zhou, and Roger H. Unger. **Liporegulation in Diet-Induced Obesity. The Antisteatotic Role of Hyperleptinemia.** *Journal of Biological Chemistry*, **276**(8):5629–5635, February 2001.

[129] Michael Lenz, Franz-Josef Müller, Martin Zenke, and Andreas Schuppert. **Principal Components Analysis and the Reported Low Intrinsic Dimensionality of Gene Expression Microarray Data**. *Scientific Reports*, **6**:25696, 2016.

[130] Chrysanthia A. Leontiou, Michael D. Hadjidaniel, Petros Mina, Pavlos Antoniou, Marios Ioannides, and Philippos C. Patsalis. **Bisulfite Conversion of DNA: Performance Comparison of Different Kits and Methylation Quantitation of Epigenetic Biomarkers That Have the Potential to Be Used in Non-Invasive Prenatal Testing**. *PLoS ONE*, **10**(8):e0135058, August 2015.

[131] Robert Lesurf, Kelsy C. Cotto, Grace Wang, Malachi Griffith, Katayoon Kasaian, Steven J. M. Jones, Stephen B. Montgomery, Obi L. Griffith, and Open Regulatory Annotation Consortium. **ORegAnno 3.0: A Community-Driven Resource for Curated Regulatory Annotation**. *Nucleic Acids Research*, **44**(D1):D126–132, January 2016.

[132] Jake Lever, Martin Krzywinski, and Naomi Altman. **Principal Component Analysis**. *Nature Methods*, **14**(7):641–642, July 2017.

[133] Xinyu Li, Xiaoqin Shi, Yi Hou, Xuemei Cao, Lei Gong, Hongying Wang, Jiayu Li, Jibin Li, Chaodong Wu, Daliao Xiao, Hongbo Qi, and Xiaoqiu Xiao. **Paternal Hyperglycemia Induces Transgenerational Inheritance of Susceptibility to Hepatic Steatosis in Rats Involving Altered Methylation on Pparα Promoter**. *Biochimica et Biophysica Acta (BBA) - Molecular Basis of Disease*, **1865**(1):147–160, January 2019.

[134] Xue-bing Li, Jun-dong Gu, and Qing-hua Zhou. **Review of Aerobic Glycolysis and Its Key Enzymes – New Targets for Lung Cancer Therapy**. *Thoracic Cancer*, **6**(1):17–24, January 2015.

[135] Zhihuan Li, Zon Weng Lai, Romain Christiano, Felipe Gazos-Lopes, Tobias C. Walther, and Robert V. Farese. **Global Analyses of Selective Insulin Resistance in Hepatocytes Caused by Palmitate Lipotoxicity**. *Molecular & Cellular Proteomics*, **17**(5):836–849, May 2018.

[136] Zhiqiang Li, Hongqi Zhang, Jing Liu, Chien-Ping Liang, Yan Li, Yue Li, Gladys Teitelman, Thomas Beyer, Hai H. Bui, David A. Peake, Youyan Zhang, Phillip E. Sanders, Ming-Shang Kuo, Tae-Sik Park, Guoqing Cao, and Xian-Cheng Jiang. **Reducing Plasma Membrane Sphingomyelin Increases Insulin Sensitivity**. *Molecular and Cellular Biology*, **31**(20):4205–4218, October 2011.

[137] Julia A. Licholai, Katrina P. Nguyen, Wambura C. Fobbs, Corbin J. Schuster, Mohamed A. Ali, and Alexxai V. Kravitz. **Why Do Mice Overeat High-Fat Diets? How High-Fat Diet Alters the Regulation of Daily Caloric Intake in Mice**. *Obesity (Silver Spring, Md.)*, **26**(6):1026–1033, June 2018.

[138] Alice Liguori, Antonella Puglianiello, Daniela Germani, Annalisa Deodati, Emanuela Peschiaroli, and Stefano Cianfarani. **Epigenetic Changes Predisposing to Type 2 Diabetes in Intrauterine Growth Retardation**. *Frontiers in Endocrinology*, **1**:5, November 2010.

[139] Karen A. Lillycrop, Emma S. Phillips, Christopher Torrens, Mark A. Hanson, Alan A. Jackson, and Graham C. Burdge. **Feeding Pregnant Rats a Protein-Restricted Diet Persistently Alters the Methylation of Specific Cytosines in the Hepatic PPARα Promoter of the Offspring**. *The British Journal of Nutrition*, **100**(2):278–282, August 2008.

[140] X Shawn Liu, Hao Wu, Xiong Ji, Yonatan Stelzer, Xuebing Wu, Szymon Czauderna, Jian Shu, Daniel Dadon, Richard A. Young, and Rudolf Jaenisch. **Editing DNA Methylation in the Mammalian Genome**. *Cell*, **167**(1):233–247.e17, September 2016.

[141] Carlos López-Otín, Maria A. Blasco, Linda Partridge, Manuel Serrano, and Guido Kroemer. **The Hallmarks of Aging**. *Cell*, **153**(6):1194–1217, June 2013.

[142] Chongyuan Luo, Petra Hajkova, and Joseph R. Ecker. **Dynamic DNA Methylation: In the Right Place at the Right Time**. *Science*, **361**(6409):1336–1340, September 2018.

[143] Inger Magnusson, Douglas L. Rothman, Lee D. Katz, Robert G. Shulman, and Gerald I. Shulman. **Increased Rate of Gluconeogenesis in Type II Diabetes Mellitus. A 13C Nuclear Magnetic Resonance Study.** *Journal of Clinical Investigation*, **90**(4):1323–1327, October 1992.

[144] Derek A. Mann. **Epigenetics in Liver Disease**. *Hepatology*, **60**(4):1418–1425, October 2014.

[145] Simona Marchisello, Antonino Di Pino, Roberto Scicali, Francesca Urbano, Salvatore Piro, Francesco Purrello, and Agata Maria Rabuazzo. **Pathophysiological, Molecular and Therapeutic Issues of Nonalcoholic Fatty Liver Disease: An Overview**. *International Journal of Molecular Sciences*, **20**(8):1948, April 2019.

[146] Loïze Maréchal, Maximilien Laviolette, Amélie Rodrigue-Way, Baly Sow, Michèle Brochu, Véronique Caron, and André Tremblay. **The CD36-PPARγ Pathway in Metabolic Disorders**. *International Journal of Molecular Sciences*, **19**(5):1529, May 2018.

[147] Kathleen R. Markan, Meghan C. Naber, Sarah M. Small, Lila Peltekian, Rachel L. Kessler, and Matthew J. Potthoff. **FGF21 Resistance Is Not Mediated by Downregulation of Beta-Klotho Expression in White Adipose Tissue**. *Molecular Metabolism*, **6**(6):602–610, June 2017.

[148] Alessandro Marsili, Cristina Aguayo-Mazzucato, Ting Chen, Aditi Kumar, Mirra Chung, Elaine P. Lunsford, John W. Harney, Thuy Van-Tran, Elena Gianetti, Waile Ramadan, Cyril Chou, Susan Bonner-Weir, Philip Reed Larsen, Jorge Enrique Silva, and Ann Marie Zavacki. **Mice with a Targeted Deletion of the Type 2 Deiodinase Are Insulin Resistant and Susceptible to Diet Induced Obesity**. *PLoS ONE*, **6**(6):e20832, June 2011.

[149] Gracia María Martín-Núñez, Rebeca Cabrera-Mulero, Elehazara Rubio-Martín, Gemma Rojo-Martínez, Gabriel Olveira, Sergio Valdés, Federico Soriguer, Luis Castaño, and Sonsoles Morcillo. **Methylation Levels of the SCD1 Gene Promoter and LINE-1 Repeat Region Are Associated with Weight Change: An Intervention Study**. *Molecular Nutrition & Food Research*, **58**(7):1528–1536, July 2014.

[150] Koichi Matsuo, John Silke, Kostadin Gramatikoff, and Walter Schaffner. **The CpG-Specific Methylase Sssl Has Topoisomerase Activity in the Presence of Mg $^{2+}$**. *Nucleic Acids Research*, **22**(24):5354–5349, 1994.

[151] Daniel Mauvoisin and Catherine Mounier. **Hormonal and Nutritional Regulation of SCD1 Gene Expression**. *Biochimie*, **93**(1):78–86, January 2011.

[152] Katarina Melzer. **Carbohydrate and Fat Utilization during Rest and Physical Activity**. *e-SPEN, the European e-Journal of Clinical Nutrition and Metabolism*, **6**(2):e45–e52, April 2011.

[153] Riaz A. Memon, Laurence H. Tecott, Katsunori Nonogaki, Anne Beigneux, Arthur H. Moser, Carl Grunfeld, and Kenneth R. Feingold. **Up-Regulation of Peroxisome Proliferator-Activated Receptors (PPAR-α) and PPAR-γ Messenger Ribonucleic Acid Expression in the Liver in Murine Obesity: Troglitazone Induces Expression of PPAR-γ-Responsive Adipose Tissue-Specific Genes in the Liver of Obese Diabetic Mice**. *Endocrinology*, **141**(11):4021–4031, November 2000.

[154] Asimina Mitrakou, Niki Katsiki, and Nebojsa Lalic. **Type 2 Diabetes Mellitus and the Elderly: An Update on Drugs Used to Treat Glycaemia**. *Current Vascular Pharmacology*, **15**(1):19–29, November 2016.

[155] Susumu Mitsutake, Kota Zama, Hazuki Yokota, Tetsuya Yoshida, Miki Tanaka, Masaru Mitsui, Masahito Ikawa, Masaru Okabe, Yoshikazu Tanaka, Tadashi Yamashita, Hiroshi Takemoto, Toshiro Okazaki, Ken Watanabe, and Yasuyuki Igarashi. **Dynamic Modification of Sphingomyelin in Lipid Microdomains Controls Development of Obesity, Fatty Liver, and Type 2 Diabetes**. *The Journal of Biological Chemistry*, **286**(32):28544–28555, August 2011.

[156] Alexandra Montagner, Arnaud Polizzi, Edwin Fouché, Simon Ducheix, Yannick Lippi, Frédéric Lasserre, Valentin Barquissau, Marion Régnier, Céline Lukowicz, Fadila Benhamed, Alison Iroz, Justine Bertrand-Michel, Talal Al Saati, Patricia Cano, Laila Mselli-Lakhal, Gilles Mithieux, Fabienne Rajas, Sandrine Lagarrigue, Thierry Pineau, Nicolas Loiseau, Catherine Postic, Dominique Langin, Walter Wahli, and Hervé Guillou. **Liver PPARα Is Crucial for Whole-Body Fatty Acid Homeostasis and Is Protective against NAFLD**. *Gut*, **65**(7):1202–1214, July 2016.

[157] Azam Moosavi and Ali Motevalizadeh Ardekani. **Role of Epigenetics in Biology and Human Diseases**. *Iranian Biomedical Journal*, **20**(5):246–258, November 2016.

[158] Jeanine S. Morey, James C. Ryan, and Frances M. Van Dolah. **Microarray Validation: Factors Influencing Correlation between Oligonucleotide Microarrays and Real-Time PCR**. *Biological Procedures Online*, **8**:175–193, 2006.

[159] Evgeny A. Moskalev, Mikhail G. Zavgorodnij, Svetlana P. Majorova, Ivan A. Vorobjev, Pouria Jandaghi, Irina V. Bure, and Jörg D. Hoheisel. **Correction of PCR-Bias in Quantitative DNA Methylation Studies by Means of Cubic Polynomial Regression**. *Nucleic Acids Research*, **39**(11):e77, June 2011.

[160] Mouse Genome Sequencing Consortium, Mikita Suyama, Glenn Tesler, Johanna Thompson, David Torrents, John Tromp, Abel Ureta-Vidal, Jade P. Vinson, Andrew C. Von Niederhausern, Michael C. Wendl, Kris Wetterstrand, Raymond Wheeler, Sophie Williams, Richard K. Wilson, Kim C. Worley, Dudley Wyman, Shiaw-Pyng Yang, Evgeny M. Zdobnov, and Eric S. Lander. **Initial Sequencing and Comparative Analysis of the Mouse Genome**. *Nature*, **420**(6915):520–562, December 2002.

[161] Miloš Mraz, Markéta Bartlova, Zdena Lacinova, David Michalsky, Mojmír Kasalicky, Denisa Haluzikova, Martin Matoulek, Ivana Dostalova, Viera Humenanska, and Martin Haluzik. **Serum Concentrations and Tissue Expression of a Novel Endocrine Regulator Fibroblast Growth Factor-21 in Patients with Type 2 Diabetes and Obesity**. *Clinical Endocrinology*, **71**(3):369–375, 2009.

[162] K. Mullis, F. Faloona, S. Scharf, R. Saiki, G. Horn, and H. Erlich. **Specific Enzymatic Amplification of DNA in Vitro: The Polymerase Chain Reaction**. *Cold Spring Harbor Symposia on Quantitative Biology*, **51**:263–273, January 1986.

[163] Michael L. Multhaup, Marcus Seldin, Andrew E. Jaffe, Xia Lei, Henriette Kirchner, Prosenjit Mondal, Yuanyuan Li, Varenka Rodriguez, Alexander Drong, Mehboob Hussain, Cecilia Lindgren, Mark McCarthy, Erik Näslund, Juleen R. Zierath, G. William Wong, and Andrew P. Feinberg. **Mouse-Human Experimental Epigenetic Analysis Unmasks Dietary Targets and Genetic Liability for Diabetic Phenotypes**. *Cell metabolism*, **21**(1):138–149, January 2015.

[164] María Carmen Muñoz, Albert Barberà, Jorge Domínguez, Josefa Fernàndez-Alvarez, Ramon Gomis, and Joan J. Guinovart. **Effects of Tungstate, a New Potential Oral Antidiabetic Agent, in Zucker Diabetic Fatty Rats**. *Diabetes*, **50**(1):131–138, January 2001.

[165] Cynthia A. Nagle, Eric L. Klett, and Rosalind A. Coleman. **Hepatic Triacylglycerol Accumulation and Insulin Resistance**. *Journal of Lipid Research*, **50**(Suppl):S74–S79, April 2009.

[166] Shalima S. Nair, Phuc-Loi Luu, Wenjia Qu, Madhavi Maddugoda, Lily Huschtscha, Roger Reddel, Georgia Chenevix-Trench, Martina Toso, James G. Kench, Lisa G. Horvath, Vanessa M. Hayes, Phillip D. Stricker, Timothy P. Hughes, Deborah L. White, John E. J. Rasko, Justin J.-L. Wong, and Susan J. Clark. **Guidelines for Whole Genome Bisulphite Sequencing of Intact and FFPET DNA on the Illumina HiSeq X Ten**. *Epigenetics & Chromatin*, **11**(1):24, May 2018.

[167] Seiji Nakamura, Toshinari Takamura, Naoto Matsuzawa-Nagata, Hiroaki Takayama, Hirofumi Misu, Hiroyo Noda, Satoko Nabemoto, Seiichiro Kurita, Tsuguhito Ota, Hitoshi Ando, Ken-ichi Miyamoto, and Shuichi Kaneko. **Palmitate Induces Insulin Resistance in H4IIEC3 Hepatocytes through Reactive Oxygen Dpecies Produced by Mitochondria**. *The Journal of Biological Chemistry*, **284**(22):14809–14818, May 2009.

[168] Jane W. Y. Ng, Laura M. Barrett, Andrew Wong, Diana Kuh, George Davey Smith, and Caroline L. Relton. **The Role of Longitudinal Cohort Studies in Epigenetic Epidemiology: Challenges and Opportunities**. *Genome Biology*, **13**(6):246, 2012.

[169] Phuongtrang Nguyen, Véronique Leray, Marianne Diez, Samuel Serisier, Jérôme Le Bloc'h, Brigitte Siliart, and Henri Dumon. **Liver Lipid Metabolism**. *Journal of Animal Physiology and Animal Nutrition*, **92**(3):272–283, June 2008.

[170] Valérie Nicolas-Frances, Ségolène Arnauld, Jacques Kaminski, Emiel Ver Loren Van Themaat, Marie-Claude Clemencet, Julie Chamouton, Anne Athias, Jacques Grober, Joseph Gresti, Pascal Degrace, Laurent Lagrost, Norbert Latruffe, and Stéphane Mandard. **Disturbances in Cholesterol, Bile Acid and Glucose Metabolism in Peroxisomal 3-ketoacylCoA Thiolase B Deficient Mice Fed Diets Containing High or Low Saturated Fat Contents.** *Biochimie*, **98**:86–101, March 2014.

[171] Fardod O'Kelly, Laure Marignol, Armelle Meunier, Thomas H. Lynch, Antoinette S. Perry, and Donal Hollywood. **MicroRNAs as Putative Mediators of Treatment Response in Prostate Cancer**. *Nature Reviews Urology*, **9**(7):397–407, July 2012.

[172] Konstantin Okonechnikov, Olga Golosova, and Mikhail Fursov. **Unipro UGENE: A Unified Bioinformatics Toolkit**. *Bioinformatics*, **28**(8):1166–1167, April 2012.

[173] Verity F. Oliver, Jun Wan, Saurabh Agarwal, Donald J. Zack, Jiang Qian, and Shannath L. Merbs. **A Novel Methyl-Binding Domain Protein Enrichment Method for Identifying Genome-Wide Tissue-Specific DNA Methylation from Nanogram DNA Samples**. *Epigenetics & Chromatin*, **6**(1):17, June 2013.

[174] Ekaterina Olkhov-Mitsel and Bharati Bapat. **Strategies for Discovery and Validation of Methylated and Hydroxymethylated DNA Biomarkers**. *Cancer Medicine*, **1**(2):237–260, October 2012.

[175] Abdulfatai B. Olokoba, Olusegun A. Obateru, and Lateefat B. Olokoba. **Type 2 Diabetes Mellitus: A Review of Current Trends**. *Oman Medical Journal*, **27**(4):269–273, July 2012.

[176] Nelly Olova, Felix Krueger, Simon Andrews, David Oxley, Rebecca V. Berrens, Miguel R. Branco, and Wolf Reik. **Comparison of Whole-Genome Bisulfite Sequencing Library Preparation Strategies Identifies Sources of Biases Affecting DNA Methylation Data**. *Genome Biology*, **19**(1):33, March 2018.

[177] Bilal Omar, Giovanni Pacini, and Bo Ahrén. **Differential Development of Glucose Intolerance and Pancreatic Islet Adaptation in Multiple Diet Induced Obesity Models**. *Nutrients*, **4**(10):1367–1381, September 2012.

[178] Maaike H. Oosterveer and Kristina Schoonjans. **Hepatic Glucose Sensing and Integrative Pathways in the Liver**. *Cellular and Molecular Life Sciences*, **71**(8):1453–1467, April 2014.

[179] David M. Ornitz and Nobuyuki Itoh. **The Fibroblast Growth Factor Signaling Pathway**. *Wiley Interdisciplinary Reviews. Developmental Biology*, **4**(3):215–266, May 2015.

[180] David Patsouris, Janardan K. Reddy, Michael Müller, and Sander Kersten. **Peroxisome Proliferator-Activated Receptor α Mediates the Effects of High-Fat Diet on Hepatic Gene Expression**. *Endocrinology*, **147**(3):1508–1516, March 2006.

[181] Michal Pawlak, Philippe Lefebvre, and Bart Staels. **Molecular Mechanism of PPARα Action and Its Impact on Lipid Metabolism, Inflammation and Fibrosis in Non-Alcoholic Fatty Liver Disease**. *Journal of Hepatology*, **62**(3):720–733, March 2015.

[182] Marta Yanina Pepino, Ondrej Kuda, Dmitri Samovski, and Nada A. Abumrad. **Structure-Function of CD36 and Importance of Fatty Acid Signal Transduction in Fat Metabolism**. *Annual review of nutrition*, **34**:281–303, May 2014.

[183] Rachel J. Perry, João-Paulo G. Camporez, Romy Kursawe, Paul M. Titchenell, Dongyan Zhang, Curtis J. Perry, Michael J. Jurczak, Abulizi Abudukadier, Myoung Sook Han, Xian-Man Zhang, Hai-Bin Ruan, Xiaoyong Yang, Sonia Caprio, Susan M. Kaech, Hei Sook Sul, Morris J. Birnbaum, Roger J. Davis, Gary W. Cline, Kitt Falk Petersen, and Gerald I. Shulman. **Hepatic Acetyl CoA Links Adipose Tissue Inflammation to Hepatic Insulin Resistance and Type 2 Diabetes**. *Cell*, **160**(4):745–758, February 2015.

[184] Rachel J. Perry, Varman T. Samuel, Kitt F. Petersen, and Gerald I. Shulman. **The Role of Hepatic Lipids in Hepatic Insulin Resistance and Type 2 Diabetes**. *Nature*, **510**(7503):84–91, June 2014.

[185] Katrin Pfuhlmann, Paul T. Pfluger, Sonja C. Schriever, Timo D. Müller, Matthias H. Tschöp, and Kerstin Stemmer. **Dual Specificity Phosphatase 6 Deficiency Is Associated with Impaired Systemic Glucose Tolerance and Reversible Weight Retardation in Mice**. *PLoS ONE*, **12**(9):e0183488, September 2017.

[186] Ruth Pidsley, Elena Zotenko, Timothy J. Peters, Mitchell G. Lawrence, Gail P. Risbridger, Peter Molloy, Susan Van Djik, Beverly Muhlhausler, Clare Stirzaker, and Susan J. Clark. **Critical Evaluation of the Illumina MethylationEPIC BeadChip Microarray for Whole-Genome DNA Methylation Profiling**. *Genome Biology*, **17**(1):208, October 2016.

[187] Inés Pineda Torra, Yalda Jamshidi, David M. Flavell, Jean-Charles Fruchart, and Bart Staels. **Characterization of the Human PPARα Promoter: Identification of a Functional Nuclear Receptor Response Element**. *Molecular Endocrinology*, **16**(5):1013–1028, May 2002.

[188] Igor P. Pogribny, Volodymyr P. Tryndyak, Courtney G. Woods, Sarah E. Witt, and Ivan Rusyn. **Epigenetic Effects of the Continuous Exposure to Peroxisome Proliferator WY-14,643 in Mouse Liver Are Dependent upon Peroxisome Proliferator Activated Receptor α**. *Mutation research*, **625**(1-2):62–71, December 2007.

[189] Geoffrey A. Preidis, Kang Ho Kim, and David D. Moore. **Nutrient-Sensing Nuclear Receptors PPARα and FXR Control Liver Energy Balance**. *The Journal of Clinical Investigation*, **127**(4):1193–1201, March 2017.

[190] Marc Prentki and Christopher J. Nolan. **Islet β Cell Failure in Type 2 Diabetes**. *Journal of Clinical Investigation*, **116**(7):1802–1812, July 2006.

[191] Qiagen. **PyroMark® Q48 Autoprep User Manual**, June 2016.

[192] Marijana Radonjic, Jorn R. de Haan, Marjan J. van Erk, Ko Willems van Dijk, Sjoerd A. A. van den Berg, Philip J. de Groot, Michael Müller, and Ben van Ommen. **Genome-Wide mRNA Expression Analysis of Hepatic Adaptation to High-Fat Diets Reveals Switch from an Inflammatory to Steatotic Transcriptional Program**. *PloS One*, **4**(8):e6646, August 2009.

[193] Maryam Rakhshandehroo, Bianca Knoch, Michael Müller, and Sander Kersten. **Peroxisome Proliferator-Activated Receptor Alpha Target Genes**. *PPAR Research*, **2010**:612089, September 2010.

[194] Vardhman K. Rakyan, Thomas A. Down, David J. Balding, and Stephan Beck. **Epigenome-Wide Association Studies for Common Human Diseases**. *Nature Reviews Genetics*, **12**(8):529–541, August 2011.

[195] Soumya Raychaudhuri, Joshua M. Stuart, and Russ B. Altman. **Principal Components Analysis to Summarize Microarray Experiments: Application to Sporulation Time Series**. *Pacific Symposium on Biocomputing. Pacific Symposium on Biocomputing*, pages 455–466, 2000.

[196] Markus Ringnér. **What Is Principal Component Analysis?** *Nature Biotechnology*, **26**(3):303–304, March 2008.

[197] Kirk M. Ririe, Randy P. Rasmussen, and Carl T. Wittwer. **Product Differentiation by Analysis of DNA Melting Curves during the Polymerase Chain Reaction**. *Analytical Biochemistry*, **245**(2):154–160, February 1997.

[198] Pia V. Röder, Bingbing Wu, Yixian Liu, and Weiping Han. **Pancreatic Regulation of Glucose Homeostasis**. *Experimental & Molecular Medicine*, **48**(3):e219, March 2016.

[199] Mayra Z. Rodriguez, Cesar H. Comin, Dalcimar Casanova, Odemir M. Bruno, Diego R. Amancio, Luciano da F. Costa, and Francisco A. Rodrigues. **Clustering Algorithms: A Comparative Approach**. *PLOS ONE*, **14**(1):e0210236, January 2019.

[200] Peter J. Rousseeuw. **Silhouettes: A Graphical Aid to the Interpretation and Validation of Cluster Analysis**. *Journal of Computational and Applied Mathematics*, **20**:53–65, November 1987.

[201] Liangyou Rui. **Energy Metabolism in the Liver**. *Comprehensive Physiology*, **4**(1):177–197, January 2014.

[202] Pawan Samdani, Meet Singhal, Neeraj Sinha, Parul Tripathi, Sachin Sharma, Kamiya Tikoo, Kanury V. S. Rao, and Dhiraj Kumar. **A Comprehensive Inter-Tissue Crosstalk Analysis Underlying Progression and Control of Obesity and Diabetes**. *Scientific Reports*, **5**:12340, July 2015.

[203] Harini Sampath and James M. Ntambi. **The Role of Stearoyl-CoA Desaturase in Obesity, Insulin Resistance, and Inflammation**. *Annals of the New York Academy of Sciences*, **1243**:47–53, December 2011.

[204] Varman T. Samuel, Sara A. Beddow, Takanori Iwasaki, Xian-Man Zhang, Xin Chu, Christopher D. Still, Glenn S. Gerhard, and Gerald I. Shulman. **Fasting Hyperglycemia Is Not Associated with Increased Expression of PEPCK or G6Pc in Patients with Type 2 Diabetes**. *Proceedings of the National Academy of Sciences of the United States of America*, **106**(29):12121–12126, July 2009.

[205] Varman T. Samuel and Gerald I. Shulman. **The Pathogenesis of Insulin Resistance: Integrating Signaling Pathways and Substrate Flux**. *The Journal of Clinical Investigation*, **126**(1):12–22, 2016.

[206] Francis W. B. Sanders and Julian L. Griffin. **De Novo Lipogenesis in the Liver in Health and Disease: More than Just a Shunting Yard for Glucose**. *Biological Reviews of the Cambridge Philosophical Society*, **91**(2):452–468, May 2016.

[207] Dominic Santoleri and Paul M. Titchenell. **Resolving the Paradox of Hepatic Insulin Resistance**. *Cellular and Molecular Gastroenterology and Hepatology*, **7**(2):447–456, November 2018.

[208] Arun Sanyal, Edgar D. Charles, Brent A. Neuschwander-Tetri, Rohit Loomba, Stephen A. Harrison, Manal F. Abdelmalek, Eric J. Lawitz, Dina Halegoua-DeMarzio, Sudeep Kundu, Stephanie Noviello, Yi Luo, and Rose Christian. **Pegbelfermin (BMS-986036), a PEGylated Fibroblast Growth Factor 21 Analogue, in Patients with Non-Alcoholic Steatohepatitis: A Randomised, Double-Blind, Placebo-Controlled, Phase 2a Trial**. *The Lancet*, **392**(10165):2705–2717, December 2018.

[209] W. Sarada and P. V. Kumar. **A Review on Clustering Techniques and Their Comparison**. *International Journal of Advanced Research in Computer Engineering & Technology*, **2**(11):2806–2812, November 2013.

[210] Osamu Sato, Naoki Takanashi, and Kiyoto Motojima. **Third Promoter and Differential Regulation of Mouse and Human Fatty Acid Translocase/CD36 Genes**. *Molecular and Cellular Biochemistry*, **299**(1-2):37–43, May 2007.

[211] Amit Saxena, Mukesh Prasad, Akshansh Gupta, Neha Bharill, Om Prakash Patel, Aruna Tiwari, Meng Joo Er, Weiping Ding, and Chin-Teng Lin. **A Review of Clustering Techniques and Developments**. *Neurocomputing*, **267**:664–681, December 2017.

[212] Robert W. Schwenk, Wenke Jonas, Sarah B. Ernst, Anne Kammel, Markus Jähnert, and Annette Schürmann. **Diet-Dependent Alterations of Hepatic Scd1 Expression Are Accompanied by Differences in Promoter Methylation**. *Hormone and Metabolic Research*, **45**(11):786–794, October 2013.

[213] Jianhua Shao, Liping Qiao, Rachel C. Janssen, Michael Pagliassotti, and Jacob E. Friedman. **Chronic Hyperglycemia Enhances PEPCK Gene Expression and Hepatocellular Glucose Production Via Elevated Liver Activating Protein/Liver Inhibitory Protein Ratio**. *Diabetes*, **54**(4):976–984, April 2005.

[214] Kfir Sharabi, Clint D. J. Tavares, Amy K. Rines, and Pere Puigserver. **Molecular Pathophysiology of Hepatic Glucose Production**. *Molecular Aspects of Medicine*, **46**:21–33, December 2015.

[215] Gemma C. Sharp and Caroline L. Relton. **Epigenetics and Noncommunicable Diseases**. *Epigenomics*, **9**(6):789–791, May 2017.

[216] Dong-Qiao Shi, Iftikhar Ali, Jun Tang, and Wei-Cai Yang. **New Insights into 5hmC DNA Modification: Generation, Distribution and Function**. *Frontiers in Genetics*, **8**:100, July 2017.

[217] David Sims, Ian Sudbery, Nicholas E. Ilott, Andreas Heger, and Chris P. Ponting. **Sequencing Depth and Coverage: Key Considerations in Genomic Analyses**. *Nature Reviews Genetics*, **15**(2):121–132, February 2014.

[218] Ulf Smith and Barbara B. Kahn. **Adipose Tissue Regulates Insulin Sensitivity: Role of Adipogenesis, de Novo Lipogenesis and Novel Lipids**. *Journal of internal medicine*, **280**(5):465–475, November 2016.

[219] Junichiro Sonoda, Mark Z. Chen, and Amos Baruch. **FGF21-Receptor Agonists: An Emerging Therapeutic Class for Obesity-Related Diseases**. *Hormone Molecular Biology and Clinical Investigation*, **30**(2), May 2017.

[220] Maud Soty, Julien Chilloux, François Delalande, Carine Zitoun, Fabrice Bertile, Gilles Mithieux, and Amandine Gautier-Stein. **Post-Translational Regulation of the Glucose-6-Phosphatase Complex by Cyclic Adenosine Monophosphate Is a Crucial Determinant of Endogenous Glucose Production and Is Controlled by the Glucose-6-Phosphate Transporter**. *1349*, **15**(4):1342–9, April 2016.

[221] Claudia Spits, Cédric Le Caignec, Martine De Rycke, Lindsey Van Haute, André Van Steirteghem, Inge Liebaers, and Karen Sermon. **Whole-Genome Multiple Displacement Amplification from Single Cells**. *Nature Protocols*, **1**(4):1965–1970, November 2006.

[222] Harald Staiger, Michaela Keuper, Lucia Berti, Martin Hrabě de Angelis, and Hans-Ulrich Häring. **Fibroblast Growth Factor 21—Metabolic Role in Mice and Men**. *Endocrine Reviews*, **38**(5):468–488, October 2017.

[223] Hilde Hermansen Steineger, Hilde Nebb Sørensen, Jonathan D. Tugwood, Steinar Skrede, Øystein Spydevold, and Kaare M. Gautvik. **Dexamethasone and Insulin Demonstrate Marked and Opposite Regulation of the Steady-State mRNA Level of the Peroxisomal Proliferator-Activated Receptor (PPAR) in Hepatic Cells**. *European Journal of Biochemistry*, **225**(3):967–974, November 1994.

[224] Monica Szabó, Beáta Máté, Katalin Csép, and Theodora Benedek. **Epigenetic Modifications Linked to T2D, the Heritability Gap, and Potential Therapeutic Targets**. *Biochemical Genetics*, **56**(6):553–574, December 2018.

[225] N. Tajunisha and V. Saravanan. **An Efficient Method to Improve the Clustering Performance for High Dimensional Data by Principal Component Analysis and Modified K-Means**. *International Journal of Database Management Systems*, **3**(1):196–205, February 2011.

[226] Sin Yee Tan, Joyce Ling Mei Wong, Yan Jinn Sim, Su Sie Wong, Safa Abdelgadir Mohamed Elhassan, Sean Hong Tan, Grace Pei Ling Lim, Nicole Wuen Rong Tay, Naveenya Chetty Annan, Subrat Kumar Bhattamisra, and Mayuren Candasamy. **Type 1 and 2 Diabetes Mellitus: A Review on Current Treatment Approach and Gene Therapy as Potential Intervention**. *Diabetes & Metabolic Syndrome: Clinical Research & Reviews*, **13**(1):364–372, January 2019.

[227] Kelly G. Ten Hagen, Timothy A. Fritz, and Lawrence A. Tabak. **All in the Family: The UDP-GalNAc:Polypeptide N-Acetylgalactosaminyltransferases**. *Glycobiology*, **13**(1):1R–16R, January 2003.

[228] The BLUEPRINT Consortium, Christoph Bock, Florian Halbritter, Francisco J. Carmona, Sascha Tierling, Paul Datlinger, Yassen Assenov, María Berdasco, Anke K. Bergmann, Keith Booher, Florence Busato, Mihaela Campan, Christina Dahl, Christina M. Dahmcke, Dinh Diep, Agustín F. Fernández, Clarissa Gerhauser, Andrea Haake, Katharina Heilmann, Thomas Holcomb, Dianna Hussmann, Mitsuteru Ito, Ruth Kläver, Martin Kreutz, Marta Kulis, Virginia Lopez, Shalima S. Nair, Dirk S. Paul, Nongluk Plongthongkum, Wenjia Qu, Ana C. Queirós, Frank Reinicke, Guido Sauter, Thorsten Schlomm, Aaron Statham, Clare Stirzaker, Ruslan Strogantsev, Rocío G. Urdinguio, Kimberly Walter, Dieter Weichenhan, Daniel J. Weisenberger, Stephan Beck, Susan J. Clark, Manel Esteller, Anne C. Ferguson-Smith, Mario F. Fraga, Per Guldberg, Lise Lotte Hansen, Peter W. Laird, José I. Martín-Subero, Anders O. H. Nygren, Ralf Peist, Christoph Plass, David S. Shames, Reiner Siebert, Xueguang Sun, Jörg Tost, Jörn Walter, and Kun Zhang. **Quantitative Comparison of DNA Methylation Assays for Biomarker Development and Clinical Applications**. *Nature Biotechnology*, **34**(7):726–737, July 2016.

[229] Robert Tibshirani, Guenther Walther, and Trevor Hastie. **Estimating the Number of Clusters in a Data Set via the Gap Statistic**. *Journal of the Royal Statistical Society: Series B (Statistical Methodology)*, **63**(2):411–423, May 2001.

[230] Nigel Turner, Greg M. Kowalski, Simon J. Leslie, Steve Risis, Christine Yang, Robert S. Lee-Young, J. R. Babb, Peter J. Meikle, Graeme I. Lancaster, Darren C. Henstridge, Phillip J. White, Edward W. Kraegen, André Marette, Gregory J. Cooney, Mark A. Febbraio, and Clinton R. Bruce. **Distinct Patterns of Tissue-Specific Lipid Accumulation during the Induction of Insulin Resistance in Mice by High-Fat Feeding**. *Diabetologia*, **56**(7):1638–1648, July 2013.

[231] Alexander H. Tuttle, Vivek M. Philip, Elissa J. Chesler, and Jeffrey S. Mogil. **Comparing Phenotypic Variation between Inbred and Outbred Mice**. *Nature Methods*, **15**(12):994, December 2018.

[232] Tatsuya Uebi, Yumi Itoh, Osamu Hatano, Ayako Kumagai, Masato Sanosaka, Tsutomu Sasaki, Satoru Sasagawa, Junko Doi, Keita Tatsumi, Kuniko Mitamura, Eiichi Morii, Katsuyuki Aozasa, Tomohiro Kawamura, Meinoshin Okumura, Jun Nakae, Hajime Takikawa, Toshio Fukusato, Minako Koura, Mayumi Nish, Anders Hamsten, Angela Silveira, Alejandro M. Bertorello, Kazuo Kitagawa, Yasuo Nagaoka, Hidehisa Kawahara, Takeshi Tomonaga, Tetsuji Naka, Shigeo Ikegawa, Noriyuki Tsumaki, Junichiro Matsuda, and Hiroshi Takemori. **Involvement of SIK3 in Glucose and Lipid Homeostasis in Mice**. *PLoS ONE*, **7**(5):e37803, May 2012.

[233] J. Van Der Vies. **Two Methods for the Determination of Glycogen in Liver**. *Biochemical Journal*, **57**(3):410–416, July 1954.

[234] Emile van Schaftingen and Isabelle Gerin. **The Glucose-6-Phosphatase System.** *Biochemical Journal*, **362**(Pt 3):513–532, March 2002.

[235] Tamas Varga, Zsolt Czimmerer, and Laszlo Nagy. **PPARs Are a Unique Set of Fatty Acid Regulated Transcription Factors Controlling Both Lipid Metabolism and Inflammation**. *Biochimica et Biophysica Acta*, **1812**(8):1007, August 2011.

[236] Antonio Vidal-Puig, Mercedes Jimenez-Liñan, Bradford B. Lowell, Andreas Hamann, E Hu, Bruce M. Spiegelman, Jeffrey S. Flier, and David E. Moller. **Regulation of PPAR Gamma Gene Expression by Nutrition and Obesity in Rodents.** *Journal of Clinical Investigation*, **97**(11):2553–2561, June 1996.

[237] Alexandre Wajngot, Visvanathan Chandramouli, William C. Schumann, Karin Ekberg, Paul K. Jones, Suad Efendic, and Bernard R. Landau. **Quantitative Contributions of Gluconeogenesis to Glucose Production during Fasting in Type 2 Diabetes Mellitus**. *Metabolism - Clinical and Experimental*, **50**(1):47–52, January 2001.

[238] Wencke Walter, Fátima Sánchez-Cabo, and Mercedes Ricote. **GOplot: An R Package for Visually Combining Expression Data with Functional Analysis**. *Bioinformatics*, **31**(17):2912–2914, September 2015.

[239] Ronald J. A. Wanders, Jos P. N. Ruiter, Lodewijk IJlst, Hans R. Waterham, and Sander M. Houten. **The Enzymology of Mitochondrial Fatty Acid Beta-Oxidation and Its Application to Follow-up Analysis of Positive Neonatal Screening Results**. *Journal of Inherited Metabolic Disease*, **33**(5):479, October 2010.

[240] Wen-Fei Wang, Si-Ming Li, Gui-Ping Ren, Wei Zheng, Yu-Jia Lu, Yin-Hang Yu, Wen-Juan Xu, Tian-He Li, Li-Hong Zhou, Yan Liu, and De-Shan Li. **Recombinant Murine Fibroblast Growth Factor 21 Ameliorates Obesity-Related Inflammation in Monosodium Glutamate-Induced Obesity Rats**. *Endocrine*, **49**(1):119–129, May 2015.

[241] Michael C. Wendl and Richard K. Wilson. **Aspects of Coverage in Medical DNA Sequencing**. *BMC Bioinformatics*, **9**:239, May 2008.

[242] Lynda M. Williams, Fiona M. Campbell, Janice E. Drew, Christiane Koch, Nigel Hoggard, William D. Rees, Torkamol Kamolrat, Ha Thi Ngo, Inger-Lise Steffensen, Stuart R. Gray, and Alexander Tups. **The Development of Diet-Induced Obesity and Glucose Intolerance in C57Bl/6 Mice on a High-Fat Diet Consists of Distinct Phases**. *PLoS ONE*, **9**(8):e106159, August 2014.

[243] Chaodong Wu, Salmaan A. Khan, and Alex J. Lange. **Regulation of Glycolysis—Role of Insulin**. *Experimental Gerontology*, **40**(11):894–899, November 2005.

[244] Zhidan Wu, Ping Jiao, Xueming Huang, Bin Feng, Yajun Feng, Shengyong Yang, Phillip Hwang, Jing Du, Yaohui Nie, Guozhi Xiao, and Haiyan Xu. **MAPK Phosphatase–3 Promotes Hepatic Gluconeogenesis through Dephosphorylation of Forkhead Box O1 in Mice**. *The Journal of Clinical Investigation*, **120**(11):3901, November 2010.

[245] Phillip Wulfridge, Ben Langmead, Andrew P. Feinberg, and Kasper D. Hansen. **Analyzing Whole Genome Bisulfite Sequencing Data from Highly Divergent Genotypes**. *Nucleic Acids Research*, page 076844, August 2019.

[246] Yue Xiong, Q.-Y. Lei, Shixin Zhao, and K-L. Guan. **Regulation of Glycolysis and Gluconeogenesis by Acetylation of PKM and PEPCK**. *Cold Spring Harbor symposia on quantitative biology*, **76**:285–289, November 2011.

[247] Dongkuan Xu and Yingjie Tian. **A Comprehensive Survey of Clustering Algorithms**. *Annals of Data Science*, **2**(2):165–193, June 2015.

[248] Nirmala Yabaluri and Murali D. Bashyam. **Hormonal Regulation of Gluconeogenic Gene Transcription in the Liver**. *Journal of Biosciences*, **35**(3):473–484, September 2010.

[249] Won-Mo Yang, Kyung-Ho Min, and Wan Lee. **Induction of miR-96 by Dietary Saturated Fatty Acids Exacerbates Hepatic Insulin Resistance through the Suppression of INSR and IRS-1**. *PLoS ONE*, **11**(12):e0169039, December 2016.

[250] Jian Ye, George Coulouris, Irena Zaretskaya, Ioana Cutcutache, Steve Rozen, and Thomas L Madden. **Primer-BLAST: A Tool to Design Target-Specific Primers for Polymerase Chain Reaction**. *BMC Bioinformatics*, **13**:134, June 2012.

[251] Yimeng Yin, Ekaterina Morgunova, Arttu Jolma, Eevi Kaasinen, Biswajyoti Sahu, Syed Khund-Sayeed, Pratyush K. Das, Teemu Kivioja, Kashyap Dave, Fan Zhong, Kazuhiro R. Nitta, Minna Taipale, Alexander Popov, Paul A. Ginno, Silvia Domcke, Jian Yan, Dirk Schübeler, Charles Vinson, and Jussi Taipale. **Impact of Cytosine Methylation on DNA Binding Specificities of Human Transcription Factors**. *Science*, **356**(6337):eaaj2239, May 2017.

[252] Wai-Shin Yong, Fei-Man Hsu, and Pao-Yang Chen. **Profiling Genome-Wide DNA Methylation**. *Epigenetics & Chromatin*, **9**:26, June 2016.

[253] Xunmei Yuan, Kazutaka Tsujimoto, Koshi Hashimoto, Kenichi Kawahori, Nozomi Hanzawa, Miho Hamaguchi, Takami Seki, Makiko Nawa, Tatsuya Ehara, Yohei Kitamura, Izuho Hatada, Morichika Konishi, Nobuyuki Itoh, Yoshimi Nakagawa, Hitoshi Shimano, Takako Takai-Igarashi, Yasutomi Kamei, and Yoshihiro Ogawa. **Epigenetic Modulation of Fgf21 in the Perinatal Mouse Liver Ameliorates Diet-Induced Obesity in Adulthood**. *Nature Communications*, **9**:636, February 2018.

[254] Daniel R. Zerbino, Premanand Achuthan, Wasiu Akanni, M. Ridwan Amode, Daniel Barrell, Jyothish Bhai, Konstantinos Billis, Carla Cummins, Astrid Gall, Carlos García Girón, Laurent Gil, Leo Gordon, Leanne Haggerty, Erin Haskell, Thibaut Hourlier, Osagie G. Izuogu, Sophie H. Janacek, Thomas Juettemann, Jimmy Kiang To, Matthew R. Laird, Ilias Lavidas, Zhicheng Liu, Jane E. Loveland, Thomas Maurel, William McLaren, Benjamin Moore, Jonathan Mudge, Daniel N. Murphy, Victoria Newman, Michael Nuhn, Denye Ogeh, Chuang Kee Ong, Anne Parker, Mateus Patricio, Harpreet Singh Riat, Helen Schuilenburg, Dan Sheppard, Helen Sparrow, Kieron Taylor, Anja Thormann, Alessandro Vullo, Brandon Walts, Amonida Zadissa, Adam Frankish, Sarah E. Hunt, Myrto Kostadima, Nicholas Langridge, Fergal J. Martin, Matthieu Muffato, Emily Perry, Magali Ruffier, Dan M. Staines, Stephen J. Trevanion, Bronwen L. Aken, Fiona Cunningham, Andrew Yates, and Paul Flicek. **Ensembl 2018**. *Nucleic Acids Research*, **46**(D1):D754–D761, January 2018.

[255] Lin Zhang, Lan Ge, Tai Tran, Kurt Stenn, and Stephen M. Prouty. **Isolation and Characterization of the Human Stearoyl-CoA Desaturase Gene Promoter: Requirement of a Conserved CCAAT Cis-Element**. *Biochemical Journal*, **357**(1):183–193, July 2001.

[256] Pili Zhang, Tianjiao Chu, N. Dedousis, Benjamin S. Mantell, Ian Sipula, Lucy Li, Kimberly D. Bunce, Patricia A. Shaw, Liora S. Katz, Jun Zhu, Carmen Argmann, Robert M. O'Doherty, David G. Peters, and Donald K. Scott. **DNA Methylation Alters Transcriptional Rates of Differentially Expressed Genes and Contributes to Pathophysiology in Mice Fed a High Fat Diet**. *Molecular Metabolism*, **6**(4):327–339, February 2017.

[257] Jia Zhou, Renee L. Sears, Xiaoyun Xing, Bo Zhang, Daofeng Li, Nicole B. Rockweiler, Hyo Sik Jang, Mayank N.K. Choudhary, Hyung Joo Lee, Rebecca F. Lowdon, Jason Arand, Brianne Tabers, C. Charles Gu, Theodore J. Cicero, and Ting Wang. **Tissue-Specific DNA Methylation Is Conserved across Human, Mouse, and Rat, and Driven by Primary Sequence Conservation**. *BMC Genomics*, **18**:724, September 2017.

[258] Michael J. Ziller, Kasper D. Hansen, Alexander Meissner, and Martin J. Aryee. **Coverage Recommendations for Methylation Analysis by Whole Genome Bisulfite Sequencing**. *Nature methods*, **12**(3):230–232, March 2015.

[259] Paul Z. Zimmet. **Diabetes and Its Drivers: The Largest Epidemic in Human History?** *Clinical Diabetes and Endocrinology*, **3**:1, January 2017.